

# Advances in Materials Science Research

Volume  
34

Maryann C. Wythers  
Editor

NOVA

Complimentary Contributor Copy



**ADVANCES IN MATERIALS SCIENCE RESEARCH**

**ADVANCES IN MATERIALS  
SCIENCE RESEARCH**

**VOLUME 34**

No part of this digital document may be reproduced, stored in a retrieval system or transmitted in any form or by any means. The publisher has taken reasonable care in the preparation of this digital document, but makes no expressed or implied warranty of any kind and assumes no responsibility for any errors or omissions. No liability is assumed for incidental or consequential damages in connection with or arising out of information contained herein. This digital document is sold with the clear understanding that the publisher is not engaged in rendering legal, medical or any other professional services.

**Complimentary Contributor Copy**

# **ADVANCES IN MATERIALS SCIENCE RESEARCH**

Additional books and e-books in this series can be found  
on Nova's website under the Series tab.



**ADVANCES IN MATERIALS SCIENCE RESEARCH**

**ADVANCES IN MATERIALS  
SCIENCE RESEARCH**

**VOLUME 34**

**MARYANN C. WYTHERS  
EDITOR**



**Complimentary Contributor Copy**

Copyright © 2018 by Nova Science Publishers, Inc.

**All rights reserved.** No part of this book may be reproduced, stored in a retrieval system or transmitted in any form or by any means: electronic, electrostatic, magnetic, tape, mechanical photocopying, recording or otherwise without the written permission of the Publisher.

We have partnered with Copyright Clearance Center to make it easy for you to obtain permissions to reuse content from this publication. Simply navigate to this publication's page on Nova's website and locate the "Get Permission" button below the title description. This button is linked directly to the title's permission page on [copyright.com](http://copyright.com). Alternatively, you can visit [copyright.com](http://copyright.com) and search by title, ISBN, or ISSN.

For further questions about using the service on [copyright.com](http://copyright.com), please contact:

Copyright Clearance Center

Phone: +1-(978) 750-8400

Fax: +1-(978) 750-4470

E-mail: [info@copyright.com](mailto:info@copyright.com).

### **NOTICE TO THE READER**

The Publisher has taken reasonable care in the preparation of this book, but makes no expressed or implied warranty of any kind and assumes no responsibility for any errors or omissions. No liability is assumed for incidental or consequential damages in connection with or arising out of information contained in this book. The Publisher shall not be liable for any special, consequential, or exemplary damages resulting, in whole or in part, from the readers' use of, or reliance upon, this material. Any parts of this book based on government reports are so indicated and copyright is claimed for those parts to the extent applicable to compilations of such works.

Independent verification should be sought for any data, advice or recommendations contained in this book. In addition, no responsibility is assumed by the publisher for any injury and/or damage to persons or property arising from any methods, products, instructions, ideas or otherwise contained in this publication.

This publication is designed to provide accurate and authoritative information with regard to the subject matter covered herein. It is sold with the clear understanding that the Publisher is not engaged in rendering legal or any other professional services. If legal or any other expert assistance is required, the services of a competent person should be sought. FROM A DECLARATION OF PARTICIPANTS JOINTLY ADOPTED BY A COMMITTEE OF THE AMERICAN BAR ASSOCIATION AND A COMMITTEE OF PUBLISHERS.

Additional color graphics may be available in the e-book version of this book.

### **Library of Congress Cataloging-in-Publication Data**

ISBN: ; 9: /3/75836/646/8"%"gDqqm#

ISSN: 2159-1997

*Published by Nova Science Publishers, Inc. † New York*

**Complimentary Contributor Copy**

# CONTENTS

<b>Preface</b>		<b>vii</b>
<b>Chapter 1</b>	Modelling of Plasma-Assisted Growth of Vertically Aligned Carbon Nanostructures <i>Igor B. Denysenko, Kostya (Ken) Ostrikov and Nikolay A. Azarenkov</i>	<b>1</b>
<b>Chapter 2</b>	Rayleigh and Brillouin Scattering Spectroscopy for Optical Material Science <i>Leonid V. Maksimov and Anatoli V. Anan'ev</i>	<b>59</b>
<b>Chapter 3</b>	Computer Study of the Removal of Heavy Metals from Graphene <i>Alexander Y. Galashev</i>	<b>115</b>
<b>Chapter 4</b>	Flexible Resistive Switching Memories: From Materials to Devices <i>Shuang Gao, Xiaohui Yi, Jie Shang, Bin Chen, Gang Liu and Run-Wei Li</i>	<b>157</b>
<b>Chapter 5</b>	Improving the Octane Number of Gasolines through the Transformation of n-Hexane into Branched Isomers <i>Angela Martins and Nelson Nunes</i>	<b>187</b>

<b>Chapter 6</b>	The Application of Strontium Dodecyl Sulfate, $\text{Sr}(\text{DS})_2$ in the Synthesis of 4,4'-Diaminotriarylmethanes-Leuco Malachite Materials	<b>211</b>
	<i>Najmeh Dashtaki and Farahnaz K. Behbahani</i>	
<b>Index</b>		<b>223</b>

## PREFACE

*Advances in Materials Science Research. Volume 34* begins with a review of results on the modelling of the plasma-assisted growth of vertically aligned carbon nanostructures (VACNs). Growth of carbon nanofibers, single-walled carbon nanotubes and other carbon nanostructures are considered, as well as studies that use the mechanistic models based on mass balance equations for species.

Next, data on the application of Rayleigh and Mandelstam-Brillouin scattering (RMBS) spectroscopy to controlling the elastic, elasto-optic, optical parameters of inorganic glasses, crystals, and glass-crystalline materials is reviewed. The possibilities of using RMBS spectroscopy for research and development of materials for optical and electro-optical fiber drawing, as well as glasses doped with rare earth ions and quantum dots, are considered.

The authors go on to propose that the purification of graphene from heavy metals can be performed by bombardment with noble gas clusters. The method of molecular dynamics is used to study the removal of copper, lead, and mercury from graphene by irradiating the target using a beam of Ar<sub>13</sub> or Xe<sub>13</sub> clusters with energies of 5–30 eV at angles of incidence 0°, 45°, 60°, and 90°.

As an indispensable component of future flexible electronics, flexible resistive switching memories have recently garnered great interest globally. As such, a comprehensive review on the recent progress in this

field is presented with a particular emphasis on materials and devices. A short discussion on the current challenges and future prospects of flexible resistive switching memories is also provided.

Following this, the authors aim to present a comprehensive examination of the different catalysts used in hydroisomerization reactions, focusing: the acid support, mainly zeolites, the precious metals that offer the hydrogenating sites and the methodologies used to produce effective bifunctional catalysts. The catalysts used in industrial refining processes as well as new research trends are surveyed.

A fast, efficient and versatile route for the synthesis of 4,4'-diamino-triarylmethanes using Sr(DS)<sub>2</sub> as a Lewis acid-surfactant-combined catalyst (LASCs) in the presence of N,N-dimethyl aniline and aryl aldehydes is reported in closing. LASCs not only act as a Lewis acid to activate substrate molecules, but also serve as a surfactant to form stable colloidal dispersion systems with organic substrates.

Chapter 1 - Results on modelling of the plasma-assisted growth of vertically aligned carbon nanostructures (VACNs) are reviewed. Growth of carbon nanofibers, single-walled carbon nanotubes and other carbon nanostructures is considered. Focus is made on studies that use the mechanistic models based on mass balance equations for species, which are adsorbed on catalyst nanoparticles or walls of the nanostructures. The growth mechanisms and the differences between the plasma- and neutral gas-grown carbon nanostructures are clarified, and the underlying physics and the key growth parameters are revealed. The analytical expressions for the VACN growth rates are presented, and effects of the ions and etching gas atoms from the ionized gas environment on the growth of the nanostructures are analysed. The analysis is carried out for the case when ions and neutrals from the plasma deposit homogeneously on the nanostructure surfaces, as well as when the deposition is inhomogeneous. The authors also present a theoretical model describing the nanostructure heating by ion and neutral gas fluxes from the plasma environment. Using the model, it is shown that fluxes from the plasma can substantially increase the temperature on the VACN top with respect to the substrate temperature. It is revealed how the temperature difference depends on the



substrate width, the VACN length, the neutral gas temperature and density, as well as the densities of the ions and atoms of the etching gas. The neutral and ion densities in plasma at the growth of the VACNs are also analysed using a 0D model for chemically active plasmas. The plasma properties, which are necessary for the growth of vertically aligned carbon nanostructures, are compared with those required for the formation of carbon nanoparticles in plasma. The results are verified by a direct comparison with the experimental data and found to be in good agreement.

Chapter 2 - Data on the application of Rayleigh and Mandelstam-Brillouin scattering (RMBS) spectroscopy to controlling the elastic, elastooptic, optical parameters of inorganic glasses, crystals, and glass-crystalline materials is generalized. The possibilities of using RMBS spectroscopy for research and development of materials for optical and electro-optical fiber drawing, as well as glasses doped with rare earth ions and quantum dots, are considered.

Chapter 3 - Efficient removal of hazardous heavy metals from the environment is an important problem, since most of these metals are highly toxic. Recently, graphene began to be used for the removal of environmental pollutants. Graphene is ineffective as an absorbent unless it is repeatedly used. This raises the problem of graphene cleaning for removal of the deposited materials. The method of molecular dynamics has been used to study the removal of copper, lead, and mercury from graphene by irradiating the target using a beam of  $\text{Ar}_{13}$  or  $\text{Xe}_{13}$  clusters with energies of 5–30 eV at angles of incidence  $0^\circ$ ,  $45^\circ$ ,  $60^\circ$ , and  $90^\circ$ . It is obtained that the cluster energy should be in the interval 20 – 30 eV for effective graphene cleaning in case of its copper contamination. There is no cleaning effect at vertical incidence ( $\theta = 0^\circ$ ) of  $\text{Ar}_{13}$  clusters. The bombardments at  $45^\circ$  and  $90^\circ$  incident angles are the most effective ones at a moderate and big amount of deposited copper respectively. The complete removal of lead from graphene with hydrogenated edges and bivalencies was achieved at the angle of incidence of  $\text{Xe}_{13}$  clusters equal to  $45^\circ$ . A major part of the film was separated from graphene in the form of an island, which, after separation, was transformed into a three-dimensional structure. The stresses present in the graphene sheet changed in the course

of bombardment, but the stressed state retained after the bombardment was terminated. The type of the distribution of stresses in graphene indicates the absence of enhancement of the stressed state in the course of bombardment. The bombardment at angles of incidence of clusters less than  $75^\circ$  substantially enhances the roughness of graphene. The complete removal of mercury from graphene with hydrogenated edges was achieved at the angles of incidence of clusters equal to  $45^\circ$  and  $60^\circ$  with the energies of the beam  $E_{Xe} \geq 15$  and  $10$  eV, respectively. The film of mercury, which has a tendency to become rolled up into a drop, is separated from graphene in the form of single atoms, dimers, trimers, and spherical droplets. In the course of the bombardment, mercury exhibits a weak cohesion with graphene. The bombardment at the angle of incidence of clusters equal to  $45^\circ$  leads to the lowest roughness of graphene. The bombardments in the entire range of the angles of cluster incidence ( $0^\circ - 90^\circ$ ) have resulted in no significant damages in the hydrogenated edges of the graphene sheet after its cleaning from both lead and mercury. Thus, the purification of graphene from heavy metals can be performed by bombardment with noble gas clusters.

Chapter 4 - As an indispensable component for future flexible electronics, flexible resistive switching memories have recently aroused great interest all around the world. In this chapter, a comprehensive review on the recent progress in this field is presented, with a particular emphasis on materials and devices. First, a brief introduction is given on the basic concepts of flexible resistive switching memories. Next, storage media as well as electrode and substrate materials used in flexible resistive switching memories are summarized in detail. Third, attention is focused on the fabrication technologies of flexible resistive switching memories and the performance of obtained devices. Finally, a short discussion on the current challenges and future prospects of flexible resistive switching memories is provided.

Chapter 5 - A tendency to eliminate benzene and other aromatic hydrocarbons from gasoline, keeping a high-octane number, is a current topic in refining industry due to strict environmental legislation. Therefore, the transformation of short chain n-paraffins (n-pentane or n-hexane) into

branched isomers, with minimal cracking, is one of the key processes in the production of high octane gasolines through catalytic hydroisomerization reactions. These reactions are generally carried out over bifunctional heterogeneous catalysts, containing small amounts of metal particles, like platinum or palladium, dispersed on an acid support such as zeolites. According to the bifunctional mechanism, linear alkanes, such as n-hexane, suffers dehydrogenation on a metallic site, resulting on n-hexene. This reactive intermediate undergoes one or more skeletal isomerization reactions on the acid sites, or even cracking, before being hydrogenating on another metallic site, resulting in a mixture of dimethylbutanes, methylpentanes, or cracking products. The balance between the number of active sites, acid and metallic, as well as the pore geometry and accessibility to molecular transport are determinant factors that influence the product distribution, being dimethylbutanes (2,2 and 2,3-dimethylbutane) the most desired products due to their higher RON (research octane number) and cracking products the ones to be avoided. This chapter aims to provide a comprehensive examination of the different catalysts used in hydroisomerization reactions, focusing: the acid support, mainly zeolites, the precious metals that offer the hydrogenating sites and the methodologies used to produce effective bifunctional catalysts. This chapter will survey the catalysts used in industrial refining processes as well as new trends from the academic research.

Chapter 6 - A fast, efficient and versatile route for the synthesis of 4,4'-diaminotriarylmethanes using  $\text{Sr}(\text{DS})_2$  as a Lewis acid-surfactant-combined catalyst (LASCs) in the presence of *N,N*-dimethyl aniline and aryl aldehydes is reported. LASCs not only act as a Lewis acid to activate substrate molecules, but also serve as a surfactant to form stable colloidal dispersion systems with organic substrates. Also, the others advantages of LASCs are easy separation and recovery, high activity, selectivity, as a Lewis acid to activate the substrate molecules and as a surfactant to help to solubilize the organic compounds in water.



*Chapter 1*

**MODELLING OF PLASMA-ASSISTED  
GROWTH OF VERTICALLY ALIGNED  
CARBON NANOSTRUCTURES**

***Igor B. Denysenko<sup>1,\*</sup>, Kostya (Ken) Ostrikov<sup>2</sup>  
and Nikolay A. Azarenkov<sup>1</sup>***

<sup>1</sup>School of Physics and Technology, V. N. Karazin Kharkiv  
National University, Kharkiv, Ukraine

<sup>2</sup>School of Chemistry, Physics and Mechanical Engineering, Queensland  
University of Technology, Brisbane, QLD, Australia;  
CSIRO-QUT Joint Sustainable Processes and Devices Laboratory,  
Commonwealth Scientific and Industrial Research Organization,  
NSW, Australia;  
Plasma Nanoscience, School of Physics,  
The University of Sydney, Sydney, NSW, Australia

**ABSTRACT**

Results on modelling of the plasma-assisted growth of vertically aligned carbon nanostructures (VACNs) are reviewed. Growth of carbon nanofibers, single-walled carbon nanotubes and other carbon nanostructures is considered. Focus is made on studies that use the

mechanistic models based on mass balance equations for species, which are adsorbed on catalyst nanoparticles or walls of the nanostructures. The growth mechanisms and the differences between the plasma- and neutral gas-grown carbon nanostructures are clarified, and the underlying physics and the key growth parameters are revealed. The analytical expressions for the VACN growth rates are presented, and effects of the ions and etching gas atoms from the ionized gas environment on the growth of the nanostructures are analysed. The analysis is carried out for the case when ions and neutrals from the plasma deposit homogeneously on the nanostructure surfaces, as well as when the deposition is inhomogeneous. We also present a theoretical model describing the nanostructure heating by ion and neutral gas fluxes from the plasma environment. Using the model, it is shown that fluxes from the plasma can substantially increase the temperature on the VACN top with respect to the substrate temperature. It is revealed how the temperature difference depends on the substrate width, the VACN length, the neutral gas temperature and density, as well as the densities of the ions and atoms of the etching gas. The neutral and ion densities in plasma at the growth of the VACNs are also analysed using a 0D model for chemically active plasmas. The plasma properties, which are necessary for the growth of vertically aligned carbon nanostructures, are compared with those required for the formation of carbon nanoparticles in plasma. The results are verified by a direct comparison with the experimental data and found to be in good agreement.

**Keywords:** carbon nanostructures, plasma enhanced chemical vapour deposition, growth models

## 1. INTRODUCTION

Vertically-aligned carbon nanostructures (VACNs, e.g., nanotubes, nanofibers, nanoribbons, nanorods, nanowires, etc. [1-10]) have attracted widespread attention in the last decades thanks to their specific electrical, mechanical, physical and chemical properties. They are potentially attractive for many applications including nanoelectronics, field emission, nanocomposites, energy storage, sensors, biomedical device, and several others [5, 7, 10-12].

VACNs can be produced by many pathways such as arc discharge [13], laser ablation [14], thermal chemical vapour deposition (CVD) [15],



and plasma enhanced chemical vapour deposition (PECVD) [16]. In particular, PECVD techniques have been successfully used for the production of well-aligned carbon nanotubes (CNTs) and carbon nanofibers (CNFs). The growth of VACNs usually takes place in presence of catalyst nanoparticles, which serve as a growth pattern for the nanostructures, activate the surface for nucleation of VACNs, and help controlling the thickness of the nanostructures [17-21].

Experiments have shown that carbon nanostructures may be grown via PECVD at significantly lower substrate temperatures and feature better alignment compared to the nanostructures synthesized in thermal CVD [5, 22]. It is supposed that the low temperature growth is due to the fact that PECVD provides highly reactive, (partially) dehydrogenated species to the catalyst. Thus, whereas a high dehydrogenation barrier must be overcome in thermal CVD on the catalyst surface, this barrier is not, or only partially, present in PECVD growth [23]. It is assumed that the electric field near the substrate is responsible for alignment of carbon nanostructures during PECVD growth. Due to the electric field effect, the vertically-aligned carbon nanostructures can be deposited in "forests" or as individual free-standing structures [24]. Plasma affects also the catalyst particles [25]. Exposure of the catalyst particles to a plasma may prevent agglomeration of the particles during nanostructure growth [20, 26] and aid in restructuring the catalyst [27]. Atomic hydrogen, which is usually produced in a large amount during PECVD, may reduce oxides, causing the catalysts to transform into their metallic state, to be catalytically active during nanostructure growth. Plasma also causes ion-induced mobility of the surface atoms and the ion bombardment erosion of the catalyst particles [23]. As a result, the plasma pretreatment may narrow the particle distribution, so that narrower diameter distributions for nanostructures grown from pretreated substrates can be obtained. Narrow-chirality distributions of single-walled carbon nanotubes (SWCNTs) may be achieved by controlling various plasma parameters in PECVD [21, 28-33]. Moreover, plasma pretreatment of catalyst nanoparticles was found to favour the growth of nanotube forests by root growth, as it binds the

catalyst nanoparticles more strongly to the substrate than thermal pretreatment [34].

However, in spite of many experimental studies and considerable success on synthesis of vertically-aligned carbon nanostructures in plasmas, modelling results are insufficient in the field because of modelling complexities. In the PECVD, processes on a substrate and in plasma are characterized by extreme ranges in both the time and length scales [35]. As a result, a realistic model for the PECVD should be divided, at least, on the following two submodels. The first submodel should describe the processes taking place on the substrate, while the second one should give information about plasma properties including the electron, ion and neutral particle densities, their drift velocities, temperatures and energy distribution functions in plasma volume. Obviously, these submodels should be coupled.

The processes taking place on the substrate during growth of VACNs can be described using different approaches. The most accurate simulations of VACNT growth are atomistic and are based on quantum mechanical methods or use the molecular dynamic (MD) technique. The simulations based on quantum mechanical methods provide very detailed and accurate information, but they are limited to very small systems and timescales of the order of 100 atoms for a few picoseconds [36]. Molecular dynamic simulations can deal with larger systems (thousands or millions of atoms) and somewhat longer timescales. Meantime, the quality of these MD simulations strongly depends on the reliability of the interatomic interaction potential used, and the MD simulations suffer also from long calculation times [36]. In present, they are limited to study only certain aspects of the growth process and cannot yet be integrated in plasma chemistry simulations.

The models for VACN growth, which can be easily integrated in plasma models, are mechanistic models. Typically, mechanistic models account for a number of physicochemical processes, such as adsorption and desorption of species at the surface of the metal catalyst particle, surface reactions (both on the catalyst surface and the substrate surface), surface and bulk diffusion, and nanostructure nucleation and growth. These

models are more macroscale (as compared with atomistic models), and mechanistic simulations require minor computational efforts as compared with atomistic simulations. However, mechanistic models are demanding the threshold energies and/or rates for different surface and bulk processes taking place on the surface or inside of the catalyst nanoparticle and the surface of VACNS. The threshold energies and rates may be obtained from atomistic calculations and/or analysis of experimental data.

In this chapter, we describe mechanistic models for the plasma-assisted growth of SWCNTs and CNFs, which are based on mass balance equations for adsorbed species, and a thermal model for study of temperature variation along a CNF and a substrate. Main results following from these models are reviewed and compared with the available experimental data on growth of CNTs and CNFs. The analytical expressions for the VACN growth rates are presented, and effects of the ions and etching gas atoms from the ionized gas environment on the growth of the nanostructures are analysed. The analysis is carried out for the case when ions and neutrals from the plasma deposit homogeneously on the nanostructure surfaces, as well as when the deposition is inhomogeneous. We also present our results on modelling of a plasma used in PECVD of VACNs. Since plasma-assisted growth of VACNs may be accompanied by formation of carbonaceous nanoparticles in plasma volume [37], properties of a plasma used for nanoparticles' formation are also analysed. Results on modelling of the plasma-assisted growth of VACNs, which are available in the literature in present, are reviewed.

The book chapter is organized as follows. In section 2, we describe surface deposition models for growth of an array of SWCNTs and an individual SWCNT. The results from these mechanistic models are also presented and analysed in this section. Section 3 presents surface diffusion and thermal models describing plasma-assisted growth of CNFs, as well as results of numerical calculations obtained using these models. In section 4, we review results on modelling of growth of different VACNs in plasma environment, which are available in the literature in present. Section 5 reviews modelling results on study of plasmas used for growth of vertically aligned carbon nanostructures and carbonaceous nanoparticles. We also

present our results on modelling of these plasma systems, which were obtained using 0D models. This chapter is concluded with a summary of main plasma effects on growth of VACNs, which were determined using modelling efforts.

## 2. MODELLING OF SWCNT GROWTH

The growth of SWCNTs in a plasma environment may be modelled using mass balance equations for adsorbed species. It was made for free-standing nanotubes as well as for the case where SWCNTs are growing in an array in [38] and [39], respectively. In both the cases, we considered closed-ended growth of SWCNTs with semi-spherical tops, assuming that the catalyst particles are anchored to the substrate and base of nanotubes [40-43] at  $x = L_{NT}$ , where  $x$  is the coordinate along a SWCNT axis, and  $L_{NT}$  is the nanotube length (Figure 1). Each nucleated SWCNT grows on a metal catalyst particle so that the pattern of the nanostructure array repeats the catalyst pattern. Carbon atoms participate in SWCNT growth when they reach the catalyst particles.

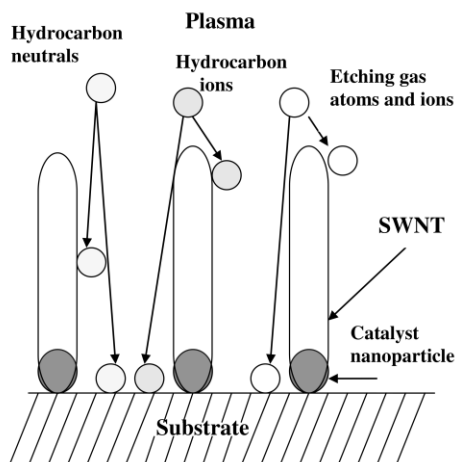


Figure 1. Schematic picture of deposition of hydrocarbon neutrals, ions and etching gas particles on the SWCNTs and substrate.

## 2.1. Surface Deposition Model for Growth of an Array of SWCNTs

First, consider the growth of an array of SWCNTs, assuming that all SWCNTs have the same length. The plasma (for example, created in a  $C_2H_2/H_2$  gas discharge) is assumed to be located above the SWCNT array. The main species that interact with the SWCNT surfaces are hydrocarbon neutrals (here  $C_2H_2$ ), hydrocarbon ions (here  $C_2H_2^+$ ), atoms or molecules of an etching gas (here atomic hydrogen H), and etching ions (here hydrogen ions  $H^+$ ). Due to the interaction of plasma species with SWCNTs, the SWCNTs and the surface between the SWCNTs are covered by  $C_2H_2$  molecules and hydrogen and carbon atoms. The total surface coverage by the particles is  $\theta_t = \theta_{CH} + \theta_H + \theta_C$ , where  $\theta_\alpha$  is the surface coverage by species  $\alpha$ . Here,  $\alpha = CH, H$  and  $C$  denote  $C_2H_2, H$  and  $C$  neutrals, respectively.

$C_2H_2$  is the key growth precursor for SWCNTs, CNFs, CNTs and nanoparticles in most of hydrocarbon plasmas, even if  $CH_4$  is the feedstock [44-46]. The atomic hydrogen and/or hydrogen ions are responsible for the removal (e.g., etching) of amorphous carbon. In  $NH_3/C_2H_2$ ,  $H_2/C_2H_2$  and  $H_2/CH_4$  plasmas, usually used for growth of carbon nanostructures, the atomic hydrogen appears mainly due to the dissociation of  $H_2$  and hydrocarbon molecules in the plasma volume [47, 48]. The  $H^+$  ions are produced by direct ionization of atomic hydrogen or dissociative ionization of molecular hydrogen and dissociation of  $H_2^+$  [47, 48]. For simplicity, only the ions  $C_2H_2^+$  and  $H^+$  were accounted for in the model. In reality, a reactive plasma contains a lot of different ions. The abundance of carbon-containing ions such as  $C_2H_2^+$  and  $C_2H^+$  was found to be connected with the amorphous carbon deposition [48, 49].

The hydrocarbon neutrals and atomic hydrogen are adsorbed and desorbed on the SWCNT surfaces as well as on the substrate surface between the SWCNTs. Generation of carbon atoms on the SWCNT surfaces is due to the following reactions: (i) thermal dissociation of  $C_2H_2$ , (ii) ion bombardment of adsorbed  $C_2H_2$  neutrals, and (iii) decomposition of  $C_2H_2^+$  ions. The carbon yield due to thermal dissociation is

$2\theta_{CH}\nu_0\nu\exp(-\delta E_i/k_B T_s)$ , where  $\delta E_i \sim 2.1$  eV is the activation energy of thermal dissociation [50],  $\nu_0 \sim 1.3 \times 10^{15}$  cm<sup>-2</sup> [51] is the number of adsorption sites per unit area,  $k_B$  is the Boltzmann constant, and  $T_s$  is the SWCNT surface temperature. It is assumed that  $T_s$  is uniform along the SWCNTs.

It is also assumed that an ion from the plasma has sufficient energy  $E_i$  ( $\geq 2.1$  eV) to decompose a single C<sub>2</sub>H<sub>2</sub> molecule on the SWCNTs. The rest of ion energy is spent on heating of the nanostructure. The carbon yield due to ion bombardment is  $2\theta_{CH}j_i$ , where  $j_i \sim n_i\sqrt{T_e/m_i}$  is the ion flux,  $T_e \sim 1.5$  eV is the plasma electron temperature, and  $n_i$  and  $m_i$  are the ion density and mass, respectively. The C<sub>2</sub>H<sub>2</sub><sup>+</sup> ions bombarding a SWCNT decompose ( $C_2H_2^+ \rightarrow 2C_{(ads)} + H_{2(plasma)}$ ) on the surface, resulting in deposition of carbon on the SWCNTs. The carbon atoms generated on the SWCNTs by thermal dissociation and ion bombardment diffuse to the catalyst particles located at  $x = L_{NT}$  at the nanotube base and incorporate into the growing SWCNTs [52]. The surface diffusion coefficient for the atoms is  $D_s = a_0^2\nu\exp(-\delta E_d/k_B T_s)$  [53], where  $a_0 \cong 0.14$  nm is the interatomic distance, and  $\delta E_d \sim 0.8$  eV is the activation energy of surface diffusion for carbon on a SWCNT surface [54, 55].

The model presented in [39] accounts for inhomogeneous deposition of the species from the plasma onto the SWCNT surfaces. Following the results of Monte-Carlo simulations [53], the flux density of impinging neutral species was assumed to be  $j_a = \tilde{n}_a\nu_{tha}\exp(-x/l^*)/4$ , where  $\tilde{n}_a$  and  $\nu_{tha}$  are the plasma bulk density and thermal velocity of species  $\alpha$  (C<sub>2</sub>H<sub>2</sub> or H), respectively;  $l^*$  is the depth of neutrals penetration into the SWCNT array which can be estimated as  $l^* \approx 1/(\pi RN)$  [53], where  $R$  is the nanotube radius and  $N$  is the SWCNT surface density. For example, when  $R = 1$  nm and  $N = 10^{11}$  cm<sup>-2</sup> (that corresponds to the distance between nanotubes  $\approx 30$  nm), the penetration depth is about 0.3  $\mu$ m. In [39], it was assumed that the depths of penetration for C<sub>2</sub>H<sub>2</sub> and H are the same. The ion flux distribution along SWCNTs depends on both the plasma and



nanoarray parameters [56]. Varying the plasma sheath and SWCNT length, fairly uniform deposition of ions on the SWCNTs can be achieved, as well as predominant deposition on the top or close to the nanostructure base. In [56], it was shown that the nearly uniform ion flux distribution can be obtained even for rather dense nanotube arrays. In [39], it was assumed that the ions deposit more homogeneously on the lateral SWCNT surfaces than neutrals, since the ion velocity along the nanotubes ( $\approx \sqrt{2E_i/m_i}$ , where  $E_i$  is the ion energy) is higher than the velocity of neutral species ( $\approx (1/4)\sqrt{8k_B T_s/\pi m_n}$ , where  $m_n$  is the neutral mass). Since the penetration depth of the plasma-generated species in the SWCNT array is proportional to their velocity along the nanotubes, the penetration depth of the plasma ions can be estimated as [39]:  $l_i^* \approx l^* \sqrt{4\pi E_i/k_B T_s}$ . The value  $l_i^*$  characterizes the scale of inhomogeneity of the ion deposition on SWCNTs.

The adsorption and desorption fluxes of the neutrals ( $C_2H_2$  and  $H$ ) on the surfaces of the SWCNTs are [39, 51]:

$$j_{cads} = j_\alpha(1 - \theta_i), \quad (1)$$

$$j_{ades} = \theta_\alpha \nu_0 \nu \exp(-E_a/k_B T_s), \quad (2)$$

where  $E_a$  is the adsorption energy.

The adsorbed species can react with the atomic hydrogen and hydrogen ions from the plasma (for example,  $C_2H_2 + H_{(plasma)} \rightarrow C_2H_{3(plasma)}$ ;  $C_2H_{2(ads)} + H^+_{(plasma)} \rightarrow C_2H_{3(plasma)}$ ), yielding gas-phase products. The consumption flux of adsorbed neutral species participating in an adsorbed-layer reaction is [51]:

$$j_{reac} = \theta_\alpha \nu_0 \sigma_{ads} (j_H + j_H^+),$$

where  $j_H$  and  $j_H^+$  are the incident fluxes of atomic hydrogen and hydrogen ions, respectively, and  $\sigma_{ads} \sim 6.8 \times 10^{-16} \text{ cm}^2$  is the cross-section of the adsorbed-layer reaction. The processes on the SWCNT surface, which were taken into account in [39], are shown in Table 1.

Taking into account the processes listed in Table 1, the mass balance equations for  $\text{C}_2\text{H}_2$ , H, and C species on a SWCNT surface are [39]

$$j_{CH}(1 - \theta_t) - \theta_{CH}L = 0, \quad (3)$$

$$(j_H + j_H^+)(1 - \theta_t) - \theta_H K = 0, \quad (4)$$

$$D_s d^2 n_c / dx^2 + 2n_{CH} \nu \exp(-\delta E_i / k_B T_s) + 2\theta_{CH} j_i + 2j_i - n_c \nu \exp(-E_{ev} / k_B T_s) - n_c \sigma_{ads} (j_H + j_H^+) = 0, \quad (5)$$

where  $n_a = \theta_a \nu_0$  is the surface concentration of the species  $\alpha$  ( $= \text{C}_2\text{H}_2$ , H, and C),  $L = \nu_0 \nu \exp(-E_a / k_B T_s) + \nu_0 \nu \exp(-E_i / k_B T_s) + \nu_0 \sigma_{ads} (j_H + j_H^+) + j_i$ , and  $K = \nu_0 \nu \exp(-E_a / k_B T_s) + \nu_0 \sigma_{ads} (j_H + j_H^+)$ .

From Equations (3) – (5), one obtains

$$D_s \frac{d^2 n_c}{dx^2} + Q_C - \frac{n_c}{\tau_a} = 0, \quad (6)$$

where  $Q_C = 2(C_1 + j_i)$  is the effective carbon flux to the SWCNT surfaces,

$$C_1 = \frac{\nu_0 \nu \exp(-\delta E_i / k_B T_s) + j_i}{1 + L j_H / (K j_{CH}) + L / j_{CH}},$$

and  $\tau_a = 1 / [2C_1 / \nu_0 + \nu \exp(-E_{ev} / k_B T_s) + \sigma_{ads} (j_H + j_H^+)]$  is the characteristic residence time of carbon species on the SWCNT surfaces.

In general, Equation (6) cannot be solved analytically. However, when the variation of the fluxes of neutrals and ions along the SWCNTs is weak,

the solution of Equation (6) can be found using the Wentzel-Kramers-Brillouin (WKB) approach. If  $\lambda_d \ll l^*, l_i^*$ , where  $\lambda_d = \sqrt{D_s \tau_a}$  is the surface diffusion length, the surface density of carbon atoms on the SWCNTs is

**Table 1. The surface processes on the SWCNTs included in the model and their corresponding parameters or functionality. Here  $\tilde{T}_s = k_B T_s$**

Processes	Functions/Parameters
Adsorption $C_2H_2(\text{plasma}) \rightarrow C_2H_2(\text{ads})$ $H(\text{plasma}) \rightarrow H(\text{ads})$ $H^+(\text{plasma}) \rightarrow H(\text{ads})$	$j_{CH}(1 - \theta_i)$ $j_H(1 - \theta_i)$ $j_H^+(1 - \theta_i)$
Desorption $C_2H_2(\text{ads}) \rightarrow C_2H_2(\text{des})$ $H(\text{ads}) \rightarrow H(\text{des})$	$\theta_{CH} \nu_0 \nu \exp(-E_a / \tilde{T}_s)$ $E_a = 2.9 \text{ eV}$ $\theta_H \nu_0 \nu \exp(-E_a / \tilde{T}_s)$ $E_a = 1.8 \text{ eV}$
Carbon evaporation $C(\text{ads}) \rightarrow C(\text{evaporation})$	$n_C \nu \exp(-E_{ev} / \tilde{T}_s)$ $E_{ev} = 1.8 \text{ eV}$
Thermal dissociation $C_2H_2(\text{ads}) \rightarrow 2C(\text{ads}) + H_2(\text{plasma})$	$n_{CH} \nu \exp(-\delta E_i / \tilde{T}_s)$ $\delta E_i = 2.1 \text{ eV}$
Ion-induced dissociation $C_2H_2^+ + C_2H_2(\text{ads}) \rightarrow 2C(\text{ads}) + H_2(\text{plasma}) + C_2H_2^+$	$2\theta_{CH} j_i$
Ion decomposition $C_2H_2^+ \rightarrow 2C(\text{ads}) + H_2(\text{plasma})$	$j_i$
Adsorbed layer reactions $C_2H_2(\text{ads}) + H(\text{plasma}) \rightarrow C_2H_3(\text{plasma})$ $C_2H_2(\text{ads}) + H^+(\text{plasma}) \rightarrow C_2H_3(\text{plasma})$ $C(\text{ads}) + H(\text{plasma}) \rightarrow CH(\text{plasma})$ $C(\text{ads}) + H^+(\text{plasma}) \rightarrow CH(\text{plasma})$ $H(\text{ads}) + H(\text{plasma}) \rightarrow H_2(\text{plasma})$ $H(\text{ads}) + H^+(\text{plasma}) \rightarrow H_2(\text{plasma})$	$\sigma_{ads} \approx 6.8 \times 10^{-16} \text{ cm}^2$
Surface diffusion of carbon atoms	$D_s = a_0^2 \nu \exp(-\delta E_d / \tilde{T}_s)$
Incorporation of carbon atoms in the SWCNT	$k = a_0 \nu \exp(-\delta E_{inc} / \tilde{T}_s)$

$$n_C \approx A \exp \left[ \int_0^x \frac{dy}{\lambda_D(y)} \right] + B \exp \left[ - \int_0^x \frac{dy}{\lambda_D(y)} \right] + Q_C \tau_a, \quad (7)$$

where  $A$  and  $B$  are constants.

To find these constants, it was assumed that  $d_x n_C = 0$  at the edge of the SWCNTs ( $x = 0$ ) and  $-D_s d_x n_C = k n_C$  at the base of the SWCNTs ( $x = L_{NT}$ ) [53]. Here,  $k = a_0 \nu \exp(-\delta E_{inc} / k_B T_s)$  is the kinetic constant (of carbon atom incorporation into the walls of the SWCNTs) and  $\delta E_{inc}$  is the energy barrier for the incorporation. It was also assumed that the energy barrier for carbon diffusion on a surface of the SWCNTs is larger than that at carbon-catalyst interface ( $\sim 0.4$  eV [17]), so that  $\delta E_{inc} = \delta E_d$  [53].

Taking into account the boundary conditions, one obtains

$$A \approx B \approx - \frac{Q_{C1} \tau_{a1}}{2(\cosh \zeta + (D_s / k \lambda_{D1}) \sinh \zeta)},$$

where  $\zeta = \int_0^{L_{NT}} (1 / \lambda_D) dx$ ,  $Q_{C1} = Q_C(x = L_{NT})$ ,  $\tau_{a1} = \tau_a(x = L_{NT})$ ,

$$\lambda_{D1} = \lambda_D(x = L_{NT}).$$

Then, the growth rate of the SWCNT forest is:

$$V_{NT} \approx -\Omega D_s d_x n_C \Big|_{x=L_{NT}} = \frac{k \Omega Q_{C1} \tau_{a1} \sinh(\zeta)}{\sinh(\zeta) + (k \lambda_{D1} / D_s) \cosh(\zeta)}, \quad (8)$$

where  $\Omega$  is the area per unit C atom in a SWCNT wall.

In the model developed in [39], it was assumed that the neutral and ionic species are also deposited between the vertically aligned SWCNTs. The deposition area is located at the same level as the base of the SWCNT forest ( $x \sim L_{NT}$ ). The deposition can be accompanied by the formation of a (usually amorphous) carbon film. The growth rate of the film is [50, 51]

$$V_{dep} = j_{dep} M_{dep} / \rho N_a, \quad (9)$$

where  $N_a$  is the Avogadro number,  $\rho$  is the film density (e.g.,  $\rho = 1.2 \text{ gcm}^{-3}$ ), and  $M_{dep} \sim 12 \text{ g mol}^{-1}$  is the mole mass of the growing film material. In Equation (9),

$$j_{dep} \sim n_C(L_{NT})v \exp(-\delta E_f / k_B T_s) + 2\delta_j j_i + j_i \theta_{CH}(L_{NT})y_s - (1 - \theta_i) \nu_0 \sigma_{bulk} (j_H + j_H^+) / 4 - j_i (1 - \theta_i) y_{sp}, \quad (10)$$

where  $\delta E_f \sim 2.3 \text{ eV}$  is the activation energy of incorporation into the film [50]. The first term in Equation (10) accounts for thermal insertion of carbon adatoms into the film from the film surface. The second term in Equation (10) describes direct incorporation of carbon-bearing ions. It was assumed that the direct incorporation takes place only at relatively large ion energies ( $E_i \geq 20 \text{ eV}$ ) [51]. Therefore,  $\delta_j = 0$  for  $E_i < 20 \text{ eV}$  and  $\delta_j = 1$  for  $E_i \geq 20 \text{ eV}$ . The third term in Equation (10) accounts for ion-induced incorporation of  $\text{C}_2\text{H}_2$  neutrals (stitching) with the stitching rate  $y_s = 2.49 \times 10^{-2} + 3.29 \times 10^{-2} E_i$  [57]. The next term in Equation (10) is due to etching of the film by atomic hydrogen and hydrogen ions, and the last term accounts for the loss of carbon atoms from the growing film due to sputtering.  $\sigma_{bulk} \sim 6.8 \times 10^{-15} \text{ cm}^2$  is the cross-section for the etching reaction,  $y_{sp}$  is the sputtering yield which depends on the ion energy  $E_i$  [51]:  $y_{sp} = -3.89 \times 10^{-7} E_i^2 + 7.04 \times 10^{-4} (E_i - 100) + 8.14 \times 10^{-2}$  for  $E_i < 100 \text{ eV}$ .

## 2.2. Results from the Model Describing Growth of an Array of SWCNTs

In [39], Equations (1)–(10) were used to analyse how the main parameters that characterize the growth of a SWCNT array [the nanostructure growth rate ( $V_{NT}$ ), the characteristic residence time of carbon

adatoms on the nanotube surfaces at  $x = L_{NT}(\tau_{a1})$ , and the growth rate of the film between carbon nanotubes ( $V_{dep}$ ] depend on the height of SWCNT array  $L_{NT}$ , temperature of SWCNT surfaces  $T_s$ , the penetration depths of neutrals and ions in SWCNT array  $l^*$  and  $l_i^*$ , and the intensities of neutral and ion fluxes.

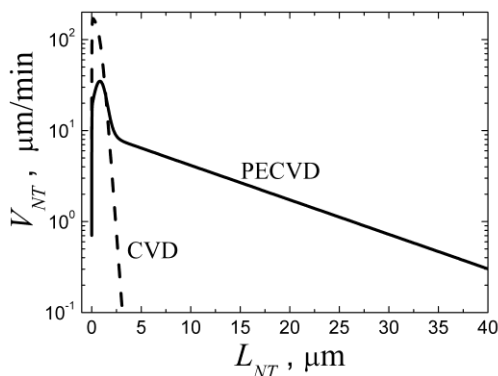


Figure 2. Dependence of growth rates of SWCNT array on SWCNT height in the thermal CVD and PECVD cases. The dependencies are obtained for  $C_2H_2$  density  $n_{CH} = 10^{14} \text{ cm}^{-3}$ , SWCNT surface temperature  $T_s = 1000 \text{ K}$ , and penetration depth of neutrals in SWCNT array  $l^* = 0.3 \text{ }\mu\text{m}$ . In the CVD case,  $n_i = n_H = 0$ , while  $n_i = 3 \times 10^{10} \text{ cm}^{-3}$ ,  $j_H = 5j_{CH}$  and  $E_i = 10 \text{ eV}$  in the PECVD case.

The SWCNT growth rates in the CVD case were compared with those in PECVD. In Figure 2, the dependencies of  $V_{NT}$  on the SWCNT array height are shown for the both cases. Obtaining these dependencies, it was assumed that ion and etching gas fluxes to the nanotubes are absent in the CVD case, while the fluxes of  $C_2H_2^+$  ions and H atoms to the SWCNTs are present in the PECVD case. It was also assumed that the flux of etching ions to the SWCNTs is small.

One can recognize from Figure 2 that the SWCNT growth rates for small nanotubes ( $\leq 1 \mu\text{m}$ ) in the CVD case are higher than those in the PECVD case, because of the losses of  $C_2H_2$  molecules and C atoms from the SWCNT surfaces through the interaction with etching gas in the PECVD case. However, for longer nanotubes ( $L_{NT} > 2.5 \mu\text{m}$ ), the growth

rates in the CVD case are much smaller than in the PECVD case. The difference in the growth rates in the PECVD and CVD cases is due to the difference in penetration depths of neutrals and ions in SWCNT array [39]. Since the ion energy is higher than the thermal energy of neutrals, the penetration depth for ions is also larger than the depth for neutrals. As a result, under the “base-growth” conditions, an array of SWCNTs formed in PECVD should be longer than that formed in CVD. This conclusion agrees well with numerous results of experimental and theoretical investigations on the growth of SWCNT forests in CVD and PECVD [53, 58].

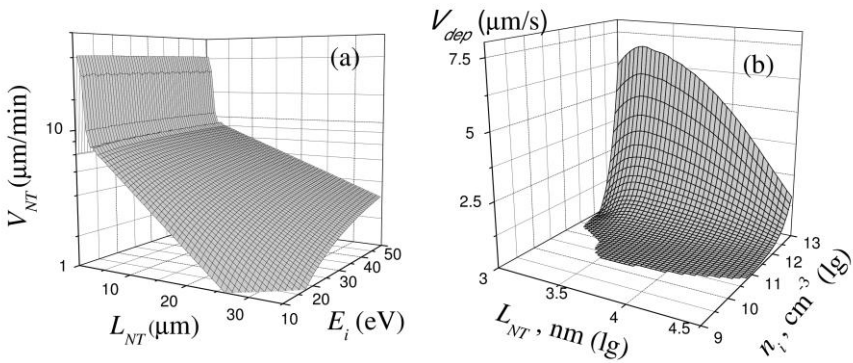


Figure 3. Dependence of growth rates of SWCNT array on height of SWCNT array  $L_{NT}$  and on hydrocarbon ion energy  $E_i$  (a), and dependence of the growth rates of amorphous film between SWCNTs on ion density  $n_i$  and on  $L_{NT}$  (b). The dependences in Figures 3 (a) and 3 (b) are obtained for  $n_i = 3 \times 10^{10} \text{ cm}^{-3}$  and  $E_i = 30 \text{ eV}$ , respectively. The other external parameters are the same as in the PECVD case (Figure 2).

At large  $L_{NT} (\gg l^*)$ , carbon production near nanotube bases ( $x \sim L_{NT}$ ) is caused mainly by  $\text{C}_2\text{H}_2^+$  decomposition. Therefore, the decrease of  $V_{NT}$  with increasing the SWCNT array height becomes smaller if the ion penetration depth increases. Since the penetration depth of ions becomes larger with increase of their energy, the growth rates for long nanotubes become higher when  $E_i$  increases (see Figure 3 (a)). For  $L_{NT} \gg l^*$ , the dependence of the growth rate on  $L_{NT}$  is mainly because of the  $L_{NT}$ -dependence of the effective carbon flux. The flux becomes smaller when the ion flux decreases [ $Q_{Cl} \approx 2j_i \sim \exp(-L_{NT}/l_i^*)$ ]. For small  $L_{NT} (< 10l^*)$ ,

ions affect slightly on the growth, and, therefore, the dependence of the growth rate on ion energy is weak (see Figure 3(a)).

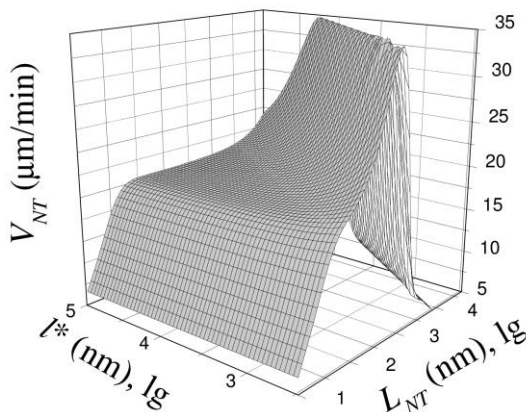


Figure 4. Dependence of SWCNT growth rates on  $L_{NT}$  and on the depth of penetration of neutrals in SWCNT array  $l^*$ . The results are obtained for  $E_i = 10$  eV. The other external parameters are the same as in Figure 3.

We also found the conditions which are suitable for formation of the amorphous film between SWCNTs. The film formation may take place at relatively high ion energies ( $\geq 20-30$  eV) [51, 59], due to the direct incorporation of hydrocarbon ions into the amorphous film (low energy ion implantation). This film can cover catalyst nanoparticles and eventually stops the growth of the SWCNTs. Even if etching gas flux to the tips of nanotubes is high, formation of the amorphous film starts at large SWCNT lengths ( $L_{NT} \gg l^*$ ), when the etching gas flux to the nanotube base becomes small (Figure 3 (b)). Formation of the film starts at smaller  $L_{NT}$  when the ion density becomes higher, due to increase of number of hydrocarbon ions which incorporate into the amorphous film.

We also analysed how the SWCNT growth rate depends on the penetration depth of neutrals in SWCNT array (Figure 4). It was found that the dependence of  $V_{NT}$  on the SWCNT array height is nonlinear. The SWCNT growth rate first increases with an increase of  $L_{NT}$ , reaches a maximum at a certain length, and then decreases. With increasing the



penetration depth  $l^*$ , the maximum of  $V_{NT}$  shifts towards larger  $L_{NT}$  values. Such behaviour of  $V_{NT}$  on  $L_{NT}$  and on  $l^*$  is due to the dependence of the SWCNT growth rate on carbon atom production and carbon loss near the nanotube base. The effective carbon flux to the nanotube base  $Q_{C1}$  becomes smaller with increasing the SWCNT array height because of decreasing  $C_2H_2$  and  $C_2H_2^+$  fluxes to the nanotube base. At small  $L_{NT}$  ( $< 10l^*$ ), the effective carbon flux is strongly affected by the flux of  $C_2H_2$  molecules. At large SWCNT lengths ( $L_{NT} > 10l^*$ ), neutral particle fluxes to the nanotube base are small, and production of carbon atoms is mainly due to decomposition of  $C_2H_2^+$  ions on the SWCNT surfaces. As a result, for large SWCNT lengths, the dependence of effective carbon flux on  $L_{NT}$  is similar to that for hydrocarbon ion flux  $j_i$  [ $Q_{C1} \approx 2j_i \sim \exp(-L_{NT}/l_i^*)$ ].

In [39], it was also studied how the SWCNT growth parameters depend on the etching gas and ion fluxes ( $j_H$  and  $j_H^+$ ). It was shown that the SWCNT growth rates decrease with increasing the etching gas flux  $j_H$ , since the losses of carbon atoms and  $C_2H_2$  molecules by their interaction with hydrogen atoms on the SWCNT lateral surfaces become higher. Consequently, the carbon residence time near the nanotube base becomes smaller. When the etching gas flux to the nanotube tips is low and the ion energy is higher than 20-30 eV (when direct ion incorporation in the amorphous film takes place [51]) formation of the film between nanotubes takes place.

If the etching gas flux to the SWCNT tips is high, the array of SWCNTs can grow while the length of SWCNTs remains smaller or comparable with the depth of penetration of hydrogen atoms in the SWCNT array. This explains why vertically aligned SWCNTs quite often can only be grown to a certain and rather limited length before no further growth can be detected [58].

The growth rate  $V_{NT}$  decreases when the flux ratio of the etching and hydrocarbon ions increases [39]. This conclusion is in an agreement with the experimental results [60], showing that energetic hydrogen ions attracted by the negatively charged substrate may significantly etch

SWCNTs. Hydrogen plasmas may also be used for selective etching of SWCNTs [61].

The formation of the amorphous film between SWCNTs may be also avoided if the flux of carbon-free ions (e.g., argon ions) is high and the ion energy is sufficient for the effective sputtering of the amorphous film. In this case, the following condition should be fulfilled:  $j_i < j_{iAr}(1-\theta_t)y_{sp}$ , where  $j_{iAr}$  is the flux of carbon-free ions, and  $y_{sp}$  is the sputtering yield. However, the ion energy should be moderate ( $< 60$  eV [62]) to avoid destruction of growing SWCNTs.

In [39], it was confirmed that etching species are necessary to prevent amorphous carbon formation in the case if hydrocarbon ion energies are higher than the threshold energy for direct incorporation of the ions in the amorphous film (low energy ion implantation) [51, 59]. In PECVD experiments on SWCNT growth, a carbon precursor gas is usually heavily diluted by gases such as  $H_2$ ,  $NH_3$ ,  $O_2$  or water, which provide etching species [63-67]. Ethanol can also be used as a carbon source and for etching [68, 69].

It was also analysed how the SWCNT growth rates and carbon residence times near the nanotube base depend on the SWCNT surface temperature  $T_s$  (Figures 5 (a) and 5 (b)). For low  $T_s$ , thermal dissociation of hydrocarbon molecules is not as effective as for high temperatures, and carbon production is mainly due to the ion bombardment of adsorbed  $C_2H_2$  molecules, as well as due to decomposition of  $C_2H_2^+$  ions. As a result, the growth rates of the nanotubes with  $L_{NT} \leq 8l^*$  increase, when the surface temperature becomes higher. At  $L_{NT} \leq 8l^*$ , the difference in  $V_{NT}$  for low  $T_s$  ( $\leq 700$  K) and high temperatures ( $\geq 1100$  K) is very high ( $\geq 100$  times). It means that the time required to synthesize the SWCNTs with  $L_{NT} \leq 2.5\mu m$  at low temperatures is much higher than at high  $T_s$ . Therefore, in most of the experiments on low-temperature growth of vertically-aligned carbon nanostructures by PECVD, the structures are rather short [22, 35]. The residence time of carbon adatoms decreases with an increase of the nanotube surface temperature due to increased loss of carbon adatoms by evaporation (Figure 5 (b)). However, with  $T_s$  increasing, carbon adatoms

move faster to the catalyst nanoparticles and this leads to the higher growth rates at small and moderate SWCNT lengths (Figure 5 (a)).

For high surface temperatures, the carbon residence time near the nanotube base depends slightly on the nanotube length, while the dependence for low  $T_s$  is strong (Figure 5(b)). This difference is explained by the importance of etching process at low  $T_s$ . For high surface temperatures, the contribution of the etching gas on the total loss of carbon adatoms from the SWCNT surfaces is rather small, and thermal effects are more important. At high  $T_s$ , the growth rate  $V_{NT}$  becomes smaller with increasing the SWCNT length for  $L_{NT} \geq 5l^*$ , mostly because of the reduced flux of hydrocarbon species to the nanotube base.

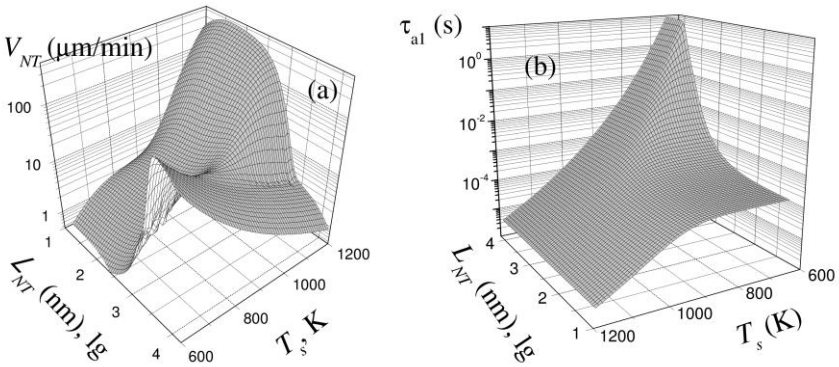


Figure 5. Dependence of  $V_{NT}$  on  $L_{NT}$  and  $T_s$  (a), and dependence of the carbon residence time on  $L_{NT}$  and  $T_s$  (b). These dependencies are obtained for  $l^* = 0.3 \mu\text{m}$ ,  $n_i = 3 \times 10^{10} \text{cm}^{-3}$ ,  $n_{CH} = 10^{14} \text{cm}^{-3}$ ,  $j_H = 5j_{CH}$ ,  $E_i = 10 \text{eV}$ , and  $j_{H^+} = 0$ .

It was found that for long nanotubes ( $L_{NT} \geq 10l^*$ ), their growth rates at low  $T_s$  may be even higher than at high  $T_s$  (Figure 5(a)). That was attributed to the longer carbon residence times  $\tau_{a1}$  at small  $T_s$  compared to high surface temperatures (Figure 5(b)). Moreover, for  $T_s \leq 950 \text{K}$ , the growth rates may become larger with increasing the length if  $l^* < L_{NT} \leq 1 \mu\text{m}$ . This increase is due to a decrease of the total surface coverage when the nanotubes become longer. This is accompanied by an increase of the adsorption flux of  $\text{C}_2\text{H}_2$  molecules on the SWCNT surfaces. At low  $T_s$  and

long nanotubes, the growth rates of the SWCNT array are rather high (Figure 5(a)). It means that the SWCNTs can be grown at low substrate temperatures only if hydrocarbon ions with energies about 10-15 eV deposit on the SWCNT surfaces.

The results of numerical studies in [39] confirmed that SWCNTs may be effectively grown by PECVD to the lengths of a few micrometres (or even more) at low substrate temperatures ( $\leq 700$  K). The low-temperature growth is one of the necessary conditions for the synthesis of SWCNTs with narrow-chirality distribution [2]. For fast growth of SWCNT arrays, it is reasonable to vary the temperature during the growth: to start at high temperatures and to decrease the growth temperature when the SWCNT length will reach a few micrometres.

The growth rate  $V_{NT}$  also depends on the density of hydrocarbon ions in the plasma [39]. It increases when  $n_i$  becomes larger, due to more effective carbon generation in ion-induced processes, which include decomposition of hydrocarbon ions, and dissociation of hydrocarbon neutrals by ion bombardment. At large nanotube lengths, when the flux of hydrocarbon neutrals to the nanotube base is low, the ion-induced processes are very important for the growth of SWCNTs. For large  $L_{NT}$ , carbon generation is mainly due to decomposition of hydrocarbon ions, and the growth rate is nearly independent on  $L_{NT}$  and may be approximated as  $V_{NT} \approx 2k\Omega_j^i \tau_{a1} / (1 + k\lambda_{D1} / D_s)$ . Thus, for large  $L_{NT}$  ( $\gg l^*$ ), the SWCNT growth rate is proportional to  $j_i$  and becomes higher with an increase of  $n_i$ . However, for  $E_i \geq 20$  eV the growth of the amorphous film between the nanotubes starts at smaller  $L_{NT}$  if the density of hydrocarbon ions in the plasma bulk becomes higher (Figure 3 (b)), because of the enhanced ion-induced reactions on the surface between SWCNTs (ion-induced incorporation of hydrocarbon neutrals and direct incorporation of carbon-bearing ions into the film).

To avoid formation of the amorphous carbon or multi-walled carbon nanotube during SWCNT synthesis, the power input in a PECVD reactor should be kept low [48]. For example, Ming et al. [65] used a plasma power as low as 15 W for SWCNT growth. The harmful effect of ions may be also avoided if an afterglow low-density plasma [28], remote plasma

systems [44, 70-72] or atmospheric pressure plasmas [58, 73-75] are used. We also found that the effects of the ion density on the SWCNT growth become more pronounced with decreasing the substrate temperature. This happens because of the lower rates of thermal dissociation, which is the main carbon production mechanism at high temperatures and small SWCNT lengths [76, 77]. When  $T_s$  is high, thermal dissociation is effective, and ions mostly contribute to the growth of long nanotubes; in this case the hydrocarbon neutral flux to the nanotube base is small. We also found that the effect of the ion density on carbon loss near the nanotube base is small. Note that the ion bombardment experiments and atomistic simulations reveal that the ion bombardment in a suitable energy range allows structural defects to be healed resulting in an enhanced nucleation of the carbon nanotube cap [76, 78, 79].

### 2.3. Modelling of Growth of an Isolated SWCNT

The growth of an isolated SWCNT in a plasma environment was modelled by Denysenko et al. [38]. The surface deposition model and main assumptions, used in the study, were similar to those described in subsection 2.1. However, the species, which deposit on the SWCNT surface in the model, were different from those considered in subsection 2.1. It was assumed that the main particles that interact with the surfaces of the SWCNTs are  $\text{CH}_3$ ,  $\text{CH}_3^+$  and H. The SWCNT surfaces and the substrate surface between the SWCNTs were assumed to be covered by H and  $\text{CH}_3$  radicals and carbon atoms C. The carbon atoms can be generated on the SWCNT surfaces by the following reactions: thermal dissociation of  $\text{CH}_3$ , ion bombardment of adsorbed  $\text{CH}_3$  radicals, and decomposition of  $\text{CH}_3^+$  ions.

The main equations of the model presented in [38] are the mass balance equations for  $\text{CH}_3$ , H, and C species on a SWCNT surface:

$$j_{CH}(1-\theta_t) - \theta_{CH}L = 0, \quad (11)$$

$$j_H(1 - \theta_i) + j_i + \theta_H M - \theta_H K = 0, \quad (12)$$

$$D_s d^2 n_c / dx^2 + n_{cH} \nu \exp(-\delta E_i / k_B T_s) + \theta_{cH} j_i y_d + j_i - n_c \nu \exp(-E_{ev} / k_B T_s) - n_c \sigma_{ads} j_H = 0, \quad (13)$$

where  $K = \nu_0 \nu \exp(-E_a / k_B T_s) + \nu_0 \sigma_{ads} j_H$ ,  $M = j_i y_d + \nu_0 \nu \exp(-\delta E_i / k_B T_s)$ ,  $L = \nu_0 \nu \exp(-E_a / k_B T_s) + \nu_0 \nu \exp(-\delta E_i / k_B T_s) + \nu_0 \sigma_{ads} j_H + j_i y_d$ , and  $y_d = E_i / \delta E_i$ .

Equation (13) was solved using the boundary conditions presented below Equation (7). As a result, it was obtained the following differential equation for the SWCNT length [53]:

$$\frac{dL_{NT}}{dt} = \frac{k\Omega Q_C \tau_a \sinh(\zeta)}{\sinh(\zeta) + (k\lambda_D / D_s) \cosh(\zeta)}, \quad (14)$$

which is similar to Equation (8).

The model for growth of an isolated SWCNT also accounted for formation of a carbon film at the substrate. The film width  $L_{dep}$  was found from Equation (9) taking into account that  $V_{dep} = dL_{dep} / dt$ .

Using Equations (9) and (14), it was analysed how  $L_{NT}$  and  $L_{dep}$  depend on the SWCNT temperature. The increase in the SWCNT length  $\Delta L_{NT} (= L_{NT} - L_0)$  for a growth time of  $t = 1$  s as a function of  $T_s$  is shown in Figure 6 (a). Here  $L_0$  is the SWCNT length at  $t = 0$ . The curves in Figure 6 (a) are obtained for  $n_{cH} = 10^{15} \text{ cm}^{-3}$ ,  $j_H = 10^{-3} \times j_{cH}$ ,  $E_i = 2.1 \text{ eV}$  ( $y_d = 1$ ),  $L_0 = 1 \text{ nm}$ , and  $n_i = 10^9$  and  $10^{10} \text{ cm}^{-3}$ . The results for CVD ( $j_i = j_H = 0$ ) are also presented in the figure.

It was obtained that at low substrate temperatures ( $T_s < 800 \text{ K}$ ), the SWCNT length in PECVD may be larger than that in CVD [Figure 6 (a)]. The SWCNT length increases with increasing ion density. The length enlargement is due to enhanced ion-induced dissociation of  $\text{CH}_3$  and decomposition of  $\text{CH}_3^+$  on the SWCNTs. At low  $T_s$ , these processes increase the effective carbon flux  $Q_C$ .

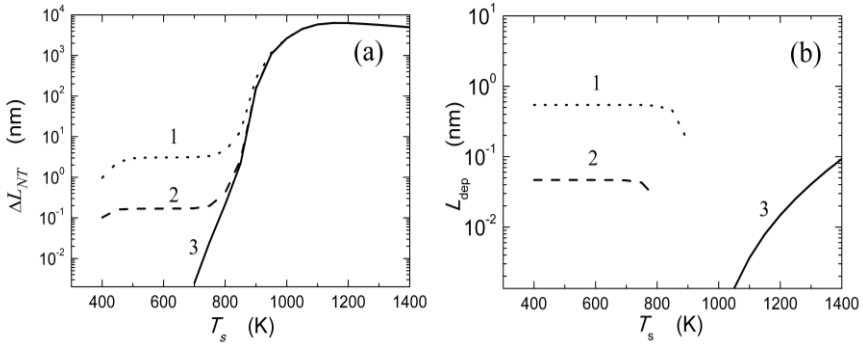


Figure 6. SWCNT length increase  $\Delta L_{NT}$  (a) and film thickness  $L_{dep}$  (b) for different ion densities:  $n_i = 10^{10} \text{ cm}^{-3}$  (curve 1) and  $10^9 \text{ cm}^{-3}$  (curve 2). The curves 3 correspond to the CVD case ( $j_i = j_H = 0$ ).

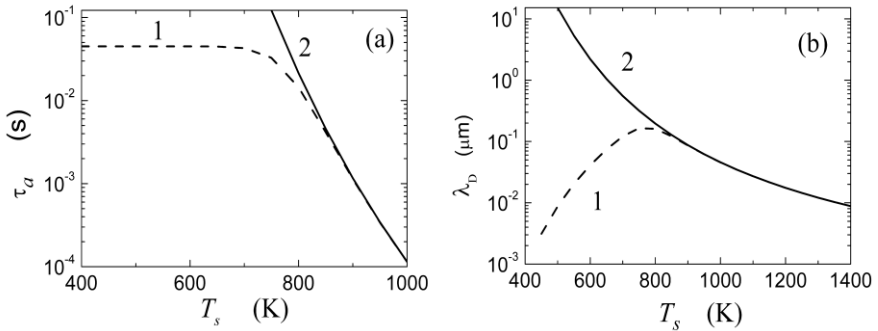


Figure 7. The characteristic residence time of carbon on the SWCNT surface (a) and the diffusion length (b) as a function of  $T_s$  for the conditions corresponding to Figure 6. The curves 1 and 2 are for the PECVD and CVD cases, respectively. The curves 1 are obtained for  $n_i = 10^{10} \text{ cm}^{-3}$ .

We found that the film thickness  $L_{dep}$  between the SWCNTs depends on the ion density [see Figure 6 (b)]. At low substrate temperatures ( $T_s < 900$  K), the film thickness becomes larger with increase of  $\text{CH}_3^+$  density due to ion-induced incorporation of  $\text{CH}_3$  neutrals and direct incorporation of  $\text{CH}_3^+$  [51]. The thickness  $L_{dep}$  decreases as the substrate temperature increases until the film growth between the SWCNTs stops at a relatively large ( $T_s > 900$  K) temperature. In CVD ( $j_i = j_H = 0$ ),  $L_{dep}$  grows with increasing  $T_s$ . The growth is due to the exponential enhancement of the

carbon flux  $n_c(L_{NT})\nu\exp(-\delta E_f/k_B T_s)$  to the solid [see Equation (10)]. Due to film etching, this growth is absent in PECVD.

We also studied how the residence time  $\tau_a$  and the diffusion length  $\lambda_D$  depend on the SWCNT temperature  $T_s$ , in the CVD and PECVD cases [38]. It was found that at low  $T_s$  ( $< 700$  K), the dependence of  $\tau_a$  on  $T_s$  in PECVD is small because the loss and generation of carbon atoms in this temperature regime are mainly from ion and atomic hydrogen deposition. At low  $T_s$ , the surface diffusion length  $\lambda_D$  becomes larger with an increase of  $T_s$  because  $D_s$  also increases. In the CVD case, both  $\tau_a$  and  $\lambda_D$  become smaller with increasing  $T_s$  in the entire temperature range (see Figures 7 (a) and 7 (b), as well as [53]), and at  $T_s \leq 800$  K they are larger than the corresponding parameters in the PECVD case. It was also found that the length  $\lambda_D$  becomes smaller with increasing the etching gas flux  $j_H$  [38] because of particle loss in the adsorbed-layer reactions.

The results on PECVD growth of an individual SWCNT are in agreement with those describing the growth of an array of SWCNTs (see previous subsection).

### 3. MODELLING OF CNF GROWTH

#### 3.1. Mechanistic Model for CNF Growth

Growth of CNFs in PECVD may also be modelled using mass balance equations for adsorbed species. A model for the plasma-assisted growth of a CNF with a metal catalyst nanoparticle on its top, based on the equations, was proposed in [80, 81]. The case when the nanofiber is erected on a substrate (for example, Si (100) substrate) of thickness  $d$  placed on a substrate-holding platform of temperature  $T_M$  was considered (Figure 8). The catalyst temperature  $T_K$  was assumed to be different from  $T_M$ . It was also assumed that the top of the catalyst nanoparticle is subject to incoming fluxes from a plasma environment. The particles, which deposit on the



catalyst surface and are accounted for in the model, are hydrocarbon neutrals  $C_2H_2$ , etching gas atoms H and hydrocarbon ions  $C_2H_2^+$ .

In the model developed in [80, 81], it was assumed that the surface of the catalyst nanoparticle is flat and circular and is covered by  $C_2H_2$ , C and H species with the surface densities  $n_{CH}$ ,  $n_C$  and  $n_H$ , respectively.

The surface processes, which were accounted for in the CNF model, are shown in Table 2. It was assumed that the carbon atoms, generated on the catalyst surface due to different processes (see Table 2), incorporate into the growing graphene sheets via surface and bulk diffusion.

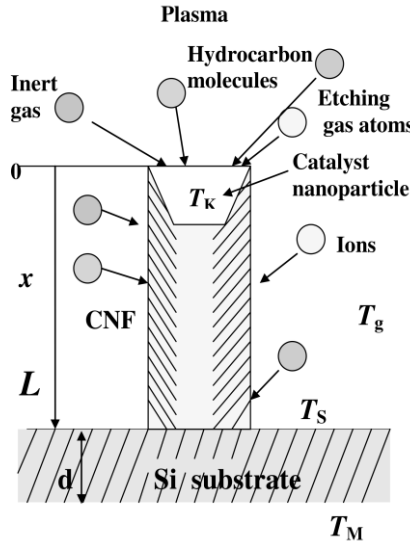


Figure 8. Schematics of particle deposition on the catalyst nanoparticle and CNF lateral surface from the gas-discharge plasma.

Taking into account the processes listed in Table 2, the mass balance equations for C,  $C_2H_2$  and H species on the catalyst surface can be written as

$$J_C + \text{div}(D_s \text{grad} n_C) - O_C = 0, \quad (15)$$

$$Q_{CH} - \theta_{CH} j_i y_d - n_{CH} v \exp(-\delta E_i / k_B T_K) = 0, \quad (16)$$

and

$$Q_H + 2n_{CH} \nu \exp(-\delta E_i / k_B T_K) = 0, \quad (17)$$

respectively.

In Equation (15),  $J_C = 2n_{CH} \nu \exp(-\delta E_i / k_B T_K) + 2\theta_{CH} j_i y_d + 2j_i$  is the carbon source term that accounts for the generation of C on the catalyst surface due to thermal (with the energy barrier  $\delta E_i$ ) and ion-induced dissociation of  $C_2H_2$ , and the decomposition of  $C_2H_2^+$ .

The second term in Equation (15) describes the carbon loss due to surface diffusion, where  $D_s = D_{s0} \exp(-E_s / k_B T_K)$  is the surface diffusion coefficient,  $D_{s0}$  is a constant, and  $E_s$  is the energy barrier for diffusion of C on the catalyst surface. The term  $O_C = n_C \nu \exp(-E_{eV} / k_B T_K) + n_C \sigma_{ads} j_H + n_C \nu \exp(-E_b / k_B T_K)$  takes into account for the carbon atom loss due to evaporation (with the energy barrier  $E_{eV}$ ), interaction with atomic hydrogen from the plasma, and C diffusion into the catalyst bulk.  $\nu_0 (\approx 1.3 \times 10^{15} \text{ cm}^{-2})$  [51] is the number of adsorption sites per unit area,  $\nu = 10^{13} \text{ Hz}$  is the thermal vibrational frequency.  $j_i = n_i \exp(k_B T_e / m_i)^{1/2}$  is the ion flux from the plasma, where  $n_i$  is the ion density in the plasma,  $T_e \approx 1.5 \text{ eV}$  is the electron temperature, and  $m_i$  is the ion mass.  $\sigma_{ads}$  is the cross-section for the reactions of adsorbed particles with the incoming hydrogen flux  $j_H$  [51].  $E_b$  is the energy barrier for bulk diffusion [22].

$Q_\alpha = j_\alpha (1 - \theta_\alpha) - n_\alpha \nu \exp(-E_{\alpha\alpha} / k_B T_K) - n_\alpha \sigma_{ads} j_H$  is the term describing the adsorption, desorption of species  $\alpha$  [subscript  $\alpha = (\text{CH}, \text{H}, \text{and C})$  stands for  $C_2H_2$ , H, and C species, respectively], and interaction of the adsorbed species  $\alpha$  with atomic hydrogen from the plasma. In the expression for  $Q_\alpha$ ,  $j_\alpha = \tilde{n}_\alpha \nu_{\text{tra}} / 4$  is the flux of the impinging species  $\alpha$ ,  $y_d \approx E_i / E_{\text{dis}}$ , where  $E_i$  is the ion energy and  $E_{\text{dis}} \approx 5.58 \text{ eV}$  is the dissociation energy for a  $C_2H_2$  molecule in a vacuum.

**Table 2. Processes that are accounted for in the model for growth of CNFs. Here  $\tilde{T}_K = k_B T_K$**

Processes	Reactions	Functions/Parameters
<i>Processes that are common for thermal CVD and PECVD</i>		
Adsorption of C <sub>2</sub> H <sub>2</sub>	C <sub>2</sub> H <sub>2(plasma)</sub> → C <sub>2</sub> H <sub>2(ads)</sub>	$j_{CH} (1 - \theta_i)$
Desorption of C <sub>2</sub> H <sub>2</sub>	C <sub>2</sub> H <sub>2(ads)</sub> → C <sub>2</sub> H <sub>2(des)</sub>	$\theta_{CH} \nu_0 \nu \exp(-E_{aCH} / \tilde{T}_K)$ , $E_{aCH} = 2.9 \text{ eV}$
Thermal dissociation	C <sub>2</sub> H <sub>2(ads)</sub> → 2C <sub>(ads)</sub> + 2H <sub>(plasma)</sub>	$n_{CH} \nu \exp(-\delta E_i / \tilde{T}_K)$ , $\delta E_i = 1.3 \text{ eV}$
Carbon evaporation	C <sub>(ads)</sub> → C <sub>(evaporation)</sub>	$n_C \nu \exp(-E_{ev} / \tilde{T}_K)$ , $E_{ev} = 1.8 \text{ eV}$
Carbon diffusion into the catalyst bulk		$n_C \nu \exp(-E_b / \tilde{T}_K)$ , $E_b = 1.6 \text{ eV}$
Bulk diffusion		$D_b = D_{b0} \exp(-E_b / \tilde{T}_K)$
Surface diffusion		$D_s = D_{s0} \exp(-E_s / \tilde{T}_K)$ , $E_s = 0.3 \text{ eV}$
Incorporation of C into graphene sheets		$k = A_k \exp(-\delta E_{inc} / k_B T_K)$ , $\delta E_{inc} = 0.4 \text{ eV}$
<i>Additional processes accounted for in PECVD</i>		
Etching gas absorption	H <sub>(plasma)</sub> → H <sub>(ads)</sub>	$j_H (1 - \theta_i)$
Etching gas desorption	H <sub>(ads)</sub> → H <sub>(des)</sub>	$\theta_H \nu_0 \nu \exp(-E_{aH} / \tilde{T}_K)$ , $E_{aH} = 1.8 \text{ eV}$
Loss of adsorbed particles (H, C, C <sub>2</sub> H <sub>2</sub> ) at interaction with H	C <sub>(ads)</sub> +H <sub>(plasma)</sub> → CH <sub>(plasma)</sub> H <sub>(ads)</sub> +H <sub>(plasma)</sub> → H <sub>2(plasma)</sub> C <sub>2</sub> H <sub>2(ads)</sub> +H <sub>(plasma)</sub> → C <sub>2</sub> H <sub>3(plasma)</sub>	$n_\alpha \sigma_{ads} j_H$ , $\sigma_{ads} \approx 6.8 \times 10^{-16} \text{ cm}^2$
Ion-induced dissociation	C <sub>2</sub> H <sub>2</sub> <sup>+</sup> +C <sub>2</sub> H <sub>2(ads)</sub> → 2C <sub>(ads)</sub> + +H <sub>2(plasma)</sub> + C <sub>2</sub> H <sub>2</sub> <sup>+</sup>	$2\theta_{CH} j_i y_d$ , $y_d \approx E_i / E_{dis}$
Ion decomposition	C <sub>2</sub> H <sub>2</sub> <sup>+</sup> → 2C <sub>(ads)</sub> +H <sub>2(plasma)</sub>	$j_i$

Equation (15) was supplemented by boundary conditions. First, it was assumed that the surface diffusion flux vanishes ( $\partial n_C / \partial r|_{r=0} = 0$ ) at the

catalyst surface centre ( $r = 0$ ). Next, the carbon atoms, while diffusing across the catalyst surface, incorporate into the graphene sheets at the border of the catalyst particle ( $r = r_p$ , where  $r_p$  is the catalyst particle radius), with the rate determined from  $-D_s dn_C/dr = kn_C$ , where  $k = A_k \exp(-\delta E_{inc}/k_B T_K)$  is the incorporation speed,  $A_k$  is a constant [53],  $\delta E_{inc}$  is the barrier for carbon atom diffusion along the CNF-catalyst interface.

### 3.2. Results from the CNF Model

Using Equations (15-17), one can obtain the following equation for the carbon surface density:

$$D_s \frac{1}{r} \frac{d}{dr} \left( r \frac{dn_C}{dr} \right) - n_C / \tau_a + Q_C = 0, \quad (18)$$

where  $\tau_a = 1/[C_1/\nu_0 + \nu \exp(-E_{ev}/k_B T_K) + \sigma_{ads} j_H + \nu \exp(-E_b/k_B T_K)]$  is the characteristic residence time of carbon atoms on the catalyst surface,  $Q_C = 2j_i + C_1$  is the effective carbon flux to the catalyst surface,  $C_1 = [2\nu_0 \nu \exp(-\delta E_i/k_B T_K) + 2j_i y_d]/[1 + Lj_H/(Kj_{CH}) + M/K + L/j_{CH}]$ ,  $L = \nu_0 \nu \exp(-E_{aCH}/k_B T_K) + j_i y_d + \nu_0 \sigma_{ads} j_H + \nu_0 \nu \exp(-\delta E_i/k_B T_K)$ ,  $M = 2\nu_0 \nu \exp(-\delta E_i/k_B T_K)$ , and  $K = \nu_0 \nu \exp(-E_{aH}/k_B T_K) + \nu_0 \sigma_{ads} j_H$ .

The solution of Equation (18) is

$$n_C(r) = Q_C \tau_a \left( 1 - \frac{(k\lambda_D/D_s)I_0(r/\lambda_D)}{I_1(r_p/\lambda_D) + (k\lambda_D/D_s)I_0(r_p/\lambda_D)} \right), \quad (19)$$

where  $I_0$  and  $I_1$  are the modified Bessel functions of the zeroth and first order, respectively. Using Equation (19), we found the surface coverages of the catalyst by carbon atoms, acetylene molecules, and atomic hydrogen,

$$\begin{cases} \theta_C(r) = n_C(r)/v_0, \\ \theta_{CH}(r) = \frac{1 - \theta_C(r)}{1 + Lj_H/(Kj_{CH}) + M/K + L/j_{CH}}, \\ \theta_H(r) = \theta_{CH}(r)(Lj_H/j_{CH} + M)/K. \end{cases} \quad (20)$$

From Equation (19) one can also get the diffusion fluxes of carbon atoms to the CNF surface,

$$J_s = -D_s \partial n_C / \partial r |_{r=r_p} \times 2\pi r_p, \quad J_v = \int_0^{r_p} (n_C D_b / r_p^2) 2\pi r dr, \quad (21)$$

over the catalyst particle's surface and through the catalyst bulk, respectively. The diffusion fluxes determine the surface and bulk diffusion growth rates  $H_s = m_C J_s / (\pi r_p^2 \rho)$  and  $H_v = m_C J_v / (\pi r_p^2 \rho)$ , respectively. Here,  $\rho \approx 2 \text{ g/cm}^3$  is the CNF material density, and  $m_C$  is the mass of a carbon atom.

From Equations (19) and (21) it follows that the surface diffusion flux may be expressed as

$$J_s = \frac{2\pi r_p k \tau_a Q_C I_1(r_p / \lambda_D)}{I_1(r_p / \lambda_D) + (k\lambda_D / D_s) I_0(r_p / \lambda_D)}. \quad (22)$$

The expression for  $J_s$  may be simplified in some limiting cases. In particular, at a low rate of C incorporation into graphene sheets [ $I_1(r_p / \lambda_D) \gg (k\lambda_D / D_s) I_0(r_p / \lambda_D)$ ], the surface diffusion flux is

$$J_s \approx 2\pi r_p k \tau_a Q_C. \quad (23)$$

From Equation (23) it follows that at low rates of C incorporation and small catalyst temperatures (when  $\tau_a$  and  $Q_C$  are about independent on  $T_K$  and are functions only of the ion and neutral particle fluxes to the catalyst

[81]) the dependence of the surface diffusion flux on the catalyst temperature is determined by that of the incorporation speed [ $\sim \exp(-\delta E_{inc}/k_B T_K)$ ].

At high incorporation rates [ $I_1(r_p/\lambda_D) \ll (k\lambda_D/D_s)I_0(r_p/\lambda_D)$ ] and small particle radius [ $r_p/\lambda_D \ll 1$ ], Equation (22) simplifies to the following equation

$$J_s \approx \pi r_p^2 Q_C,$$

i.e., the surface diffusion flux depends only on the effective carbon flux to the catalyst surface.

Using Equations (19), (21) and (22), the growth rates as functions of the catalyst temperature were obtained numerically [81].

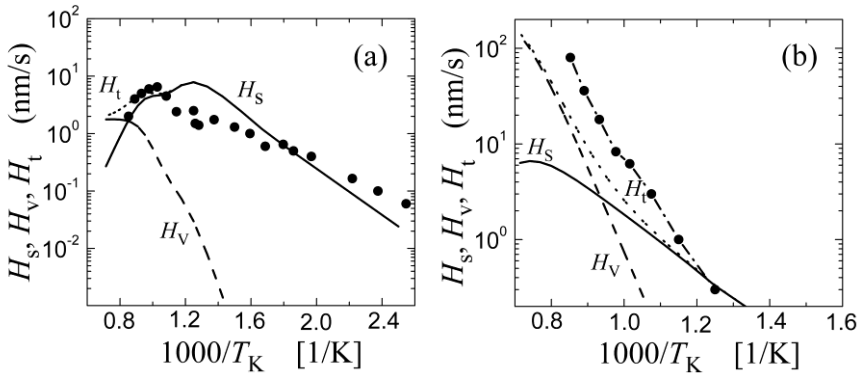


Figure 9.  $H_s$ ,  $H_v$  and  $H_t = H_v + H_s$  as functions of the catalyst temperature

in PECVD (a) and CVD (b). In the PECVD case,  $\tilde{n}_{CH} = 7 \times 10^{14} \text{ cm}^{-3}$ ,

$\tilde{n}_H = 3 \times 10^{-2} \tilde{n}_{CH}$ ,  $E_i = 500 \text{ eV}$ ,  $n_i = 3 \times 10^{10} \text{ cm}^{-3}$ , and  $r_p = 25 \text{ nm}$ . In the CVD case,  $\tilde{n}_{CH} = 10^{17} \text{ cm}^{-3}$ . The circles correspond to experimental data taken from [22, 82].

In Figure 9 (a), the dependencies of  $H_s$ ,  $H_v$ , and  $H_t = H_v + H_s$  on the catalyst temperature are shown for the PECVD case. The curves are compared with the experimental data of Hofmann et al. [22, 83]. One can

see in this figure that the surface diffusion curve fits best to the experimental data of Hofmann et al. [22, 83] in the broad range of  $T_K$ . The surface diffusion curve was obtained for the following parameters:  $n_{CH} = 7 \times 10^{14} \text{ cm}^{-3}$ ,  $n_H = 3 \times 10^{-2} n_{CH}$ ,  $E_i = 500 \text{ eV}$ ,  $n_i = 3 \times 10^{10} \text{ cm}^{-3}$ , and  $r_p = 25 \text{ nm}$ .

Assuming  $j_H = j_i = 0$  in Equations (19), (21) and (22), we also calculated the growth rates for the CVD case (Figure 9 (b)). The rates calculated for the CVD case (using  $n_{CH} = 10^{17} \text{ cm}^{-3}$ , and  $r_p = 25 \text{ nm}$ ) are very close to the experimental results of Ducati et al. [82]. The results of calculations show that at lower temperatures ( $1000/T_K > 1.2$ ), surface diffusion controls the growth whereas at higher temperatures ( $1000/T_K < 0.9$ ), CNF growth is due to bulk diffusion. In the range  $0.9 < 1000/T_K < 1.2$ , both bulk and surface diffusion contribute to the CVD growth.

Using the surface deposition model, we also studied how the ion and atomic hydrogen fluxes from the plasma affect the CNF growth rate  $H_t$ . The growth rates  $H_t$  as functions of  $1000/T_K$  are presented in Figures 10 (a) and 10 (b) for different ion and hydrogen atom densities in the plasma. One can see from Figure 10 (a) that at low catalyst temperatures the growth rate increases with increasing  $n_i$ . This increase is mostly due to the enhanced ion-induced dissociation of  $C_2H_2$  on the catalyst nanoparticles. On the other hand, Figure 10 (b) shows that  $H_t$  decreases with increasing  $n_H$  because of the larger loss of  $C_2H_2$  and C species in reactions with impinging hydrogen atoms (Table 2).

Using Equations (19) and (20), one can also find the effective sticking coefficients  $\chi_\alpha$ , which are necessary for a plasma model. The effective sticking coefficient  $\chi_\alpha$  describes the consumption (or production) flux of each neutral species that participates in the surface processes. The sticking flux may be written as  $[2\chi_\alpha j_\alpha / (2 - \chi_\alpha)]$  [51, 84], approaching  $\chi_\alpha j_\alpha$  for  $\chi_\alpha \ll 1$ .

Taking into account the reactions listed in Table 2, the effective sticking coefficients for  $C_2H_2$  and H may be found from the equation

$$j_\alpha(1-\theta_i) - n_\alpha v \exp(-E_{a\alpha}/k_B T_K) = 2\chi_\alpha j_\alpha / (2 - \chi_\alpha). \quad (24)$$

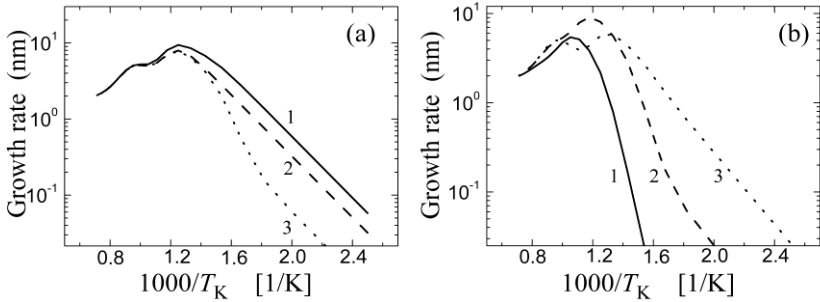


Figure 10. The growth rate  $H_t$  (a) for  $\bar{n}_H = 3 \times 10^{-2} \bar{n}_{CH}$  and  $n_i = 5 \times 10^{11}$  (curve 1),  $5 \times 10^{10}$  (curve 2), and  $5 \times 10^9$  (curve 3) cm<sup>-3</sup>. The CNF growth rate  $H_t$  (b) for  $n_i = 10^{10}$  cm<sup>-3</sup> and  $\bar{n}_H = \bar{n}_{CH}$  (curve 1),  $\bar{n}_H = 0.1 \bar{n}_{CH}$  (curve 2), and  $\bar{n}_H = 0.01 \bar{n}_{CH}$  (curve 3). The other parameters are the same as in Figure 9 (a).

### 3.3. Thermal Model for CNF Growth

To study the energy exchange between the plasma and the growing CNFs, the surface deposition model presented in previous subsection should be coupled with a thermal model. In [53], the thermal model was developed on the basis of the steady-state heat conductance approximation. In the approximation, the temperature distribution along the CNFs and the substrate (in the  $x$ -direction in Figure 8) may be described by the following equation [85]:

$$\frac{d}{dx} \left[ \lambda_c \frac{dT}{dx} \right] + Q_T(T) / \delta = 0. \quad (25)$$

In Equation (25),  $Q_T(T)$  is the heat release function,  $\lambda_c$  is the CNF heat conductance and  $\delta$  is the CNF wall thickness. The heat release



function  $Q_T(T)$  accounts for the carbon nanofiber - inert gas collisional heat exchange, the energy gain due to ion bombardment, and the heat loss due to thermal radiation from the CNFs [85].

Equation (25) should be supplemented by boundary conditions. We assumed that the temperature at the CNF-substrate interface ( $x = L$ )  $T_s$  is known. The heat flux at the CNF end ( $x = 0$ ) was assumed to be continuous, i.e.,  $-\lambda_C dT/dx|_{x=0} = j_{\text{cat}}$ , where  $j_{\text{cat}}$  is the heat flux to the catalyst surface from the plasma environment. The heat flux  $j_{\text{cat}}$  accounts for the heat release on the catalyst surface due to the chemisorption of hydrocarbon molecules, ion bombardment and incorporation of carbon atoms from the catalyst surface to the CNF structure; the heat dissipation at ion-induced dissociation and collisions of the neutral gas molecules with the catalyst; the heat release at diffusion of carbon atoms from the catalyst surface to its bulk and in the reactions of  $C_2H_2$ , C and H with atomic hydrogen from the plasma; and the energy loss from the catalyst in thermal dissociation,  $C_2H_2$  desorption and C evaporation. The expression for  $j_{\text{cat}}$  is presented in [85].

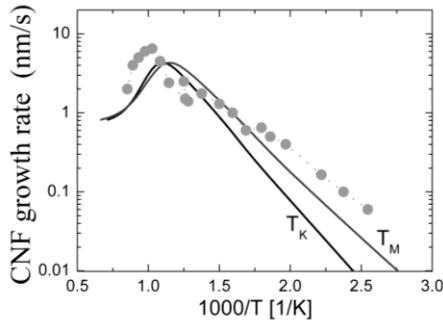


Figure 11. The CNF growth rate  $H_r$  as a function of  $T_K$  and of  $T_M$ . The circles correspond to the experimental data from [22]. The results are obtained for  $\tilde{n}_{CH} = 10^{15} \text{ cm}^{-3}$ ,  $\tilde{n}_H = 3 \times 10^{-3} \tilde{n}_{CH}$ ,  $E_i = 300 \text{ eV}$ ,  $n_i = 5 \times 10^{11} \text{ cm}^{-3}$ ,  $r_p = 50 \text{ nm}$ ,  $d = 1 \text{ mm}$ ,  $\delta = 0.6r_p$ ,  $j_g = 300j_{CH}$ , and  $T_g = 1000 \text{ K}$ , where  $j_g$  is the flux density of inert gas to the CNF surface.

**Table 3.**  $T_K-T_M$  as a function of  $T_K$ . The results in columns 2, 3 and 4 correspond to  $T_K-T_M$  for the  $(j_i \neq 0, j_H \neq 0)$ ,  $(j_i \neq 0, j_H = 0)$ , and  $(j_i = 0, j_H \neq 0)$  cases, respectively.

The other parameters are the same as in Figure 11

$T_K$ (K)	$T_K-T_M$ (K)		
	$j_i \neq 0, j_H \neq 0$	$j_H = 0$	$j_i = 0$
400	46.48	46.47	37.24
800	45.36	45.33	26.03
1000	30.44	30.43	1.62
1100	14.84	14.84	-20.94
1200	-9.51	-9.51	-54.76
1300	-46.28	-46.28	-105.01

The temperature dependence across the Si substrate was found from the following equation

$$\frac{d}{dx} \left[ \lambda_{\text{Si}} \frac{dT}{dx} \right] = 0, \quad (26)$$

where  $\lambda_{\text{Si}}$  is the heat conductance of the silicon substrate. Equation (26) should be supplemented by boundary conditions. We assumed that the temperature at the interface of the substrate with the substrate-holding platform ( $x = L+d$ ) is known and is equal to  $T_M$  [85]. At the substrate-nanofiber boundary ( $x = L$ ), the heat flux was assumed to be continuous:

$$\lambda_{\text{Si}} \frac{dT}{dx} \Big|_{L+0} = \lambda_{\text{Si}} \frac{dT}{dx} \Big|_{L-0}.$$

Using the thermal model and the model for CNF growth described in subsections 3.1 and 3.2, it was shown that fluxes from the plasma environment can substantially increase the temperature of the catalyst nanoparticle located on top of the CNF with respect to the substrate-holding platform temperature [85]. The difference between the

catalyst temperature and the substrate-holding platform temperature  $\Delta T (= T_K - T_M)$  is a function of the CNF length  $L$ , the substrate thickness  $d$ , the inert gas density  $n_g$  and temperature  $T_g$ , as well as the densities of the ions  $n_i$  and the atoms of etching gas  $n_H$ .

In Figure 11, the dependences of the CNF growth rate  $H_t$  on the catalyst temperature  $T_K$  and on the temperature at the interface between the substrate and the substrate-holding platform  $T_M$  are shown.

Plotting the curves in Figure 11, the CNF length was taken to be 500 nm which is about the length observed in experiments on PECVD at  $T_K = 500$  K [22]. From Figure 11 one can see that the dependence  $H_t$  on  $T_M$  fits better to the experimental data of Hofmann et al. [22] than the dependence  $H_t$  on  $T_K$ . The growth rates corresponding to  $T_M$  are larger than the rates corresponding to  $T_K$  in the low temperature range ( $1000/T_K > 1.2$ ). Note that in many experiments on PECVD of CNFs and related nanostructures the reported surface temperature is actually the temperature at the interface between the holding platform and the substrate [86, 87].

To make it clear which species are responsible for the difference between the catalyst temperature and the substrate-holding platform temperature, we calculated the difference  $\Delta T$  as a function of  $T_K$  under different assumptions in the thermal model. First, it was assumed that the hydrogen atoms and ions affect the heating of the CNFs and the catalyst nanoparticles (see the second column in Table 3). Second, we assumed that the hydrogen atoms do not affect the heating of the CNFs and the catalyst nanoparticles (see the third column in Table 3). Their effect was accounted for only in the CNF growth model (see subsections 3.1 and 3.2). The case, when the heating effect of ions is neglected, was also considered (see the fourth column in Table 3). It was found that the heating effect of etching gas is less pronounced as compared with the effects of neutral gas and ion fluxes (see Table 3).

Meantime, the ion heating effect may be important. For example, for  $T_K = 400$  K, the difference between the catalyst temperature and that of the substrate-holding platform at  $j_i = 0$  is about 25% smaller than the difference at  $j_i \neq 0$  (Table 3). The inert gas molecules heat the CNFs and

the catalyst nanoparticles at small temperatures ( $T_K < T_g$ ) and take the heat away from the nanostructures at  $T_K > T_g$ . The ions and the atoms of the etching gas heat the CNFs and the catalyst nanoparticles in the whole range of temperatures. Due to the ion bombardment, the catalyst nanoparticle temperature may be higher than the substrate-holding platform temperature, even if  $T_g < T_K$  (see the results in Table 3 for  $T_K = 1100$  K).

It was also analysed how the difference  $T_K - T_M$  depends on the substrate thickness. In Table 4, the temperatures  $T_M$  and  $T_K$  for different substrate thicknesses are shown. The magnitude  $|\Delta T|$  becomes larger if the width  $d$  increases (Table 4). We also found that the magnitude  $|T_M - T_K|$  increases with increasing the CNF length, the neutral gas density, the ion density, and the hydrogen atom density, as well as with an increase in the difference between the temperature of the inert gas molecules and the catalyst temperature [85].

Using the thermal model, it was also found that for relatively short CNFs ( $L \leq 1$  mm), the variation of the temperature along the CNF is small [85]. This is consistent with the theoretical results on the CVD carbon nanotube growth of Louchev et al. [53]. The temperature of catalyst nanoparticles differs from that of the substrate-holding platform mainly due to the temperature variation along the Si substrate.

**Table 4.  $T_M$  as a function of  $T_K$  for different substrate thicknesses. The results are obtained for the same parameters as in Table 3**

$T_K$ (K)	$T_M$ (K)			
	$d = 0.5$ mm	$d = 1$ mm	$d = 3$ mm	$d = 5$ mm
400	376.27	353.52	270.91	199.09
800	776.85	754.64	673.81	603.34
900	879.77	860.27	788.50	725.03
1000	984.57	969.56	913.31	862.28
1100	1092.53	1085.16	1056.62	1029.49
1400	1448.56	1501.80	1788.85	2424.63

#### **4. OTHER MODELLING RESULTS ON GROWTH OF CARBON NANOSTRUCTURES**

The surface diffusion model for CNF growth, which is presented in subsections 3.1 and 3.2, was extended by Mehdipour et al. [88]. The model was coupled with a plasma sheath model. The effects of variation in the plasma sheath parameters and substrate potential on the carbon nanofiber growth characteristics, such as the growth rate, the effective carbon flux to the catalyst surface, and surface coverages, were investigated. It was shown that variations in the parameters, which change the sheath width, mainly affect the growth parameters at the low catalyst temperatures, whereas the other parameters such as the gas pressure, ion temperature, and percentages of the hydrocarbon and etching gases, strongly affect the carbon nanofiber growth at higher temperatures. Gupta et al. [89] developed a theoretical model to study the nucleation and catalytic growth of carbon nanofibers in a plasma environment. Additionally to the processes described in subsection 3.1, the model in [89] accounts for the charging of CNFs, plasma sheath effects, and the effects relevant to the formation of catalyst nanoparticles as a result of etching of thin catalyst film in the plasma. It was shown that the size of the catalyst nanoparticles depends strongly on the etching gas density, and the growth rate of CNF increases with a decrease in catalyst nanoparticle size. It was also found that the CNF tip diameter becomes smaller and the graphene layers tilt away from the growth axis as hydrogen content in the growth atmosphere increases.

The surface diffusion model for growth of an isolated SWCNT, which is presented in subsection 2.3, was extended by Marvi et al. [90]. The extended model includes the plasma sheath and surface diffusion modules. Using the model, the plasma-related effects on the characteristics of SWCNT growth were studied. It was found that in the presence of reactive radicals in addition to energetic ions inside the plasma sheath area, the effective carbon flux, and the growth rate of SWCNT increase. It was shown that the concentration of atomic hydrogen and hydrocarbon radicals in the plasma plays an important role in the SWCNT growth. The optimum

substrate temperature and applied DC bias were estimated to maximize the growth rate of the single-walled carbon nanotubes. In [91], a mechanistic model was developed to explain and quantify the common experimental observations of the possibility of the narrow diameter/chirality distribution of SWCNT grown in low-temperature plasma experiments [20, 92-95], where the catalyst structures (which also turn out to be critical in the chirality-selective nanotubes growth [29]) can be preserved from unwanted deformation, coagulation, etc., which are usual artefacts of high-temperature CVD processes [96]. The model includes a combination of the plasma sheath, ion/radical transport, species creation/loss, plasma-surface interaction, heat transfer, surface/bulk diffusion, graphene layer nucleation, and bending/lift-off modules [91]. It was shown that the constructive interplay between the plasma and the Gibbs-Thomson effect can lead to the effective nucleation and lift-off of small graphene layers on small metal catalyst nanoparticles. It was also found that in plasma much thinner nanotubes with narrower chirality distributions can nucleate at much lower process temperatures and pressures compared to thermal CVD.

In [97], a mechanism and model for the vertical growth of platelet-structured vertically aligned single-crystalline carbon nanostructures by the formation of graphene layers on a flat top surface were proposed and verified experimentally. It was demonstrated that plasma-related effects lead to self-sharpening of tapered nanocones to form needlelike nanostructures. Formation of carbon nanotip microemitter structures was investigated by Levchenko and co-workers by means of multiscale hybrid numerical simulations, taking into account the gas-phase dynamics and the surface self-organization [98, 99]. It was found that vertical alignment obtained in the carbon nanostructures grown by PECVD is due, at least in part, to the fact that the electric field at the plasma sheath drives the charged building units and polarizes neutral building units, aligning them to stack in the nanoassembly. Using a Monte Carlo (MC) approach, Tam and Ostrikov showed that much longer SWCNTs can be grown in a plasma environment than in CVD [100, 101]. MC simulations also confirmed that the increase of the plasma density in the magnetic field leads to longer nanotubes [102].

May, Mankelevich et al. [103-106] developed a model describing the growth of ultrananocrystalline and nanocrystalline diamond (UNCD and NCD, respectively) films in PECVD, which gives information about the growth process itself and describes the plasma chemistry. The model accounts for 9 gas–surface reactions, including the H abstraction to form surface sites, and the subsequent reactions of H and hydrocarbon radicals with these surface sites. In [106], a general mechanism for the deposition of NCD from CH<sub>4</sub>/H<sub>2</sub> gas mixtures and for UNCD films from Ar/CH<sub>4</sub>/H<sub>2</sub> gas mixtures was proposed.

The mechanistic models for growth of carbon nanostructures, described earlier, have shown to be very effective for obtaining a better understanding of the nanostructure growth processes. Mechanistic simulations are rather simple and require minor computational effort compared to atomistic simulations. However, the mechanistic modelling provides only a qualitative picture on the nanostructure growth, and it depends strongly on the availability and correctness of reaction rate coefficients and activation energies of the many processes involved. The input data for mechanistic modelling, such as activation energies and reaction rate coefficients, can be obtained by a careful analysis of experimental data on the growth of carbon nanostructures, by *ab initio* (i.e., first principles) methods or by classical molecular dynamics (MD) simulations.

Many researchers have carried out the atomistic simulations on the growth of carbon nanostructures. The results of the atomistic simulations are reviewed in [23, 107]. However, most of these simulations was related to the thermal CVD growth and was not specific for the PECVD growth. Nevertheless, the simulations for the CVD growth provide much information that is relevant also for the PECVD growth, although it should be realized that certain key aspects in this respect are missing. In particular, the models for CVD growth do not account for the effects concerning the application of an electric field, ion bombardment, chemical etching, and the presence of radicals instead of neutral gas molecules. Recently, some of these plasma effects were accounted for in atomistic simulations.

Neyts et al. studied the effects of electric field [108] and Ar ion bombardment [76] on the growth of CNTs in the plasma at the atomic level by hybrid MD/force-biased MC (MD/fbMC) simulations [109, 110]. It was shown how applying an electric field assists SWCNTs to grow in the direction of the electric field. It was also found that the bombardment of Ar ions in a limited but well-defined energy window of 10–25 eV leads to better nucleation and defect healing of the SWCNT cap. Employing reactive molecular dynamics simulations, Neyts and Bogaerts demonstrated that ion irradiation in a higher energy window of 10–35 eV may also heal network defects after the nucleation stage through a non-metal-mediated mechanism, when the carbon network is no longer in contact with the metal nanocatalyst [111]. In [62], using the same approach, it was demonstrated how plasma-based deposition allows low-temperature growth of carbon nanotubes. It was shown how ion bombardment during the growth affects the carbon dissolution and precipitation process and how a narrow ion energy window allows CNT growth at 500 K. It was also shown how CNTs in contrast cannot be grown in thermal CVD at this low temperature, but only at high temperature. In [3], it was reported on atomic scale simulations of cap nucleation of single-walled carbon nanotubes from hydrocarbon precursors. In [112], nucleation and growth of graphitic networks on Ni-nanoclusters from hydrocarbon molecules was studied. It was observed that graphitic islands on the catalyst are typically not fully dehydrogenated at their edges, leading to their vertical orientation. Khalilov et al. found that these vertical graphenes gradually lose their hydrogen atoms, allowing them to curve over the surface, connect, and form a continuous graphitic network [112]. It was concluded that this leads to either cap formation or encapsulation of the nanocatalyst. In [113] a computational approach with experimental support was employed to study the plasma-based formation of Ni nanoclusters, Ni-catalysed CNT growth and subsequent etching processes, in order to understand the underpinning nanoscale mechanisms. It was found that hydrogen is the dominant factor in both the re-structuring of a Ni film and the subsequent appearance of Ni nanoclusters, as well as in the CNT nucleation and etching processes.



## 5. MODELLING OF THE PLASMA CHEMISTRY FOR THE SYNTHESIS OF CARBON NANOSTRUCTURES

The models describing the growth of carbon nanostructures in PECVD demand the flux densities and energies of neutral and charged particles, which deposit on the nanostructures from the plasma environment. These plasma parameters may be obtained from gas discharge models.

Delzeit et al. [114] carried out a study of growing multi-walled CNTs on silicon substrates with multilayered Al/Fe catalysts in an inductively coupled  $\text{CH}_4/\text{H}_2$  plasma. Using a zero-dimensional model, it was shown that  $\text{C}_2\text{H}_2$ ,  $\text{CH}_3$  and  $\text{H}$  particles are the major neutral species formed in the plasma at gas pressures of 1-3 Torr at different inlet compositions and input powers [114]. It was also reported that an increase of the input power is accompanied by an increase of the C and CH densities.

Denysenko et al. [115] developed a zero-dimensional model for an inductively  $\text{Ar}/\text{CH}_4/\text{H}_2$  high-density plasma used for growth of carbon nanocones at low pressures of the order of 100 mTorr. The plasma had the diameter 32 cm and height 23 cm. It was found that the deposited cation fluxes exceeded those of radical neutrals (see Figure 12).

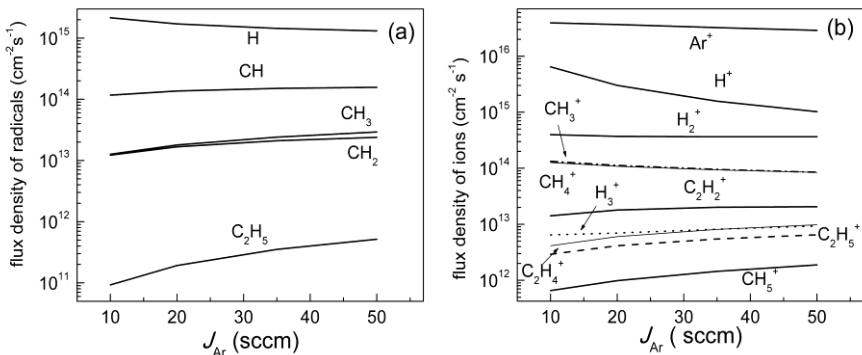


Figure 12. Deposited flux density of radical neutrals (a) and ions (b) as a function of the flow rate of argon  $J_{\text{Ar}}$  for the input power  $P_{\text{in}} = 2$  kW, and the flow rates of methane and hydrogen 6 sccm and 12.4 sccm, respectively.

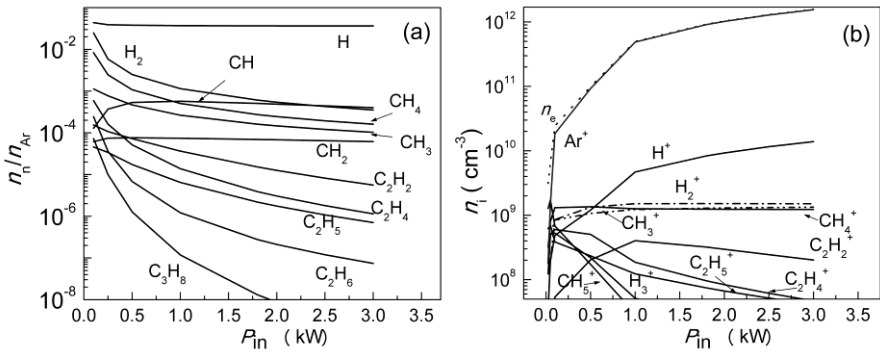


Figure 13. Computed densities of neutrals (a), which are normalized on  $n_{Ar} (= 6.4 \times 10^{14} \text{ cm}^{-3})$ , and ion densities as functions of the input power for the argon flow rate 35 sccm. Other conditions are the same as in Figure 12.

In [115], it was also shown that both densities of methane and molecular hydrogen drop dramatically with increasing the input power  $P_{in}$ . In the power range of the VACN growth ( $P_{in} = 1.8\text{-}3 \text{ kW}$ ), methane and hydrogen densities in the plasma were found to be much smaller than in the absence of the discharge. Argon atoms were found to be the predominant neutral species (the calculated argon density  $n_{Ar}$  was  $6.4 \times 10^{14} \text{ cm}^{-3}$  for  $J_{Ar} = 35 \text{ sccm}$ ). The density of hydrogen atoms was found to be approximately 25 times smaller than the argon density. The density of molecular hydrogen at low input powers was comparable to that of atomic hydrogen, and was diminishing with  $P_{in}$  (Figure 13 (a)). The latter decrease was attributed to the enhanced dissociation of hydrogen molecules at higher input powers accompanied by the rise in the electron density  $n_e$  (Figure 13 (b)). Due to the high electron densities, the conversion rates of  $\text{CH}_4$  and  $\text{H}_2$  for  $P_{in} = 1.8\text{-}3 \text{ kW}$  were found to be very high ( $\sim 99\%$ ) that was in good agreement with the results of the quadrupole mass spectrometry (QMS) measurements [115]. The enhanced  $\text{H}_2$  dissociation is accompanied by the rise of the ratio of the densities of  $\text{H}$  and  $\text{H}_2$  species, which can exceed 10 at elevated powers (Figure 13 (a)). Due to more intense electron-neutral collisions at higher electron densities, the densities of  $\text{CH}_3$ ,  $\text{C}_2\text{H}_2$ ,  $\text{C}_2\text{H}_4$ ,  $\text{C}_2\text{H}_5$ ,  $\text{C}_2\text{H}_6$ , and  $\text{C}_3\text{H}_8$  species also decreased with increasing input power. On the other hand, the  $\text{CH}$  and  $\text{CH}_2$  densities

became larger with  $P_{in}$ . The latter was attributed to the smaller sizes of CH and CH<sub>2</sub> molecules relative to other hydrocarbon species. The results of QMS measurements confirmed that the densities of H<sub>2</sub>, CH<sub>4</sub>, CH<sub>3</sub>, C<sub>2</sub>H<sub>2</sub> and C<sub>2</sub>H<sub>4</sub> species drop with increasing  $P_{in}$  [115].

Plasmas, used in the growth of vertically-aligned carbon nanostructures, have been also studied applying the models which account for the plasma inhomogeneity [116-119]. In [118], using a one-dimensional model, it was demonstrated that the feedstock gases (C<sub>2</sub>H<sub>2</sub>/NH<sub>3</sub> in the case under study) were efficiently dissociated at higher plasma powers, which resulted in a decrease in the growth rate because of decreasing density of the growth precursor (C<sub>2</sub>H<sub>2</sub>). Using a one-dimensional fluid model, the contributions of radicals and ions to CNT growth in CH<sub>4</sub> and CH<sub>4</sub>/H<sub>2</sub> plasmas were investigated in [120, 121]. Analysing numerical and experimental results, it was suggested that the positive ions, CH<sub>3</sub> and C<sub>2</sub>H<sub>5</sub> were the main species which supply carbon to the substrate. The hydrogen effect on CNT formation was also studied in [121]. In [122], the number densities and fluxes of nanoassembly precursor species in an inductively coupled Ar/H<sub>2</sub>/C<sub>2</sub>H<sub>2</sub> plasma, which was used in PECVD of vertically-aligned carbon nanostructures, were studied using a two-dimensional model. It was found that the main species can be separated by their function into working units and building units. Working units serve for surface preparation via activation or passivation of the solid surface, while the carbon-bearing species act as building blocks for different nanostructures. In [123, 124], a parameter study was carried out for an inductively coupled plasma used for the synthesis of carbon nanotubes and carbon nanofibres, by means of the 2D hybrid plasma equipment model. The plasma properties were studied for different gas mixtures at low and moderate pressures. It was found that C<sub>2</sub>H<sub>2</sub>, C<sub>2</sub>H<sub>4</sub> and C<sub>2</sub>H<sub>6</sub> are the predominant molecules in CH<sub>4</sub> containing plasmas besides the feedstock gas, and serve as carbon sources for CNT/CNF formation [123, 124].

Gas discharges used in PECVD of ultrananocrystalline and nanocrystalline diamond films were also studied applying different numerical approaches. In [103-106], the gas phase composition in a hot

filament (HF) and microwave (MW) plasma CVD system for (U)NCD growth was calculated using a 2D model. Based on the model calculations, it was explained why in their experiments UNCD films can be grown much more easily in the MW plasma than in the HF CVD reactor. Furthermore, it was found that the densities of  $\text{CH}_3$ , C and  $\text{C}_2\text{H}$  are larger than that of  $\text{C}_2$ , suggesting that these species are more important precursors for UNCD growth [103, 105]. A 2D model for a dc arc jet reactor, used for microcrystalline diamond and NCD deposition, was presented in [125]. It was predicted that C and CH are the main radical species bombarding the growing (nano)diamond surface. A quasi-analytical space-time-averaged kinetic model for an rf  $\text{C}_2\text{H}_2/\text{H}_2/\text{Ar}$  plasma used for nanocrystalline diamond film deposition, with special focus on the underlying mechanisms driving the nonequilibrium plasma chemistry of  $\text{C}_2$ , was developed in [126-128]. In [129, 130], the properties of an  $\text{Ar}/\text{H}_2/\text{CH}_4$  microwave discharge used for NCD deposition were studied by means of experiments and 0D plasma chemistry modelling.

Many authors studied properties of gas discharges used for growth of carbonaceous nanoparticles. Stoykov et al. [131] developed a model describing the chemical clustering kinetics in a low-pressure acetylene rf discharge. This model accounted for neutral-neutral reactions, electron induced H-abstraction, electron attachment, and ion-ion neutralization, as well as diffusion losses to the reactor walls. A detailed numerical simulation of the nucleation of nanoparticles in a capacitively coupled  $\text{C}_2\text{H}_2$  plasma was carried out in [132]. It was found that both positive ions and negative ions may participate as precursors in the initial stage of particle formation in acetylene discharges [132]. It was also noted that anions have a larger chance to finally end up in powder formation because they are trapped in the plasma due to their negative charge [132]. Some new mechanisms for negative ion formation and growth, as compared with those considered in [132], were proposed in [133]. A hybrid model for simulations of a 13.56 MHz discharge in a  $\text{C}_2\text{H}_2/\text{Ar}$  mixture at a gas pressure of 75 mTorr was developed by Ariskin et al. [134]. It was shown that a small injection of acetylene (5.8%) in argon changes significantly the plasma parameters. It was found that the densities of negatively and

positively charged heavy hydrocarbons in the  $C_2H_2/Ar$  plasma are sufficiently large to be precursors for the formation of nanoparticles in the discharge volume [134]. The influence of the fraction of acetylene in the mixture of  $Ar/C_2H_2$  on the negative ion density was also studied, and it was found that the nanoparticles are accumulated near the sheath–plasma boundaries at initial stage of growth. In [135], the effects of gas dilution on the chemistry of macromolecules and nucleation of nanoparticles in a low pressure radio-frequency acetylene discharge were analysed by employing a one dimensional multi-fluid model.  $Ar$ ,  $He$ , and  $H_2$  were used for the dilution with different percentages, keeping the total gas inlet constant. The nanoparticle coagulation in argon-acetylene plasma was studied in [136].

We also studied properties of an  $Ar/C_2H_2$  plasma used for growth of carbonaceous nanoparticles. We considered a plasma of 22 cm radius and 32.4 cm height. The total gas pressure was nearly 40 mTorr, and the flow rates of argon and acetylene were 10.1 sccm and 1.11 sccm, respectively. The discharge parameters were corresponding to those in the experiment on growth of nanoparticles of Hinz et al. [137]. In the experiment, the input power  $P_{in}$  was 9 W. The plasma properties were analysed using a 0D model.

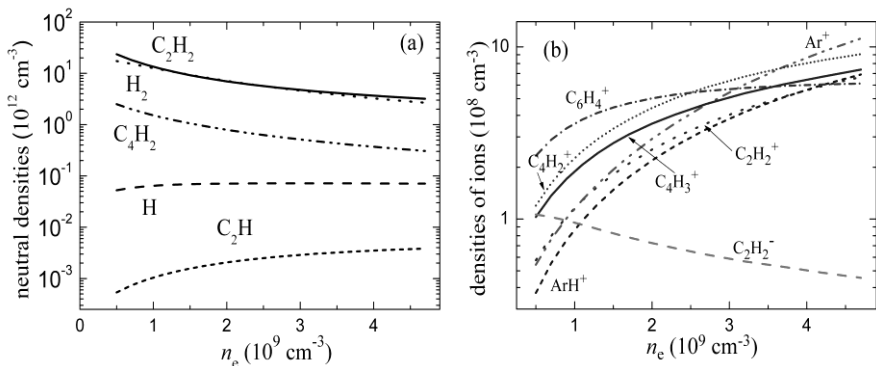


Figure 14. The densities of neutral species (a) and ions (b) in an  $Ar/C_2H_2$  plasma as functions of the electron density for the conditions which are typical for growth of carbonaceous nanoparticles.

In Figure 14 (a), the calculated spatially-averaged densities of the predominant hydrogen-containing neutrals as functions of the electron density are shown (the case of  $P_{\text{in}} = 9$  W corresponds to  $n_e \approx 4.5 \times 10^9 \text{ cm}^{-3}$ ). For the experiment conditions ( $P_{\text{in}} = 9$  W), argon atoms are found to be the predominant neutral particles in the discharge ( $n_{\text{Ar}} = 1.2 \times 10^{15} \text{ cm}^{-3}$ ), while the acetylene density is 346 times smaller than the argon density. The density of molecular hydrogen is nearly 15% smaller than the acetylene density. The  $\text{C}_2\text{H}_2$  density is nearly 10 times larger than that of  $\text{C}_4\text{H}_2$  and nearly  $10^3$  times larger than the  $\text{C}_2\text{H}$  density. The density of atomic hydrogen is 4.9 times smaller than that of  $\text{C}_4\text{H}_2$ . The densities of  $\text{C}_2\text{H}_2$ ,  $\text{H}_2$  and  $\text{C}_4\text{H}_2$  are decreasing with an increase of  $n_e$ , while the densities of  $\text{H}$  and  $\text{C}_2\text{H}$  increase (Figure 14 (a)). The decrease of  $\text{C}_2\text{H}_2$ ,  $\text{H}_2$  and  $\text{C}_4\text{H}_2$  densities is due to the enhancement of the neutral particle loss in collisions with electrons and positive ions. The increase of  $\text{C}_2\text{H}$  and  $\text{H}$  densities with increasing  $n_e$  is due to the enhancement of the radicals' production in different processes involving electrons and positive ions.

It was also studied how the densities of main ions in the plasma depend on the electron density (Figure 14 (b)). It was found that the densities of positive ions grow with an increase of  $n_e$  because of the enhancement of the ion production in reactions involving electrons and ions. The density of  $\text{C}_6\text{H}_4^+$  is larger than that of other ions for small electron densities, while the ions  $\text{Ar}^+$  are the predominant ions at large  $n_e$ . The density of negative ions  $\text{C}_2\text{H}^-$  is decreasing with an increase of electron density because of the enhancement of the  $\text{C}_2\text{H}^-$  loss in collisions with positive ions and hydrogen atoms. For the experiment conditions ( $P_{\text{in}} = 9$  W), argon ions dominate over other ions in the  $\text{Ar}/\text{C}_2\text{H}_2$  plasma, while the densities of  $\text{C}_4\text{H}_2^+$  and  $\text{C}_2\text{H}_2^+$  are respectively 13% and 59% smaller than that of  $n_{\text{Ar}}^+$ . The difference in the densities of  $\text{C}_2\text{H}_2^+$ ,  $\text{ArH}^+$  and  $\text{C}_6\text{H}_4^+$  is small. The  $\text{C}_4\text{H}_3^+$  density is nearly 24% smaller than the density of  $\text{C}_4\text{H}_2^+$ , while the density of  $\text{C}_2\text{H}_2^+$  is 63 times larger than that of  $\text{C}_2\text{H}_3^+$ . The density of negative ions  $\text{C}_2\text{H}^-$  is 12.1 times smaller than the density of  $\text{C}_2\text{H}_2^+$ . Comparing Figure 13 with Figure 14, one can see that the plasma composition in the case of growth of carbon nanocones is similar to that for growth of carbonaceous

nanoparticles, especially in the case of low electron density. In particular, the density of Ar is essentially larger than that of hydrocarbon neutrals and molecular hydrogen in both cases. However, for the case of VACN growth, the densities of CH, CH<sub>3</sub>, CH<sub>4</sub> and CH<sub>2</sub> are larger than the density of C<sub>2</sub>H<sub>2</sub>, while in case corresponding to Figure 14, acetylene molecules dominate over other hydrocarbon neutrals. For small electron densities ( $n_e \leq 10^9 \text{ cm}^{-3}$ ), the anion density in the case of growth of nanoparticles is nearly the same as that of positively-charged hydrocarbon ions. As it was mentioned earlier, it is widely assumed that hydrocarbon anions are the main precursors of the particle formation [132]. It is also supposed that the density of anions in plasmas used for formation of CNTs and CNFs is essentially smaller than the density of cations [36]. The densities of Ar<sup>+</sup>, H<sup>+</sup> and H<sub>2</sub><sup>+</sup> for the VACN growth conditions ( $P_{\text{in}} \sim 2 \text{ kW}$ ) are larger than the densities of hydrocarbon ions (Figure 13 (b)), while the density of Ar<sup>+</sup> is nearly the same as the densities of hydrocarbon cations for the case of nanoparticles' growth (Figure 14(b)). The density of C<sub>2</sub>H<sup>-</sup> anions becomes smaller when the electron density grows because of an enhancement of the anions' loss in collisions with positive ions (see Figure 14 (b) and [133]). Therefore, to avoid the nanoparticle formation in experiments on growth of VACNs, one has to keep the ion density by relatively large. However, even at large input powers during VACN growth, the formation of nanoparticles may take place in plasma regions with low electron/ion densities [37]. The nanoparticles formed in plasma volume during VACN growth should be keeping far away from the substrate with growing VACNs, for example, by applying different forces to the nanoparticles [138].

## CONCLUSION

Thus, we have reviewed the results on modelling of the plasma-assisted growth of vertically aligned carbon nanostructures. Focus was made on the studies that use the mechanistic models based on mass balance equations for species, which are adsorbed on catalyst nanoparticles or walls of the nanostructures. The analytical expressions for the growth rates

of CNFs and SWCNTs have been presented, and effects of the ions and etching gas atoms from the ionized gas environment on the growth of the nanostructures have been analysed. It has been also shown that the energy exchange between the plasma and the growing nanostructures may be investigated using the thermal model presented in subsection 3.3. The results from the mechanistic models are in good agreement with the available experimental data on synthesis of the vertically-aligned carbon nanostructures. Since the models for description of plasma-surface interaction require information about plasma properties, we also reviewed the modelling results on study of plasmas used for formation and growth of different carbon nanomaterials. The properties of a plasma used for growth of VACNs have been compared with the properties of that used for growth of carbonaceous nanoparticles.

Using the modelling results for plasma-surface interaction, specific conditions under which a low-temperature plasma environment benefits the VACN growth can be formulated. The main advantages of PECVD, as compared with thermal CVD, for growth of VACNs are the following:

- Ion-induced dissociation of hydrocarbon neutrals and decomposition of hydrocarbon ions on VACN and catalyst nanoparticle surfaces are essential sources of carbon atoms required for VACN growth. These two processes, unavailable in thermal CVD, become dominant at low substrate temperatures. This makes it possible to grow VACNs at much higher rates than that in CVD at low temperatures. The growth enhancement in PECVD may also be due to the deposition of radicals and neutrals in excited states [139].
- The height of a SWCNT array in a plasma can be much larger than in thermal CVD because the penetration depth of hydrocarbon ions in the SWCNT array is much larger than for the neutral species. Consequently, the ions can reach the catalyst nanoparticles at the “foot” of the SWCNT array and bring the carbon atoms to the nanoparticles at larger SWCNT array heights compared to hydrocarbon neutrals in the thermal CVD case.



- Reasonably strong fluxes of etching gas can completely etch away the amorphous carbon films developing between the VACNs. In PECVD of SWCNTs, this keeps the anchored catalyst nanoparticles accessible to the carbon adatoms which then eventually reach the CNT base and are incorporated into the growing structure.
- The etching gas fluxes can prevent oversupply of carbon material to the catalyst nanoparticles and can condition the VACN walls and the catalyst against unwanted adsorbates. This facilitates the diffusion of carbon adatoms toward the catalyst nanoparticles or the diffusion on the catalyst surface. Hydrogen atoms affect essentially the re-structuring of catalyst nanoparticles, as well as in the CNT nucleation processes [113].
- Atomistic simulations confirm that an electric field near substrate, which presents usually in PECVD, assists carbon nanostructures to grow in the direction of the electric field [108]. Ion bombardment of catalyst nanoparticles during the growth may affect the carbon dissolution and precipitation process. If the ion energy is in the energy window of 10–25 eV, the bombardment may facilitate to better nucleation and defect healing of the SWCNT cap, and may allow CNT growth at 500 K [62].
- The vertically-aligned carbon nanostructures may be postprocessed in the same discharge chambers where they were deposited. Varying the plasma and sheath parameters and controlling plasma-extracted ion fluxes, one can selectively dope, coat, or functionalize different areas on nanostructure surfaces [56].

## REFERENCES

- [1] Helveg, S.; López-Cartes, C.; Sehested, J.; Hansen, P. L.; Clausen, B. S.; Rostrup-Nielsen, J. R.; Abild-Pedersen, F.; Nørskov, J. K. *Nature* 2004, 427, 426-429.

- [2] Ostrikov, K.; Neyts, E. C.; Meyyappan, M. *Adv. Phys.* 2013, 62, 113-224.
- [3] Khalilov, U.; Bogaerts, A.; Neyts, E. C. *Nat. Commun.* 2015, 6, 10306.
- [4] Yang, H. Y.; Han, Z. J.; Yu, S. F.; Pey, K. L.; Ostrikov, K.; Karnik, R. *Nat. Commun.* 2013, 4, 2220.
- [5] Melechko, A. V.; Merkulov, V. I.; McKnight, T. E.; Guillorn, M. A.; Klein, K. L.; Lowndes, D. H.; Simpson, M. L. *Appl. Phys.* 2005, 97, 041301.
- [6] Mozetič, M.; Cvelbar, U.; Sunkara, M. K.; Vaddiraju, S. *Adv. Mater.* 2005, 17, 2138–2142.
- [7] Ostrikov, K. *Rev. Mod. Phys.* 2005, 77, 489.
- [8] Xu, M.; Xu, S.; Chai, J. W.; Long, J. D.; Ee, Y. C. *Appl. Phys. Lett.* 2006, 89, 251904.
- [9] Sharma, S.; Sunkara, M. K. *Nanotechnology* 2004, 15, 130-134.
- [10] Meyyappan, M.; Delzeit L.; Cassell, A.; Hash D. *Plasma Sources Sci. Technol.* 2003, 12, 205–216.
- [11] Ostrikov, K.; Murphy, A. B. *J. Phys. D: Appl. Phys.* 2007, 40, 2223.
- [12] Patera, L. L.; Africh, C.; Weatherup, R. S.; Blume, R.; Bhardwaj, S.; Castellarin-Cudia, C.; Knop-Gericke, A.; Schloegl, R.; Comelli, G.; Hofmann, S.; Cepek, C. *ACS Nano* 2013, 7, 7901 –7912.
- [13] Akita, S.; Kamo, S.; Nakayama, Y. *Jpn. J. Appl. Phys.* 2002, 41, L487.
- [14] Poretzky, A. A.; Geohegan, D. B.; Schittenhelm, H.; Fan, X.; Guillorn, M. A. *Appl. Surf. Sci.* 2002, 197-198, 552-562.
- [15] Cassell, A. M.; Raymakers, J. A.; Kong, J.; Dai, H. *J. Phys. Chem. B*, 1999, 103, 6484–6492.
- [16] Merkulov, V. I.; Melechko, A. V.; Guillorn, M. A.; Simpson, M. L.; Lowndes, D. H.; Whealton, J. H.; Raridon, R. J. *Appl. Phys. Lett.* 2002, 80, 4816- 4818.
- [17] Hofmann, S.; Czanyi, G.; Ferrari, A. C.; Payne, M. C.; Robertson, J. *Phys. Rev. Lett.* 2005, 95, 036101.
- [18] Charlier, J. C.; Amara, H.; Lambin, Ph. *ACS Nano* 2007, 1, 202–207.

- [19] Ding, F.; Harutyunyan, A. R.; Yakobson, B. I. *Proc. Natl. Acad. Sci. USA*, 2009, 106, 2506–2509.
- [20] Ghorannevis, Z.; Kato, T.; Kaneko, T.; Hatakeyama, R. *J. Am. Chem. Soc.* 2010, 132, 9570–9572.
- [21] Sankaran, R. M. *J. Phys. D.: Appl. Phys.* 2011, 44, 174005.
- [22] Hofmann, S.; Ducati, C.; Kleinsorge, B.; Robertson, J. *Appl. Phys. Lett.* 2003, 83, 4661–4663.
- [23] Neyts, E. C. *J. Vac. Sci. Technol. B* 2012, 30, 030803.
- [24] Kato, T.; Hatakeyama, R. *Chem. Vap. Depos.* 2006, 12, 345–352.
- [25] Yang, J.; Esconjauregui, S.; Xie, R.; Sugime, H.; Makaryan, T.; D'Arسيé, L.; Gonzalez Arellano, D. L.; Bhardwaj, S.; Cepek, C.; Robertson, J. *J. Phys. Chem. C* 2014, 118, 18683–18692.
- [26] Saheb, N.; Iqbal, Z.; Khalil, A.; Hakeem, A. S.; Al-Aqeeli, N.; Laoui, T.; Al-Qutub, A.; Kirchner, R. *J. Nanomater.* 2012, 2012, 1–13.
- [27] Cantoro, M.; Hofmann, S.; Pisana, S.; Scardaci, V.; Parvez, A.; Ducati, C.; Ferrari, A. C.; Blackburn, A. M.; Wang, K. Y.; Robertson, J. *Nano Lett.* 2006, 6, 1107–1112.
- [28] Li, Y. M.; Mann, D.; Rolandi, M.; Kim, W.; Ural, A.; Hung, S.; Javey, A.; Cao, J.; Wang, D. W.; Yenilmez, E.; Wang, Q.; Gibbons, J. F.; Nishi, Y.; Dai, H. *Nano Lett.* 2004, 4, 317–321.
- [29] Chiang, W. H.; Sankaran, R. M. *Nat. Mater.* 2009, 8, 882–886.
- [30] Kim, U. J.; Lee, E. H.; Kim, J. M.; Min, Y. S.; Kim, E.; Park, W. *Nanotechnology* 2009, 20, 295201.
- [31] Qu, L.; Du, F.; Dai, L. *Nano Lett.* 2008, 8, 2682–2687.
- [32] Ostrikov, K.; Mehdipour, H. *J. Am. Chem. Soc.* 2012, 134, 4303–4312.
- [33] Ostrikov, K. *J. Phys. D: Appl. Phys.* 2011, 44, 174003.
- [34] Esconjauregui, S.; Bayer, B.; Fouquet, M.; Wirth, C.; Yan, F.; Xie, R.; Ducati, C.; Baecht, C.; Castellarin-Cudia, C.; Bhardwaj, S. *J. Appl. Phys.* 2011, 109, 114312.
- [35] Meyyappan, M. *J. Phys. D: Appl. Phys.* 2009, 42, 213001.
- [36] Bogaerts, A.; Eckert, M.; Mao, M.; Neyts, E. *J. Phys. D: Appl. Phys.* 2011, 44, 174030.

- [37] Rutkevych, P.P.; Ostrikov, K.; Xu, S.; Vladimirov, S. V. *J. Appl. Phys.* 2004, *96*, 4421–4428.
- [38] Denysenko, I.; Ostrikov, K.; Yu, M. Y. *J. Appl. Phys.* 2007, *102*, 074308.
- [39] Burmaka, G.; Denysenko, I. B.; Ostrikov, K.; Levchenko, I.; Azarenkov, N. A. *Plasma Process. Polym.* 2014, *11*, 798–808.
- [40] Keidar, M.; Raitses, Y.; Knapp, A.; Waas, A. M. *Carbon* 2006, *44*, 1022–1024.
- [41] Reich, S.; Li, L.; Robertson, J. *Chem. Phys. Lett.* 2006, *421*, 469–472.
- [42] Hofmann, S.; Sharma, R.; Ducati, C.; Du, G.; Mattevi, C.; Cepek, C.; Cantoro, M.; Pisana, S.; Parvez, A.; Cervantes-Sodi, F.; Ferrari, A. C.; Dunin-Borkowski, R.; Lizzit, S.; Petaccia, L.; Goldoni, A.; Robertson, J. *Nano Lett.* 2007, *7*, 602–608.
- [43] Levchenko, I.; Ostrikov, K.; Mariotti, D.; Murphy, A. B. *J. Appl. Phys.* 2008, *104*, 073308.
- [44] Zhong, G.; Hofmann, S.; Yan, F.; Telg, H.; Warner, J. H.; Eder, D.; Thomsen, C.; Milne, W. I.; Robertson, J. *J. Phys. Chem. C* 2009, *113*, 17321–17325.
- [45] Woo, Y. S.; Jeon, D. Y.; Han, I. T.; Lee, N. S.; Jung, J. E.; Kim, J. M. *Diamond Relat. Mater.* 2002, *11*, 59–66.
- [46] Winter, J.; Berndt, J.; Hong, S. H.; Kovacevic, E.; Stefanovic, I.; Stepanovic, O. *Plasma Sources Sci. Technol.* 2009, *18*, 034010.
- [47] Sode, M.; Schwarz-Selinger, T.; Jacob, W. *J. Appl. Phys.* 2013, *114*, 063302.
- [48] Zheng, J.; Yang, R.; Xie, L.; Qu, J.; Liu, Y.; Li, X. *Adv Mater.* 2010, *22*, 1451–1473.
- [49] Teo, K. B. K.; Chhowalla, M.; Amaratunga, G. A. J.; Milne, W. I.; Hasko, D. G.; Pirio, G.; Legagneux P.; Wyczisk. F.; Pribat, D. *Appl. Phys. Lett.* 2001, *79*, 1534–1536.
- [50] Louchev, O. A.; Dussarrat, C.; Sato, Y. *J. Appl. Phys.* 1999, *86*, 1736–1744.
- [51] Mantzaris, N. V.; Gogolides, E.; Boudouvis, A. G.; Rhallabi, A.; Turban, G. *J. Appl. Phys.* 1996, *79*, 3718–3730.

- [52] Louchev, O. A.; Sato, Y.; Kanda, H. *Phys. Rev. E* 2002, *66*, 011601.
- [53] Louchev, O. A.; Laude, T.; Sato, Y.; Kanda, H. *J. Chem. Phys.* 2003, *118*, 7622–7635.
- [54] Krasheninnikov, A. V.; Nordlund, K.; Lehtinen, P. O.; Foster, A. S.; Ayuela, A.; Nieminen, R. M. *Phys. Rev. B* 2004, *69*, 073402.
- [55] Krasheninnikov, A.V.; Nordlund, K.; Lehtinen, P. O.; Foster, A. S.; Ayuela, A.; Nieminen, R. M. *Carbon* 2004, *42*, 1021–1025.
- [56] Levchenko, I.; Ostrikov, K.; Tam, E. *Appl. Phys. Lett.* 2006, *89*, 223108.
- [57] Reinke, P.; Jakob, W.; Moller, W. *J. Appl. Phys.* 1993, *74*, 1354–1362.
- [58] Nozaki, T.; Ohnishi, K.; Okazaki, K.; Kortshagen, U. *Carbon* 2007, *45*, 364–374.
- [59] Robertson, J. *Diamond Relat. Mater.* 1994, *3*, 361–368.
- [60] Fanelli, F.; Di Renzo, G.; Fracassi, F.; d’Agostino, R. *Plasma Process. Polym.* 2009, *6*, S503–S507.
- [61] Hassanien, A.; Tokumoto, M.; Umek, P.; Vrbanič, D.; Mozetič, M.; Mihailovič, D.; Venturini, P.; Pejovnik, S. *Nanotechnology* 2005, *16*, 278–281.
- [62] Shariat, M.; Hosseini, S. I.; Shokri, B.; Neyts, E. C. *Carbon* 2013, *65*, 269–276.
- [63] Zhong, G.; Iwasaki, T.; Honda, K.; Fukurawa, Y.; Ohdomari, I.; Kawarada, H. *Jpn. J. Appl. Phys.* 2005, *44*, 1558–1561.
- [64] Zhong, G.; Iwasaki, T.; Honda, K.; Furukawa, Y.; Ohdomari, I.; Kawarada, H. *Chem. Vap. Dep.* 2005, *11*, 127–130.
- [65] Min, Y. S.; Bae, E. J.; Oh, B. S.; Kang, D.; Park, W. *J. Am. Chem. Soc.* 2005, *127*, 12498–12499.
- [66] Zhang, G. Y.; Mann, D.; Zhang, L.; Javey, A.; Li, Y. M. *Proc. Natl. Acad. Sci. USA*, 2005, *102*, 16141–16145.
- [67] Lee, D. H.; Lee, W. J.; Kim, S. O. *Chem. Mat.* 2009, *21*, 1368–1374.
- [68] Su, L. F.; Wang, J. N.; Yu, F.; Sheng, Z. M.; Chang, H.; Pak, C. H. *Chem. Phys. Lett.* 2006, *420*, 421–425.
- [69] Oida, S.; Sakai, A.; Nakatsuka, O.; Ogawa, M.; Zaima, S. *Appl. Surf. Sci.* 2008, *254*, 7697–7702.

- [70] Peltekis, N.; Mausser, M.; Kumar, S.; McEvoy, N.; Murray, C.; Duesberg, G. *Chem. Vap. Dep.* 2012, 18, 17–21.
- [71] Ohashi, T.; Kato, R.; Ochiai, T.; Tokune, T.; Kawarada, H. *Diamond Relat. Mater.* 2012, 24, 184–187.
- [72] Wang, Y. Y.; Gupta, S.; Nemanich, R. J. *Appl. Phys. Lett.* 2004, 85, 2601–2604.
- [73] Nozaki, T.; Karatsu, T.; Ohnishi, K.; Okazaki, K. *Carbon* 2010, 48, 232–238.
- [74] Mariotti, D.; Sankaran, R. M. *J. Phys. D: Appl. Phys.* 2011, 44, 174023.
- [75] Mariotti, D.; Sankaran, R. M. *J. Phys. D: Appl. Phys.* 2010, 43, 323001.
- [76] Neyts, E. C.; Ostrikov, K.; Han, Z. J.; Kumar, S.; van Duin, A. C. T.; Bogaerts, A. *Phys. Rev. Lett.* 2013, 110, 065501.
- [77] Mehdipour, H.; Ostrikov, K. *ACS Nano* 2012, 6, 10276–10286.
- [78] Shariat, M.; Shokri, B.; Neyts, E. C. *Chem. Phys. Lett.* 2013, 590, 131–150.
- [79] Yuan, L.; Zhong, X.; Shu, Q.; Wu, X.; Xia, Y. *J. Phys. D: Appl. Phys.* 2007, 40, 7766.
- [80] Denysenko, I.; Ostrikov, K. *Appl. Phys. Lett.* 2007, 90, 251501.
- [81] Denysenko, I.; Ostrikov, K.; Cvelbar, U.; Mozetic, M.; Azarenkov, N. A. *J. Appl. Phys.* 2008, 104, 073301.
- [82] Ducati, C.; Alexandrou, I.; Chhowalla, M.; Amaratunga, G. A. J.; Robertson, J. *J. Appl. Phys.* 2002, 92, 3299–3303.
- [83] Hofmann, S.; Kleinsorge, B.; Ducati, C.; Ferrari, A. C.; Robertson, J. *Diamond Relat. Mater.* 2004, 13, 1171–1176.
- [84] Motz, H.; Wise, H. *J. Chem. Phys.* 1960, 32, 1893.
- [85] Denysenko, I.; Ostrikov, K. *J. Phys. D: Appl. Phys.* 2009, 42, 015208.
- [86] Tsakadze, Z. L.; Ostrikov, K.; Long, J. D.; Xu, S. *Diamond Relat. Mater.* 2004, 13, 1923–1929.
- [87] Tsakadze, Z. L.; Ostrikov, K.; Xu, S. *Surf. Coat. Technol.* 2005, 191, 49–53.

- [88] Mehdipour, H.; Ostrikov, K.; Rider, A. E. *Nanotechnology* 2010, *21*, 455605.
- [89] Gupta, R.; Sharma S. C.; Sharma, R. *Plasma Sources Sci. Technol.* 2017, *26*, 024006.
- [90] Marvi, Z.; Xu, S.; Foroutan, G.; Ostrikov, K. *Phys. Plasmas* 2015, *22*, 013504.
- [91] Ostrikov, K.; Mehdipour, H. *ACS Nano* 2011, *5*, 8372–8382.
- [92] Qu, L.; Du, F.; Dai, L. *Nano Lett.* 2008, *8*, 2682–2687.
- [93] Kato, T.; Hatakeyama, R. *ACS Nano* 2010, *4*, 7395–7400.
- [94] Volotskova, O.; Fagan, J. A.; Huh, J. Y.; Phelan, F. R.; Shashurin, A.; Keidar, M. *ACS Nano* 2010, *4*, 5187–5192.
- [95] Hatakeyama, R.; Kaneko, T.; Kato, T.; Li, Y. F. *J. Phys. D: Appl. Phys.* 2011, *44*, 174004.
- [96] Naumov, A.; Kunestov, O. A.; Harutyunyan, A. R.; Green, A. A.; Hersam, M. C.; Resasco, D. E.; Nikolaev, P. N.; Weisman, R. B. *Nano Lett.* 2009, *9*, 3203–3208.
- [97] Levchenko, I.; Ostrikov, K.; Long, J. D.; Xu, S. *Appl. Phys. Lett.* 2007, *91*, 113115.
- [98] Levchenko, I.; Ostrikov, K.; Keidar, M.; Xu, S. *J. Appl. Phys.* 2005, *98*, 064304.
- [99] Levchenko, I.; Ostrikov, K.; Keidar, M.; Xu, S. *Appl. Phys. Lett.* 2006, *89*, 033109.
- [100] Tam, E.; Ostrikov, K. *Appl. Phys. Lett.* 2008, *93*, 261504.
- [101] Tam, E.; Ostrikov, K. *Nanotechnology* 2009, *20*, 375603.
- [102] Keidar, M.; Levchenko, I.; Arbel, T.; Alexander, M.; Waas, A. M.; Ostrikov, K. *Appl. Phys. Lett.* 2008, *92*, 043129.
- [103] May, P. W.; Harvey, J. N.; Smith, J. A.; Mankelevich, Y. A. *J. Appl. Phys.* 2006, *99*, 104907.
- [104] Mankelevich, Y. A.; Rakhimov, A. T.; Suetin, N. V. *Diamond Relat. Mater.* 1998, *7*, 1133–1137.
- [105] May, P. W.; Smith, J. A.; Mankelevich Y. A. *Diamond Relat. Mater.* 2006, *15*, 345–352.
- [106] May, P. W.; Mankelevich, Y. A. *J. Appl. Phys.* 2006, *100*, 024301.

- [107] Elliott, J. A.; Shibuta, Y.; Amara, H.; Bichara, C.; Neyts, E. C. *Nanoscale*, 2013, 5, 6662–6676.
- [108] Neyts, E. C.; van Duin, A. C. T.; Bogaerts, A. *J. Am. Chem. Soc.* 2012, 134, 1256–1260.
- [109] Mees, M. J.; Pourtois, G.; Neyts, E. C.; Thijsse, B. J.; Stesmans, A. *Phys. Rev. B* 2012, 85, 134301.
- [110] Neyts, E. C.; Thijsse, B. J.; Mees, M. J.; Bal, K. M.; Pourtois, G. *J. Chem. Theory Comput.* 2012, 8, 1865–1869.
- [111] Neyts, E. C.; Bogaerts, A. *Carbon* 2014, 77, 790–795.
- [112] Khalilov, U.; Bogaerts, A.; Neyts, E. C. *Nanoscale* 2014, 6, 9206–9214.
- [113] Khalilov, U.; Bogaerts, A.; Hussain, S.; Kovacevic, E.; Brault, P.; Boulmer-Leborgne, C.; Neyts, E. C. *J. Phys. D: Appl. Phys.* 2017, 50, 184001.
- [114] Delzeit, L.; McAninch, I.; Cruden, B. A.; Hash, D.; Chen, B.; Han, J.; Meyyappan, M. *J. Appl. Phys.* 2002, 91, 6027–6033.
- [115] Denysenko, I. B.; Xu, S.; Long, J. D.; Rutkevych, P. P.; Azarenkov, N. A.; Ostrikov, K. *J. Appl. Phys.* 2004, 95, 2713–2724.
- [116] Teo, K. B. K.; Hash, D. B.; Lacerda, R. G.; Rupesinghe, N. L.; Bell, M. S.; Dalal, S. H.; Bose, D.; Govindan, T. R.; Cruden, B. A.; Chhowalla, M.; Amaratunga, G. A. J.; Meyyappan, M.; Milne, W. I. *Nano Lett.* 2004, 4, 921–926.
- [117] Bell, M. S.; Teo, K. B. K.; Lacerda, R. G.; Milne, W. I.; Hash, D. B.; Meyyappan, M. *Pure Appl. Chem.* 2006, 78, 1117–1126.
- [118] Hash, D.; Bose, D.; Govindan, T. R.; Meyyappan, M. *J. Appl. Phys.* 2003, 93, 6284–6290.
- [119] Hash, D. B.; Bell, M. S.; Teo, K. B. K.; Cruden, B. A.; Milne, W. I.; Meyyappan, M. *Nanotechnology* 2005, 16, 925–930.
- [120] Okita, A.; Suda, Y.; Ozeki, A.; Sugawara, H.; Sakai, Y.; Oda, A.; Nakamura, J. *J. Appl. Phys.* 2006, 99, 014302.
- [121] Okita, A.; Suda, Y.; Oda, A.; Nakamura, J.; Ozeki, A.; Bhattacharyya, K.; Sugawara, H.; Sakai, Y. *Carbon* 2007, 45, 1518–1526.



- [122] Ostrikov, K.; Yoon, H.; Rider, A. E.; Vladimirov, S. V. *Plasma Process. Polym.* 2007, 4, 27–40.
- [123] Mao, M.; Bogaerts, A. *J. Phys. D: Appl. Phys.* 2010, 43, 205201.
- [124] Mao, M.; Bogaerts, A. *J. Phys. D: Appl. Phys.* 2010, 43, 315203.
- [125] Mankelevich, Yu. A.; Ashfold, M. N. R.; Orr-Ewing, A. J. *J. Appl. Phys.* 2007, 102, 063310.
- [126] Gordillo-Vázquez, F. J.; Albella, J. M. *Plasma Sources Sci. Technol.* 2002, 11, 498–512.
- [127] Gordillo-Vázquez, F. J.; Albella, J. M. *J. Appl. Phys.* 2003, 94, 6085–6090.
- [128] Gordillo-Vázquez, F. J.; Albella, J. M. *Plasma Sources Sci. Technol.* 2004, 13, 50–57.
- [129] Lombardi, G.; Hassouni, K.; Bénédic, F.; Mohasseb, F.; Ropcke, J.; Gicquel, A. *J. Appl. Phys.* 2004, 96, 6739–6751.
- [130] Hassouni, K.; Mohasseb, F.; Bénédic, F.; Lombardi, G.; Gicquel, A. *Pure Appl. Chem.* 2006, 78, 1127–1145.
- [131] Stoykov, S.; Eggs, C.; Kortshagen, U. *J. Phys. D: Appl. Phys.* 2001, 34, 2160–2173.
- [132] De Bleecker, K.; Bogaerts, A.; Goedheer, W. *Phys. Rev. E* 2006, 73, 026406.
- [133] Mao, M.; Benedikt, J.; Consoli, A.; Bogaerts, A. *J. Phys. D: Appl. Phys.* 2008, 41, 225201.
- [134] Ariskin, D. A.; Schweigert, I. V.; Alexandrov, A. L.; Bogaerts, A.; Peeters, F. M. *J. Appl. Phys.* 2009, 105, 063305.
- [135] Akhouni, A.; Foroutan, G. *Phys. Plasmas* 2017, 24, 053516.
- [136] Liu, X. M.; Li, Q. N.; Li, R. *Chin. Phys. B* 2016, 25, 065203.
- [137] Hinz, A. M.; von Wahl, E.; Faupel, F.; Strunskus, T.; Kersten, H. *J. Phys. D: Appl. Phys.* 2015, 48, 055203.
- [138] Vladimirov, S. V.; Ostrikov, K.; Samarian, A. A. *Physics and Applications of Complex Plasmas*; 1-86094-572-4; Imperial College Press: London, 2005; 141-190.
- [139] Woo, Y. S.; Han, I. T.; Park, Y. J.; Kim, H. J.; Jung, J. E.; Lee, N. S.; Jeon, D. Y.; Kim, J. M. *Jpn. J. Appl. Phys.* 2003, 42, 1410–1413.



*Chapter 2*

**RAYLEIGH AND BRILLOUIN SCATTERING  
SPECTROSCOPY FOR OPTICAL  
MATERIAL SCIENCE**

*Leonid V. Maksimov\*, DSc  
and Anatoli V. Anan'ev, PhD*

S. I. Vavilov State Optical Institute, Saint Petersburg, Russia

**ABSTRACT**

Data on the application of Rayleigh and Mandelstam-Brillouin scattering (RMBS) spectroscopy to controlling the elastic, elasto-optic, optical parameters of inorganic glasses, crystals, and glass-crystalline materials is generalized. The possibilities of using RMBS spectroscopy for research and development of materials for optical and electro-optical fiber drawing, as well as glasses doped with rare earth ions and quantum dots, are considered.

---

\* Corresponding Author Email: [leonid.maksimov@mail.ru](mailto:leonid.maksimov@mail.ru).

**Keywords:** Rayleigh, Mandelshtam, Brillouin, Raman, scattering, Landau-Placzek ratio, glass, glass-ceramics, electrooptical fiber, segregation, rare-earth ions, quantum dots

## INTRODUCTION

Despite almost a century since the first prediction (L. Brillouin) of the fine structure of the spectrum of monochromatic light scattered by a condensed substance, the use of Brillouin scattering in optical material science remains less extensive than one might expect [1]. The effect was independently theoretically analyzed by L. Mandelshtam and named Mandelshtam-Brillouin (MB) scattering in Russian literature [2].

It was found that light scattering by adiabatic density fluctuations caused by thermal atomic oscillations in matter can be considered as the modulation of light by elastic hyper sound waves. It should be noted that corresponding frequency shift was estimated so small ( $\sim 20$  GHz) that observation of MB components needed significant experimental skills. At the first time the thin structure of light scattering spectrum of the condensed matter was observed by E. Gross [3, 4].

In contrast, the isothermal density fluctuations caused by translation motion of atoms lead to elastic scattering of light wave. In the case of sufficiently small as compared to the wavelength of incident light, independently appearing and disappearing fluctuations, not causing multiple scattering the type of light scattering can be referred to the Rayleigh one [5, 6].

Therefore, information on the role of fluctuations of both types in light scattering is contained in the ratio of Rayleigh intensity and MB scattering of the Rayleigh and Mandelstam-Brillouin spectrum (RMBS), which is the so-called Landau-Placzek ratio.

The review is aimed at analyzing the possibilities of RMBS spectroscopy as a method for controlling the parameters of optical materials, mainly glasses, and its usage for research and development (R&D) of new optical materials.

## MAIN THEORETICAL RELATIONSHIPS

The theory of RMBS of thermodynamically equilibrium media comprehensively described in [7] was adapted to nonequilibrium media in [8]. Below are the main relationships needed to process RMBS spectra of optical materials.

In the case of an isotropic solid, in particular glass, the RMBS spectrum excited by optical radiation of frequency  $\nu$  includes the Rayleigh (elastic) scattering component and the doublets shifted by  $\pm \Delta\nu_l$  (Mandel'shtam-Brillouin – MB shift) and  $\pm \Delta\nu_t$  with respect to  $\nu$ . These shifts, caused by modulation of the exciting light by longitudinal ( $l$ ) and transverse ( $t$ ) hypersonic waves propagating in a solid, can be written as:

$$\frac{\Delta\nu_l}{\nu} = 2n \frac{v_l}{c} \sin \frac{\theta}{2} \quad (1)$$

$$\frac{\Delta\nu_t}{\nu} = 2n \frac{v_t}{c} \sin \frac{\theta}{2} \quad (2)$$

where  $n$  is the index of light scattering medium at  $\nu = 1/\lambda$  where  $\lambda$  is the wavelength,  $v_l$ ,  $v_t$  are the velocities of longitudinal and transverse hyper sound waves, respectively,  $c$  is the light velocity in vacuum,  $\theta$  is the scattering angle.

Hence, hyper sound velocities can be easily determined through Eqs. (1, 2) and, consequently, high frequency values of longitudinal  $c_{11} = \rho v_l^2$  and transverse  $c_{44} = \rho v_t^2$  moduli, where  $\rho$  is the density of glass.

Integral intensities of light modulated by longitudinal (LA phonons),  $I^{MB}$ , and transverse (TA phonons),  $I^T$ , hyper sound waves can be written as Eq. 3 and Eq. 4, correspondingly [9]:

$$I^{MB} = I_{VV} = I_0 V_s \pi^2 kT \frac{n^8 |p_{12}|^2}{\lambda^4 c_{11}} (1 + \cos^2 \theta) \quad (3)$$

$$I^T = I_{VH} = I_{HV} = I_0 V_s \pi^2 kT \frac{n^8 |p_{44}|^2}{\lambda^4 c_{11}} (1 + \cos^2 \theta) \quad (4)$$

where  $I_0$  is the intensity of exciting light,  $I_{VV}$ ,  $I_{VH}$ ,  $I_{HV}$  are the intensities of RMBS spectrum components measured at vertical ( $V$ ) and horizontal ( $H$ ) polarizations of exciting (the first symbol) and scattered (the second symbol) light, correspondingly,  $p_{ij}$  are Pockels tensor components,  $V_s$  is the scattering volume,  $k$  is the Boltzmann constant,  $T$  is the temperature in  $K$ .

It should be noted that RMBS spectrum of liquid is limited by Rayleigh scattering line and MBS doublet if  $v_t \rightarrow 0$ , while RMBS spectrum of crystal depends on its optical and acoustic anisotropy and orientation of a sample relative to exciting light beam. In this case RMBS spectrum will contain up to 12 Stokes and 12 anti-Stokes components [10].

At first, it was found that the scattering of light by glasses was more intense than one would expect on the basis of measurements and estimations made for simple liquids and crystals. Excessive elastic scattering of light by glass was explained by the “freezing” of index fluctuations due to translational motion of atoms in a glass melt, which was much slower than the thermal vibrations causing MB scattering [8, 9].

Bearing in mind that numerous experiments have shown that the elastic scattering of light by glasses followed, as a rule, Rayleigh law, the intensity of Rayleigh scattering by a single component glass can be written as [9]:

$$I^P = I_0 V_s \pi^2 \frac{n^8 |p_{12}|^2}{\lambda^4 c_{11}} (1 + \cos^2 \theta) kT_f \left[ \beta_{T_f}^0 - (\rho v_\infty^2)^{-1} \right] \quad (5)$$

where  $I^P$  is the integral intensity of Rayleigh scattering by “frozen-in” isothermal density fluctuations,  $T_f$  is the fictive temperature at which the translational motion of atoms in the process of glass melt cooling is being stopped,  $v_\infty$  is the “instantaneous” (at frequency  $\rightarrow \infty$ ) sound velocity,  $\beta_{T_f}^0$  is the isothermal (at frequency  $\rightarrow 0$ ) static compressibility.

Then the Landau-Placzek ratio is [8]:

$$R_{L-P}^{\rho} = \frac{I^{\rho}}{2 \cdot I_{MB}} = \frac{T_f}{T} \left[ \beta_{T_f}^0 (\rho v_{\infty}^2) - 1 \right] \quad (6)$$

The authors [11] found that variation of sound velocity in glasses at room temperature in the kHz - GHz frequency range was negligibly small, which made it possible to adopt  $v_s$  and  $v_t$  in Eqs 1, 2 as “instantaneous” sound velocities.

Then

$$R_{L-P}^{\rho} = \frac{T_f}{T} \left[ \beta_{T_f}^0 c_{11} - 1 \right] \quad (7)$$

The fact is that the Rayleigh scattering of single component glasses is caused not only by the “frozen-in” density fluctuations, but “frozen-in” fluctuations of anisotropy, as well. This means that the Landau-Placzek ratio should be written as:

$$R_{L-P} = R_{L-P}^{\rho} + R_{L-P}^{anis} = \frac{I^{\rho}}{2 \cdot I_{MB}} + \frac{I^{anis}}{2 \cdot I_{MB}} \quad (8)$$

where  $R_{L-P}^{anis}$  is the contribution of anisotropy fluctuations in Landau-Placzek ratio,  $I^{anis}$  is the intensity of Rayleigh scattering by anisotropy fluctuations.

These contributions into Rayleigh scattering can be obtained from RMBS spectra measured at  $VV$  and  $VH$  polarizations [12]. If the depolarization coefficient,  $\Delta_V$ , is the ratio of Rayleigh scattering intensities measured at various polarizations,  $\Delta_V = I_{VH}^{RS}/I_{VV}^{RS}$ , and  $\theta = 90^\circ$  then

$$I_{iso}^{RS} = I_{VV}^{RS} - \left( \frac{4}{3} \right) I_{VH}^{RS} \quad (9)$$

where  $I_{iso}^{RS}$  is the intensity of isotropic Rayleigh scattering.

Hence,

$$R_{L-P}^{\rho} = R_{L-P} \left( 1 - \left( \frac{4}{3} \right) \Delta_V \right) \quad (10)$$

In the case of multicomponent glasses

$$R_{L-P} = R_{L-P}^{\rho} + R_{L-P}^{anis} + R_{L-P}^C = \frac{I^{\rho}}{2 \cdot I^{MB}} + \frac{I^{anis}}{2 \cdot I^{MB}} + \frac{I^C}{2 \cdot I^{MB}} \quad (11)$$

where  $R_{L-P}^C$ ,  $I^C$  are the contributions of “frozen-in” concentration,  $C$ , fluctuations caused by stopped diffusive motion of ions in a glass melt into Landau-Placzek ratio and Rayleigh scattering intensity of glass, correspondingly.

For binary glasses it can be presented in the form:

$$R_{L-P}^C \sim \frac{T_D (\partial n / \partial C)_{PT}^2 \langle \Delta C^2 \rangle}{2 \cdot I^{MB}} \quad (12)$$

where  $T_D$  is the temperature of stopped diffusive motion in glass melt,  $\langle \Delta C^2 \rangle$  is the mean square concentration fluctuation,  $P$  is the pressure.

These are the basic relationships that can be used for qualitative interpretation of experimental data. More detailed theoretical analysis can be found elsewhere [6, 7, 13].

## FEATURES OF RMB SPECTROSCOPY

Observation of thin structure of light scattering spectrum should meet some requirements. As is well-known, thermal density fluctuations can be considered as a result of interference of elastic Debay waves and the scattered light as a result of light diffraction on elastic waves [6]. It means that thin structure can be observed at fixed angle when the Bragg condition



for wave vectors of incident, scattered and acoustic wave will be fulfilled (Eq. 13).

$$\mathbf{k}' - \mathbf{k} - \mathbf{q} = 0 \quad (13)$$

where  $\mathbf{k}'$ ,  $\mathbf{k}$  are the wave vectors of scattered, incident light wave,  $\mathbf{q}$  is the wave vector of hyper sound wave.

As follows from Eqs. 1, 2, the relative uncertainty of a spectral shift,  $\delta(\Delta\nu)/\Delta\nu$ , caused by aperture,  $\delta\theta$ , broadening:

$$\frac{\delta(\Delta\nu)}{\Delta\nu} = \frac{1}{2} \cot \frac{\theta}{2} \delta\theta \quad (14)$$

Therefore, one might expect that the most precise measurements of spectral shifts aperture can be performed at  $\theta = 180^\circ$  if the dependence of inherent width of MB lines proportional to  $(1 - \cos\theta)$  would be considered as negligible [6]. Scattering of light wave by acoustic phonons leads to much smaller spectral shifts (tenths of  $\text{cm}^{-1}$ ) than the scattering by optical phonons in the case of Raman scattering (hundreds of  $\text{cm}^{-1}$ ). Though RMBS spectrum can be recorded by grating monochromators the scanning Fabry-Perot interferometers (FPI) turned out to be more suitable for RMBS spectroscopy [14, 15] (See Figure 1).

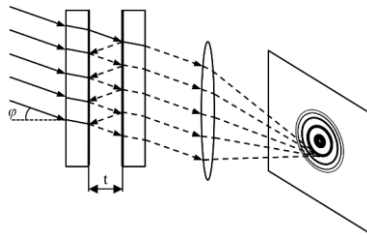


Figure 1. Forming interference pattern in Fabry-Perot interferometer.

Positions of interference maxima follow:

$$2tn \cos \varphi = k \lambda \quad (15)$$

where  $t$  is the thickness of IFP,  $n$  is the index of medium between plates of FPI,  $\varphi$  is the angle of incident light flux relative IFP plates,  $k$  is the interference order [16].

Earlier MB scattering was recorded by photographic method as satellites around main rings of an interference pattern at lamp excitation of scattering [6]. Later the appearance of lasers and high sensitive detectors made it possible to use scanning FPI and determine spectral parameters more precisely. Evidently, scanning of interference pattern may be realized by varying  $t$ ,  $n$  or  $\varphi$  that leads to the change in radii of interference rings located in the plane of exit diaphragm. Part of the interference pattern cut out by a pin hole or ring diaphragm is being recorded by a detector system. Comprehensive reviews on scanning FPI technique can be found in [17].

Nowadays, the simplest and non-expensive pressure scanned and fast scanning piezoelectric FPIs are widely used. The scanning by pressure is based on varying of  $n$  by inlet of a gas in an evacuated chamber with FPI inside. Scanning of interference pattern occurs because  $P \sim n \sim k$ . For example, the variation of pressure about 1 atm. leads to passing not less than 3 interference orders through the exit diaphragm of FPI with  $t = 3$  mm. Homemade FPIs of this type are described elsewhere [18, 19, 20, 21].

Piezoelectric scanning is based on varying  $t$  by applying voltage to one of FPI mirror holders made of piezoelectric material. This technique found wide range of applications in study of glasses and crystals [17].

Nowadays the leading position among manufactures of piezoelectric FPI applicable for optical material characterization (Burleigh Instruments Inc., Tropel Inc., Thorlabs Inc., and others) belongs to the JRS Scientific Instruments, which first demonstrated the drastic improvement of the contrast of interference pattern in multi passing FPI.

The usefulness of coupling two synchronized FPIs, thus avoiding the overlapping of different orders of interference, was also recognized. Original optical scheme of multi pass piezoelectric FPI allowed to achieve the contrast of interference pattern up to  $10^{15}$  [22, 23].

Comparison of results of studying the temperature induced evolution of nanostructure of low alkali silicate glasses by means of pressure

scanning IFP and multi-pass piezoelectric scanning IFP clearly demonstrates advantages of the latter [24, 25].

Exotic variants of scanning by  $\varphi$ , that is the inclination of rays with respect to optical axis, were tested in set-ups with the prism of revolution or the objective with varying focus distance [26, 27, 28] Nowadays, the first successful attempt of coming back to application of non-scanning IFP to optical material characterization was made in [29]. It resulted to significant lowering (up to 5 times) the uncertainty of spectral shift measurements.

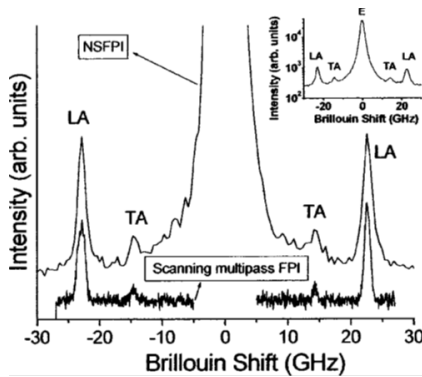


Figure 2. Brillouin spectra of a fused quartz glass measured by NSFPI and a conventional tandem multipass FPI. LA and TA denote the longitudinal and transverse mode, respectively. The inset shows the Brillouin spectrum in a semilog plot, which was measured by NSFPI with an acquisition time of 3 s without using the iris. E means the elastic component. Fujiwara cube-shaped quartz glass was purchased from Fujiwara Scientific Company, Tokyo, Japan, and its OH concentration was less than 8 ppm [29]. Reproduced from *Rev Sci Instr.* 2002, 73, 4390-4392 with the permission of AIP Publishing.

Measurement of RMBS spectrum intensities needs the usage of a high sensitive detector because light scattering coefficients of optical materials may be as low as  $10^{-7} \text{ cm}^{-1}$  [30]. On the other hand, light scattering should be excited by continuous-wave laser with working wavelength in the middle of transparency window of optical material transmission spectra to avoid background luminescence of trace impurities lowering the contrast of interference pattern [31, 32]. For this reason the conventional photoelectrical detection of light flux appears inapplicable and photo

counting system based on detection of current pulses caused by single photons was found the most suitable for usage in RMBS spectrometers [33, 34].

## APPLICATION OF RMBS SPECTROSCOPY TO OPTICAL MATERIAL CHARACTERIZATION

The usage of RMBS spectroscopy for the characterization of glasses subjected to thermal or pressure influence is considered in [35]. Below some arguments in favor of using RMBS spectroscopy for controlling parameters included in the specification of glasses for various applications are presented. As follows from Table 1 RMBS spectrum of glass is a source of information about its optical, elasto-optical, and elastic parameters. To determine Landau-Placzek ratio from RMBS spectrum accurately it is necessary to estimate uncertainty caused by the usage of maximal values of spectrum intensities instead of the integral ones.

$$R_{L-P}^{int} = \frac{\delta v_C^T + \delta v_\rho^T + \delta v^A}{\delta v_{C_{MB}}^T + \delta v_A} R_{L-P}^{max} \quad (16)$$

where  $R_{L-P}^{int}$ ,  $R_{L-P}^{max}$  are the Landau-Placzek ratios as the ratios of integral and maximal intensities of Rayleigh and Mandelshtam-Brillouin scattering, correspondingly,  $\delta v_C^T$  and  $\delta v_\rho^T$  are the true full width at half maximum (FWHM) of Rayleigh line depending on time of appearance and disappearance of concentration and isobaric density fluctuations,  $\delta v_{C_{MB}}^T$  is the true FWHM of MB line caused by damping of hyper sound wave in the matter,  $\delta v^A$  is the FWHM of instrumental contour. In the case of inorganic glasses  $\delta v_C^T \approx 0$  because it is a function of diffusion coefficient which is close to zero at room temperature,  $\delta v_\rho^T \approx 5 \cdot 10^{-3} \text{ cm}^{-1}$  is a function of thermal diffusivity [6, 8].

If  $\delta v^A = 0.09 \text{ cm}^{-1}$  the RMBS spectrometer then  $R_{L-P}^{int} \approx 1.04 R_{L-P}^{max}$  [36]. Below only  $R_{L-P}^{max}$  values are used. Comparison of adiabatic  $p_{ij}$  values taken from RMBS measurements (GHz frequencies) with isothermal ones

taken from measurements at steady state loading of glass showed that the difference was less than the measurement uncertainty [8, 11, 37].

**Table 1. Parameters of glasses obtained from RMBS spectra**

Parameter of RMBS spectrum	Parameter of a glass	Formulation
Landau-Placzek ratio, $R_{L-P} = \frac{I^R}{2 \cdot I^{MB}}$	Rayleigh scattering loss coefficient, $\alpha_s$	$\alpha_s = (R_{L-P} + 1) \frac{8\pi^3 kT}{3 \lambda^4} (n^4 p_{12})^2 c_{11}$
Mandelstam-Brillouin shift, $\Delta v_l$	Longitudinal hypersonic velocity, $v_l$	$\frac{\Delta v_l}{v} = 2n \frac{v_l}{c} \sin \frac{\theta}{2}$
Transverse shift, $\Delta v_t$	Transverse hypersonic velocity, $v_t$	$\frac{\Delta v_t}{v} = 2n \frac{v_t}{c} \sin \frac{\theta}{2}$
Intensity of MB component, $I^{MB}$	Pockels coefficient, $p_{12}$	$p_{12} = p_{12}^0 \left( \frac{I^{MB}}{I_0^{MB}} \right)^{\frac{1}{2}} \left( \frac{c_{11}}{c_{11}^0} \right)^{\frac{1}{2}} \left( \frac{n^0}{n} \right)^4 \left( \frac{n+1}{n^0+1} \right)^2$
Intensity of transverse component, $I^T$	Pockels coefficient, $p_{44}$	$p_{44} = p_{44}^0 \left( \frac{I^{MB}}{I_0^{MB}} \right)^{\frac{1}{2}} \left( \frac{c_{44}}{c_{44}^0} \right)^{\frac{1}{2}} \left( \frac{n^0}{n} \right)^4 \left( \frac{n+1}{n^0+1} \right)^2$
Parameters included in glass specifications	Longitudinal modules, $c_{11}$	$c_{11} = \rho v_l^2$
	Shear modules, $c_{44}$	$c_{44} = \rho v_t^2$
	Compression modules, $K$	$K = c_{11} - \frac{4}{3} c_{44}$
	Young modules, $E$	$E = \frac{9c_{11}c_{44}}{3K + c_{44}}$
	Poisson ratio, $\sigma$	$\sigma = \frac{E}{2c_{44}} - 1$
	Photoelastic coefficient, $B_{\parallel}$	$B_{\parallel} = \frac{n^3}{2E} (p_{11} - 2\sigma p_{12})$
	Photoelastic coefficient, $B_{\perp}$	$B_{\perp} = \frac{n^3}{2E} [(1 - \sigma)p_{12} - \sigma p_{11}]$
	Optical stress coefficient, $C$	$C = B_{\parallel} - B_{\perp}$ $C = (1 + \sigma)[p_{11} - p_{12}]$

Therefore, RMBS spectrometer provides measurement of 9 glass parameters, i.e., replaces several measuring stands. Comparison of accuracy of spectroscopic and acoustic techniques is shown in Table 2.

**Table 2. Typical accuracy of RMBS and acoustic measurements at room temperature**

Parameter	Uncertainty, $\pm$ %				
	RMBS			Acoustics	
	[38]	[11, 39]	[31]	[38]	[40]
Landau-Placzek ratio,	5				
Rayleigh scattering loss coefficient, $\alpha_s$	10	10			
Mandelshtam-Brillouin shift, $\Delta v_l$	0.1				
Longitudinal hypersonic velocity, $v_l$	0.3	0.4	1	0.1	0.13
Longitudinal modulus, $c_{11}$	1		2	0.2	
Transverse shift, $\Delta v_t$	0.3*				
Transverse hypersonic velocity, $v_t$	1*	0.8	1	0.1	0.25
Shear modulus, $c_{44}$	2	1.6	2	0.2	
Young' modulus, $E$ :	3	2.5	3	0.5	0.8
Poisson ratio, $\sigma$	3	5	3	0.7	0.7
Pockels coefficient, $p_{12}$	5	3	10		
Pockels coefficient, $p_{44}$			20		

Note: \*  $R_{L-P} < 200$ , in other cases the accuracy of  $\Delta v_t$  measurement decreases while peaks of RMBS spectra at  $\Delta v_t$  become hardly observable.

As follows from the data in Table 1 and 2, RMBS spectroscopy may be considered as alternative technique applicable for metrological control of optical glasses. In addition, location of focused laser beam inside a glass volume and detecting RMBS in small solid angle ensures the measuring local parameters of gradient index glass samples, for example, fiber preforms [41].

## APPLICATION OF RMBS SPECTROSCOPY TO RESEARCH AND DEVELOPMENT (R&D) OF OPTICAL MATERIALS

### Crystals

As follows from the theoretical analysis of molecular scattering by a crystal its spectrum includes a set of doublets caused by modulation of light wave by elastic waves of various types [6]. For this reason, estimation of Landau-Placzek ratio from RMBS spectrum requires accurate alignment of a sample relative to excited laser beam. Intensity of Rayleigh scattering

by a single crystal proportional to temperature is expectably so low that makes selection of true molecular scattering from elastic scattering on defects extremely difficult experimental task. Therefore, only several  $R_{L,P}$  values of crystals were found (see Figures 3-5 and Table 3).

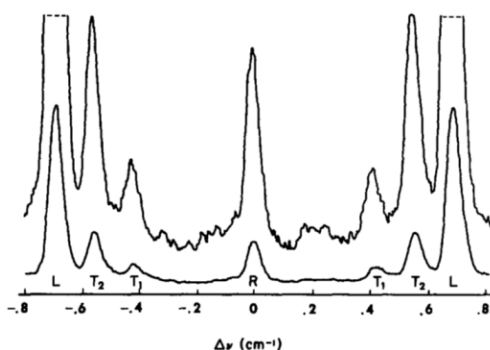


Figure 3. Brillouin spectra of crystalline  $\text{SiO}_2$  where Rayleigh peak (R), longitudinal (L), and 2 transverse ( $T_1$ ,  $T_2$ ). Brillouin peaks at two different gains [42]. Reproduced from *Appl Phys Lett*. 1966, vol. 9, 157-159 with the permission of AIP Publishing.

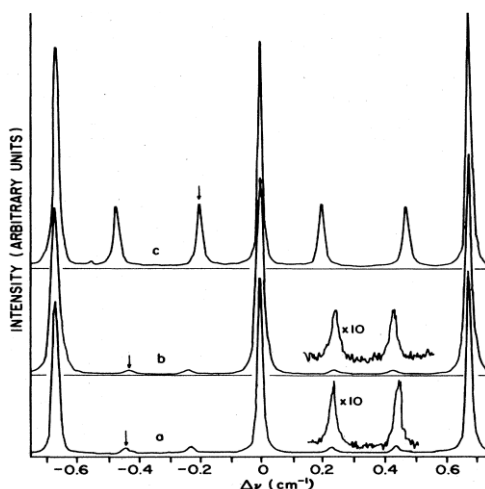


Figure 4. Brillouin spectra of crystalline (a,b) and molten (c) KCl. Free spectral range of  $0.667 \text{ cm}^{-1}$ . a,  $T = 707^\circ\text{C}$ , b,  $T = 770^\circ\text{C}$ , and c,  $T = 810^\circ\text{C}$ . The Rayleigh peaks are approximately 7000 counts/sec in all three spectra. The arrows indicate the Stokes LA Brillouin component associated with the central Rayleigh line [43]. Reproduced from *Phys Rev B*. 1985, vol. 31, 2456-2463 with the permission of APS Publishing.

**Table 3. Landau-Placzek ratios of crystals and their melts**

Crystals				
	$R_{L,P}$	$\nu_l, \text{cm}^{-1}$	$\nu_t, \text{cm}^{-1}$	Ref
NaF	0.1-0.05			[44]
NaF at 980 K *	$\sim 14$	$\sim 0.23$		
KBr	$0.99 \pm 0.22$ $12.62 \pm 3.6$			[45]
CaF <sub>2</sub>	$6.7 \pm 0.5$	$0.729 \pm 0.03$	$0.423 \pm 0.03$	
Al <sub>2</sub> O <sub>3</sub> (sapphire)	0.6			[47]
Al <sub>2</sub> O <sub>3</sub> (sapphire) + Ni	8.5			[47]
Diamond	2.7			[46]
SiO <sub>2</sub>	0.06			[47]
SiO <sub>2</sub> **	$\sim 0.1$			[42]
Melts				
KCl ( $\sim 1083$ K)*	$\sim 2$	$\sim 0.2$		
SiO <sub>2</sub> ( $\sim 1900$ K)	$7.50 \pm 0.01$			[48]
SiO <sub>2</sub> ( $\sim 1900$ K) **	$\sim 7$			[49]

Note: \* - taken from Figure 3. \*\* - taken from Figures in the papers.

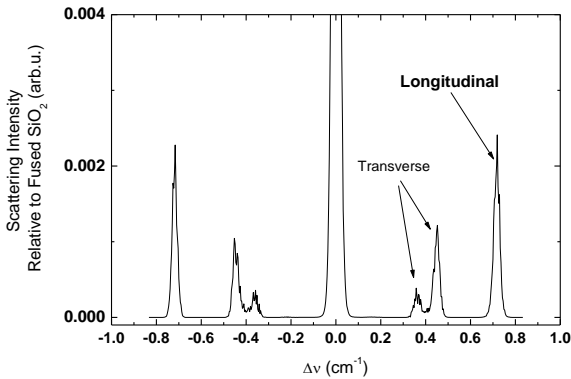


Figure 5. RMBS spectrum of CaF<sub>2</sub> after 256 iterations of Bayesian deconvolution taken in circle polarization of incident light.  $I^{\text{RS}}(\text{CaF}_2) = 0.02 I^{\text{RS}}(\text{fused SiO}_2)$ .

Nevertheless, RMBS spectroscopy is widely used for determination of elastic moduli and Pockels coefficients in solid state studies that requires high optical quality of a crystal and its careful alignment relative to excited laser beam. Theoretical basis for determining elastic and elastic-optic constants from the line positions in RMBS spectra of crystals was developed in [50].



Results of corresponding theoretical analysis ensures the possibility to use RMBS spectroscopy in studying of external influence such as temperature or pressure on phase transitions in crystal or overcooling of melt and glass forming [51, 52, 53, 54, 55].

## GLASSES

### Single Component Glasses

Glass was defined as an inorganic product of fusion, which has been cooled to a solid state condition without crystallizing or as a non-crystalline solid that exhibits a glass transition temperature,  $T_g$ . Above the glass transition temperature glass exhibits properties of liquid and below  $T_g$  it retains liquid structure in rigid form [56, 57].

Therefore, on the contrary to crystals, the glasses inherit structure of their melts “frozen-in” at temperature at which viscosity of melts becomes so high that it any translational motion of atoms or ions is stopped. Glass forming oxides seem to be the best objects to verify the model of “freezing” isobaric density fluctuations. Analysis of RMBS data for single component glasses seems meaningful taking into account the possibility to verify Eq. 7 and estimate the influence of manufacturing technology on glass parameters causing Rayleigh and MB scattering.

From the practical viewpoint one can expect that key factors significant for minimization of Rayleigh scattering loss coefficient in glass as a material for optical communication fibers will be determined. Because the difference of glass density at fictive and room temperatures as a rule does not exceed 0.5% Eq.7 can be rewritten as:

$$R_{L-P}^{\rho} = \frac{T_f}{T} \left[ \left( \frac{v_l}{v_{0,T_f}} \right)^2 - 1 \right] \quad (17)$$

where  $v_{0,T_f}$  is the equilibrium sound velocity that is at zero frequency. This value can be found by extrapolating  $v = v(T)$  taken at various sound frequencies to  $T_f$ .

The latter can be found through frequency dependences of sound velocity taken in the temperature range extended from glass melt to room temperature. The systematic experiments were performed in Catholic University (Washington, DC, US) and Saint Petersburg State University (Saint Petersburg, Russia) [58, 59]. As follows from [58, 59] the “freezing” isothermal density fluctuations occurs when the time of their appearance and disappearance approaches to reciprocal rate of glass melt cooling. The latter takes place at the viscosity close to  $10^{13}$  P that is  $T_f \approx T_g$ .

### GLASSY SiO<sub>2</sub> (Silica Glass, Quartz Glass, Molten Quartz)

As is-well known, the revolution in information transmission systems became real in large part because there was a suitable material for drawing optical fiber. Such material turned out to be silica because of its unique optical and physical-chemical properties. As a result, the problem of optical losses, in particular, losses on Rayleigh scattering in silica glass, has become the focus of attention of researchers.

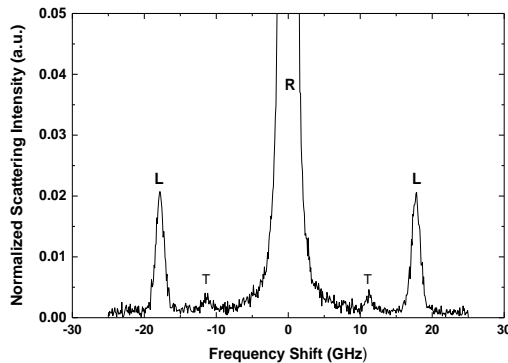


Figure 6. RMBS spectrum of silica glass KI (Russia). RMBS was excited by He-Ne laser ( $\lambda = 632.8$  nm) and measured at VV + VH polarization. Scattering angle is  $90^\circ$ ,  $R$  is the Rayleigh scattering component,  $L$  and  $T$  are the longitudinal (Brillouin) and transverse lines, correspondingly.

Considering the difference in the indices of silica glass and crystalline modifications of SiO<sub>2</sub>, one might expect a difference in intensities of Rayleigh scattering by glasses obtained from gaseous or solid raw materials because of trace concentrations of microcrystals. If Mandelshtam-Brillouin components of RMBS spectrum are taken as the internal reference one can estimate Rayleigh scattering coefficient,  $\alpha_s$ . (See Table 1). Typical RMBS spectrum of commercial silica glass is shown in Figure 6.

**Table 4. Landau-Placzek ratios of silica glasses produced under various technologies**

Landau-Placzek ratio	Glassy SiO <sub>2</sub>			
	Type of technology			
	I melting quartz grains in vacuum	II melting quartz grains in H <sub>2</sub> + O <sub>2</sub>	III high temperature hydrolysis of SiCl <sub>4</sub> in H <sub>2</sub> + O <sub>2</sub>	IV oxidation of SiCl <sub>4</sub> in high frequency plasma
21.9 [8]		Homosil, US		
23.0 ± 0.2		KV, Russia		
24.5 ± 0.5			KU-1, Russia Corning 7940, US	
25.5 ± 0.5		KV, Russia	Thermal Syndicate UK	Corning 7943, US
26.5 ± 0.5	KI, Russia			
30.5 ± 0.5				KUVI-1, Russia

As follows from Table 4 the Landau-Placzek ratio does not change more than 25%. The validity of this method for estimating  $\alpha_s$  from RMBS spectra is confirmed by results of direct measurements of  $\alpha_s$  in silica glasses [60].

At the same time, it should be taken into account that silica glasses of various types differ in the content of trace impurities and the cooling conditions [61]. The impurities affect the temperature behavior of viscosity and, consequently, solidification conditions. It should result to varying both  $T_f$  and  $\beta_{T_f}^0$ . Therefore,  $\alpha_s$  can be lowered by 20% by reducing these parameters due to special dopants added to raw materials. Special

additional heat treatment of silica glass can lead to lower  $\alpha_s$ , as well [62, 63, 64, 65].

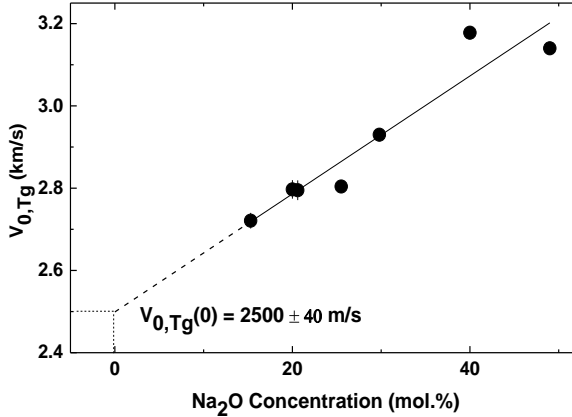


Figure 7. Equilibrium sound velocity at  $T_g$  as a function of Na<sub>2</sub>O-SiO<sub>2</sub> glass composition. The data is taken from [66].

**Table 5. Comparison of RMBS, high temperature acoustic (HTA) and SAXS measurement results**

Glassy SiO <sub>2</sub>	$T_f$ , K	$\beta_{T_g}^0$ , TPa <sup>-1</sup>	$c_{11}$ , GPa	$R^p$ (HTA)	$R^p$ (RMBS)	$R^p$ (SAXS)	$\alpha_s$ , dB/km $\lambda = 632.8$ nm
KI (Russia)	1443 [30]	$73 \pm 1$	78.50 [30]	$22.9 \pm 0.3$	$23 \pm 1$		
Homosil (US) [8]	1473	68.0	77.857	21.5 [8]	21.9		3.9
Corning (US)						$25 \pm 1$ [67]	

On the other hand, the concentration fluctuations of dopants can be an additional source of Rayleigh scattering. Thus, a decrease in the loss of Rayleigh scattering by silica glass is possible due to the optimization of temperature-temporal cooling conditions and concentrations of specially selected dopants. Difficulty of acoustic measurements of molten silica necessitated to use a series of sound velocity - temperature curves for Na<sub>2</sub>O-SiO<sub>2</sub> glass melts to find composition dependence of  $v_{0,T_f}$  shown in Figure 7.

Table 5 shows that the values of  $R^p$  determined by various experimental techniques coincide within measurement uncertainty. The small value of  $R^{anis}$  agrees with the idea of constructing a network of silica glass from tetrahedra connected by vertices. It indicates the small value of depolarization coefficient. Coincidence of Landau-Placzek values taken from RMBS, high temperature acoustics and SAXS data confirms the validity of Eq. 7, that is the model of “freezing” index fluctuations at glass melt cooling, and opens the opportunity to determine  $\beta_{T_f}^0$  from RMBS spectrum of a single component glass.

### GLASSY B<sub>2</sub>O<sub>3</sub>

Studying boron oxide by RMBS spectroscopy and high temperature acoustic technique meets some difficulties because of the impact of structurally bonded OH groups on its properties while concentration of these groups is a function of temperature-temporal synthesis conditions. Besides, high hygroscopicity is a significant obstacle to obtaining reliable values of Landau-Placzek ratio due to parasitic scattering from hydrolyzed surfaces of the glass sample. Light scattering by glassy B<sub>2</sub>O<sub>3</sub> is illustrated by RMBS spectrum in [68].

A feature of Rayleigh scattering by boron oxide, both in the glassy and in the liquid state, is the large contribution of anisotropic scattering, which finds a natural explanation within the framework of constructing a network from triangles [BO<sub>3</sub>] or boroxol rings [B<sub>6</sub>O<sub>6</sub>] [12].

Anomalous temperature dependency of ultrasound velocity measured at various frequencies discourages the correct determination of  $\beta_{T_f}^0$ . Along with the melts of aluminum oxide, antimony, and also water, the melt of boric oxide refers to liquids in which the temperature coefficient of velocity is positive (the so-called “water-like anomaly”).

The growth of sound velocity with temperature of the melt was explained in terms of the two-structure model of B<sub>2</sub>O<sub>3</sub> that is by decomposition of large complexes into smaller ones with an increase in the proportion of dense packed molecular groups [69]. As in the previous case,

a series of sound velocity - temperature curves for  $\text{Na}_2\text{O}-\text{B}_2\text{O}_3$  glass melts was used to find composition dependence of  $v_{0,T_f}$  shown in Figure 8.

Experimental results are collected in Table 6.

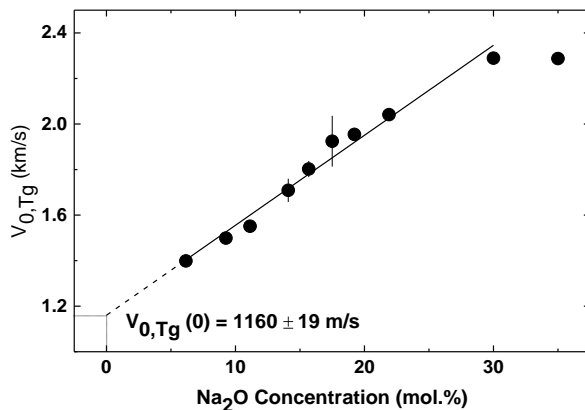


Figure 8. Equilibrium sound velocity at  $T_g$  as a function of  $\text{Na}_2\text{O}-\text{B}_2\text{O}_3$  glass composition. The data is taken from [69].

**Table 6. RMBS, high temperature acoustic, and SAXS measurement results of  $\text{B}_2\text{O}_3$**

$\text{H}_2\text{O}$ content	$\beta_{T_g}^0$ , $\text{TPa}^{-1}$	$c_{11}$ , GPa	$R^\rho$ (HTA)	$R_{L-P}$	$R^\rho$ (RMBS)	$R^\rho$ (SAXS)
	$410 \pm 20$	21.0 [70]	$13.9 \pm 0.7$			
Dehydrated						$10 \pm 1$ [67]
Dehydrated	390 [8]	20.71 [8]			13.3 [8]	
Dehydrated	390 [12]	22 [12]		$21.0 \pm 0.6$ [12]	$12.6 \pm 0.6$ *	
$\leq 1.6$ mol.%				$32 \pm 2$ [71]		

Note: \* - estimated from [12].

As follows from Table 6, the accurate evaluation of the factors mentioned above makes it possible to prove the validity of Eq.7 for the boron oxide. It should be noted that in the “fragile” glass boron oxide, the transverse velocity of sound is not zero even at temperatures significantly exceeding the melting point [72].

## GLASSY GeO<sub>2</sub>

RMBS and high temperature acoustic data is shown in Figures 9, 10 that opens the opportunity to verify the validity of Eq. 7 for glassy GeO<sub>2</sub>. The problem is that the samples of glassy GeO<sub>2</sub>, synthesized and studied in various laboratories, are characterized by a considerable scatter of both micro- (Landau-Placzek ratio, Rayleigh scattering loss coefficient, depolarization coefficient) and macroscopic (density, index, etc.) parameters exceeding the measurement uncertainty [36].

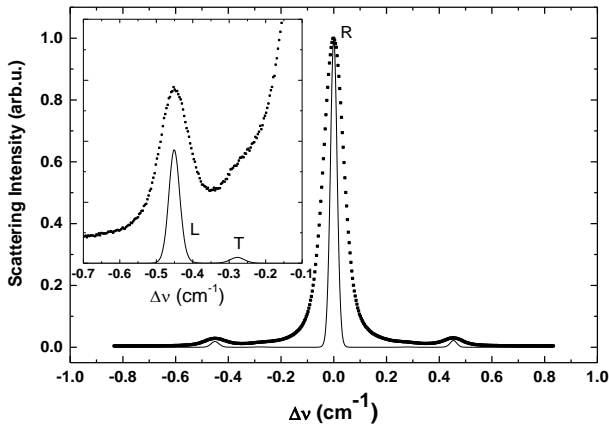


Figure 9. RMBS spectrum of glassy GeO<sub>2</sub> taken in VV + VH polarization before (dots) and after 256 iterations of Bayesian deconvolution (lines). RMBS was excited by He-Ne laser ( $\lambda = 632.8$  nm) were taken at VV + VH polarization. Scattering angle is  $90^\circ$ , R is the Rayleigh scattering component, L and T are the longitudinal (Brillouin) and transverse lines, correspondingly [36].

Therefore, one can suppose that there is another source of light scattering losses in addition to the “frozen-in” density and anisotropy fluctuations. Plausible explanation was put forward based on the model of ‘polymorphous’ constitution of glassy GeO<sub>2</sub> built from both GeO<sub>2</sub> and GeO units [73, 74]. It means that glassy GeO<sub>2</sub> should be considered as a binary glass of  $(100-x)\text{GeO}_2-x\text{GeO}$  system where  $x$  is a function of the synthesis conditions. Increase in the portion of GeO in the system causes

the growth of refractive index and density that is followed by the decrease in glass transition temperature (Figure 11).

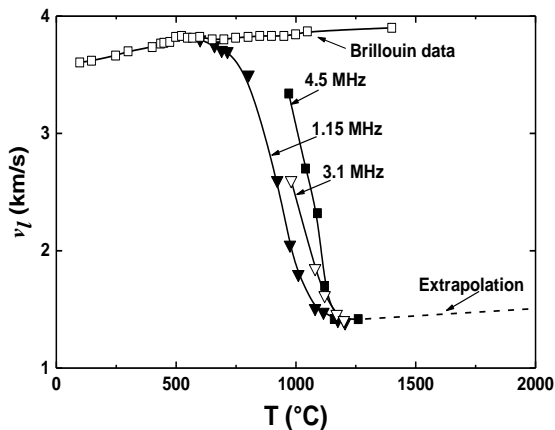


Figure 10. Temperature dependence of longitudinal sound velocity in  $\text{GeO}_2$  glass and melt at hypersonic and ultrasonic frequencies; extrapolation is shown by dash line [36].

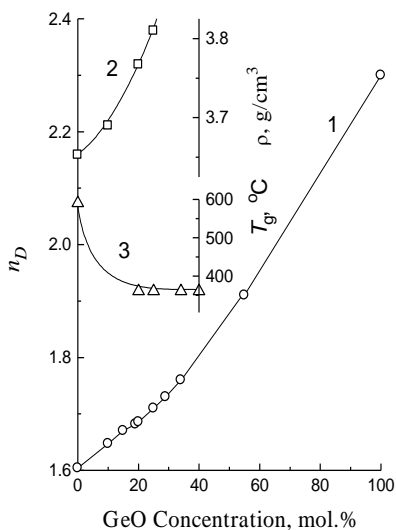


Figure 11. Index  $n_D$  (1), density  $\rho$  (2), and glass transition temperature  $T_g$  (3) as functions of composition of  $x\text{GeO}-(100-x)\text{GeO}_2$  glasses. Lines are drawn as guides for eye [36].



**Table 7. RMBS, high temperature acoustics, and SAXS measurement results of GeO<sub>2</sub>**

Synthesis conditions, Ref.	$\beta_{Tg}^0$ , TPa <sup>-1</sup>	$c_{11}$ , GPa	$n$ $\lambda = 632.8$ nm	$R^p$ (HTA)	$R_{L-P}$ (RMBS)	$\Delta v$	$R^p$ (RMBS)	$\alpha_s$ , dB/km $\lambda = 632.8$ nm
1450°C 2h [36]	140 ± 10	51 ± 2	1.6040 ± 0.0002	18 ± 1	19.5 ± 0.5	0.05	18.3 ± 0.5	8.0
1100°C [75]		51.4 ± 0.5*	1.6075 (n <sub>D</sub> )		24			16.4 **
[8]		51.54	1.6110 ± 0.0002		24.3	0.31		
[76]					68.7			

Notes: \* calculated from the data in [75]. \*\* calculated from the data in [75].

One can conclude that the growth of index is connected with the structure densifying because polarizability estimated through the Lorentz–Lorenz formula was found to be constant. RMBS and HTA data is shown in Table 7.

High depolarization coefficient of Rayleigh scattering is explained by the presence in glassy GeO<sub>2</sub> not only 4-fold coordinated but 6-fold coordinated (hexagonal) anisotropic GeO<sub>2</sub> as well.

Variability of glassy GeO<sub>2</sub> parameters is caused by “freezing” both valence GeO ↔ GeO<sub>2</sub> and coordination [GeO<sub>4</sub>] ↔ [GeO<sub>6</sub>] equilibria at different redox and temperature-temporal conditions of glass melting and melt cooling [36]. Therefore, comparison of RMBS and HTA measurement results allows identifying the origin of excessive Rayleigh scattering losses and improving the regime of glass synthesis.

## GLASSY P<sub>2</sub>O<sub>5</sub>

In view of its high reactivity with respect to water, it cannot be directly studied by spectroscopic and ultrasonic methods. For this reason, several glasses of  $x\text{La}_2\text{O}_3-(100-x)\text{P}_2\text{O}_5$  were synthesized, the chemical resistance and optical quality of which allowed obtaining reliable values of the Landau-Placzek ratio. The results are shown in Figure 12.

The estimation of  $R^\rho$  was based on the results of high temperature acoustic study of  $\text{La}_2\text{O}_3\text{-P}_2\text{O}_5$  melts, which gave  $v_{0,T_g} = 1900 \pm 100 \text{ m}\cdot\text{s}^{-1}$ . As follows from Table 8, there is a significant discrepancy between the results of different methods that can be explained by the presence of uncontrolled water content in samples of glassy  $\text{P}_2\text{O}_5$  synthesized under various conditions. In this case, glass  $\text{P}_2\text{O}_5$  should be considered as a binary glass with “frozen” concentration fluctuations contributing into Rayleigh scattering intensity and, as a consequence, into Landau-Plazek ratio.

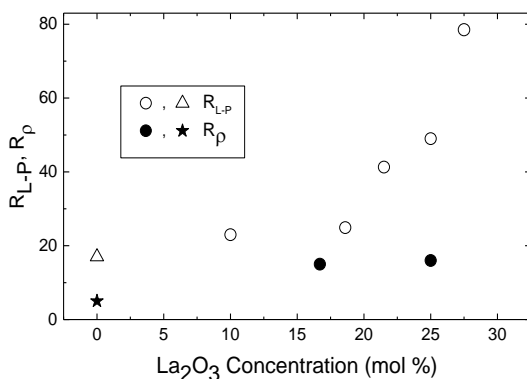


Figure 12. Dependences of Landau-Plazek ratio,  $R_{L-P}$ , and contribution of “frozen-in” density fluctuations,  $R_\rho$ , on composition of  $\text{La}_2\text{O}_3\text{-P}_2\text{O}_5$  glasses. ★ is the value of  $R_\rho$ , calculated from HTA; △ is the value of  $R_{L-P}$ , calculated from [77].

**Table 8. RMBS, high temperature acoustics, and SAXS measurement results of  $\text{P}_2\text{O}_5$**

$T_g/T$	$\beta_{T_g}^0$ , TPa <sup>-1</sup>	$c_{11}$ , GPa	$R^\rho$ (HTA)	$R_{L-P}$ (RMBS)	$R_{L-P}$ (SAXS)
$2.0 \pm 0.2$	$90 \pm 10$ *	40.55 [78]	$5 \pm 1$	No data	No data
2.2 [79]	220 [79]	40 [79]	No data	No data	17 **

Notes: \* estimated on the base of assumption that  $v_{0,T_g}(\text{P}_2\text{O}_5)$  does not differ from  $v_{0,T_g}(\text{La}_2\text{O}_3 \cdot 5\text{P}_2\text{O}_5) = v_{0,T_g}(\text{La}_2\text{O}_3 \cdot 3\text{P}_2\text{O}_5) = 1900 \text{ m}\cdot\text{s}^{-1}$ ; \*\* calculated from [79].

## GLASSY TeO<sub>2</sub>

Interest in TeO<sub>2</sub> as the main component of tellurite glasses is due to their features (low attenuation coefficient of ultrasound, high magneto-optical constant, high dielectric constant, high quantum yield of luminescence of rare-earth (RE) ions in tellurite hosts, high index in visible range, etc.) that makes tellurite glasses the valuable material for a number of practical applications, in particular, for manufacturing acousto- and magneto-optical components, laser devices, gradient-index elements, etc.).

Glass TeO<sub>2</sub> cannot be obtained because of its high crystallization ability, which decreases with the addition of the second component [80]. Nevertheless  $R^{\rho}$  can be estimated from the results of high temperature acoustic study of R<sub>2</sub>O-TeO<sub>2</sub> (R = Li, Na, K) glass melts [81]. Extrapolation of the temperature dependences of  $\rho v^2(T)$  to  $T_g$  makes it possible to determine  $(\rho v^2)_{T_g}^0$  depending on the concentration of alkali oxide. Extrapolation to zero content of alkali oxide gives  $\beta_{T_g}^0$  of tellurium oxide.

Results are shown in Table 9. Therefore, Rayleigh scattering losses in glass forming oxides originate from nano scaled density fluctuations “frozen-in” at a glass melt cooling. Growth of Rayleigh scattering losses can be explained by variation of cooling conditions, appearance of “frozen-in” concentration fluctuations in glass forming melts due to specially embedded dopants, trace impurities such as water, or partial reduction of an oxide.

**Table 9. RMBS, HTA, and SAXS measurement results of TeO<sub>2</sub>**

$T_g/T$	$\beta_{T_g}^0$ , TPa <sup>-1</sup>	$c_{11}$ , GPa	$R^{\rho}$ (HTA)	$R_{L-P}$ (RMBS)	$R_{L-P}$ (SAXS)
1.92 ± 0.07	70 ± 7	60 ± 4	6.3 ± 0.7	No data	No data

## BINARY GLASSES: CONSTANT COMPOSITION GROUPS

Addition of oxides-modifiers, i.e., oxides, which under ordinary cooling conditions of the melt are not capable of transition to the glassy

state, to glass forming oxides makes it possible to synthesize a continuous series of glasses in a wide range of compositions [82]. The use of RMBS spectroscopy in combination with Raman spectroscopy allows to study the relationship between inhomogeneous structure of a glass and its composition and to reveal the compositions of glasses with minimal Rayleigh scattering loss coefficient, which may turn out to be smaller than in single component (silica) glass.

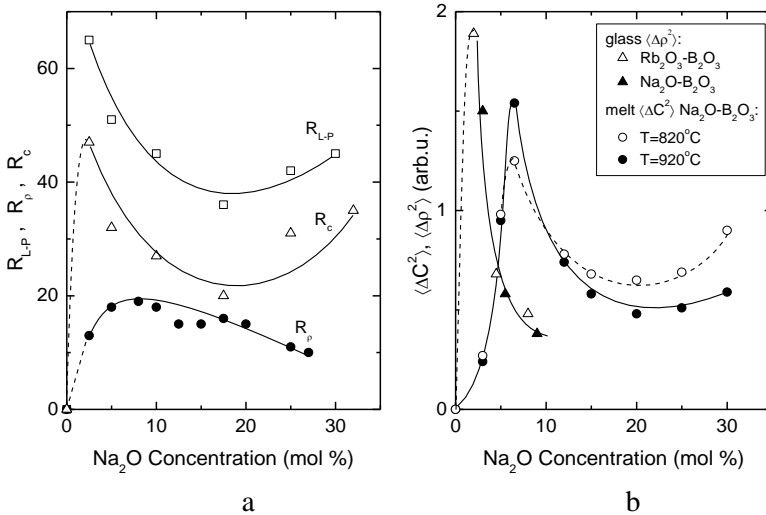


Figure 13. (a) Dependences on the composition of Na<sub>2</sub>O-B<sub>2</sub>O<sub>3</sub> glasses of Landau-Placzek ratio,  $R_{L-P}$ , of the contribution to  $R_{L-P}$  from “frozen-in” isobaric density fluctuations,  $R_p$ , and the contribution to  $R_{L-P}$  from “frozen-in” concentration fluctuations,  $R_c$ . (b) Dependences of mean square concentration fluctuations,  $\langle \Delta C^2 \rangle$ , on the composition of Na<sub>2</sub>O-B<sub>2</sub>O<sub>3</sub> melts at 820° C and 920° C [65]. Dependences of the mean square difference in electronic densities of inhomogeneities and glass host,  $\langle \Delta \rho^2 \rangle$ , on the composition of Na<sub>2</sub>O-B<sub>2</sub>O<sub>3</sub> and Rb<sub>2</sub>O<sub>3</sub>-B<sub>2</sub>O<sub>3</sub> glasses. [83, 84]. Lines are drawn as guides for eye. Reproduced from *Glass Physics and Chemistry* 1989, vol. 51, 1223-1237 with the permission of Maik Nauka.

Although silica glass is the main material for optical fiber drawing up to now, the search for new materials that allow expanding the assortment of optical fibers for information transmitting and processing systems remains in the focus of interests of glass scientists.

Dependences in Figure 13 evidence that the thermodynamically equilibrium fluctuation inhomogeneities in a glass forming melt actually remain in the glass while chemical inhomogeneities, that is “frozen-in” concentration fluctuations, dominate in Rayleigh scattering intensity by glasses. SAXS results indicate that dimensions of these inhomogeneities lie in the nanometer range.

The growth of scattering by “frozen-in” fluctuations with increasing alkali oxide concentration is explained by an increase in the crystallization ability of glasses as their compositions approach the glass formation boundary of  $\text{Na}_2\text{O}-\text{B}_2\text{O}_3$  system. Maximum in the low-alkali composition range indicates the tendency to subliquidus immiscibility that was observed in several alkali-containing binary systems. It remains unclear what are the species the concentration fluctuations of which are being “frozen-in” that determine the main part of Rayleigh scattering losses of glasses. Combined analysis of RMBS and Raman scattering data contains an answer to the question.

When processing the Raman spectra of  $\text{Na}_2\text{O}-\text{SiO}_2$ ,  $\text{Na}_2\text{O}-\text{B}_2\text{O}_3$ ,  $\text{BaO}-\text{B}_2\text{O}_3$ ,  $\text{R}_2\text{O}-\text{GeO}_2$ ,  $\text{RF}-\text{GeO}_2$  ( $\text{R} = \text{Na}, \text{K}$ ) glasses and others using the Wallace-Katz method, it was established that the spectra can be represented as an additive sum of 3-4 spectral forms of an unchanged contours and varying intensities from a glass to glass [85, 86]. Processing of the Raman spectra on the base of Wallace-Katz technique gave the number of linearly independent rows of the matrix constructed from the intensities at fixed frequencies for each experimental spectrum.

It led to identification of components referred to groups with constant stoichiometry (constant composition groups – CCGs) playing the role of glass components [87, 88]. A set of macroscopic parameters of CCGs (density, index, elastic moduli, etc.) can be found from Raman scattering spectra. It opens the opportunity to calculate the values of glass parameters on the base of glass composition that makes elaboration of novel glasses easier.

Expectably, the glasses built from the groups of single type only should be low-scattering ones that are illustrated by Figure 14.

In addition, the optical inhomogeneity of chemically inhomogeneous binary glasses can be minimized when indices of inhomogeneities and their surrounding coincide (the effect of internal immersion). As follows from Eq. 12 compositions of low-scattering glasses can be found in the vicinity of extrema of index-composition curves.

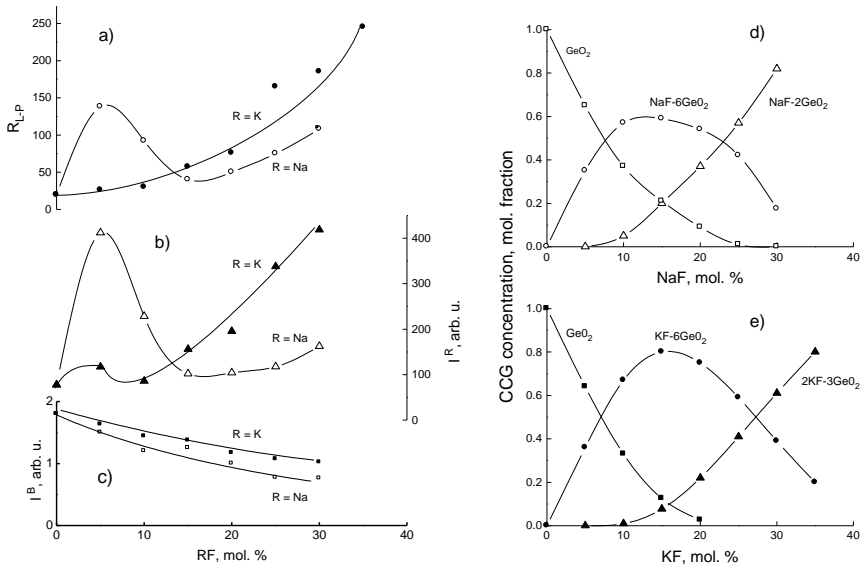


Figure 14. Dependences on  $xRF-(100-x)GeO_2$  ( $R = Na, K$ ) (mol. %) glass composition of: a) Landau-Placzek ratio,  $R_{L-P} = I^R/2I^{MB}$ ; b) Intensity of Rayleigh scattering,  $I^R$ ; c) Intensity of Mandelstam-Brillouin scattering,  $I^B$ ; d) Concentrations of CCGs of: a)  $GeO_2$ ,  $NaF \cdot 2GeO_2$ ,  $NaF \cdot 6GeO_2$ ; b)  $GeO_2$ ,  $KF \cdot 6GeO_2$ ,  $2KF \cdot 3GeO_2$  [89]. Reproduced from *J Appl Spectr.* 1989, vol. 51, 1223-1237 with the permission of the Institute of Physics at National Academy of Science of Belarus

## TERNARY GLASSES

The application of RMBS spectroscopy to study glasses of the system with subliquidus miscibility gap ( $Na_2O-B_2O_3-SiO_2$ ) which was well studied by SAXS and electron microscopy demonstrated the high sensitivity of Landau-Placzek ratio to the “frozen-in” fluctuation inhomogeneities of nanometer scale [90]. The application of RMBS spectroscopy to polycation

glasses evidenced the lowering of Rayleigh scattering losses of glasses with approximately equal percentage of various alkali or alkali-earth oxides due to the well-known polycation effect [91].

## **MULTICOMPONENT GLASSES**

Multicomponent optical glasses are convenient for their studying by RMBS spectroscopy due to their high optical quality and chemical resistance. However, the finding the relationships of spectral parameters with composition and structure of these glasses presents seems significant difficult. Nevertheless, such attempts have been made by a number of authors. This has made it possible to establish empirical relationships between the optical, elastic, and elasto optic parameters of glasses and their composition [38].

Studying the optical strength of crystals and glasses led to the hypothesis about relationship between the bulk optical breakdown threshold and intensity of Rayleigh scattering. It can originate from the defects in crystals and “frozen-in” index inhomogeneities in glasses [92, 93].

Thus, in glass-forming systems consisting of a glass-forming oxide and modifying oxides, it is possible to obtain glasses with high chemical homogeneity, which ensures minimal Rayleigh scattering losses.

## **ELECTROOPTICAL GLASSES FOR FIBER DRAWING**

Electrooptical (EO) effect in optical media – change of refractive index resulting in arising of birefringence of the media under applied electric field – is in use to control propagation and parameters of optical radiation (amplitude, polarization, phase, etc.). Usage of optical waveguiding microstructures, which are similar to conventional microwave waveguides, allows to localize propagation of light inside a region, the specific

transverse dimensions of which are of order of several optical wavelengths, that are several micrometers [94].

Due to that feature the modulation of light in such structures can be provided by the driving voltage that is essentially less than the voltage applied to the bulk structures and the necessary electric fields up to  $10 \text{ V}/\mu\text{m}$  can be achieved applying voltage of several volts. The driving electric fields and voltages can be decreased if the length of EO structures is increased since the effect is accumulating with increasing optical path.

Conventional (bulk) and optical waveguide (integrated) EO structures are presently widely used in the systems for processing and transmitting information and in optical sensors. Bulk structures are mainly in use for processing optical images. Integrated versions of EO systems are used as light modulators and modulators/switches in fiber-optical lines in multipurpose systems for information transmitting, particularly, in systems for telecommunication [95].

Necessary features of EO structures are as follows: low insertion losses, low driving voltage, and fast response (response time down to  $10^{-10}$  s), possibility of effective coupling with optical fibers under use. This means that dimensions and refractive index profiles of the elements to be coupled must coincide, manufacturing technology should be effective to ensure low cost in the case of mass production.

Anisotropic crystalline materials are traditionally in use to make EO devices. EO phenomenon in the materials is linear one (linear dependence of index change on driving electric field – Pockels effect). The materials demonstrate fast response, and the driving electric field is of order  $1 \text{ V}/\mu\text{m}$ .

At present, the techniques to produce strip and slab optical waveguide structures have been developed on the base of  $\text{LiNbO}_3$  and KTP crystals. Disadvantages of crystalline materials include limited dimensions, complicated and energy consuming production technology, poor possibility to make crystalline-based optical fibers, high optical losses being inserted in fiber-optical lines by crystalline modulators due to the significant difference in indices of the conventionally used fibers and EO crystals.

In the case of isotropic materials, particularly glasses, the index change,  $\Delta n$ , under applied electric field,  $E = U/d$  is the electric field,  $U$  is



the applied electric voltage,  $d$  is the distance between electrodes, (Kerr effect) is

$$\Delta n = B \cdot \lambda \cdot E^2 \quad (18)$$

Since EO interaction depends on the ratio of external field and interatomic electrical field ( $\sim 10^8$  V/m), the quadratic phenomenon is usually weaker than the linear one. Usually, the fields that allow to get the same index change as in the case of linear EO phenomenon are essentially higher, and the typical field is  $\sim 30$  V/ $\mu\text{m}$ .

**Table 10. Kerr coefficients of several EO crystalline materials and nitrobenzene**

EO material	Kerr coefficient, $B$ , $10^{-16} \text{ m}^2/\text{V}^2$ , $\lambda = 632.8 \text{ nm}$ , $T = 300 \text{ K}$
Crystal [97]	
(Na,K)NbO <sub>3</sub>	1,000,000
NaNbO <sub>3</sub>	800,000
(Na,Pb)NbO <sub>3</sub>	670,000
(Li,Na,K)NbO <sub>3</sub>	500,000
BaTiO <sub>3</sub>	500,000
Liquid	
Nitrobenzene [98]	$19,700 \pm 100$
Glass	
Silica glass [98]	$0.55 \pm 0.1$

As a rule, such fields cannot be put in practice because the necessary voltages are too high to be applied to a modulator. That is why glasses are not in use as working media for EO modulators even though EO response time for glasses lies in picosecond range. Anyway the preference of glasses comparatively to the anisotropic EO materials in use is undoubted due to less expensive production technology and the opportunity to draw EO fibers. Finally, losses occurring due to the coupling of optical waveguide structures with fiber-optical line could be decreased through decreasing their index difference.

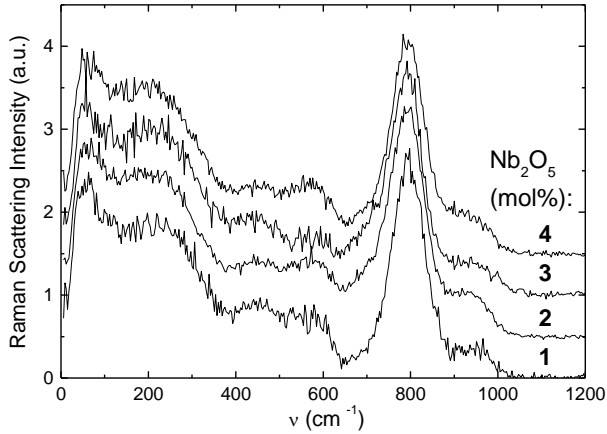


Figure 15. Contour of the spectral forms extracted from Raman spectra of  $(5\text{Li}_2\text{O}-5\text{Na}_2\text{O})-(90-x)\text{GeO}_2-x\text{Nb}_2\text{O}_5$  glasses ascribed to CCGs  $(\text{Li}, \text{Na})\text{NbO}_3 \cdot n\text{GeO}_2$ . HV polarization. Numbers at the curves are  $\text{Nb}_2\text{O}_5$  concentrations in mol. % [99]. Reproduced from *Proc SPIE*. 2003, vol. 5122, 87-93 with the permission of SPIE.

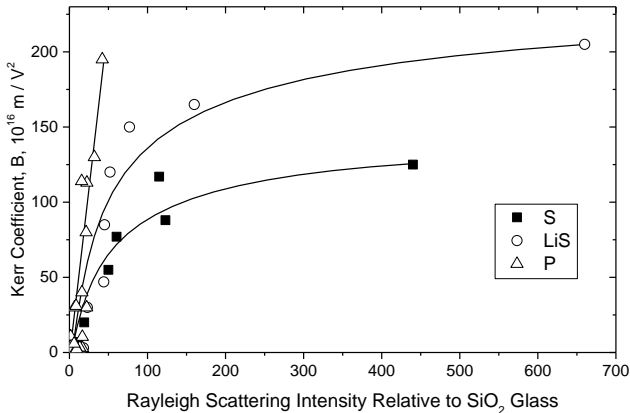


Figure 16. Relationship between Kerr coefficient,  $B$ , and Rayleigh scattering losses of sodium niobate silicate (S), lithium niobate silicate (LiS), and alkali niobate phosphate glasses (P) [100]. Curves are drawn as a guide for eye [100].

Therefore, elaboration of EO glasses suitable to produce optical fibers with the driving fields less than  $10 \text{ V}/\mu\text{m}$  opens the way to design EO fibers that can provide modulation of the light propagating through the

fiber. This will result in transmission and modulation of optical signals in a single element. Weak EO effect can be used in this case since rather long optical fibers can be made. As follows from Table 10, silica glass, the main material for drawing optical fibers, is characterized by minimum Kerr coefficient. The decision lies in the elaboration of niobium containing glasses containing CCGs with stoichiometry of an EO crystal [96].

Processing of Raman scattering spectra allowed identifying the EO active CCGs in glass structure that is shown in Figure 15.

Combination of RMBS and Raman scattering data opens the way to optimization of glass compositions taking into account that the growth of Nb percentage in glass leads to the growth of not only Kerr coefficient but Rayleigh scattering loss coefficient. Results are summarized in Figure 16.

Window of opportunities of manufacturing EO Kerr fibres from multicomponent inorganic glasses was considered in [100]. Phase shift  $\phi$  between orthogonal components of a linear polarised beam is:

$$\phi = 2\pi BE^2 l \quad (19)$$

where  $l$  is the length of sample to which the electric field is applied.

Then the halfwave length  $l_{\lambda/2}$  ensuring  $\phi = \pi$  at halfwave field  $E_{\lambda/2}$  is:

$$l_{\lambda/2} = \frac{1}{2BE_{\lambda/2}^2} \quad (20)$$

Solid area in Figure 17 represents the range of  $l_{\lambda/2}$  values for the glasses and glass ceramics under study.

It resulted to elaboration of EO Kerr fiber drawn from a pair of multicomponent niobium silicate glasses ensuring the signal modulation due to Kerr effect. Its depth was found close to that of EO Pockels fiber drawn from PMMA [101, 102].

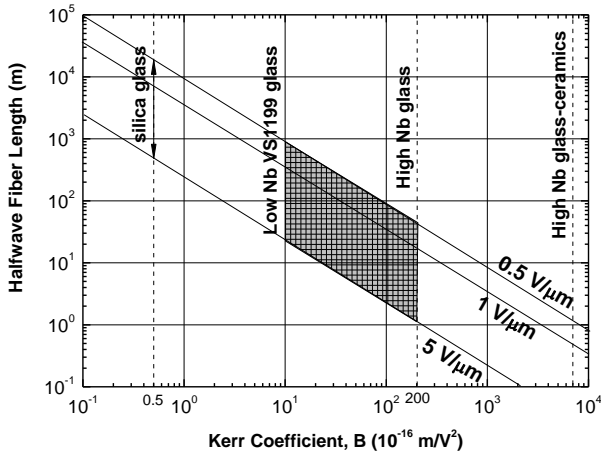


Figure 17. Relationship between halfwave length,  $l_{\lambda/2}$ , and Kerr coefficient,  $B$ , at various halfwave fields  $E_{\lambda/2} = U_{\lambda/2} / d$ . Solid area represents the range of  $l_{\lambda/2}$  values for the glasses and glass ceramics under study.

## RARE-EARTH (RE) DOPED GLASSES: SEGREGATION OF DOPANTS

For decades it was believed that doped atoms or ions (dopants) were distributed in glass host randomly, which was justified by the unordered glass structure as a consequence of high-temperature synthesis conditions. In the following the dopants are understood as atoms or ions of elements that impart specific properties to a glass, such as color, luminescence, radiation resistance, electro-optical properties, and the like. The total concentration of dopants is assumed to be small in comparison with the concentrations of the modifier and the glass former oxides, while crystal-chemical arrangement of dopants is controlled by the structure of glass host.

Assignment of glass components to glass formers, modifiers, or dopants is found to be the most suitable for the description of RE-doped alkali containing silicate, borate and germanate glasses but extension of the model to other glass forming systems needs the additional clarification [103].

As is well-known, in alkali glasses there are two types of structural polyhedra: weak-polar network forming ( $[\text{SiO}_2]$ ,  $[\text{B}_2\text{O}_3]$ ,  $[\text{GeO}_4]$ , etc.) and strongly polar ( $[\text{SiO}_4]^{-n}$ ,  $[\text{BO}_4]^{-n}$ ,  $[\text{GeO}_4]^{-n}$ , etc.) ones. The intensive exchange of ligands in melt allows a dopant to create its local surrounding from both polar and nonpolar ligands, while the very presence of a modifier determines the appearance of a polar polyhedron, and the effect of the modifier type is secondary.

Dopants are, as a rule, two or trivalent ions of elements with partially filled  $d^n$  or  $f^n$  shells. Analysis of chemical bonding dopants with ligands led to the conclusion that they should form their local surrounding from the most polar structural elements [103].

To date, a vast amount of experimental and theoretical studies have been performed on the effect of glass host composition and dopants concentration on their spectroscopic and luminescent properties, which is primarily due to the need for the development of novel glasses - active media of bulk and fiber lasers and amplifiers [104, 105, 106, 107].

Common viewpoint is that variation of the spectroscopic parameters (contours, intensities, position of the maxima, inhomogeneous broadening of spectral lines in absorption and luminescence spectra), and the kinetic (decay time and quantum yield of luminescence) parameters of RE doped glasses with glass host composition are interpreted in terms of changes in composition and structure of the nearest surrounding of RE ions.

At the same time, the data on alkali-enriched fluctuation inhomogeneities in a glassy host (see Figure 13) and on the growth of RE oxide solubility with an increase in alkalinity of glass melt (see Figure 18) suggests the possibility of nonrandom spatial distribution of RE ions in the melt that is their preferable bonding with its polar (alkali-enriched) areas.

Thus, varying the ratio of glass former and modifier concentrations should lead to a change in local concentration of RE ions, while the total amount of them in glass melt is fixed. The ability to register these changes is determined by both the distribution coefficient of dopants between the polar and nonpolar areas of a glass melt and sensitivity of the chosen experimental technique. The phenomenon of selective entering dopants

into fluctuation inhomogeneities of a glass was named the dopant segregation [103].

In the case of enhancing chemical differentiation of a glass, which can lead to phase decomposition (crystallization, liquid or subliquidus immiscibility), one should expect an increase in segregation followed by accumulating dopants in one of the phases [109, 110]. This effect should be taken into account at elaboration of glass ceramic saturable absorbers for Q – switched lasers [111].

Increasing dopant concentration in the glass-forming system with a constant ratio of modifier/glass former concentrations can lead to the total consumption of the polar component to form local surroundings of doped ions. It should cause their “sticking together” that is the formation of clusters of dopants using common polar surroundings.

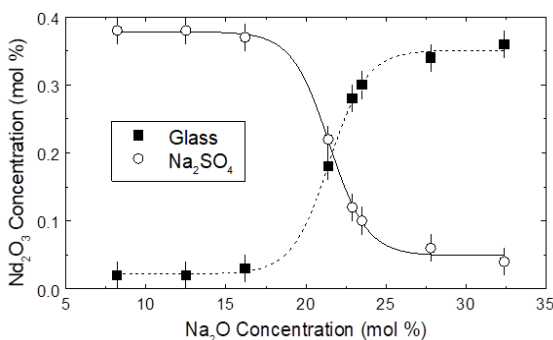


Figure 18. Composition dependencies of concentration of Nd<sub>2</sub>O<sub>3</sub> in Na<sub>2</sub>O-B<sub>2</sub>O<sub>3</sub> glass forming melt and Na<sub>2</sub>SO<sub>4</sub> buffer melt at 1000°C as a function of glass forming melt composition [108]. Reproduced from *Adv Mater Res.* 2008, vol. 39-40, 41-44 by permission of Wiley-VCH Verlag GmbH & Co. KGaA.

Variants of dopant segregation and clustering are drawn below. It should be emphasized that doped ions in a multicomponent single-phase glass selectively enter the alkali enriched fluctuation inhomogeneities. The latter should cause the growth of Rayleigh scattering intensity due to an increase in index difference between inhomogeneities saturated with dopants and glass forming network in comparison to a glass without any dopants

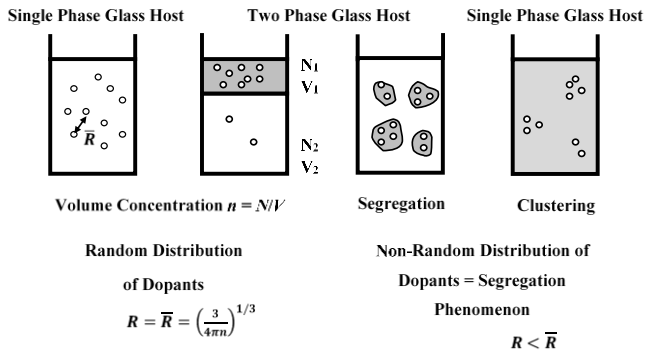


Figure 19. Spatial distribution of dopants in the single phase and two phase glass forming melts.

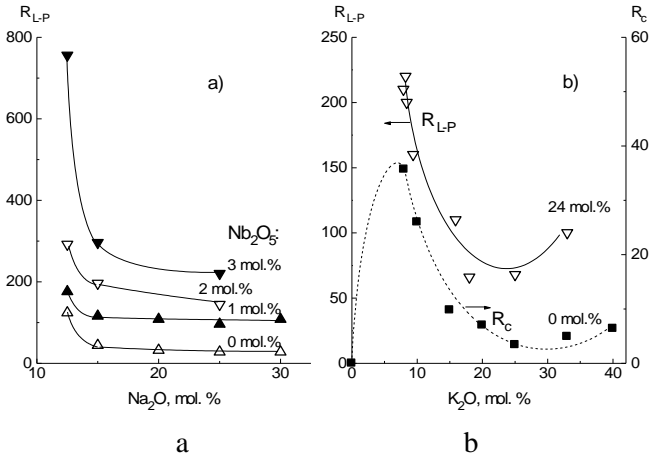


Figure 20. Composition dependencies of (a) Landau–Placzek ratio,  $R_{L-P}$ , of Nb doped alkali borosilicate glasses and (b) Pb doped potassium silicate glasses; composition dependence of contribution into Landau–Placzek ratio from “frozen-in” concentration fluctuations,  $R_c$ , for undoped potassium silicate glasses [112]. Reproduced from *Phys. Chem. Glasses: Eur. J. Glass Sci. Technol. B*, June 2012, 53 (3), 107–114 with the permission of Society of Glass Technology Publishing.

Therefore, one can expect the so-called “decoration” of concentration fluctuations of a glass host by dopants due to the segregation phenomenon that should be taken into account in elaboration of multicomponent glasses for optical and EO fiber drawing (See Figure 20).

Application of RMBS spectroscopy to R&D of RE doped glasses makes it possible to find correlations between dependencies of Landau-Placzek ratio and kinetic parameters of RE ions luminescence on a glass host composition that are shown in Figure 21 [112].

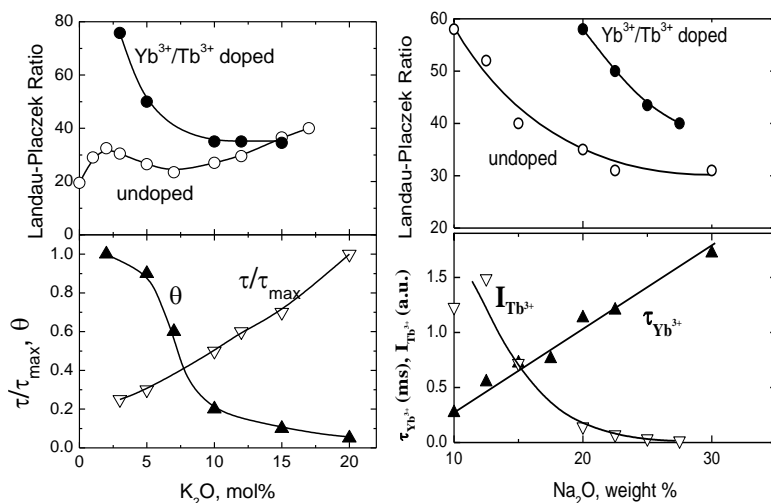


Figure 21. Composition dependences of Landau–Placzek ratio for undoped and doped with  $\text{Yb}^{3+}$  and  $\text{Tb}^{3+}$  glasses, lifetime  $\text{Yb}^{3+}$  luminescence,  $\tau$ , ( $\lambda \approx 0.9 \mu\text{m}$ ) and intensity of anti-Stokes  $\text{Tb}^{3+}$  luminescence ( $\lambda = 0.542 \mu\text{m}$ ) for  $x\text{Na}_2\text{O}-(80-x)\text{B}_2\text{O}_3-20\text{SiO}_2$  and  $x\text{K}_2\text{O}-(100-x)\text{GeO}_2$  glasses. Percentage of dopants: (a)  $\text{Yb}_2\text{O}_3 - 1 \text{ wt\%}$ ,  $\text{Tb}_2\text{O}_3 - 1 \text{ wt\%}$  and (b)  $\text{Yb}_2\text{O}_3 - 4 \text{ wt\%}$ ,  $\text{Tb}_2\text{O}_3 - 6 \text{ wt\%}$ . Curves are drawn as guides for eye [112]. Data is taken from [113, 114]. Reproduced from *Phys. Chem. Glasses: Eur. J. Glass Sci. Technol. B*, June 2012, 53 (3), 107–114 with the permission of Society of Glass Technology Publishing.

From a practical point of view, it is important that real RE-RE ions separations should be shorter than those calculated in terms of their random distribution in a glass host. This means that varying the glass host composition at constant concentration of dopants allows to bring RE ions closer to each other or to separate them. The first seems to be important for optimizing the composition of glasses - radiation converters, the second - to optimize the composition of laser glasses [114].

Segregation of RE ions can be minimized in glassy metaphosphates. Their chain structure and saturated coordination bonding –  $[\text{PO}_4]$



tetrahedra with two non-bridge oxygen atoms ensure the random spatial distribution of RE ions connecting metaphosphate groups together in a glass network. It can be illustrated by Table 11 in which results of glassy metaphosphates studies by various techniques have been collected.

**Table 11. RMBS, high temperature acoustics (HTAS), and SAXS data for some glass forming metaphosphates**

Meta phosphate	$T_g/T$ T = 298 K	$R^p$ (HTAS)	$R_{L-P}$ (SAXS)	$R_{L-P}$ (RMBS)
NaPO <sub>3</sub>	1.86 ± 0.03	7.0 ± 0.7	5.6 ± 0.6	10.5 ± 2
Cd(PO <sub>3</sub> ) <sub>2</sub>	2.38 ± 0.05		29.5	30 ± 2
Ba(PO <sub>3</sub> ) <sub>2</sub>	2.43 ± 0.03		16.0 ± 0.8	15.0 ± 0.5
Al(PO <sub>3</sub> ) <sub>3</sub>	3.52 ± 0.08	17 ± 1	35 ± 2	49 ± 2
Y(PO <sub>3</sub> ) <sub>3</sub>	3.58	21 ± 1		45 ± 5
La(PO <sub>3</sub> ) <sub>3</sub>	3.0 ± 0.2	17 ± 1		35 ± 5

Note: The data is taken from [115].

As stated in Table 11, glassy metaphosphates are characterized by high chemical homogeneity and, expectably, maximum RE-RE separations. Shortening RE-RE separations and enhancement of up-conversion was achieved by adding modifiers in the phosphate system that led to accumulation of RE ions in metaphosphate areas [116].

The possibilities of controlling arrangement of RE ions in phosphate glasses through segregation were opened when fluorine was introduced into the phosphate system. The results of fluorophosphate glass studies, in particular, RE-doped Ba(PO<sub>3</sub>)<sub>3</sub>-MgCaSrBaAl<sub>4</sub>F<sub>14</sub> glasses, by means of a set of structurally sensitive methods (absorption and luminescence spectra, kinetics of luminescence, ESR, SAXS, Raman and RMB scattering) have evidenced the segregation of RE-ions into phosphate areas of the glassy network. It was explained by small polarizability of fluorine in comparison with tetrahedra – [PO<sub>4</sub>] and the tendency of RE ions to increasing covalency of the bonding that leads to their association with phosphate groups [117, 118, 119, 120].

One of the factors on which the laser power depends is the volume concentration of RE ions the increase of which in silica and silicate glasses is hampered by the growth of their crystallization ability and the clustering

of RE ions, which leads to a decrease in decay time and quantum yield of luminescence.

**Table 12. RMBS data on experimental silica glasses doped with Nd and Al**

Dopant, wt%		$R_{L-P}$	$a_s/a_s(\text{SiO}_2)$	$\tau, \mu\text{s}$	Ref
Nd <sub>2</sub> O <sub>3</sub>	Al <sub>2</sub> O <sub>3</sub>				
0	0	$23 \pm 1$	1.0		*
1	0			<10	[123]
0.5	1.5			425	[124]
0.5	0.83	$39.7 \pm 0.5$	$1.44 \pm 0.05$		**
1.0	1.66	$48.3 \pm 0.5$	$1.80 \pm 0.08$	423	**
1.5	2.49	$74.0 \pm 0.5$	$2.64 \pm 0.09$	362	**

Note: \* commercial silica glass KI (Russia).

\*\* Experimental silica glasses (Institute of Silicate Chemistry, Saint Petersburg, Russia).

To prevent this undesirable effect, in particular, the special impurities – alkali cations, aluminum or phosphorus are embedded into silica glass. It was concluded that RE ions are associated with aluminum-enriched glass areas, while RE-O-Si and RE-O-RE bonds are replaced by RE-O-Al bonds. Optimization of the ratio of the concentrations of Al and Nd makes it possible to reduce the concentration quenching of Nd<sup>3+</sup> luminescence and approximate the lifetime of Nd<sup>3+</sup> (<sup>4</sup>F<sub>3/2</sub>) to the radiation one (460 μs) [121, 122]. The change in Rayleigh scattering loss coefficient with concentration of RE dopant and Al<sub>2</sub>O<sub>3</sub> is illustrated in Table 12. The above experimental results indicate that optimization of modifier-glass former concentration ratio is the effective way to control the probability of electron excitation energy transfer between RE ions due to a change in real RE-RE separations.

## GLASSES WITH NANOCRYSTALS

Since the discovery of unique properties of semiconductor nanocrystals (quantum dots – QDs) dispersed in solid or liquid media

caused by the spatial confinement of charge carrier motion, a number of highly sensitive methods have been used to study the dependences of physical properties of QDs on composition of a host and temperature-temporal conditions of QDs precipitation that should open the way to elaboration of novel QD doped materials with remarkable spectral-luminescent parameters [125, 126, 127].

The possibilities of using RMBS in combination with absorbance spectroscopy to determine the concentration and size of QDs were demonstrated for the PbS doped  $\text{Na}_2\text{O} - \text{ZnO} - \text{Al}_2\text{O}_3 - \text{SiO}_2$  glass. This required a modification of the RMBR formalism to estimate the contribution of QDs into Rayleigh scattering and, consequently, Landau-Placzek ratio, taking into account the fact that QDs not only scatter but also effectively absorb the incident radiation.

In this case the contribution of QDs in Landau-Placzek,  $R_{L-P}^{QD}$ , and Rayleigh scattering intensity,  $I_R^{QD}$ , can be written as: [128, 129]

$$R_{L-P}^{QD} = R_{L-P} - R_{L-P}^h = \frac{I_R^{QD}}{2 \cdot I_{MB}} = \frac{16\pi^2 N_0 a^6}{n_D^4 p_{12}^2 \left(\frac{k_B T}{\rho v_l^2}\right)} \left| \frac{m^2 - 1}{m^2 + 2} \right|^2 \quad (21)$$

where  $R_{L-P}^h$  is the Landau-Placzek ratio of a glass host,  $m$  is the relative index  $m = n_p/n_m$ ,  $n_p = (n + ik)/n_m$  is the complex index of QD,  $n_m$  is the index of glass host,  $a$  is the radius of QD,  $N_0$  is the number of QDs per unit volume. Figure 22 illustrates the growth of Landau-Placzek ratio in glass due to precipitation of QDs.

The growth of Rayleigh scattering and Landau-Placzek ratio is accompanied by changes in absorption spectrum of the glass shown in Figure 23.

It was found that QD radius determined from the position of 1S exciton band,  $\Delta E$ , in the absorption spectrum via Eq. 22 made it possible the estimation of QD concentration from Landau-Placzek ratio of the glass [129]

$$\log_{10}a = 0.154 - 0.802\log_{10}(\Delta E) \quad (22)$$

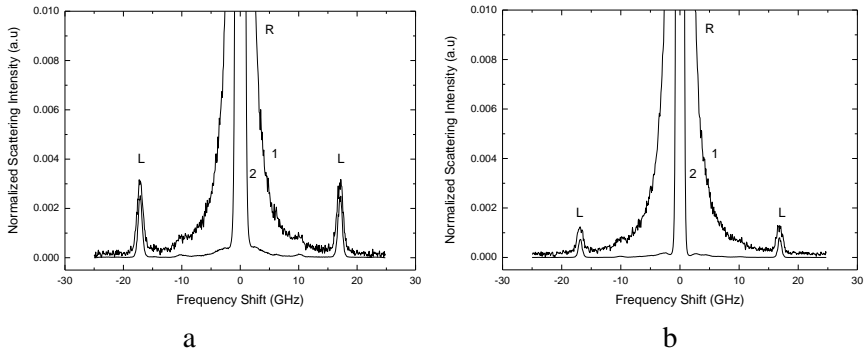


Figure 22. RMBS spectra of (a) primary heat treated (450°C/150hrs) and (b) secondary heat treated (450°C/150hrs + 490°C/107hrs) glass under study before (1) and after 16 iterations of Bayesian deconvolution procedure (2). R is the Rayleigh scattering component, L is the Mandelshtam-Brillouin scattering doublet. VV+VH polarization, scattering angle is 90°,  $\lambda = 632.8$  nm. Landau-Placzek ratios,  $R_{L-P}$ , and Mandelshtam-Brillouin shifts,  $\Delta\nu_l$ , equal  $R_{L-P} = 80 \pm 4$ ,  $\Delta\nu_l = 0.450 \pm 0.008$  cm<sup>-1</sup> (a) and  $R_{L-P} = 170 \pm 8$ ,  $\Delta\nu_l = 0.450 \pm 0.008$  cm<sup>-1</sup> (b) [129].

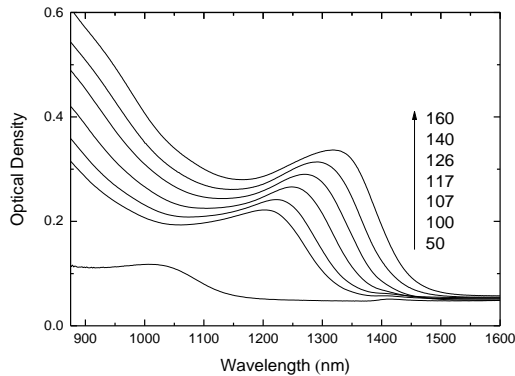


Figure 23. Evolution of absorption spectra with increase of the secondary heat treatment duration. Annealing time (hours) is given in the insert [129].

The additional opportunity lies in combination of RMBS with low-frequency Raman scattering data that can ensure determination both the dimensions and concentration of quantum dots in glass, too [130]. Thus,

RBMS should be considered as a new tool for characterization of QD-doped glass that can be used in R&D of novel Q-doped materials.

## **SOME QUESTIONS AND CHALLENGES**

Elaboration of materials that combine the advantages of both crystals and glasses is one of the most important directions in materials science. As is well known, R&D of glass ceramics by means of controlled volume crystallization of glass ensured the manufacturing of a wide assortment of commercial products.

Improving operational parameters, in particular, light scattering losses through the ordered arrangement of precipitated microcrystals remains the subject of intensive research. If crystallization of glass is preceded by its subliquidus phase decomposition the ordering of microcrystals in a glass host can be a consequence of the decomposition under the spinodal mechanism.

As is shown for potassium-silicate glasses with the consolute temperature below the glass transition ones, dependences of Landau-Placzek ratio on the temperature-temporal heat treatment conditions made it possible to investigate the evolution of microinhomogeneous structure of glass long before its supposed phase decomposition [24]. Later the improving of RMBS experimental technique opened the way to study glass systems with experimentally determined subliquidus miscibility gaps [25]. Accurate RMBS study of subliquidus phase decomposition might promote the elaboration of novel transparent glass-ceramics.

It was predicted that the presence of nano or microinhomogeneities in a glass that differ from their surroundings in composition and structure and, consequently, in the physical and optical parameters (temperature dependences of density and index, thermal expansion coefficient, etc.) should cause the reversible change in the intensity of Rayleigh scattering by a glass with its temperature. Supposedly, the intensity of elastic light scattering should increase with decreasing temperature [131]. The latter

can lead to nonlinearity of the function  $1/R_{L-P} = 2I^{MB}/I^R = b T$ , where  $b$  is the coefficient.

However, up to now the reliable experimental evidences of this effect have not been obtained up to now [12, 49, 132, 133].

## CONCLUSION

Rayleigh and Mandelshtam-Brillouin scattering spectrometer is an effective tool for measuring optical (Rayleigh scattering loss coefficient, optical stress coefficient, photoelastic coefficients) and physical (hyper sound velocities, elastic moduli) parameters of optical materials which replaces several optical and acoustic stands.

Rayleigh and Mandelshtam-Brillouin scattering spectroscopy can be used for R&D of low scattering glasses for communication fibers, glasses for electrooptical fibers of information transmitting and processing systems, rare-earth doped glasses for lasers and optical radiation converters. Rayleigh and Mandelshtam-Brillouin scattering spectroscopy combined with absorbance spectroscopy seems the productive technique for studying semiconductor nanocrystals (quantum dots) in glass hosts.

In general, combined application of Rayleigh and Mandelshtam-Brillouin, Raman scattering, absorbance spectroscopy, high temperature acoustic measurements opens the opportunities of understanding and controlling the nanostructure of optical materials.

## REFERENCES

- [1] Brillouin, L. *Ann Phys.* 1922, vol. 17, 88-122.
- [2] Mandelshtam L. I. *Zhurnal Russkogo Fiziko-Khimicheskogo Obchshestva.* 1926, vol. 58, 381-386. [*J. Rus Phys Chem Soc.* 1926, vol. 58, 381-386].
- [3] Gross, E. *Nature.* 1930, vol. 126, 201-202.

- [4] Gross, E. Z. *Phys.* 1930, vol. 63, 685-687. [*J. Physics.* 1930, vol. 63, 685-687].
- [5] Van de Hulst, H. C. *Light Scattering by Small Particles*; John Wiley & Sons: London, UK, 1957; 470 p.
- [6] Fabelinskii, I. L. *Molecular Scattering of Light*; Plenum: New York, NY, US, 1968, 622 p.
- [7] Dil, J. G. *Rep Prog Phys.* 1982, vol. 45, 285-334.
- [8] Schroeder, J. In *Treatise on Material Science and Technology*; Tomozawa, M., Doremus, R. H. Ed.; Glass 1; Academic Press: New York, NY, US, 1977; vol. 12, pp 157-222.
- [9] Schroeder, J.; Mohr, R.; Macedo, P. B.; Montrose, S. J. *J. Amer Ceram Soc.* 1973, vol. 56, 510-514.
- [10] Vladimirkisii, V. V. *Doklady Akademii Nauk SSSR.* 1941, vol. 31, 866-870. [*Proc Acad Sci USSR.* 1941, vol.31, 866-870].
- [11] Ritus, A. I. *Trudy FIAN.* 1982, vol.137, 3-80 [*Proc Phys Inst Acad Sci USSR.* 1982, vol. 137, 3-80].
- [12] Bucaro, J. A.; Dardy, H. D. *J. Appl Phys.* 1974, vol.45, 2121-2124.
- [13] Mazzacurati, V.; Nardone, V.; Ruicco, G.; Signorelli, G. *Phil Magazine B.* 1989, vol. 59, 3-15.
- [14] Martinez V.; Martinet, C.; Champagnon, B.; Le Parc, R. *J. Non-Cryst Solids.* 2004, vol. 345–346, 315-318.
- [15] Novikov, B. V. *Physics-Uspeski.* 2000, vol. 43, 105-107. [*Adv Phys.* 2000, vol. 43, 105-107]
- [16] Zaidel, A. N.; Ostrovskaya, G. V.; Ostrovskii, Yu. I. *Tekhnika i praktika spektroskopii [Apparatus and Practice of Spectroscopy]*; Nauka Publ.: Moscow, SU, 1976, 392 p.
- [17] Demtröder, W. *Laser Spectroscopy I. Basic Principles*; Springer-Verlag: Berlin, Heidelberg GE, 2014, 498 p.
- [18] Cooper, V. G.; Gupta, B. K.; May A. D. *Appl Opt.* 1972, vol. 11, 2265-2268.
- [19] Bielski, A.; Dokurno W.; Lisicki, E. *Optica Applicata.* 1981, vol. 11, 151-160. [*Appl Optics.* 1981, vol. 11, 151-160].

- [20] Konstantinov, A. V.; Maksimov L. V.; Togatov, D. M. *Optiko-mekhanicheskaya promy- shlennost.* 1986, vol. 6, 21-22. [*Optic Mechan Industry*. 1986, vol.6, 21-22].
- [21] Błachowicz, T. *Rev Sci Instr.* 2000, vol. 71, 2988-2991.
- [22] Nizzoli, F.; Sandercock, J. R. In *The Modern Physics of Phonons: Transport, Surfaces and Simulations*; Horton, G. K.; Maradudin, A. A.; Ed.; NHPG: Amsterdam, NL, 1990, Vol. 6, pp 281-336.
- [23] Scarponi, F.; Mattana, S.; Corezzi, S.; Caponi, S.; Comez, L.; Sassi, P.; Morresi, A.; Paolantoni, M.; Urbanelli, L.; Emiliani, C.; Roscini, L.; Corte, L.; Cardinali, G.; Palombo, F.; Sandercock, J. R.; Fioretto, D. *Phys Rev X*. 2017, vol. 7, 031015, 1-11.
- [24] Schroeder, J.; Montrose. C. J.; Macedo, P. B. *J. Chem Phys.* 1975, vol. 63, 2907-2912.
- [25] Hodroj, A.; Simon, P.; Florian, P.; Chopinet, M. H.; Vaills, Y. J. *Amer Ceram Soc.* 2013, vol. 96, 2339-2673.
- [26] Katzenstein, J. *Appl Opt.* 1965, vol. 4, 263-266.
- [27] Platisa, M. *Fizika*. 1973, vol. 5, 83–91. [*Physics*. 1973, vol. 5, 83–91.]
- [28] Kiselev, B. A.; Frishman, I. G. *Optiko-mekhanisheskaya promyshlennost.* 1989, vol. 1, 29-30. [*Optic Mechan Industry*. 1989, vol. 1, 29-30.]
- [29] Ko, Jae-Hyeon; Kojima, Seiji. *Rev Sci Instr.* 2002, vol. 73, 4390-4392.
- [30] *Opticheskoe Steklo-Optisches Glas (SSSR-DDR)* [*Optical Glass*]; Moscow-Jena: SU- GE
- [31] Heiman, D.; Hellwarth, R. W.; Hamilton, D. S. *J. Non-Cryst Solids*. 1979, vol. 69, 1-25.
- [32] Karapetyan, G. O.; Kiselev, B. A.; Konopatkin, S. N.; Maksimov, L. V.; Frishman, I. G. *Sov Phys - Solid State*. 1983, vol. 25, 864-865.
- [33] Darlington, E. H.; Haviland, J. R. *Appl Optics*. 1989, vol. 28, 565-572.
- [34] Basden, A.; Haniff, Ch.; Mackay, C. In *Scientific Detectors for Astronomy: The Beginning of a New Era*; Amico, P.; Beletic, J. W.;



- Beletic, J. E.; Ed.; Kluwer Academic Publ.: Dordrecht, NL, 2005, pp 593-597.
- [35] Kieffer, J. In *Modern Glass Characterization*; Affatigato M.; Ed.; Wiley&Sons: Hoboken, NJ, US, 2015, pp. 107-157
- [36] Anan'ev, A. V.; Bogdanov, V. N.; Champagnon, B.; Ferrari, M.; Karapetyan, G. O.; Maksimov L. V.; Smerdin, S. N.; Solovyev, V. A. *J. Non-Cryst Solids*. 2008, vol. 354, 3049–3058.
- [37] Heiman, D.; Hamilton, D. S.; Hellwarth, R. W. *Phys Rev B*. 1979, vol. 19, 6583-6592.
- [38] Anan'ev, A. V.; Ananyev, V. A.; Bogdanov, V. N.; Maksimov, L. V. *Phys. Chem.Glasses: Eur. J. Glass Sci. Technol*. 2015, vol. 56, 15-23.
- [39] Manenkov, A. A.; Prokhorov, A. M.; Ritus, A. I. *Fizika Tvergogo Tela*. 1975, vol. 17, 1111-1117. [*Solid State Phys*. 1975, vol.17, 1111-1117.]
- [40] Barnes, J. M.; Hiedemann, E. A. *J. Acoust Soc Amer*. 1956, vol. 28, 1218-1221.
- [41] Lagakos, N.; Bucaro, J. A.; Huges, R. *Appl Opt*. 1980, vol. 19, 3668-3670.
- [42] Shapiro, S. M.; Gammon R. W.; Cummins, H. Z. *Appl Phys Lett*. 1966, vol. 9, 157-159.
- [43] Qiu, S. L.; Bunten, R. A. J.; Dutta, M.; Mitchell, E. W. J.; Cummins, H. Z. *Phys Rev B Cond Matter*. 1985, vol. 31, 2456-2463.
- [44] Pohl, D.; Schwarz, S. E. *Phys Rev*. 1973, vol. 7, 2735-2739.
- [45] Frederics, W. J.; Collins, P. R. *J. Phys Chem Solids*. 1984, vol. 45, 471-479.
- [46] Jackson, H. E.; Harley, R. T.; Lindsay, S. M.; Anderson, M. W. *Phys Rev Lett*. 1985, vol. 54, 459-461.
- [47] Danileiko, Yu. K.; Manenkov, A. A.; Nechitailo, V. S.; Ritus, A. I. *Sov. J. Quant Electron*. 1975, vol. 4, 1005-1008.
- [48] Krol, D. M.; Lyons, K. B.; Brawer, S. A.; Kurkijan, C. R. *Phys Rev B Condens Matter*. 1986, vol. 33, 4198-4202.
- [49] Bucaro, J. A.; Dardy, H. D. *J. Appl Opt*. 1974, vol. 45, 5324-5329.
- [50] Vacher, R.; Boyer L. *Phys Rev B*. 1972, vol. 6, 639-673.

- [51] Catlow, C. R. A.; Comins, T. J. D.; Germane, F. A.; Harley, R. T.; Hayes, W. *J. Phys C Solid State Phys.*, 1978, vol. 11, 3197-3212.
- [52] Benedek, G. B.; Fritsch, K. *Phys Rev.* 1966, vol. 149, 647-662.
- [53] Aramomi, Sh.; Matsuda, Yu; Kojima, S. *J. Non-Crystal Solids.* 2014, vol. 401, 142-146.
- [54] Polian, A. *J. Raman Spectr.* 2003, vol. 34, 633-637.
- [55] Yakovlev, L. A.; Shustin, O. A. In *Light Scattering Near Phase Transitions*; Eds.; Cummins, H. Z.; Levanyuk, A. P. *Modern Problems in Condensed Matter Sciences*, Elsevier: BV, NL, 1983; Vol: 5, 605-637.
- [56] ASTM Glass Designation C162-166.
- [57] Elliott, S. R. *Physics of Amorphous Materials*; Longman: London, UK, 1984, 386 p.
- [58] Laberge, N. L.; Vasilescu, V. V.; Montrose, C. J.; Macedo, P. B. *J. Amer Ceram Soc.* 1973, vol. 10, 506-509.
- [59] Bogdanov, V. N.; Nemilov, S. V.; Solovyev, V. A.; Mikhailov, I. G.; Borisov, B. F.; Nikonov A. M. *Fizika I Khimiya Stekla.* 1978, vol. 4, 47-55. [*Glass Phys Chem.* 1978, vol. 4, 47-55].
- [60] Sakaguichi, Sh.; Todoroli Sh. *J. Amer Ceram Soc.* 1996, vol. 79, 2821-2824.
- [61] Leko, V. K.; Mazurin, O. V. *Svoistva kvatsevogo stekla [Properties of Silica Glass]*; Nauka Publ.: Leningrad, SU, 1985, 166 p.
- [62] Saito, K.; Ikushima, A. J.; Ito, T.; Itoh, A. *J. Appl Phys.* 1997, vol.11, 7129-7134.
- [63] Pevnitskii, I. V.; Khalilov, V. Kh. *Fizika I Khimiya Stekla.* 1989, vol. 15, 428-432. [*Glass Phys Chem.* 1989, vol. 15, 428-432].
- [64] Champagnon, B.; Chemarin, C.; Duval, E.; Le Park, R. *J. Non-Cryst Solids.* 2000, vol. 274, 81-86.
- [65] Sakaguich, Sh.; Todoroki, Sh. *Jpn. J. Appl Phys.* 1998, vol. 37, Suppl. 37-1, 56-58.
- [66] Nikonov, A. M.; Bogdanov, V. N.; Nemilov, S. V.; Shono, A. A.; Mikhailov, I. G. *Fizika i Khimiya Stekla.* 1982, vol. 8, 694-703. [*Glass Phys Chem.* 1982, vol. 8, 694-703].

- [67] Golubkov, V. V. *Fizika I Khimiya Stekla*. 1992, vol. 18, 57-69. [*Glass Phys Chem*. 1992, vol. 18, 57-69].
- [68] Yagi, T. *Physica B+C*. 1988, vol. 150, 265-270.
- [69] Bogdanov, V. N.; Mikhailov I. G.; Nemilov S. V. *Akusticheskij Zhurnal*. 1974, vol. 20, 511-517. [*Acoust J*. 1974, vol. 20, 511-517].
- [70] Mazurin, O. V.; Streltsina M. V.; Shvaiko-Shvaikovskaya, T. P. *Single-Component and Binary Non-Silicate Oxide Glasses. Handbook of Glass Data, Part B*; Physical Science Data 15; Elsevier-Science Publ.: Amsterdam, NL, 1985, 805 p.
- [71] Bogdanov, V. N.; Solovyev, V. A.; Chernysheva, E. O. *Fizika I Khimiya Stekla*. 1982, vol. 8 491-494. [*Glass Phys Chem*. 1982, vol. 8 491-494.]
- [72] Grimsditch, M.; Bhadra, R.; Torell, L. M. *Phys Rev Lett*. 1989, vol. 62, 2616-2619.
- [73] Neuville, J. P.; Turnbull, D. *Discuss. Faraday Soc*. 1970, vol. 50, 182-190.
- [74] Smith, K. H.; Shero, E.; Chizmeshya, A.; Wolf, G. H. *J. Chem Phys*. 1995, vol. 102, 6851-6857.
- [75] Devyatych, G.G.; Dianov, E.M.; Karpychev, N. S.; Mazavin, S. M.; Machiskii, V. M.; Neustruev, B. V.; Nikolaichik, A. V.; Prokhorov, A. M.; Ritus, A. I.; Sokolov, N. I.; Yushin, A. S. *Sov J. Quant Electronics*. 1980, vol. 10, 900-902.
- [76] Schroeder, J.; Tsoukala, V. G., Floudas, G. A.; Thompson, D. A. *J. Non-Cryst Solids*. 1988, vol. 102, 295-301.
- [77] Sakaguich, Sh.; Todoroki, Sch. *Applied Optics*. 1997, vol.36, 6809-6814.
- [78] Patel, N. D.; Bridge, B.; Waters, D. N. *Phys Chem Glasses*. 1983, vol. 24, 122-125.
- [79] Kranold, R.; Walter, G.; Stachel, D; Barz, A. *Glastech Ber Glass Sci Technol*. 1998, vol. 71C, 512-515.
- [80] Mallowany, R. A. *Tellurite Glasses. Handbook*. Physical Properties and Data; CRC Press; FL, US, 2002.
- [81] Kieffer, J.; Masnik, J. E.; Nikolayev, O. *Phys Rev B*. 1998, vol. 58, 694-705.

- [82] Rawson H. *Inorganic Glass Forming Systems*; Academic Press: London and New York: UK, US, 1967, 312 p.
- [83] Porai-Koshts, E. A.; Golubkov, V. V. *Wiss Z Friedrich -Schiller Univ Jena Math – Nat R.* 1979, vol. 28, 265-276. [*Proc. Friedrich-Schiller Univ Jena Math – Nat R.* 1979, vol. 28, 265-276].
- [84] Karapetyan, G. O.; Maksimov, L. V. *Sov J. Glass Phys Chem.* 1989, vol. 15, 175-194.
- [85] Wallace, R. M.; Katz, S. M. *J. Phys Chem.* 1964, vol. 68, 3890-3892.
- [86] Spjotrol, E.; Martens, H.; Volden, R. *Technometrics.* 1982, vol. 24, 173-180.
- [87] Mukhitdinova, I. A.; Yanush, O. V. *Fizika i Khimiya Stekla.* 1989, vol. 15, 34-51. [*Glass Phys Chem.* 1989, vol. 15, 34-51.]
- [88] Markova, T. S.; Yanush, O. V.; Polyakova, I. G.; Pevzner, B. Z.; Kluev, V. P. *Glass Phys Chem.* 2005, vol. 31, 721-733.
- [89] Karapetyan, G. O.; Kabanov, V. O.; Konstantinov, A. V.; Maksimov, L. V.; Yanush, O. V. *J. Appl Spectr.* 1989, vol. 51, 1223–1237.
- [90] Karapetyan G. O., Konstantinov A. V., Maksimov L. V., Reznichenko P. V. *Sov J. Glass Phys Chem.* 1987, vol. 13, 7-12.
- [91] Maksimov, L. V. *Glastechin. Ber- Glass Sci and Techol.* 1998, vol. 71C, 408-411.
- [92] Danileiko. Yu. K.; Manenkov, A. A.; Nechitailo V. S.; Ritus A. I. *Sov J. Quant Electron,* 1975, vol. 4, 1005-1008.
- [93] Karapetyan, G. O.; Maksimov, L. V. *Sov J. Quant Electron,* 1984, vol. 14, 1231-1233
- [94] Zhilin, A. A.; Karapetyan, G. O.; Lipovskii, A. A.; Maksimov, L. V.; Petrovskii G. T.; Tagantsev, D. K. *Glass Phys Chem.* 2000, vol. 26, 242-246.
- [95] Karapetyan, G. O.; Lipovskii, A. A.; Loboda, V. V.; Maksimov, L. V.; Svistunov, D. V.; Tagantsev, D. K.; Tatarintsev, B. V.; Vetrov, A. A. *Proc SPIE.* 2001, vol. 4323, 23-28.
- [96] Lipovskii, A. A.; Tagantsev, D. K.; Vetrov, A. A. *J. Non-Cryst Solids.* 2003, vol. 318, 268-283.

- [97] Layton M. M.; Herzog, H. *J. Amer. Ceramic Soc.* 1967, vol. 50, p. 369-375.
- [98] Vetrov, A. A.; Lipovskii, A. A.; Tagantsev, D. K. *Instrum Exper Techn.* 2002, vol. 45, 550–554.
- [99] Anan'ev, A.; Karapetyan, G.; Lipovskii, A.; Maksimov, L.; Pankov, D.; Tagantsev, D.; Vetrov A.; Yanush, O. *Proc SPIE.* 2003, vol. 5122, 87-93.
- [100] Anan'ev, A.; Karapetyan, G.; Lipovskii, A.; Maksimov, L.; Polukhin, V.; Tagantsev, D.; Tatarintsev, B.; Vetrov A.; Yanush O. *J. Non-Cryst Solids.* 2005, vol. 351, 1046–1053.
- [101] Welker, D.; Torstenrude, J.; Garvey, D. W.; Canfield, B.; Kusyik, M. G. *Optics Lett.* 1998, vol. 23, 1826-1828.
- [102] Vetrov, A.; Ivanov, V. N.; Polukhin, V. N.; Tatarintsev, B. V.; Kobelke, J.; Bartelt, H. Patent RU #2 247 414. Publ. 27.02.2005.
- [103] Dmitryuk, A. V., Karapetyan, G.O., Maksimov, L.V. *J. Appl Spectr.* 1975, vol.22, 119-141.
- [104] Luo, Zundu; Huang, Yidong; Chen, Xueyuan. *Spectroscopy of Solid-state Laser and Luminescent Materials; Chapter 9. Spectral Properties of Laser Glasses*; Nova Science Publ. Inc., New York, NY. US; 2007, pp. 231-274.
- [105] Ter-Mikirtychev, Valerii (Vartan). *Fundamentals of Fiber Lasers and Fiber Amplifiers*; Springer Series in Optical Sciences, Vol. 181; Springer, Cham (ZG), CH 2013, 7-36.
- [106] *Current Trends on Lanthanide Glasses and Materials*. Nadyala, S. H. Ed. Book series Materials Research Foundations; Materials Research Forum LLC; Mitterville, PA, US; 2017, Vol. 8, 193 p.
- [107] Yen, W. M. *Optical Spectroscopy of Ions in Inorganic Glasses*; In *Optical Spectroscopy of Glasses*; Zshokke, I. Ed.; *Physics and Chemistry of Materials with Two-Dimensional Structures. Series C. Molecular Structures*. Publ. D. Reidel Publ Company: Dordrecht, NL, 1986, pp. 23-64.
- [108] Anan'ev, A.; Maksimov, L. *Adv Mater Res.* 2008, vol. 39-40, 41-44.
- [109] Mortier, M. *Philosoph Mag. Part B.* 2002, vol. 82, 745-753.

- [110] Loiko, P. A.; Dymshits, O. S.; Skoptsov, N. A.; Malyarevich, A. M.; Zhilin, A. A.; Alekseeva I. P.; Tsenter, M. Y.; Bogdanov, K. V.; Mateos, X.; Yumashev, K. V. *J. Phys Chem Solids*. 2017, vol. 103, 132-141.
- [111] Shepilov, M. P.; Dymshits, O. S.; Zhilin, A. A.; Golubkov, V. V.; Kalmykov, A. E.; Myacoedov, A. V.; Hubetsov, A. A.; Zapalova, S. S. *J. Non-Cryst Solids*, 2017, vol. 473, 152-169.
- [112] Anan'ev, A.; Bogdanov, V.; Maksimov L.; Yanush, O. *Phys. Chem. Glasses: Eur. J. Glass Sci. Technol. B*, 2012, 53, 107–114.
- [113] Antipenko B. M.; Dmitryuk, A. V.; Zubkova V. G.; Karapetyan, G. O. *Fizika I Khimiya Stekla*. 1978, vol. 4, 188-190. [*Glass Phys Chem*. 1978, vol.4, 188-190]
- [114] Dmitryuk, A. V.; Karapetyan, G. O.; Manenkov, A. A.; Osiko, V. V.; Ritus, A. I.; Shcherbakov, I. A. *Sov J. Quant Electron*. 1977, vol. 7, 943-945.
- [115] Maksimov, L. V.; Anan'ev, A. V.; Bogdanov, V. N. *IOP Conf. Series: Mater Science Engineer*. 2011, vol. 23, 012027, 1-5.
- [116] Goldner, P.; Schaudel, B.; Prassas, M.; Auzel, L. *J. Luminec*. 2000, vol. 87-89, 688-690.
- [117] Bocharova, T. V.; Mironov, A. M.; Karapetyan, G. O. *Inorg Mater*. 2005, vol. 41, 892– 899.
- [118] Bocharova, T. V.; Karapetyan, G. O.; Mironov, A. M.; Tagil'tseva, N. O.; Yanush, O. V. *Glass Phys Chem*. 2005, vol. 31, 420–426.
- [119] Bocharova, T.; Golubkov, V.; Karapetyan, G.; Mironov A.; Tagil'tseva, N. *Proc SPIE*. 2006, vol. 5946, 594603.
- [120] Bocharova, T. V.; Adam, J. L.; Karapetyan, G. O.; Smektala, F.; Mironov, A. M.; Tagil'tseva, N. O. *J. Phys Chem Solids*. 2007, vol. 68, 978-982.
- [121] Sen,S.; Rakhmatullin, R.; Gubaidullin, R.; Pöppl, A. *Phys Rev. B* 2006, vol. 74, 100201(R), 1-4.
- [122] Monteil, A.; Chaussedent, S.; Alombert-Goget, G.; Gaumer, N.; Obriot, J.; Ribeiro, S. J. L.; Messaddeq, Y.; Chiasera, A.; Ferrari, M. *J.Non-Cryst Solids*. 2004, vol. 348, 44–50.

- [123] Thomas, I. M.; Payne, S. A.; Wilke, G. D. *Proc. SPIE*. 1992, vol. 1758, 622-629.
- [124] .Xiang, Q.; Zhou, Y.; Lam, Y. L.; Ooi, B. S.; Chan, Y. C.; Kam, C. H. *Proc. SPIE* 2000, vol. 3896, p .433-437.
- [125] Ekimov, A .I.; Onushchenko, A. A. *JETP Letters*, 1981, vol. 34, 345-349.
- [126] Efros, A. L.; Efros, Al. L. *Sov. Phys. Semiconduct.* 1982, vol. 16, 772-775.
- [127] Brus, L. E. J. *Chem Phys.* 1984, vol. 80, 4403-4409.
- [128] Anan'ev, A. V.; Maksimov, L. V.; Onushchenko, A. A.; Savost'yanov, V. A. *J. Opt Technol.* 2014, vol. 81, 735-736.
- [129] Shepilov, M.; Anan'ev, A.; Maksimov, L.; Savostyanov, V.; Golubkov, V.; Onushchenko P.; Ananyev, V.; Onushchenko, A. *J. Non-Crystal Solids.* 2016, vol. 450, 156-163.
- [130] Champagnon, B.; Andrianasolo, B.; Ramos, A.; Gandais, M.; Allais, M.; Benoit, J. P. *Appl Phys.* 1993, vol. 73, 2775-2780.
- [131] Vladimirskii, V. V. *Doklady Akademii Nauk SSSR.* 1942, vol. 36, 251-252. [Proc Acad Sci USSR. 1942, vol. 36, 251-252].
- [132] Kul'bitskaya, M. N.; Romanov, V. P.; Chernysheva, E. O.; Shutilov, V. A. *Fizika i Khimiya Stekla.* 1976, vol. 2, 183-185. [Glass Phys Chem. 1976, vol. 2, 183-185.]
- [133] Vacher, R.; Pelous, J. *Phys Rev B.* 1976, vol. 14, 823-828.

## BIOGRAPHICAL SKETCHES

### *Anatoli Anan'ev*

**Affiliation:** S. I. Vavilov State Optical Institute

**Education:** Saint Petersburg Polytechnical University, (Department of Radiophysics, 1986), PhD (S. I. Vavilov State Optical Institute, 1992), Russia.

**Research and Professional Experience:** Investigation of fluctuation nanoinhomogeneities in inorganic glasses by Rayleigh and Mandelshtam-Brillouin scattering (RMBS) spectroscopy combined with Raman scattering and high temperature acoustic studies, R&D of low-scattering and electro-optic glasses for fiber drawing, water soluble phosphate glasses for fertilizers, design of experimental stands for RMBS, low absorption characterization in bulk glass, fiber optical low-coherence reflection interferometry, second harmonic generation, electro-optic characterization, luminescence and spectroscopic studies, laser scattering indicatrix characterization, design of software for high performance computing on graphics processing units and FPGA.

**Professional Appointments:**

- 2015 – 2017 Krylov State Research Centre, senior researcher
- 2011 – Course Design Bureau, lead software development engineer
- 2000 – S. I. Vavilov State Optical Institute, senior researcher
- 1998 – 1999 École Polytechnique Fédérale de Lausanne, engineer
- 1986 – 1998 S. I. Vavilov State Optical Institute, trainee/researcher

**Publications from the Last 3 Years:**

1. Anan'ev, V. A., Lipovskii, A., Tagantsev, D. K. “Is frozen space charge responsible for SHG in poled silicate glasses only?” *Journal of Non-Crystalline Solids*, 2017, Vol. 458, pp. 118–120.
2. Shepilov, M., Anan'ev, A., Maksimov, L., Savostyanov, V., Golubkov, V., Onushchenko, P., Ananyev, V., Onushchenko, A. “Landau-Placzek Ratio of an Inorganic Glass with PbS Quantum Dots” *Journal of Non-Crystalline Solids*, 2016, Vol. 450, pp. 156–163.
3. Dmitryuk, A. V., Anan'ev, A. V., Maksimov, L. V., Savost'yanov, V. A., Tatarintsev, B. V., Zhilin, A. A. Park Eonsang, Baik Chan-Wook “Spectroscopic Properties of Highly Concentrated Nd<sup>3+</sup>



Doped Antimony-Phosphate Glass for Microchip Lasers” *Glass Physics and Chemistry*, 2015, Vol. 41, No. 2, pp. 137–144.

4. Anan’ev, V., Ananyev, V. A., Bogdanov, V. N., Maksimov, L. V. “Characterization of optical glasses by Rayleigh and Mandel’shtam–Brillouin scattering and high temperature acoustic methods. Part 1. Flint glasses” *Physics and Chemistry of Glasses: European Journal of Glass Science and Technology Part B - 2015*, Vol. 56, No. 1, pp. 15–23.

### ***Leonid Maksimov***

**Affiliation:** S. I. Vavilov State Optical Institute

**Education:** Saint Petersburg State University (Physics Department, 1970), PhD (Saint Petersburg Technological Institute, 1977), Dr Sc (Institute of Silicate Chemistry at Russian Academy of Science, 1998)  
RUSSIA

**Research and Professional Experience:** Investigation of fluctuation nanoinhomogeneities in inorganic glasses by Rayleigh and Mandelshtam-Brillouin scattering spectroscopy combined with Raman scattering and high temperature acoustic studies, R&D of low-scattering and electro-optic glasses for fiber drawing, glasses with nanocrystals (quantum dots), water soluble phosphate glasses for fertilizers.

#### **Professional Appointments:**

- Since 1989 S. I. Vavilov State Optical Institute,
- Team leader, project manager
- 1981 – 1989 Saint Petersburg Polytechnic University,
- Senior/leading researcher
- 1970 – 1981 S. I. Vavilov State Optical Institute,
- Trainee/researcher, junior researcher, researcher

**Honors:** Academician I. V. Grebenshchikov's Medal from the Russian Optical Society

**Publications from the Last 3 Years:**

1. Shepilov, M., Anan'ev, A., Maksimov, L., Savostyanov, V., Golubkov, V., Onushchenko, P., Ananyev, V., Onushchenko, A. "Landau-Placzek Ratio of an Inorganic Glass with PbS Quantum Dots" *Journal of Non-Crystalline Solids*, 2016, Vol.450, pp.156–163.
2. Dmitryuk, A. V., Anan'ev, A. V., Maksimov, L. V., Savost'yanov, V. A., Tatarintsev, B. V., Zhilin, A. A. Park Eonsang, Baik Chan-Wook "Spectroscopic Properties of Highly Concentrated Nd<sup>3+</sup> Doped Antimony-Phosphate Glass for Microchip Lasers." *Glass Physics and Chemistry*, 2015, Vol. 41, No. 2, pp. 137–144.
3. Anan'ev, A. V., Maksimov, L. V., Onushchenko, A. A., Savost'yanov, V. A. "The Scattering of Visible Radiation in Glasses with Lead Sulfide Nanocrystals" *J. Opt. Technol.* 2014, Vol. 81 (12), pp. 735-736.

*Chapter 3*

## COMPUTER STUDY OF THE REMOVAL OF HEAVY METALS FROM GRAPHENE

*Alexander Y. Galashev\**

Institute of High Temperature Electrochemistry, Ural Branch,  
Russian Academy of Sciences, Yekaterinburg, Russia

### ABSTRACT

Efficient removal of hazardous heavy metals from the environment is an important problem, since most of these metals are highly toxic. Recently, graphene began to be used for the removal of environmental pollutants. Graphene is ineffective as an absorbent unless it is repeatedly used. This raises the problem of graphene cleaning for removal of the deposited materials. The method of molecular dynamics has been used to study the removal of copper, lead, and mercury from graphene by irradiating the target using a beam of Ar<sub>13</sub> or Xe<sub>13</sub> clusters with energies of 5–30 eV at angles of incidence 0°, 45°, 60°, and 90°. It is obtained that the cluster energy should be in the interval 20 – 30 eV for effective graphene cleaning in case of its copper contamination. There is no cleaning effect at vertical incidence ( $\theta = 0^\circ$ ) of Ar<sub>13</sub> clusters. The bombardments at 45° and 90° incident angles are the most effective ones at a moderate and big amount of deposited copper respectively. The

---

\* Corresponding Author Email: galashev@ihite.uran.ru.

complete removal of lead from graphene with hydrogenated edges and bivalencies was achieved at the angle of incidence of  $\text{Xe}_{13}$  clusters equal to  $45^\circ$ . A major part of the film was separated from graphene in the form of an island, which, after separation, was transformed into a three-dimensional structure. The stresses present in the graphene sheet changed in the course of bombardment, but the stressed state retained after the bombardment was terminated. The type of the distribution of stresses in graphene indicates the absence of enhancement of the stressed state in the course of bombardment. The bombardment at angles of incidence of clusters less than  $75^\circ$  substantially enhances the roughness of graphene. The complete removal of mercury from graphene with hydrogenated edges was achieved at the angles of incidence of clusters equal to  $45^\circ$  and  $60^\circ$  with the energies of the beam  $E_{\text{Xe}} \geq 15$  and 10 eV, respectively. The film of mercury, which has a tendency to become rolled up into a drop, is separated from graphene in the form of single atoms, dimers, trimers, and spherical droplets. In the course of the bombardment, mercury exhibits a weak cohesion with graphene. The bombardment at the angle of incidence of clusters equal to  $45^\circ$  leads to the lowest roughness of graphene. The bombardments in the entire range of the angles of cluster incidence ( $0^\circ - 90^\circ$ ) have resulted in no significant damages in the hydrogenated edges of the graphene sheet after its cleaning from both lead and mercury. Thus, the purification of graphene from heavy metals can be performed by bombardment with noble gas clusters.

**Keywords:** argon, bombardment, clusters, copper, graphene, lead, mercury, molecular dynamics, xenon

## 1. INTRODUCTION

Graphene has unique physical properties and energy-band structures. It is possible now to receive graphene of a small size with the help of different technologies. However, there is a new technology of graphene film production of the size up to 70 cm [1]. Graphene can be used in different membranes due to its highest flexibility and mechanical strength. As an absorbing material, graphene is an effective one only in the case of multiple using. Consequently, the question of graphene cleaning of deposited substances arises. In addition, there was a need to develop an effective method for releasing copper from a scrap copper-graphene electrodes recently used in electrochemical devices operating in aggressive

environments. Graphene coating on copper significantly (by one and a half orders of magnitude) increases the resistance of the metal to electrochemical degradation. The copper has a significant practical interest. The surface pollutions on graphene are removed by ion beam [2]. The bombardment with the cluster beam can be an effective method of graphene cleaning. It is important here however to find the correct bombardment energy to avoid the damage of graphene membrane. Molecular dynamics (MD) simulation of plasma interaction on a graphite surface has shown that the graphite surface absorbs the most part of hydrogen atoms when the energy of the incident beam is 5 eV [3]. At the same time almost all hydrogen atoms are reflected from the surface at the beam energy 15 eV. Vertical bombardment by Ar<sub>10</sub> clusters with kinetic energy  $E_k < 30$  eV executed in MD model does not result in the break of graphene sheet during 100 runs [4]. Graphene is broken at  $E_k = 40$  eV.

The ion track lithographic method uses the passage of energetic ions through nanoholes in the mask and subsequent bombing of the graphene sheet only within a limited nanoregion. It is important to investigate in detail the entire lithographic process to predict how nanostructures can be produced in the suspended graphene sheet using this method. The present study will contribute to achieving this goal. Controlled ion parameters obtained in our simulation will be used to obtain desirable defective structures. No experimental studies have been performed so far to produce such cluster ions to irradiate the target containing graphene. Furthermore, it has been shown that the theory of irradiation effects for bulk targets does not always lead to satisfactory results for the low-dimensional materials, such as graphene [5, 6]. It is quite obvious that an atomically thin target of graphene requires explicit consideration of the atomic structure [7, 8].

The trace amounts of metals always occur in the natural biosphere. The presence of some of them even in a low concentration requires rapid oxidation because metals in higher concentrations and products in low oxidation states can be toxic and dangerous. Unfortunately, the difference between permissible and dangerous concentration levels is small [9, 10]. PbS belongs to the most frequently occurring trace compounds in nature. It is used in electrical batteries, small arms, and X-ray units and as a pigment

in domestic metallic mixtures. The detection of industrial lead in the environment is of considerable importance. Until now, lead has been determined by various methods such as spectrophotometry [11, 12], liquid–liquid extraction [13, 14], turbidimetry [15, 16], and electrochemical measurements [17]. Some of these methods are inaccurate because of the low limits of detection and harmful solvents. In recent years, solid-phase extraction has been used for the determination of Pb traces. The trace amounts of Pb in aqueous media are detected with the aid of a surfactant covered with modified f-OH graphene.

The negligibly small amounts of heavy metals can be removed from air and water using filters with graphene membranes. However, in this case, the filters should be subsequently cleaned for the removal of a metal deposit. Lead has a low energy of adhesion with perfect graphene (0.2 eV) [18]; however, the binding energy of Pb atoms with graphene at a divacancy boundary is very considerable (3.4 eV) [19]. A heavy metal film can be removed from graphene by the bombardment of the latter with noble gas clusters [20–23]. The simulation of a cluster bombardment process showed that the energy transferred upon the impact should be entirely released in a critical region near the surface in order to obtain a maximum effect [24–26]. It was experimentally demonstrated that, on the incidence of a beam of Xe atoms onto the surface of graphite at an incident angle of  $55^\circ$ , the energy transferred to the phonon modes of the surface is approximately 20% smaller than that in the case of a vertically directed beam [27]. In this case, the Xe atoms are scattered on the smooth surface of graphite even at energies of several tens of eV. The energies of the cluster beams used were much lower than the energies of beams in the experiments oriented to the sputtering of a bombarded substance.

Mercury is the only metal among the most abundant ones that remains liquid at room temperature. The study of the adsorption of mercury on activated carbon was, as a rule, carried out experimentally. There is a limited number of theoretical studies concerning this theme. Steckel [28] investigated the interaction between elemental mercury and a single benzene ring in order to explain the mechanism through which elemental mercury is bound with carbon. Padak et al. [29] investigated the effect of

different surface functional groups and halogens present on the surface of activated carbon on the adsorption of elemental mercury. It has been established that the addition of halogen atoms intensified the adsorption of mercury. In [30], Padak and Wilcox have demonstrated a thermodynamic approach to the examination of the mechanism of binding of mercury and its capture in the form of  $\text{HgCl}$  and  $\text{HgCl}_2$  on the surface of activated carbon. The energies of different possible surface complexes have been determined. In the presence of chlorine, the mercury atoms strongly cohere to the surface. In the case of dissociative adsorption, Hg can undergo desorption, while  $\text{HgCl}$  remains on the surface. The compound  $\text{HgCl}_2$  was not found on the stable carbon surface [31]. Understanding of the mechanism of the adsorption of mercury on activated carbon is important for the development of efficient technologies for capturing mercury.

Mercury is one of the most toxic heavy metals, and its presence is due to a combination of natural processes (volcanic activity, erosion of the mercury-containing sediments, etc.) and anthropogenic activity (extraction of minerals, pollution from the leather-dressing production and metallization of objects). Adsorption is considered to be one of the most efficient and economical methods of removing mercury from wastewater and air. Recently, graphene membranes began to be used for capturing super small amounts of substances [32]. The repeated application of graphene in the filters requires its nondestructive cleaning from the adsorbates. The removal of metals from graphene can be produced by its irradiation by a beam of rare-gas clusters [20, 21, 23, 33–35]. The use of cluster beams for the surface cleaning is more efficient than the application of ion beams to this purpose. In this case, the energy of a cluster grows in proportion to the number of atoms in the cluster at the same velocity of the projectile and, thus, it is possible to avoid large optical aberrations in the focusing systems. Bombardment using cluster projectiles proves to be much more sparing in comparison with the ionic bombardment, since a cluster projectile cannot penetrate the target so deeply as an atomic analog. In the prospect, application of the cluster beams will make it possible to create a number of fundamentally new technologies of the surface cleaning and to develop a new generation of ionic sources.

The aim of the present work is to investigate stability of the thin metal (Cu, Pb, Hg) film on graphene under noble gas ( $\text{Ar}_{13}$  or  $\text{Xe}_{13}$ ) clusters bombardment with kinetic energies 5, 10, 20 and 30 eV and incident angles of the cluster beam  $90^\circ$ ,  $75^\circ$ ,  $60^\circ$ ,  $45^\circ$ , and  $0^\circ$ .

## 2. METHODS

Below, we present a computer model of a copper film on graphene and the used scheme of its bombardment by clusters  $\text{Ar}_{13}$ . The models of Pb and Hg films on a graphene substrate were created in a similar way. The bombardment of these targets was carried out by the  $\text{Xe}_{13}$  clusters. The graphene sheet is placed on a copper substrate which does not allow C atoms to move vertically downwards. Thereby the movement of the sheet under the influence of cluster impacts was completely excluded. Copper substrate was a slice of five atomic layers of the FCC lattice, the lattice (100) plane served as a surface of the slice. This surface has a square shape, 10 atoms Cu are located along the edge of this square, and the entire slice contained 1,000 Cu atoms. Graphene sheet of size  $3.4 \times 2.8$  nm containing 406 atoms of C is placed on the substrate and fully fitted into this square. In the chosen coordinate system, the graphene sheet had “zigzag” edges along the  $x$  axis and the “armchair” edges - in the direction of the  $y$  axis. Initially all the atoms C have coordinates  $z = 0$ . Substrate atoms were fixed, but interacted with C atoms of the graphene and atoms of the metal film. Boundary conditions at the edges of graphene were free. It allows investigating the stability of edges to external dynamic loads.

The copper film formation on the graphene was simulated by separate MD calculation in two steps. At the first step Cu atoms were placed over the centers of noncontiguous graphene cells so that the distance between Cu and C atoms would be equal to the distance of  $2.243 \text{ \AA}$  calculated by the density functional theory [36]. Onto this loose film consisting of 49 copper atoms, another 51 Cu atoms were deposited at random. In the initial state copper film presented three-dimensional structure with an



ordered lower base (adjacent to graphene) and irregular and not flat top layer. Then the system composed of 100 Cu atoms and 406 C atoms was equilibrated in the MD calculation over a duration of 1 million time steps ( $\Delta t = 0.2$  fs). Numerical solution of the equations of motion was carried out by the fourth-order Runge–Kutta method. The target obtained in this manner was subsequently bombarded with icosahedral  $\text{Ar}_{13}$  clusters during 1 ns.

In the case of vertical bombardment ( $\theta = 0^\circ$ ) the virtual rectangular two-dimensional  $5 \times 5$  grid covers the graphene sheet. The virtual grid is lifted over the graphene sheet at a distance of 1.5 nm. Every grid node gives the initial position for  $\text{Ar}_{13}$  cluster living 8 ps. The lifetime includes time of flight and time of interaction with the target. After this time, the Ar atoms of the decayed cluster were excluded from consideration and a new cluster  $\text{Ar}_{13}$  was launched from a different point cluster sources. In the case of inclined bombardment, five starting points for placing the centers of the  $\text{Ar}_{13}$  clusters were uniformly spaced apart on a line parallel to the  $y$  axis (the “armchair” direction). This line was displaced to the left (along the  $x$  axis) from the left edge of graphene by a distance of 1.5 nm and raised to such a height (in the direction of the  $z$  axis) to provide an effective impact to the copper film. Interval equal to the  $L_x$  length of the graphene sheet in the axial direction (the direction of “zigzag”) was divided into 25 equal segments of length  $L_i = L_x / 25$ . Five point cluster sources moved horizontally forward at a distance  $L_i$  at the beginning of each cycle (except for the first); thus, the cluster impacts line moved. As a result, the graphene sheet was covered with 125 evenly spaced points to target cluster impacts.

### 3. CALCULATION

Calculations were performed by the classical molecular dynamics method. In this study, we used three types of empirical potentials describing the carbon–carbon (in graphene), metal – metal, and metal –

carbon interactions. Representations of the interactions in graphene were based on the use of the Tersoff potential [37]

$$V_{ij} = f_c(r_{ij}) \left[ A \exp(-\lambda^{(1)} r_{ij}) - B b_{ij} \exp(-\lambda^{(2)} r_{ij}) \right], \quad (1)$$

$$f_c(r_{ij}) = \begin{cases} 1, & r_{ij} < R^{(1)} \\ \frac{1}{2} + \frac{1}{2} \cos[\pi(r_{ij} - R^{(1)})/(R^{(2)} - R^{(1)})], & R^{(1)} < r_{ij} < R^{(2)} \\ 0 & r_{ij} > R^{(2)} \end{cases}, \quad (2)$$

$$\begin{aligned} & r_{ij} < R^{(1)} \\ & R^{(1)} < r_{ij} < R^{(2)}, \\ & r_{ij} > R^{(2)} \end{aligned}$$

where  $b_{ij}$  is the multi-particle bond-order parameter describing in what manner the bond-formation energy (attractive part  $V_{ij}$ ) is created at local atomic arrangement because of the presence of the neighboring atoms. The potential energy is a multi-particle function of atomic positions  $i$ ,  $j$ , and  $k$  is determined by parameters

$$b_{ij} = \left( 1 + \beta^n \xi^{n_i} \right)^{-1/(2n)}, \quad (3)$$

$$\xi_{ij} = \sum_{k \neq i, j} f_c(r_{ij}) g(\theta_{ijk}), \quad (4)$$

$$g(\theta_{ijk}) = 1 + \frac{c^2}{d^2} - \frac{c^2}{\left[ d^2 + (h - \cos \theta_{ijk})^2 \right]}, \quad (5)$$

where  $\xi$  is the effective coordination number,  $g(\theta_{ijk})$  is a function of the angle between  $r_{ij}$  and  $r_{ik}$ , which stabilizes the tetrahedral structure.

This potential was successfully tested on many single- and multi-component systems with covalent chemical bonding [38, 39]. However, the

transition to the simulation of two-dimensional systems (for example, in graphene) with covalent bonding revealed some difficulties in using this potential. The main disadvantages were as follows: the interaction was represented only by short-range covalent forces, and the contributions from the interactions with neighbors of the second and higher orders were not considered. Simulation with this potential led to cracking of the graphene sheet even at low temperatures. Another serious disadvantage was in existence of the net torsional moment appearing because of the lack of mutual compensation of the torsional moments determined by bonds around each atom. As a result, there occurred rotation of the graphene sheet (most frequently, counterclockwise). This effect impeded simulation of nanocomposites and made a difficult structural analysis. In the proposed model, the mentioned disadvantages were eliminated in the following way. The scale of covalent interaction in the model was increased from 0.21 to 0.23 nm. Outside the covalent interaction, we used very weak attractive Lennard–Jones interaction with the parameters taken from [40]. To prevent rotation of the graphene sheet, the “retardation” at each atomic site of the graphene atomic was provided by the force  $-dV_{ij}^{\text{tors}}(\Omega_{kijl})/dr_{ij}$ , where the torsional potential  $V_{ij}^{\text{tors}}(\Omega_{kijl})$  is represented by the expression [40]

$$V_{ij}^{\text{tors}}(\Omega_{kijl}) = \varepsilon_{kijl} \left[ \frac{256}{405} \cos^{10} \left( \frac{\Omega_{kijl}}{2} \right) - \frac{1}{10} \right], \quad (6)$$

and the torsion angle  $\Omega_{kijl}$  is defined as the angle between the planes, of which one plane is specified by the vectors  $\mathbf{r}_{ik}$  and  $\mathbf{r}_{ij}$ , and the other plane, by the vectors  $\mathbf{r}_{ij}$  and  $\mathbf{r}_{jl}$ :

$$\cos \Omega_{kijl} = \frac{\mathbf{r}_{ji} \times \mathbf{r}_{ik} \cdot \mathbf{r}_{ij} \times \mathbf{r}_{jl}}{|\mathbf{r}_{ji} \times \mathbf{r}_{ik}| |\mathbf{r}_{ij} \times \mathbf{r}_{jl}|}. \quad (7)$$

The height of the barrier  $\varepsilon_{kijl}$  for the rotation was taken from [40].

The Sutton–Chen potential was successfully used for simulating both bulk metals and metallic clusters [41]. The Sutton–Chen potential energy is written as

$$U^{\text{SC}} = \varepsilon \left[ \frac{1}{2} \sum_i \sum_{j \neq i} V(r_{ij}) - c \sum_i \sqrt{\rho_i} \right], \quad (8)$$

where

$$V(r_{ij}) = (a/r_{ij})^n, \quad \rho_i = \sum_{j \neq i} (a/r_{ij})^m, \quad (9)$$

where  $\varepsilon$  is the parameter having the dimensionality of energy;  $c$  is the dimensionless parameter;  $a$  is a parameter having the dimensionality of length that is commonly chosen to be the lattice parameter;  $m$  and  $n$  are positive integers ( $n > m$ ). The power form of the contributions makes it possible to successfully joint the short-range interactions, which are represented by  $N$ -particle terms with the Van der Waals “tail” that determines long-range interaction. For copper and lead, we used the Sutton–Chen potential parameters as follows:  $m = 6$ ,  $n = 9$ ,  $\varepsilon = 12.382$  meV,  $c = 39.432$  and  $m = 7$ ,  $n = 10$ ,  $\varepsilon = 5.5765$  meV,  $c = 45.778$ , respectively [41]. The pair potential that was utilized for a description of the Hg–Hg interactions was proposed in [42] in the following form:

$$V_{\text{Sch}}(r) = U_{\text{Sch}}(\lambda r) = \sum_{j=3}^9 a_2^* r^{-2j}, \quad (10)$$

The authors of [42] corrected the original Schwerdtfeger (SCH) potential [43] for mercury dimer by scaling distances using the coefficient  $\lambda = 1.167$ . The  $a_2^*$  parameters represented in [42] correspond to the density of liquid Hg at  $T = 300$  K.

The copper–carbon interaction was described using the Morse potential

$$V(r_{ij}) = D_0 \left[ \exp\{-2\alpha(r_{ij} - r_m)\} - 2\exp\{-\alpha(r_{ij} - r_m)\} \right]. \quad (11)$$

The simulation was performed with the Cu-C Morse potential parameters as follows:  $D_0 = 87$  meV,  $\alpha = 17$  nm<sup>-1</sup>, and  $r_m = 0.22$  nm [44]. The lead–carbon, mercury–carbon, argon–argon, and xenon–xenon interactions were given by the Lennard-Jones potential [45–48]:  $\sigma_{\text{Pb-C}} = 0.3362$  nm,  $\varepsilon_{\text{Pb-C}} = 38.0$  meV,  $\sigma_{\text{Hg-C}} = 0.3321$  nm,  $\varepsilon_{\text{Hg-C}} = 1.266$  meV,  $\sigma_{\text{Ar-Ar}} = 0.3405$  nm,  $\varepsilon_{\text{Ar-Ar}} = 10.323$  meV,  $\sigma_{\text{Xe-Xe}} = 0.410$  nm,  $\varepsilon_{\text{Xe-Xe}} = 19.043$  meV. The Morse potential was used to describe the interactions between the Pb or Hg atoms and the substrate Cu ones. Parameters of this potential were calculated from data of [49, 50].

The interaction between the noble gas atoms and the atoms of metals (Cu, Pb, Hg) and C was determined by purely repulsive Moliere potential [51]

$$\Phi = A \left\{ 0.35 \exp\left(-0.3 \frac{r}{a}\right) + 0.55 \exp\left(-1.2 \frac{r}{a}\right) + 0.10 \exp\left(-6.0 \frac{r}{a}\right) \right\}, \quad (12)$$

Where  $A = Z_i Z_j \frac{e^2}{r}$ ,  $Z_i$  and  $Z_j$  are the atomic numbers of the  $i$  and  $j$  atoms,  $e$  is the elementary charge,  $r$  is the distance between the atoms,  $a$  is the Firsov screening length [52]

$$a = 0.885 a_0 \left( Z_i^{1/2} + Z_j^{1/2} \right)^{-2/3}. \quad (13)$$

Here  $a_0$  is the Bohr radius.

Defects substantially enhance the adhesion of metals to graphene. The most frequent defects in graphene are divacancies. The sheet of graphene used for deposition of the lead had four divacancies rather uniformly distributed over its surface. Hydrogenation was used for the strengthening of the divacancy edges and boundaries. The CH groups formed at the edges and sites nearest to the divacancy center were simulated in accordance with the monatomic diagram [53]. The C–CH and CH–CH interactions were represented by the Lennard-Jones potential [53]. The partial functionalization of graphene in the form of the addition of the hydrogen atoms to its edges stabilizes the structure without leading to an increase in interatomic distances and without creating roughness over the entire surface.

The stress at the site of the  $i$  th atom of the Cu or Pb film is defined as [41]

$$\sigma_{\alpha\beta}(i) = B \sum_{i \neq j}^k \left[ -n(a/r_{ij})^{n+2} + m\alpha(1/\sqrt{\rho_i} + 1/\sqrt{\rho_j})(a/r_{ij})^{m+2} \right]_{ij}^{\alpha, \beta}, \quad (14)$$

Where  $B = \frac{\varepsilon}{2a^2\Omega_i}$ , the volume corresponding to an individual atom  $\Omega_i$  can be associated with the volume of the Voronoi polyhedron related to the  $i$  th atom.

To calculate the stresses induced in graphene, the graphene sheet was divided into elementary areas. The atomic stresses  $\sigma_J^i(l)$  in the  $l$  th elementary area for each of directions  $x$ ,  $y$  and  $z$  with a current index  $J$  are determined by calculating the atomic kinetic energies in this area and projections of forces acting on the  $l$  th area from all other atoms

$$\sigma_J^i(l) = \frac{1}{k} \left\langle \sum_i^k \frac{1}{\Omega_i} (m v_j^i v_j^i) \right\rangle + \frac{1}{S_l} \left\langle \sum_i^k f_J^i \right\rangle, \quad (15)$$

where  $k$  is the number of atoms at the  $l$ th area;  $\Omega_i$  is the volume per atom;  $m$  is the atomic mass;  $v_j^i$  is the  $J$ th velocity projection of atom  $i$ ; and  $S_l$  is the area of the  $l$ th area. Angular brackets indicate the averaging over time. In this case, the compressive stresses can have plus and minus signs, according to directions of forces  $f_j^i$ . In this regard, the microscopic stress  $\sigma_j^i(l)$  differs from the macroscopic ones  $\bar{\sigma}_j < 0$ .

The self-diffusion coefficient was determined by the mean square displacement of the atoms  $\langle [\Delta \mathbf{r}(t)]^2 \rangle$  as

$$D = D_{xy} + D_z = \lim_{t \rightarrow \infty} \frac{1}{2\Gamma} \langle [\Delta \mathbf{r}(t)]^2 \rangle, \quad (16)$$

where  $\Gamma = 3$  is the dimension of space,  $D_{xy}$  and  $D_z$  are the horizontal and vertical components of the self-diffusion coefficient.

The density profile of the metallic film was calculated as follows:

$$\rho(z) = \frac{n(z)\sigma_{\text{Me}}^3}{\Delta h S_{xy} N_z}, \quad (17)$$

where  $n(z)$  is the number of metal atoms in the layer parallel to the plane of the graphene,  $\sigma_{\text{Me}}$  is the effective diameter of the metal atom,  $\Delta h$  is the width of the layer,  $S_{xy}$  is the area of the graphene surface, and  $N_z$  is the number of tests.

The surface roughness (or the profile deviation arithmetic average) was calculated as

$$R_a = \frac{1}{N} \sum_{i=1}^N |z_i - \bar{z}|, \quad (18)$$

where  $N$  is the number of nodes (atoms) on the surface of graphene  $z_i$  is the atomic level,  $\bar{z}$  is the graphene surface level,  $z_i$  and  $\bar{z}$  are the values determined at the same instant.

The total energy of free one-sheet graphene obtained at  $T = 300$  K was  $-7.02$  eV, which is consistent with the result of a quantum-mechanical calculation ( $-6.98$  eV) [54]. The melting temperature  $T_m$  of a  $\text{Pb}_{201}$  cluster with a free surface, which was determined in a special calculation, was 417 K. This is consistent with MD calculations at  $T_m = 412$  K [55], which were also performed with the Suttner–Chen potential. In both cases,  $T_m$  was determined based on a potential energy jump. The value of the isochoric heat capacity of liquid mercury at this temperature ( $28.4 \text{ J}/(\text{mol} \cdot \text{K})$ ) calculated in the MD model agrees with the experimental value of  $26.9 \text{ J}/(\text{mol} \cdot \text{K})$ .

## 4. RESULTS

### 4.1. Copper

There is no graphene surface cleaning after vertical bombardment at energy  $5 - 20$  eV. Bombardment with the 10 and 20 eV energies gives significant damage of graphene edges up to knocking out carbon atoms. The copper film becomes looser and Cu atoms form a column. The graphene sheet is partly cleaned of copper atoms after bombardment with energy 20 eV at the incident angle  $\theta = 75^\circ$ . Graphene is almost cleaned of Cu atoms at angles  $\theta = 45^\circ$  and  $\theta = 60^\circ$ . In every case after finishing of inclined bombardment, the graphene sheet together with the substrate is removed in parallel or perpendicular (down) direction with respect to its initial position. It allowed removing copper from graphene totally only after bombardment at  $45^\circ$ . In the case of bombardment by the method of the “nap of the earth” flight (incident angle  $0^\circ$ ) a big amount of metal atoms is still on the graphene surface when the emitted cluster energy is 10 eV. But the number of copper atoms is reduced at energy 20 eV (Figure 1). At any cluster incident angle, the mobility of Cu atoms in the horizontal plane exceeds considerably (in order) the mobility of ones in the vertical direction. After the first cycles of cluster impacts, there are high values of



$D_{xy}$  components, especially, at the incident angle  $\theta = 60^\circ$  (Figure 2a). It seems reasonable because the copper film has not yet adapted to the bombardment. The more intensive fluctuations and significantly higher  $D_{xy}$  values testify continuous fast destruction of the copper film during clusters impacts at incident angle  $45^\circ$ . The vertical components  $D_z$  of the copper film self-diffusion coefficient have mostly the same behavior as  $D_{xy}(n)$  function (Figure 2b).

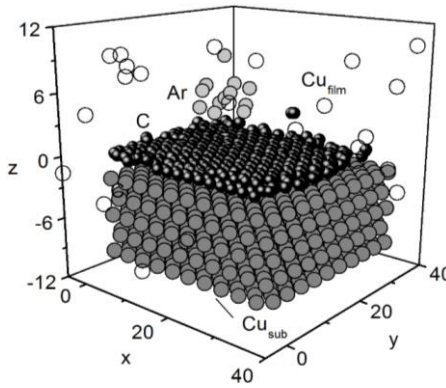


Figure 1. Configuration of a system “copper film on the graphene sheet with the copper substrate” bombarded by  $\text{Ar}_{13}$  cluster with energy 20 eV during final impacts cycle at the incident angle  $\theta = 90^\circ$ . Coordinates are in angstroms.

Stresses in  $xy$  plane of copper film at every bombardment have extensive fluctuations which become weaker during the last impact series. At all incident angles excluding  $\theta = 90^\circ$ , the  $\sigma_{zz}$  stresses are considerably higher than  $\sigma_{zx}$  and  $\sigma_{zy}$  ones. At  $\theta = 90^\circ$  and energy of 10 eV, the  $\sigma_{zx}$ ,  $\sigma_{zy}$  and  $\sigma_{zz}$  stress components for metal film in the horizontal plane have comparably low values during the whole run (Figure 3a,  $\sigma_{zz}$  is only shown). For the energy 20 eV at the initial target bombardment ( $n \leq 10$ ) there are significant fluctuations of all stress components in the horizontal plane. The  $\sigma_{zz}$  component has the most intensive fluctuations. Such fluctuations at the energy of bombardment clusters 20 and 30 eV are

connected with impacts of the Ar atoms compressing the film and knocking out Cu atoms. The fluctuation size of  $\sigma_{zz}$  value is further decreased because of metal film loosening in the vertical direction.

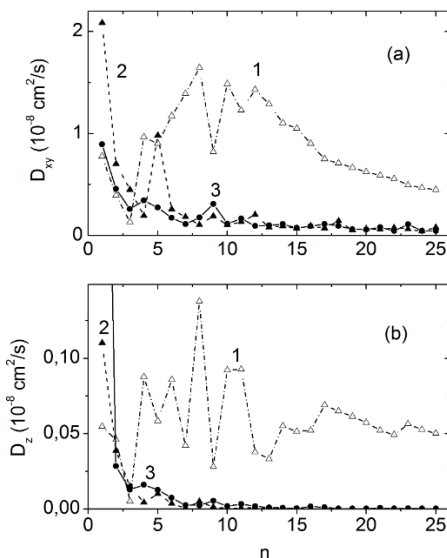


Figure 2. (a) the horizontal  $D_{xy}$  and (b) the vertical  $D_z$  components of self-diffusion coefficient of Cu film for series of bombardments by  $\text{Ar}_{13}$  clusters at kinetic energy 20 eV and different incident angles: (1) 45°, (2) 60°, (3) 75°;  $n$  is the cycles each of 5 impacts.

On the contrary, stress distribution in the graphene sheet does not almost depend on the direction of the incident cluster beam. Cluster impacts are mainly weakened by the copper film. Stresses distribution in graphene between the rows in the “armchair” direction at  $\text{Ar}_{13}$  cluster bombardment with energies 10 and 20 eV at  $\theta = 90^\circ$  is shown in Figure 3b. Because of strong shot-interacting bonds in graphene, there are no essential differences between stresses values of  $\sigma_{xx}$ ,  $\sigma_{yy}$  and  $\sigma_{zz}$  for series of cluster bombardment with energies 10 and 20 eV. The  $\sigma_{zx}$  and  $\sigma_{zy}$  stresses are uniformly distributed in the plane of the graphene sheet. For both energies the maximum  $\sigma_{zz}$  stress in this area of graphene sheet

exceeds by 4–7 times the maximum values of  $\sigma_{zx}$  and  $\sigma_{zy}$  stresses. It is connected with impulses transmitted to graphene from the Cu atoms, which they get as a result of interactions with the Ar atoms.

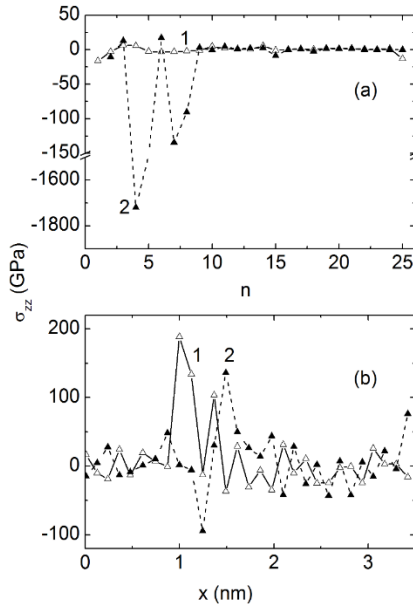


Figure 3. (a)  $\sigma_{zz}$  stress in  $xOy$  plane of metal film and (b)  $\sigma_{zz}$  stresses distribution in the graphene sheet by the rows of C atoms along the “armchair” direction for bombardment series by  $Ar_{13}$  clusters at incident angle  $\theta = 90^\circ$  with energies: (1) 10 eV, (2) 20 eV.

The graphene roughness increases significantly by the end of bombardment. It does not depend on the incident angle and energy of  $Ar_{13}$  clusters’ beam. Significant growth of roughness is limited by rigid bonds in graphene. The roughness  $R_a$  of the graphene sheet rises non monotonically during bombardment (Figure 4). When the clusters energy is 10 eV the increase of  $R_a$  is slow with low values. There are considerable fluctuations of  $R_a(n)$  function especially in the values range of  $10 \leq n \leq 25$  when energies are 20 and 30 eV. The decrease of the initial growth of roughness in the case of energy 20 eV is connected with the reduction of final  $R_a$

value because of the smoothing effect. At the final bombardment step, the  $\text{Ar}_{13}$  cluster flies rather low over graphene surface and “polishes” it not meeting the Cu atoms.

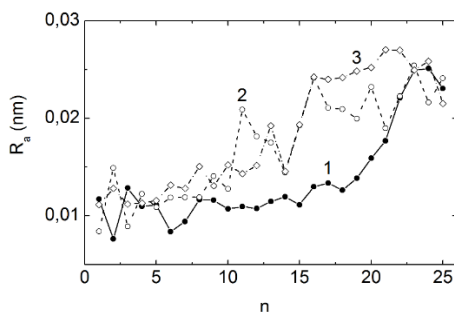


Figure 4. Roughness of the graphene surface at bombardment of “metal film on the graphene sheet with the copper substrate” system by  $\text{Ar}_{13}$  clusters at incident angle  $\theta = 90^\circ$  with energies: (1) 10 eV, (2) 20 eV, (3) 30 eV.

## 4.2. Lead

Investigation of the influence of the incidence angle of clusters  $\text{Xe}_{13}$  on the result of the bombardment of a lead film on graphene showed that the best degree of purification of graphene is achieved at the angle  $\theta = 60^\circ$  [56–58]. This case is considered in this section.

As a result of bombardment with 5 eV clusters, the film of Pb remained on the graphene. In this case, a small part of metal atoms was knocked out from the film, and the film itself was bent to keep contact with graphene only in its middle part; that is, the film edges became raised.

Bombardment with a beam energy of 10 eV led to the complete separation of a Pb film from the graphene. Only an insignificant part of the Pb atoms was not knocked out from the film, and the major portion went away in the form of a dense cluster.

In general, the similar behavior was also observed on the bombardment with a beam energy of 15 eV (Figure 5). However, in this case, the major portion of the film was immediately detached away from graphene to a

small distance. Since it was conically shaped expanded upwards, it was again forced against graphene at the cone apex under the impacts of  $\text{Xe}_{13}$  clusters.

We found that further increase in the cluster beam energy did not facilitate the removal of the Pb film from graphene. Thus, as a result of bombardment with an energy of 20 eV, the film was not separated from graphene with loss of a portion of individual knocked-off atoms. Two atoms were stuck in divacancies, and they helped to retain the film on graphene by attracting other Pb atoms. The film had close contact with graphene at the center. The film edges were elevated. Using the 30 eV  $\text{Xe}_{13}$  clusters crushed the film of lead and pushed several Pb atoms through divacancies. A small lead cluster was arranged at the front edge of graphene without loss in binding with the base layer. Since of hydrogenation, the graphene edges remained intact even after bombardment with energy of 30 eV.

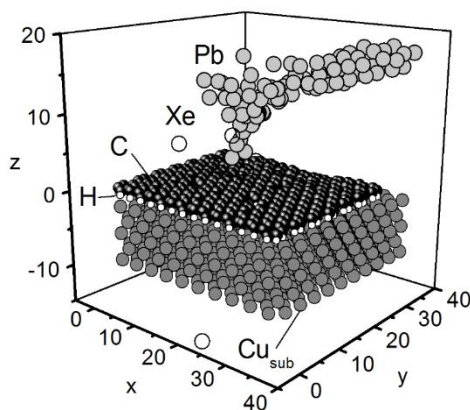


Figure 5. Configuration of the lead film–partially hydrogenated graphene system after bombardments at the incident angle of  $60^\circ$  with a 15 eV  $\text{Xe}_{13}$  cluster energy. Coordinates are in angstroms.

Figure 6 demonstrates the vertical profiles of density. Bombardment with a cluster energy of 5 eV left a sufficiently monolithic film on graphene. Moreover, in the course of bombardment, the Pb atoms located

in the lattice dimples of the honeycomb type formed by the C atoms, retained their positions, as evidenced by the sharp peak at 0.237 nm. A small number of single atoms descended into divacancies or moved away from the film as confirmed by presence of the separate low peaks.

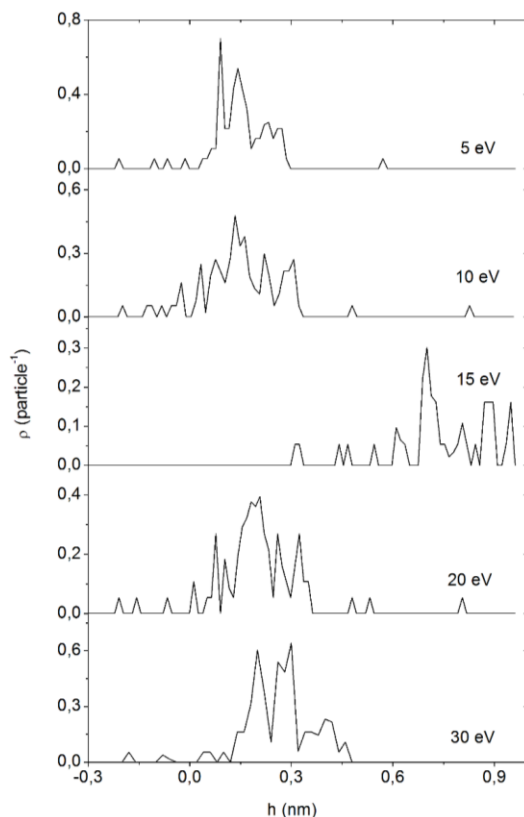


Figure 6. Lead film density profiles obtained in the course of the cluster bombardments of a target with different energies; the level  $h = 0$  corresponds to the vertical mark of presence of the C atoms in graphene.

Approximately the same pattern of the arrangement of Pb atoms was observed at a 10-eV energy of the  $\text{Xe}_{13}$  clusters. The film thickness increased due to swelling under the impacts of the clusters, and the number of separated Pb atoms increased. At the end of the bombardment, the film

separated from graphene and fast moved away to the distance greater than 1 nm. The new film position is not reflected in the profile  $\rho(z)$ .

The fast rise of the entire film at the distance  $r > 0.3$  nm over graphene occurred at the energy of bombarding clusters of 15 eV. The density profile in the whole was shifted to the right. At the cluster beam energies  $E_{Xe} > 15$  eV, the film was either unseparated from the graphene (20 eV) or broken into separate pieces (30 eV). At the energy of 20 eV, a noticeable number of the Pb atoms were pushed through divacancies, and single scattered Pb atoms were also present. Penetration of the lead atoms to the reverse side of graphene was insignificant at energies of 30 eV. In this case, the knocked out film pieces fast moved away to distances greater than 1 nm, and they are not reflected in the profile  $\rho(z)$ .

The horizontal component  $D_{xy}$  of mobility of the Pb atoms tends to decrease as the energy of bombarding clusters is increased up to 20 eV (Figure 7). However, the value of  $D_{xy}$  sharply increases under the cluster energy 30 eV. This fact shows to change in the nature of deformation in the film of lead under the action of the cluster beam. The vertical component  $D_z$  of mobility of the Pb atoms does not exhibit a significant lift at a beam energy of 30 eV, but it manifests a sharp burst at the energy of 10 eV. This burst is caused by the detachment and fast removal of the major portion of the film from graphene. In general, the vertical component of mobility of the Pb atoms is lower by almost an order of magnitude than of the horizontal mobility.

The curves of  $D_{xy}(E_{Xe})$  and  $D_z(E_{Xe})$  for the C atoms in graphene (Figure 8) are mainly consistent in shape with analogous curves for the Pb atoms (Figure 7). Presence of the local minimum at  $E_{Xe} = 15$  eV in place of the local maximum in the curve  $D_{xy}(E_{Xe})$  for graphene is the exception. Furthermore, at low energies ( $E_{Xe} \leq 10$  eV), the values of  $D_{xy}$  are even higher than those at the energy  $E_{Xe} = 30$  eV when the Pb atoms injected into dimples produce local pressing and decrease mobility of the C atoms in the horizontal directions. The burst in the function  $D_z(E_{Xe})$  at  $E_{Xe} = 10$

eV for graphene is impressive the same as that in an analogous function for the lead. This is most likely indicative of the fact that the impacts of  $\text{Xe}_{13}$  clusters, which caused the detachment and fast withdrawal of the film, arrived directly at the graphene surface, and the  $\text{Xe}_{13}$  atoms were scattered upward, pushed in the opposite direction the loosely lying Pb film, and removed it from graphene. An insignificant increase in the value of  $D_z$  for the C atoms at the energy  $E_{\text{Xe}} = 30$  eV is related to the presence of the rigid C–C bonds and the absence of the graphene integrity damage.

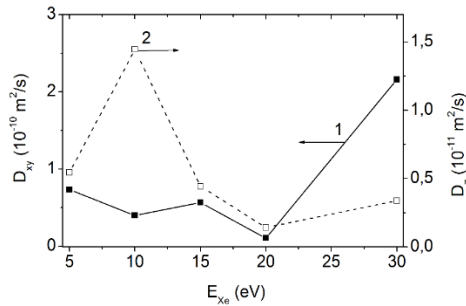


Figure 7. Horizontal  $D_{xy}$  and vertical  $D_z$  components of the coefficient of mobility of the Pb atoms obtained as a result of the entire bombardment as functions of the energy of bombarding  $\text{Xe}_{13}$  clusters.

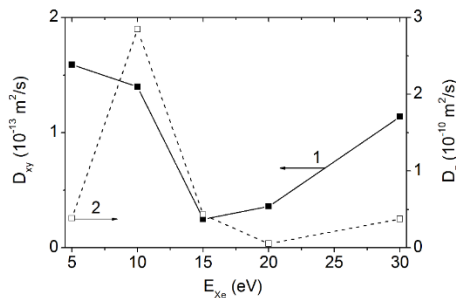


Figure 8. Horizontal  $D_{xy}$  and vertical  $D_z$  components of the coefficient of mobility of the C atoms of graphene as functions of the energy of bombarding  $\text{Xe}_{13}$  clusters.

The study of evolution of the stresses  $\sigma_{xx}$ ,  $\sigma_{yy}$  and  $\sigma_{zz}$  in the cases of removal of the Pb film from graphene ( $E_{\text{Xe}} = 10$  and  $15$  eV) showed that



their smooth relaxation occurred only during the first series of impacts. Already in the course of the fifteen cycles of impacts, strong changes in the stresses created by horizontal forces ( $\sigma_{xx}$  and  $\sigma_{yy}$ ) were observed, especially, at the final stage. In this case, the stress created by vertical forces ( $\sigma_{zz}$ ) increased much more intensively.

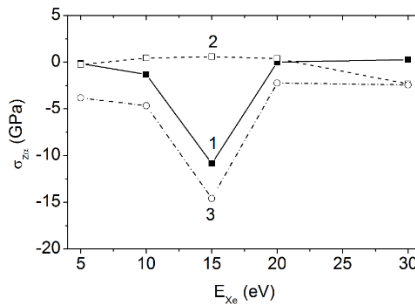


Figure 9. Basic stresses (1)  $\sigma_{xx}$  (2)  $\sigma_{yy}$  and (3)  $\sigma_{zz}$  in the film of Pb obtained as a result of the complete bombardment as functions of the energy of bombarding  $Xe_{13}$  clusters.

After 100 cycles of bombardment, the stresses  $\sigma_{xx}$  and  $\sigma_{yy}$  became even more significant. Over the course of this series, the stresses  $\sigma_{zz}$  strengthened almost continuously. In general, the stresses  $\sigma_{xx}$ ,  $\sigma_{yy}$  and  $\sigma_{zz}$  in graphene along the  $x$  axis obtained after 100 cycles of impacts were no higher than the stresses resulting from the five cycles of bombardment. In other words, in the course of the entire bombardment, increase in the local stresses in graphene was not observed. Note that the value of the stresses  $\sigma_{zz}$  created by vertical forces was much greater (by a factor of to  $\sim 2$ ) than the stresses  $\sigma_{xx}$  and  $\sigma_{yy}$ , which appeared due to the application of horizontal forces.

In view of a specific shape taken by the film of the lead after bombardment with an energy of 15 eV, the final stresses  $\sigma_{xx}$  and  $\sigma_{zz}$  in the film were considerably different from analogous stresses obtained after bombardments with other energies of the  $Xe_{13}$  clusters (Figure 9). At the

same time, the function  $\sigma_{zy}(E_{Xe})$  has a smooth shape; that is, the value of  $\sigma_{zy}$  at  $E_{Xe} = 15$  eV is not strongly different from the values of this stress obtained at other  $E_{Xe}$ . All of three stresses have values of the same order of magnitude (in the majority of cases, the absolute value of  $\sigma_{zz}$  is somewhat greater) with the exception of the value of  $\sigma_{zy}$  at  $E_{Xe} = 15$  eV.

Dependence of the resulting stresses  $\sigma_{zx}$ ,  $\sigma_{zy}$  and  $\sigma_{zz}$  in graphene on the energy  $E_{Xe}$  only partially correlates with the behavior of analogous characteristics in the Pb film (Figure 10). The behavior of only the quantity  $\sigma_{zz}$  is similar in many respects to that of the corresponding stress in the metallic film. Here, the dip of the curve of  $\sigma_{zz}(E_{Xe})$  into the region of negative values was also observed at  $E_{Xe} = 15$  eV. However, the value of  $\sigma_{zz}$  did not reach positive values at  $E_{Xe} = 20$  eV as was the case in the film of lead. The function  $\sigma_{zx}(E_{Xe})$  was characterized by a smoother behavior, whereas the function  $\sigma_{zy}(E_{Xe})$  for the film of Pb exhibited this property. The function  $\sigma_{zy}(E_{Xe})$  for graphene exhibited the maximum at  $E_{Xe} = 15$  eV. The largest negative stress ( $\sigma_{zy}$ ) caused by the horizontal forces in the direction of the  $y$  axis appeared at  $E_{Xe} = 5$  eV, and stress of the same sign from vertical forces ( $\sigma_{zz}$ ) appeared at  $E_{Xe} = 15$  eV.

As a rule, the roughness of graphene  $R_a$  almost does not increase with the energy  $E_{Xe}$  of the bombardment of a target at the angle of incidence  $\theta = 60^\circ$  (Figure 11). The maximum roughness reached at  $E_{Xe} = 10$  eV was caused by the early detachment of the Pb film from graphene, as a result of which graphene directly took a great number of the impacts of  $Xe_{13}$  clusters.

Figure 11 compares the function  $R_a(E_{Xe})$  at  $\theta = 60^\circ$  with analogous functions obtained at incident angles of  $0^\circ$  and  $90^\circ$ , i.e., with the vertical and horizontal directions of bombardment. The difference in the roughness of graphene subjected to the uniform (in terms of  $Xe_{13}$  cluster energy and

intensity) bombardment with different angles of incidence can be greater than 40% (at  $E_{Xe} = 10$  eV). The smooth function  $R_a(E_{Xe})$  was obtained under low-level bombardment; in this case, the roughness maximum was reached at  $E_{Xe} = 15$  eV.

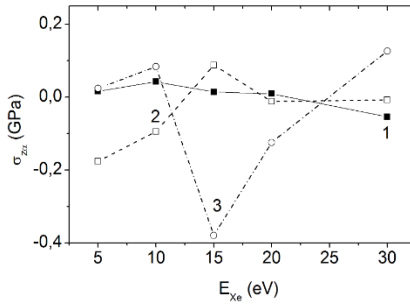


Figure 10. Basic stresses  $\sigma_{z\alpha}$ : (1)  $\sigma_{zx}$  (2)  $\sigma_{zy}$  and (3)  $\sigma_{zz}$  in graphene obtained as a result of the complete bombardment as functions of the energy of bombarding  $Xe_{13}$  clusters.

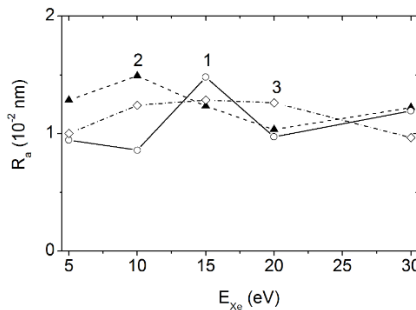


Figure 11. Dependence of roughness of the graphene on the energy of bombarding  $Xe_{13}$  clusters at the incident angles of (1)  $0^\circ$ , (2)  $60^\circ$ , and (3)  $90^\circ$ .

### 4.3. Mercury

At the temperature of 300 K, mercury is in the liquid state (melting point  $T_m = 234$  K). If the attraction forces between the Hg atoms exceed the forces of cohesion of the mercury film with graphene, the film

contracts into a droplet. In order to investigate the opportunity rolling the film into the droplet, we carried out the MD calculation of the Hg film on graphene at  $T = 300$  K using 10 million time steps in absence of the cluster bombardment. A drop of mercury on the graphene sheet close to a spherical shape was obtained as a result of this calculation. In this case, a substantial part of the lower surface of the drop (that is in contact with graphene) was flat. Thus, the film of mercury that was simulated based on the Schwerdtfeger interaction potential has a tendency to roll into a drop. The cluster bombardment using 125 impacts with the angle of incidence  $0^\circ$  did not lead to any significant removal of mercury from graphene at all energies of  $\text{Xe}_{13}$  clusters in the range of 5 – 30 eV. As a rule, more than half of the Hg atoms after the completion of the bombardment related near the graphene, as before it. The bombardment at the angle of incidence equal to  $45^\circ$  was considerably more successful [59–62]. In this case, beginning with the energy of the beam equal to 15 eV, graphene was almost completely cleaned off the mercury. Only single atoms could remain connected with the graphene sheet; moreover, the majority of these atoms were retained at the edges of the sheet. The remaining atoms of Hg were scattered far beyond the limits of the graphene sheet predominantly in two directions (in the horizontal direction at a sharp angle to the axis  $x$ , and upward). As a rule, the Hg atoms were knocked out from the film one by one and less frequently in the form of dimers and trimers. However, at the energies of the cluster beam  $E_{\text{Xe}} \geq 15$  eV there was always a drop of mercury separated from the graphene. Increase in the angle of incidence of the  $\text{Xe}_{13}$  clusters to  $60^\circ$  led to the removal of mercury from graphene at the energy of the beam of 10 eV (Figure 12). A subsequent increase in the energy of the cluster beam at  $\theta = 60^\circ$  did not give the desired result: graphene was not cleaned off the mercury.

Dependences of the internal energy  $E_{\text{Hg}}$  of mercury and the energy of mercury-graphene interaction  $E_{\text{C-Hg}}$  on the energy of the incident cluster beam at angles  $\theta = 0^\circ$ ,  $45^\circ$  and  $60^\circ$  are shown in Figure 13. As it seen from the figure, from 3% (in the case of  $E_{\text{Xe}} = 5$  eV) to 1% ( $E_{\text{Xe}} \geq 15$  eV) of the energy of the cluster beam is transferred to mercury. Hence, from

97% to 99% of the beam energy is scattered in the graphene and substrate. This result agrees with the data of [63].

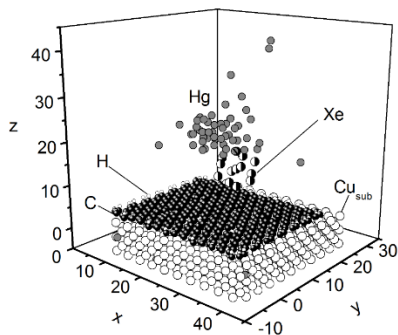


Figure 12. Configuration of a system consisting of a mercury film on a partially hydrogenated imperfect graphene sheet after bombardment by a beam of  $\text{Xe}_{13}$  clusters at the angle of incidence  $60^\circ$  and the energy 10 eV. The coordinates of atoms are given in angstroms.

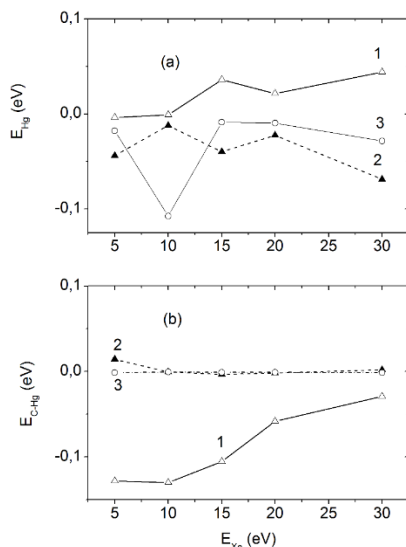


Figure 13. Dependences of the interaction energy: (a) Hg–Hg and (b) C–Hg of mercury film laying on graphene on the energy of the cluster beam at various incident angles of the  $\text{Xe}_{13}$  clusters: (1)  $\theta = 0^\circ$ , (2)  $\theta = 45^\circ$  and (3)  $\theta = 60^\circ$ .

Rebound velocity demonstrates that the graphene absorbs a considerable amount (up to 97%) of the energy of the impacting particle. The idea of using graphene for energy dissipation of indenter was proposed in [64]. The mercury film on graphene has the highest  $E_{\text{Hg}}$  value, i.e., it has the lowest stability, when the bombardment is carried out at the angle  $\theta$  of  $0^\circ$ . However, in this case the  $E_{\text{C-Hg}}$  has the smallest value, i.e., the Hg film is more strongly bound to graphene than at angles of incidence  $\theta = 45^\circ$  and  $60^\circ$ . Attenuation of the bond between the Hg film and graphene when the energy of the cluster beam increases at the angle of incidence  $\theta = 0^\circ$  begins at  $E_{\text{Xe}} = 15$  eV. The bond of the Hg film to graphene disappears for almost all energy values at the angles  $\theta$  of  $45^\circ$  and  $60^\circ$ .

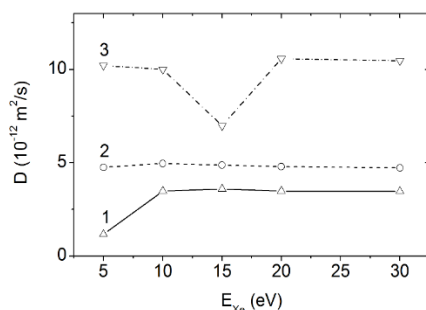


Figure 14. Self-diffusion coefficients of the Hg atoms calculated for the cases of bombardment of the target at the angles of incidence (1)  $0^\circ$ , (2)  $45^\circ$ , and (3)  $60^\circ$  depending on the energies of the cluster beam  $E_{\text{Xe}}$ .

With the increase of the angle of incidence of the xenon clusters, there occurs an increase in the self-diffusion coefficient of mercury atoms; especially, this is noticeable on going from the angle  $\theta = 45^\circ$  to the angle  $60^\circ$ . The lowest value of the self-diffusion coefficient of Hg atoms is observed upon the vertical bombardment with the energy of  $\text{Xe}_{13}$  clusters of 5 eV (Figure 14). At energies  $E_{\text{Xe}} > 10$  eV and at the angle of incidence  $\theta = 0^\circ$ , there is a very weak dependence of the self-diffusion coefficient on the energy of the falling clusters. The similar weak dependence is manifested in the entire range of cluster energies at the angle of incidence

$\theta = 45^\circ$ . At the angle  $\theta = 60^\circ$ , the  $D(E_{Xe})$  function has the deep minimum at 15 eV. The origin of this minimum is most likely connected with the fact that the bombardment with such energy of clusters provides the fastest rolling of the mercury film into a drop, from which the Hg atoms can be kicked out only with difficulty. Except for this specific feature, no significant changes in the behavior of the coefficient of self-diffusion is observed under the variations of the energy  $E_{Xe}$  with the angle of incidence  $\theta = 60^\circ$ .

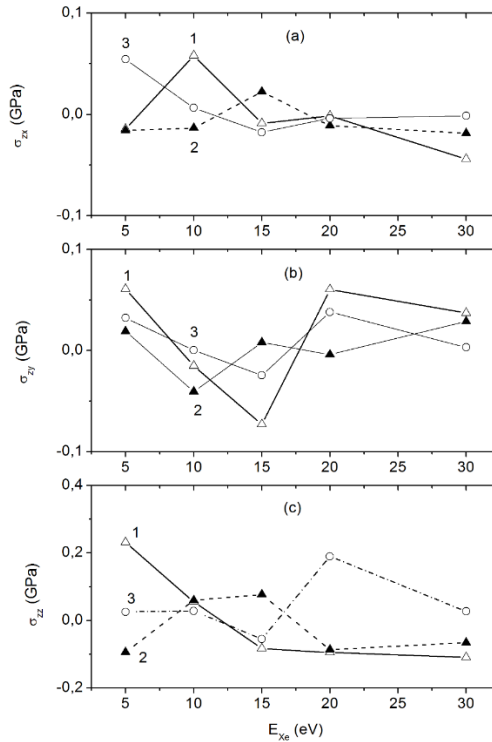


Figure 15. Components of the stress tensor in graphene ((a)  $\sigma_{xz}$ , (b)  $\sigma_{xy}$ , (c)  $\sigma_{zz}$ ) obtained for the cases of the bombardment of targets at the angles of incidence (1)  $0^\circ$ , (2)  $45^\circ$ , and (3)  $60^\circ$  depending on the energies of the cluster beam  $E_{Xe}$ .

Dependences of the stresses in the plane of graphene caused by the horizontal (Figures 15a, 15b) and vertical (Figure 15c) forces exhibit a

complex behavior, which is different for different angles of incidence. As a rule, the stresses  $\sigma_z$  created by the vertical forces are noticeably higher than the stresses  $\sigma_x$  and  $\sigma_y$  that appear due to the action of the horizontal forces. At cluster energies  $E_{Xe}$  that lead to the detachment of the majority of Hg atoms from graphene, the stress has relatively low values. Recall that this occurs at energies  $E_{Xe} > 15$  eV at the angle of incidence  $45^\circ$  and at  $E_{Xe} = 10$  eV at the angle  $\theta = 60^\circ$ .

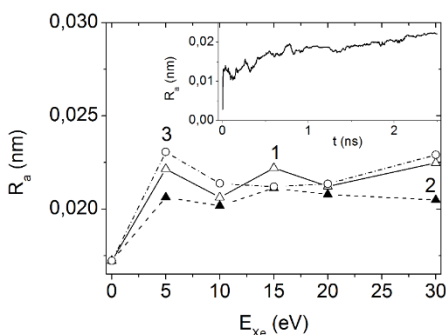


Figure 16. Roughness of graphene obtained as a result of bombardments of the target at the angles of incidence (1)  $0^\circ$ , (2)  $45^\circ$ , and (3)  $60^\circ$  at the energies of the cluster beam  $E_{Xe}$ ; inset shows the change in the roughness of graphene in the course of the bombardment of the target by  $Xe_{13}$  clusters at the angle of incidence  $0^\circ$  and at the energy of the cluster beam 15 eV.

The roughness  $R_a$  of graphene increases continuously in the course of cluster bombardment. The inset in Figure 16 gives a representation of the variation of the function  $R_a(t)$  in time in the case of bombardment with the energy of  $Xe_{13}$  clusters 15 eV at the angle of incidence  $0^\circ$ . The bombardment has a significant effect on the roughness of graphene. The magnitude of  $R_a$  increases by 20 – 40%, even as a result of the bombardment with the energy of clusters equal to only 5 eV; the effect is strongest at the angle of incidence  $60^\circ$ . The form of functions obtained under different values of the energy of the Xe clusters is shown in Figure 16. It seen that the bombardment at the angle of  $\theta = 45^\circ$  leads to the lowest



values of  $R_a$ . Thus, after this bombardment at the beam energy equal to 30 eV, the value of  $R_a$  proves to be below the appropriate characteristics that correspond to the angles of incidence of  $0^\circ$  and  $60^\circ$  by 9.6% and 11.8%, respectively.

## 5. DISCUSSION

All graphene-based devices must unavoidably be electrically contacted to the outside world by metal contacts. Graphene films can be made by catalytically decomposing hydrocarbon precursors over thin films of copper. Wrinkles in a graphene film have a negative impact on electronic properties by introducing strains that reduce the electron mobility. Often, the final product must be a single-layer graphene film. Graphene-based membranes could be used to capture carbon dioxide from certain industrial processes, such as coal burning, and there to reduce greenhouse emissions. Graphene could cheaply and easily remove salt from the seawater. With properly sized holes, graphene sheets may be able to serve as all-purpose filters.

The present study is expected to provide predictive design capability for controlling the surface patterns and stresses in nanotechnology products. For example, the improved understanding could help to make biocompatible surfaces for medical devices. When the argon ions hit the copper surface, they penetrate it knocking away the nearby atoms Cu like billiard balls in a process that is akin at the atomic level to melting or evaporation.

We carried out the bombardment of graphene by the argon clusters with low energy in the way not to damage the graphene when cleaning the metal. The cluster bombardment with significantly higher energy can cause sputter of material with covalent bonds as observed when Si is bombarded with 15 keV  $C_{60}^+$  [65]. In this experimental work, the incident angle is increased from  $0^\circ$  to  $60^\circ$ . Hill and Blenkinsopp [65] observed a higher sputter yield of Si at  $45^\circ$  than at normal incident angle. Molecular

dynamics simulations [66] of the bombardment of a silicon crystal with  $C_{60}$  are used to understand and interpret the puzzling experimental results [65]. At both incident angles, all of the carbon atoms in the projectile become deposited in the substrate by forming the SiC bonds, but for the angle  $45^\circ$  the MD simulation more energy is deposited near the surface creating the larger Si yield [66]. Thus, the incident angle of  $45^\circ$  is, also, the most favorable at sputtering material with a covalent bond under irradiation of the high-energy ion beam.

The stresses in the copper film relax rather quickly (especially  $\sigma_z$ ) as a result of its plasticity and due to a large loss of atoms. Local stresses in graphene relax in order slowly due to the presence of the hard bonds and do not disappear even after the bombardment. This indicates its crystalline nature. Presence of local stresses even in thermodynamic equilibrium is a characteristic feature of ordinary three-dimensional crystals. Instability of two-dimensional crystals with respect to the displacement of atoms in the third dimension is well known and experimentally expressed in a rippled graphene surface. Cluster bombardment of the target greatly enhances this instability and ultimately leads to the surface topography characterized by a large (with respect to the value  $R_a$  of the non-bombarded graphene) roughness.

Calculations using density functional theory for the main crystallographic planes of a number of metals, such as Ag, Au, Cu, Pt, and Al predict weak binding to graphene [67]. However, there is a group of metals such as Ni, Co, Pd, for which substantially stronger binding occurs due to hybridization between graphene and  $d$ -metal states. Therefore, the results obtained here for the Cu-coated graphene are also valid for the cluster bombardment of a graphene sheet with deposited noble metals or aluminum. At the same time, it is not critical how the metal is placed on the graphene sheet. However, the energy of the cluster beam necessary for graphene cleaning may require some adjustment due to significant differences in masses of the elements.

It is of interest to compare the results of the study of removing the films of copper and lead by the bombardment with clusters of rare gases

with the present investigation of the purification of graphene from mercury. First of all, the different mechanisms of the detachment of these heavy metals from graphene during the irradiation of the target by a cluster beam should be noted. In the case of the bombardment of the copper film with  $\text{Ar}_{13}$  clusters, separate Cu atoms are knocked out [20, 21, 23, 33–35]. No regime of bombardment led to the separation of fairly large fragments of the Cu film from graphene.

When the lead film is bombarded, separate atoms are also knocked out, but the prevailing mechanism of the removal of the metal from graphene is the separation of islands of the Pb film from the substrate [68]. Only when detached away from graphene, the island experiences a transformation from a two-dimensional to a three-dimensional structure.

Mercury is separated from graphene in a different way. The unique behavior of mercury is due to its liquid state and poor wetting the graphene; as a result, the Hg film has a tendency to roll into a drop. For this reason, both separate atoms and droplets of significant size are separated from graphene in the course of bombardment. Let us emphasize that it is precisely a drop that is torn off, rather than an island with a two-dimensional morphology.

There are several other differences in processes of the removal of the film of heavy metals from graphene. Thus, the film of copper is not completely removed from graphene, even at an energy of the beam 30 eV at angles of incidence  $0^\circ$  and  $60^\circ$  [21, 23]; and the most efficient method is removal using cluster bombardment at an angle  $\theta = 45^\circ$ . In the case of lead, the most efficient procedure can be considered as irradiation by a cluster beam at the angles of incidence  $0^\circ$  and  $60^\circ$ . In this case, graphene was completely cleaned of metal at energies of the beam 10 and 15 eV. The complete cleaning was also achieved at the angle  $\theta = 45^\circ$ , but in this case the energy of the cluster beam required was equal to 20 eV. The greatest effect from the bombardment of the mercury-on-graphene target is obtained at the angle of incidence of  $45^\circ$ . At this angle of incidence, graphene is cleaned of Hg at all energies  $E_{\text{Xe}} \geq 15$  eV. A less stable cleaning effect was achieved at the angle of incidence  $60^\circ$ . In the case of the angle of incidence  $0^\circ$ , no significant removal of mercury from graphene

occurs in the range of energies of the beam 5 – 30 eV. Thus, the removal of different heavy metals requires different conditions for bombardment and occurs via different mechanisms.

To check the correctness of the results, we also conducted calculations with another pair potential for mercury and another potential describing the mercury–graphene interaction. The Hg–Hg interactions were determined based on applying the potential proposed by Silver and Goldman (SG potential) with the parameters given in [69]. Here, we obtained results close to those where the SCH potential served as the potential function for mercury. In the calculations that applied the SG potential upon bombardment, the Hg film was faster transformed into the drop and was separated from the graphene. The complete removal of mercury from graphene was only achieved at the angle of incidence of  $45^\circ$  at  $E_{xe} \geq 15$  eV. When using the Morse potential with the parameters given in [70] for the representation of Hg–C interactions, mercury under the bombardment was separated from graphene more difficult, and the complete cleaning at the angle  $\theta = 45^\circ$  was achieved at the energies  $E_{xe} \geq 20$  eV.

## CONCLUSION

Incident angle  $\theta = 45^\circ$  is the most effective one for graphene cleaning of copper by bombardment with the argon clusters. Cluster beam energy should be no less than 20 eV. Stresses in the copper film relax fast as a result of its plasticity and due to a large loss of atoms. Local stresses in graphene relax rather slowly due to the presence of the hard bonds and do not disappear even after the bombardment; this indicates its crystalline nature. Cluster bombardment of the target greatly enhances this instability and ultimately leads to the surface topography characterized by a large (relative to the value  $R_a$  of non-bombarded graphene) roughness. To use such a cleaning method, it is important to protect graphene edges because they can be strongly damaged. If it is possible to execute accurate bombardment, then the “nap of the earth” flight method is here the most

effective one. The total cleaning can be obtained with the emitted clusters energy 20 eV and higher. The graphene edges in such a cleaning method are less damaged. The prediction model for nanopattern evolution during cluster bombardment can guide the nanomanufacturing processes.

We studied the bombardment of a Pb film on graphene by clusters with energies from 5 to 30 eV. The best cleaning effect was achieved at  $E_{Xe} = 10$  eV. The Pb film can also be removed (on point contact) for the cluster energy 15 eV. Use of the higher beam energies is ineffective because of pushing the Pb atoms into divacancies and impression of the metal atoms into dimples on graphene. The hydrogenated edges of graphene do not acquire noticeable damage even after the bombardment with 30-eV clusters. For example, unlike copper, the prevailing mechanism in the process of lead removal is the detachment of the major portion of the film from graphene rather than the knocking out the separate Pb atoms. This is evident from analysis of the density profiles of the system and the energy dependence of the mobility components of Pb atoms. The bombardment of graphene after the removal of a film leads to a considerable increase in the vertical component of mobility of the C atoms. Stresses in the lead film that remained on graphene increased in the course of bombardment, whereas analogous stresses in graphene were not accumulated with time. The highest stresses occurred in the detached film of lead, which increased its vertical size and took a torch shape, are the result of the action of both the vertical and horizontal forces. In this case, an increase in the internal stress was also extended to graphene. The graphene subjected to direct bombardment with 10 eV clusters acquired the greatest roughness as a result of the rapid removal of the Pb film.

The behavior of the system “mercury–on–partially–hydrogenated–graphene” has been investigated under irradiation by a beam of  $Xe_{13}$  clusters with energies of 5 – 30 eV at the angles of incidence  $0^\circ$ ,  $45^\circ$ , and  $60^\circ$ . Over a wide range of energies ( $E_{Xe} \geq 15$  eV), the almost complete removal of mercury from graphene was only achieved at the angle of incidence of  $45^\circ$ . The film of mercury, which has a tendency to become rolled up into a drop, is separated from the graphene in the form of single

atoms, dimers, trimers, and spherical droplets. In the course of the bombardment, mercury exhibits a weak cohesion with graphene. The smallest change in the components of mobility of the Hg atoms under the variation of the energy of the cluster beam occurs at the angle of incidence of  $45^\circ$ . At the energies of the cluster beam under consideration, the stresses in the plane of graphene caused by the vertical forces noticeably exceed the stresses created by the horizontally directed forces regardless the angle of incidence. The roughness of graphene increases noticeably in the course of cluster bombardment. The lowest roughness is demonstrated by graphene subjected to irradiation with the beam of clusters with the angle of incidence of  $45^\circ$ . The hydrogenated edges of graphene do not suffer of noticeable damages at all the energies investigated and at all the angles of incidence of the bombarding clusters.

## REFERENCES

- [1] Hawaldar, R., Merino, P., Correia, M. R., Bdkin, I., Grácio, J., Méndez, J., Martín-Gago, J. A. & Singh, M. K. (2012). Large-area high-throughput synthesis of monolayer graphene sheet by hot filament thermal chemical vapor deposition. *Sci. Rep.*, 2, 682 (1–10).
- [2] Siokou, A., Ravani, F., Karakalos, S., Frank, O., Kalbac, M. & Galiotis, C. (2011). Surface refinement and electronic properties of graphene layers grown on copper substrate: An XPS, UPS and EELS study. *Appl. Surf. Sci.*, 257, 9785–9790.
- [3] Saito, S., Ito, A. & Nakamura, H. (2010). Molecular dynamics simulation of the incident angle dependence of reactions between graphene and hydrogen atom. *Plasma and Fusion Res.*, 5, S2076 (1–4).
- [4] Inui, N., Mochiji, K. & Moritani, K. (2008). Actuation of a suspended nano-graphene sheet by impact with an argon cluster. *Nanotechnology*, 19, 505501 (1–7).

- [5] Krasheninnikov, A. V. & Nordlund, K. (2010). Ion and electron irradiation-induced effects in nanostructured materials. *J. Appl. Phys.*, *107*, 071301 (1–70).
- [6] Garcia, H., Castán, H., Duenas, S., Bailon, L., Campabadal, F., Rafi, J. M. & Tsunoda, I. (2013). 2 MeV electron irradiation effects on bulk and interface of atomic layer deposited high-k gate dielectrics on silicon, *Thin Solid Films*, *534*, 482–487.
- [7] Galashev, A. E. & Polukhin, V. A. (2013). Computer study of the physical properties of a copper film on a heated graphene surface. *Phys. Solid State*, *55*, 1733–1738.
- [8] Ahlgren, E., Kotakoski, J., Lehtinen, O. & Krasheninnikov, A. V. (2012). Ion irradiation tolerance of graphene as studied by atomistic simulations. *Appl. Phys. Lett.*, *100*, 233108 (1–4).
- [9] Luoma, S. N. (1983). Bioavailability of trace metals to aquatic organisms – a review. *Sci. Total Environ.*, *28*, 1–22.
- [10] Hummers, W. & Offeman, R. (1958). Preparation of graphitic oxide. *J. Am. Chem. Soc.*, *80*, 1339–1339.
- [11] Choi, Y. S. & Choi, H. S. (2003). Sensitized spectrophotometric determination of trace Cu(II) in cationic surfactant media. *Bull. Korean. Chem. Soc.*, *24*, 222–224.
- [12] Zaijan, L., Yuling, Y., Jian, T. & Jiaomai, P. (2003). Spectrophotometric determination of trace lead in water after preconcentration using mercaptosephadex. *Talanta*, *60*, 123–130.
- [13] Kara, D., Alkan, M. & Cakir, U. (2001). Copper extraction from aqueous solution by pentaery thrityltetrabenzylamine. *Turk. J. Chem.*, *25*, 293–303.
- [14] Sonawale, S. B., Ghalsasi, Y. V. & Argekar, A. P. (2001). Extraction of lead(II) and copper(II) from salicylate media by tributylphosphine oxide. *Anal. Sci.*, *17*, 285–289.
- [15] Manzoori, J. L. & Bavili-Tabrizi, A. (2002). The application of cloud point preconcentration for the determination of Cu in real samples by flame atomic absorption spectrometry. *Microchem. J.*, *72*, 1–7.
- [16] Chen, J. & Teo, K. C. (2001). Determination of cadmium, copper, lead and zinc in water samples by flame atomic absorption

- spectrometry after cloud point extraction. *Anal. Chim. Acta*, *450*, 215–222.
- [17] Yuan, S., Chen, W. & Hu, S. (2004). Simultaneous determination of cadmium (II) and lead (II) with clay nanoparticles and anthraquinone complexly modified glassy carbon electrode. *Talanta*, *64*, 922–928.
- [18] Gao, H., Zhou, J., Lu, M., Fa, W. & Chen, Y. (2010). First-principles study of the IVA group atoms adsorption on graphene. *J. Appl. Phys.*, *107*, 114311.
- [19] Ma, D. & Yang, Z. (2011). First-principles studies of Pb doping in graphene: stability, energy gap and spin–orbit splitting. *New J. Phys.*, *13*, 123018.
- [20] Galashev, A. E. & Polukhin, V. A. (2014). Compaction of a copper film on graphene by argon-beam bombardment: Computer experiment. *J. Surf. Invest.: X-ray, Synchrotr. Neutron Tech.*, *8*, 1082–1088.
- [21] Galashev, A. E. & Polukhin, V. A. (2014). Removal of copper from graphene by bombardment with argon clusters: Computer experiment. *Phys. Met. Metallogr.*, *115*, 697–704.
- [22] Galashev, A. E. & Rakhmanova, O. R. (2014). Mechanical and thermal stability of graphene and graphene-based materials. *Phys. Usp.*, *57*, 970–989.
- [23] Galashev, A. E. & Galasheva, A. A. (2014). Molecular dynamics simulation of copper removal from graphene by bombardment with argon clusters. *High Energy Chem.*, *48*, 112–116.
- [24] Russo, M. F. Jr. & Garrison, B. J. (2006). Mesoscale energy deposition footprint model for kiloelectronvolt cluster bombardment of solids. *Anal. Chem.*, *78*, 7206–7210.
- [25] Russo, M. F., Jr. Szakal, C., Kozole, J., Winograd, N. & Garrison, B. J. (2007). Sputtering yields for C<sub>60</sub> and Au<sub>3</sub> bombardment of water ice as a function of incident kinetic energy. *Anal. Chem.*, *79*, 4493–4498.
- [26] Smiley, E. J., Winograd, N. & Garrison, B. J. (2007). Effect of cluster size in kiloelectronvolt cluster bombardment of solid benzene. *Anal. Chem.*, *79*, 494–499.



- [27] Watanabe, Y., Yamaguchi, H., Hashinokuchi, M., et al. (2005). Trampoline motions in Xe–graphite (0 0 0 1) surface scattering. *Chem. Phys. Lett.*, *413*, 331–334.
- [28] Steckel, J. A. (2005). Ab initio modelling of neutral and cationic Hg–benzene complexes. *Chem. Phys. Lett.*, *409*, 322–330.
- [29] Padak, B., Brunetti, M., Lewis, A. & Wilcox, J. (2006). Mercury binding on activated carbon. *Environ. Prog.*, *25*, 319–326.
- [30] Padak, B. & Wilcox, J. (2007). Understanding mercury binding on activated carbon. *Carbon*, *47*, 2855–2864.
- [31] Huggins, F. E., Huffman, G. P., Dunham, G. E. & Senior, C. L. (1999). XAFS examination of mercury sorption on three activated carbons. *Energy Fuels*, *13*, 114–121.
- [32] Cao, Y. & Li, X. (2014). Adsorption of graphene for the removal of inorganic pollutants in water purification: A review. *Adsorption*, *20*, 713–727.
- [33] Galashev, A. E. (2014). Computer simulation of argon cluster bombardment of a copper–graphene film. *Fiz. Mezomekh.*, *17*, 67–73.
- [34] Galashev, A. Y. (2015). Computer study of the removal of Cu from the graphene surface using Ar clusters. *Compt. Mater. Sci.*, *98*, 123–128.
- [35] Galashev, A. Y. & Rakhmanova, O. R. (2015). Computer simulation of the bombardment of a copper film on graphene with argon clusters. *Chin. Phys. B*, *24*, 020701 (1–4).
- [36] Xu, Z. & Buehler, M. J. (2010). Interface structure and mechanics between graphene and metal substrates: a first-principles study, *J. Phys.: Condens. Matter.*, *22*, 485301.
- [37] Tersoff, J. (1988). New empirical approach for the structure and energy of covalent systems. *Phys. Rev. B: Condens. Matter.*, *37*, 6991–7000.
- [38] Galashev, A. Y. (2012). A computer study of the Raman spectra of the (GaN)<sub>129</sub>, (SiO<sub>2</sub>)<sub>86</sub>, and (GaN)<sub>54</sub>(SiO<sub>2</sub>)<sub>50</sub> nanoparticles. *Russ. J. Phys. Chem. B*, *6*, 441–447.
- [39] Galashev, A. Y. (2014). Computer study of the Raman spectra and infrared optical properties of gallium nitride and gallium arsenic

- nanoparticles with SiO<sub>2</sub> core and shell. *J. Nanopart. Res.*, *16*, 2351 (1–18).
- [40] Stuart, S. J., Tutein, A. V. & Harrison, J. A. (2000). A reactive potential for hydrocarbons with intermolecular interactions. *J. Chem. Phys.*, *112*, 6472–6486.
- [41] Rafii-Tabar, H. (2000). Modelling the nano-scale phenomena in condensed matter physics via computer-based numerical simulations. *Phys. Rep.*, *325*, 239–310.
- [42] Kutana, A. & Giapis, K. P. (2006). Atomistic simulations of electrowetting in carbon nanotubes. *Nano Lett.*, *6*, 656–661.
- [43] Schwerdtfeger, P., Boyd, P. D. N., Briennes, S., McFearets, J. S., Dolg, M. Liao, M. S. & Schwarz, W. H. E. (1993). The mercury–mercury bond in inorganic and organometallic compounds. A theoretical study, *Inorg. Chim. Acta*, *213*, 233–246.
- [44] Oluwajobi, A. & Chen, X. (2011). The effect of interatomic potentials on the molecular dynamics simulation of nanometric machining. *Int. J. Autom. Comput.*, *8*, 326–332.
- [45] Kim, Y. M. & Kim, S. C. (2002). Adsorption/desorption isotherm of nitrogen in carbon micropores. *J. Korean Phys. Soc.*, *40*, 293–299.
- [46] Arkundato, A., Su’ud, Z., Abdullah, M. & Sutrisno, W. (2013). Study of liquid lead corrosion of fast nuclear reactor and its mitigation by using molecular dynamics method. *Int. J. Appl. Phys. Math.*, *3*, 1–6.
- [47] Li, F. Y. & Berry, R. S. (1995). Dynamics of Xe Atoms in NaA zeolites and the 129Xe chemical shift. *J. Phys. Chem.*, *99*, 2459–2468.
- [48] Galashev, A. Y. (2016). Modeling of forced desorption processes in a regenerable graphene sorbent for elemental mercury capture. *J. Phys. Chem. C*, *120*, 13263–13274.
- [49] Chiang, K. N., Chou, C. Y., Wu, C. J., Huang, C. J. & Yew, M. C. (2009). Analytical solution for estimation of temperature-dependent material properties of metals using modified Morse potential. *ICCES*, *9*, 130–141.

- [50] Bonechi, A. & Moraldi, M. (1998). Interaction-induced polarizability invariants and the interatomic potential of the mercury diatom. *J. Chem. Phys.*, *109*, 5880–5885.
- [51] Moore, M. C., Kalyanasundaram, N., Freund, J. B. & Johnson, H. T. (2004). Structural and sputtering effects of medium energy ion bombardment of silicon. *Nucl. Instrum. Meth. Phys. Res.*, *225*, 241–255.
- [52] Smith, R., Harrison, D. E. Jr. & Garrison, B. J. (1989). keV particle bombardment of semiconductors: A molecular-dynamics simulation. *Phys. Rev. B*, *40*, 93–101.
- [53] Lamari, F. D. & Levesque, D. (2011). Hydrogen adsorption on functionalized graphene. *Carbon*, *49*, 5196–5200.
- [54] Davydov, S. Yu. (2012). Energy of substitution of atoms in the epitaxial graphene-buffer layer SiC substrate system. *Phys. Solid State*, *54*, 875–882.
- [55] Jin, Z. H., Sheng, H. W. & Lu, K. (1999). Melting of Pb clusters without free surfaces. *Phys. Rev. B*, *60*, 141–149.
- [56] Galashev, A. E. (2016). Molecular-dynamic simulation of the bombardment of a lead film on graphene by Xe<sub>13</sub> clusters. *Phys. Met. Metallogr.*, *117*, 246–253.
- [57] Galashev, A. E. & Polukhin, V. A. (2016). Simulation of the removal of a lead film from graphene by the irradiation of a target with a beam of xenon clusters. *Rus. J. Phys. Chem. B*, *10*, 15–22.
- [58] Galashev, A. Y. & Rakhmanova, O. R. (2017). Molecular-dynamic calculation of effects appearing in removing a lead film from graphene. *J. Engineering Phys. Thermophys.*, *90*, 1026–1034.
- [59] Galashev, A. E. & Polukhin, V. A. (2015). Computer modeling of the structure and properties of mercury films on graphene. *Rus. J. Phys. Chem. A*, *89*, 1429–1433.
- [60] Galashev, A. E. & Galasheva, A. A. (2015). Mercury removal from graphene by bombardment with xenon clusters: computer simulation. *High Energy Chem.*, *49*, 347–351.

- [61] Galashev, A. E. (2016). Molecular-dynamic simulation of the removal of mercury from graphene via bombardment with xenon clusters. *Phys. Met. Metallogr.*, *117*, 238–245.
- [62] Galashev, A. E. (2016). Computer simulation of the xenon<sub>cluster</sub> bombardment of mercury on graphene. *J. Surf. Invest.: X-ray, Synchrotr. Neutron Tech.*, *10*, 15–22.
- [63] Hosseini-Hashemi, S. & Sepahi-Boroujeni, A. (2017). Elastic impact response of a nonlocal rectangular plate. *Int. J. Solids Struct.*, *109*, 93–100.
- [64] Yang, L. & Tong, L. (2016). Suspended monolayer graphene traps high-speed single-walled carbon nanotube. *Carbon*, *107*, 689–696.
- [65] Hill, R. & Blenkinsopp, P. (2004). The development of C<sub>60</sub> and gold cluster ion guns for static SIMS analysis. *Appl. Surf. Sci.*, *231*, 936–939.
- [66] Krantzman, K. D., Kingsbury, D. B. & Garrison, B. J. (2007). Cluster induced chemistry at solid surfaces: Molecular dynamics simulations of keV C<sub>60</sub> bombardment of Si. *Nucl. Instrum. Methods. Phys. Res. B*, *255*, 238–241.
- [67] Vanin, M., Mortensen, J. J., Kelkkanen, A. K., Garcia-Lastra, K. S., Thygesen, J. M. & Jacobsen, K. W. (2010). Graphene on metals: A van der Waals density functional study. *Phys. Rev. B*, *81*, R081408.
- [68] Galashev, A. E. & Galasheva, A. A. (2015). Computer simulation of cluster bombardment of a lead film on graphene. *High Energy Chem.*, *49*, 117–121.
- [69] Munro, L. J. & Johnson, J. K. (2001). An interatomic potential for mercury dimer. *J. Chem. Phys.*, *114*, 5545–5551.
- [70] Duval, M. C. & Soep, B. (1987). Potential characteristics of the mercury–methane van der Waals complex. *Chem. Phys. Lett.*, *141*, 225–231.

*Chapter 4*

# **FLEXIBLE RESISTIVE SWITCHING MEMORIES: FROM MATERIALS TO DEVICES**

*Shuang Gao, Xiaohui Yi, Jie Shang, Bin Chen,  
Gang Liu\* and Run-Wei Li†*

CAS Key Laboratory of Magnetic Materials and Devices,  
Ningbo Institute of Materials Technology and Engineering,  
Chinese Academy of Sciences, Ningbo, China  
Zhejiang Province Key Laboratory of Magnetic Materials  
and Application Technology, Ningbo Institute of Materials Technology  
and Engineering, Chinese Academy of Sciences, Ningbo, China

## **ABSTRACT**

As an indispensable component for future flexible electronics, flexible resistive switching memories have recently aroused great interest all around the world. In this chapter, a comprehensive review on the recent progress in this field is presented, with a particular emphasis on materials and devices. First, a brief introduction is given on the basic concepts of flexible resistive switching memories. Next, storage media as well as electrode and substrate materials used in flexible resistive

---

\* Corresponding Author Email: liug@nimte.ac.cn.

† Corresponding Author Email: runweili@nimte.ac.cn.

switching memories are summarized in detail. Third, attention is focused on the fabrication technologies of flexible resistive switching memories and the performance of obtained devices. Finally, a short discussion on the current challenges and future prospects of flexible resistive switching memories is provided.

**Keywords:** flexible, resistive switching, resistive random access memory, nonvolatile memory

## 1. INTRODUCTION

With the rapid development of Internet of Things (IoT) and the increasing concern on human health monitoring, flexible electronics has become an increasingly important development direction of future electronics [1, 2]. As an indispensable component, memory devices should also be flexible to guarantee that the entire electronic systems have superior flexible performance [3]. However, conventional Si-based memories, including volatile static and dynamic random access memories (SRAM and DRAM) and nonvolatile Flash memory, are incompatible with flexible electronics due to their intrinsic brittleness and the need for high-temperature process. Also, the volatility of SRAM and DRAM, as well as the low operation speed (write/erase time:  $\sim 1$  ms/ $\sim 0.1$  ms) and poor endurance ( $\sim 10^6$  write/erase cycles) of flash memory are unfavorable for practical use [4]. Therefore, the development of flexible memories based on novel mechanisms, structures and materials are urgently needed.

Resistive switching memories, also known as resistive RAMs (RRAMs), are an emerging and promising nonvolatile memory concept with simple electrode/insulator/electrode sandwich-like cell structures [4]. This enables resistive switching memories to be easily integrated using passive crossbar array architectures for real applications, where each crosspoint is a memory cell occupying only a small area of  $4F^2$  ( $F$ : the minimum feature size), as shown in Figure 1a–b. Under external electrical stimuli, memory cells can be reversibly switched between a high resistance state (HRS or OFF state) and a low resistance state (LRS or ON state), as

shown in Figure 1b–d. The switching from HRS to LRS is denoted as a set process, with its opposite as a reset process. If the set and reset processes need the same electrical polarity, related switching behaviors are called unipolar (Figure 1c) and otherwise bipolar (Figure 1d). The involved switching mechanisms include ion migration, [5, 6, 7, 8] charge trapping/de-trapping, [9, 10] thermochemical reaction, [11] etc. [4].

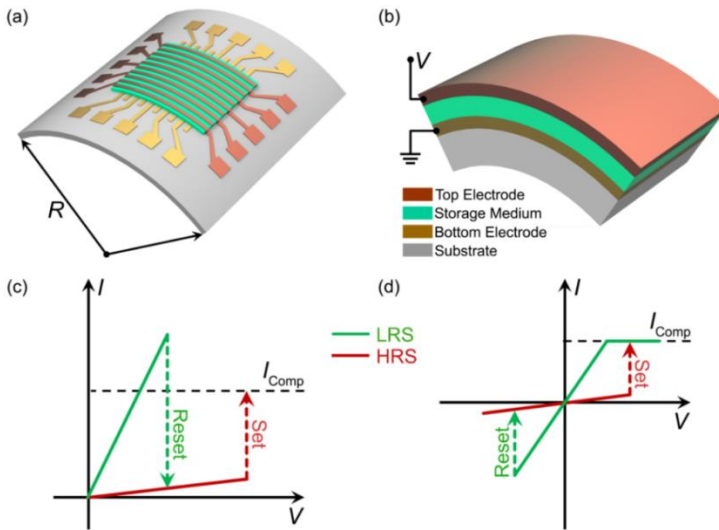


Figure 1. Schematic device structure and  $I$ - $V$  characteristics of flexible resistive switching memories. (a) Schematic of a flexible crossbar resistive switching memory array bent with radius  $R$ . (b) Schematic memory cell structure with measurement configuration. Schematic  $I$ - $V$  characteristics of (c) unipolar and (d) bipolar resistive switching behaviors, where  $I_{Comp}$  denotes the compliance current during the set process to prevent the device from permanent breakdown.

Besides simple cell structures and easy integration, resistive switching memories have extremely rich choices in active materials, [4] including oxides, [12, 13, 14] chalcogenides, [15] nitrides, [16, 17] small molecules, [18] polymers [19, 20] and organic-inorganic composites [21, 22, 23]. Meanwhile, they have demonstrated excellent miniaturization potential ( $<10$  nm), [24] fast operation speed ( $<1$  ns), [25] low energy consumption ( $<0.1$  pJ) [24] and high switching endurance ( $>10^{12}$  cycles) [26]. These characteristics together make resistive switching memories highly suitable

for flexible applications. Key performance parameters of flexible resistive switching memories include the minimum bending radius, the maximum bending strain, the bending endurance, the switching endurance under bending, and the data retention time under bending. Under a given bending radius  $R$  (Figure 1a), the real bending strain on memory cells can be roughly calculated to be  $d/(2R)$ , where  $d$  represents the substrate thickness [27]. This is because the thickness of memory cells (mostly  $<1 \mu\text{m}$ ) is usually much smaller than that of substrate (mostly  $>10 \mu\text{m}$ ) and thus can be reasonably ignored for strain calculation [8, 14].

In the past few years, flexible resistive switching memories have inspired a great amount of research interest all around the world. Besides the main application of data storage, they have been explored preliminarily for novel logic-in-memory [28, 29] and synaptic emulation [30, 31] applications. In this chapter, a comprehensive review on the recent progress in flexible resistive switching memories is presented, with a particular emphasis on materials (Section 2) and devices (Section 3).

## 2. MATERIALS

Resistive switching memories usually have electrode/insulator/electrode sandwich structures, wherein the insulator layer provides a material platform for the switching to occur and thus is also known as the storage media. Substrates are also necessary for integration. To make the device flexible, all components must comply with bending during operation while maintaining their electrical functions.

### 2.1. Storage Media

Since resistive switching and information memorizing occur within, the storage media plays a crucial role in determining the performance of flexible resistive switching memories. The study of flexible resistive switching memories started with inorganic storage media. As early as



2008, Kim et al. [32] reported the first inorganic flexible resistive switching device that used  $\text{AlO}_x$  as the media layer and worked properly under bending with 27.5 mm radius. Since then, a large number of inorganic materials have been explored as storage media for flexible memories. Among them, binary oxides are dominating candidates, including  $\text{AlO}_x$ , [12, 32]  $\text{SiO}_x$ , [33, 34]  $\text{TiO}_x$ , [35, 36]  $\text{NiO}_x$ , [13, 37]  $\text{CuO}_x$ , [38, 39]  $\text{ZnO}_x$ , [40, 41]  $\text{GeO}_x$ , [42, 43]  $\text{MoO}_x$ , [30]  $\text{SmO}_x$ , [44]  $\text{LuO}_x$ , [45]  $\text{HfO}_x$ , [8, 46]  $\text{WO}_x$ , [14, 47] etc. Complex oxides such as  $\text{ZnSnO}_3$  [48] and  $\text{BaTi}_{0.95}\text{Co}_{0.05}\text{O}_3$ , [49] nitrides including hBN [16, 50] and  $\text{C}_3\text{N}_4$ , [17]  $\text{Ag}_2\text{Se}$ , [15]  $\text{Cs}_3\text{Bi}_2\text{I}_9$  [51] and a-Si, [52, 53] were also explored as storage media. For example, Ji et al. [14] reported a flexible  $\text{WO}_x$  resistive switching device that can work under bending with 5.53 mm radius, whereas Hu et al. [51] reported a flexible  $\text{Cs}_3\text{Bi}_2\text{I}_9$  resistive switching device showing a bending radius of 9 mm.

It is noteworthy that the intrinsic brittleness of inorganic storage media usually makes these devices only capable of working under relatively low bending conditions, normally with a bending radius of  $>5$  mm or bending strain of  $<2\%$  [14, 51]. Nevertheless, the high compatibility of their fabrication procedure with the standard CMOS technology and the superior switching performance still encourage the inorganic storage media the primary choice for practical applications. In order to improve the mechanical flexibility of inorganic storage media without sacrificing their electrical performance, Shang et al. [8] developed a new strategy of designing the  $\text{HfO}_x$  switching layer with a mixed amorphous-nanocrystalline microstructure. In the mixed structure of the  $\text{HfO}_x$  layer, the amorphous parts residing between the nano crystals not only help to release the strains accumulated during bending operation, but also guide the formation and reliable evolution of pseudo-straight conductive filaments. As such, the fabricated resistive switching device exhibits excellent memory performance with switching randomness of  $<4.3\%$ , endurance  $>10^7$  cycles and data retention  $>10$  years at the bending radius of 6 mm, as shown in Figure 2. The good resistive switching characteristics of such inorganic storage media (in particular binary oxide materials) makes them promising candidates for electronic systems where electrical

reliability is the primary consideration while moderate mechanical flexibility will be an extra advantage.

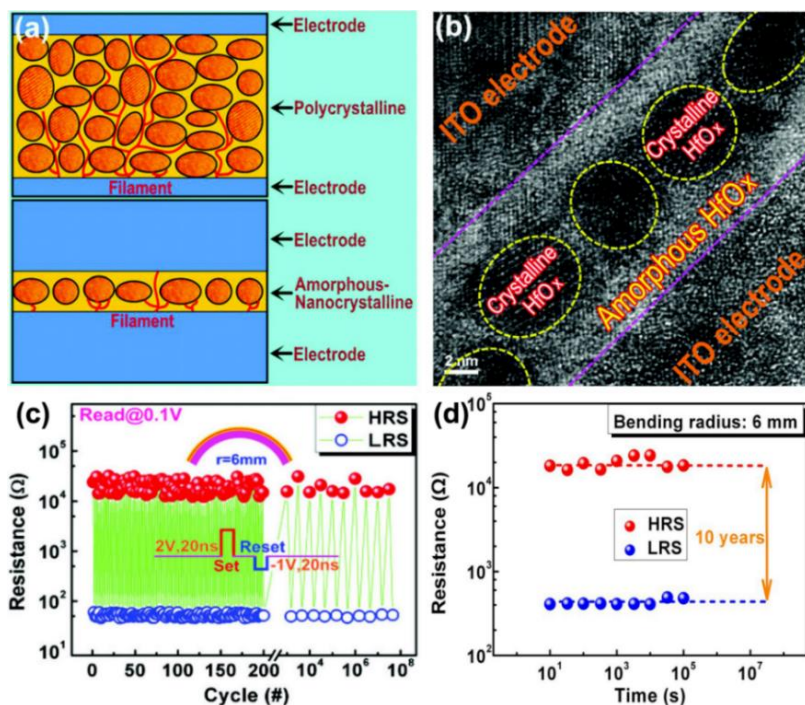


Figure 2. Switching performance of a flexible HfO<sub>x</sub> resistive switching device. (a) Schematic illustration of the formation of branched conducting filaments in a polycrystalline HfO<sub>x</sub> layer (upper panel) and of pseudo-straight conducting filaments in a mixed amorphous-nanocrystalline HfO<sub>x</sub> layer. (b) Cross-sectional high-resolution transmission electron microscopy (TEM) image of the device, revealing clearly the mixed amorphous-nanocrystalline microstructure of HfO<sub>x</sub>. (c) Endurance performance of the device at a 6 mm bending radius in pulse-mode operation. (d) Data retention characteristic of the device at a 6 mm bending radius. Reproduced with permission from Ref. 8. Copyright © 2017, The Royal Society of Chemistry.

To make resistive switching memories more flexible, carbon and organic storage media (referred to as organic materials in the following sections) were intentionally introduced in this field and are attracting a rapidly increasing amount of research interest in recent years. The intrinsic mechanical performance of organic materials, together with their simple solution processability and light-weight characteristics, makes them good

candidates for flexible electronics and allow low-cost fabrication and integration into large-area applications. Many organic materials have been reported to show resistive switching characteristics and explored for flexible memories thus far. Examples are graphene oxide (GO), [54, 55] polymers (e.g., chitosan, [19] lignin, [56] parylene [57], pEGDMA, [58] PFT-PI, [59] PI, [60] pV3D3 [20] and starch [61]), polymeric composites (e.g., PEO:PVK, [62] PI:PCBM, [63] PMMA:P3HT, [64] PMMA:PCBM [65] and PS:PCBM [66]), organic-inorganic composites (e.g., cellulose:Ag, [22] PMMA:graphene, [21] PMMA:graphite, [68] PVA:MoS<sub>2</sub>, [69] PVOH:hBN, [23] PVOH:ZnSnO<sub>3</sub> [70] and PVP:grapheme [71]), and organic-inorganic hybrid materials (e.g., CH<sub>3</sub>NH<sub>3</sub>PbI<sub>3</sub> [72, 73] HKUST-1 [74] and ZIF-8 [75]).

Generally, polymers and organic composites appear as the best choices in terms of mechanical flexibility. For instance, the recorded highest bending strain of flexible resistive switching memory to date is 6.28% as obtained in PS:PCBM composite, [66] shown in Figure 3a–b. On the other hand, employing organic-inorganic composites and hybrid materials as the storage media will lead to simultaneous optimization of device flexibility and memory performance, through combining the mechanical feature of organic materials and electrical reliability of inorganic storage media. To achieve this end, Pan et al. [74] at Ningbo Institute of Materials Technology and Engineering CAS has developed a modified laboratory scale liquid-phase epitaxy (LPE) facility, through which high quality metal-organic framework thin films of HKUST-1 with the thickness of ~130 nm and roughness of ~4 nm can be prepared on gold-coated polyethylene terephthalate (PET) substrates. The entire synthetic process is conducted in a N<sub>2</sub> atmosphere continuously without being exposed to ambient conditions, thus avoiding possible contamination from the air. The automatic LPE facility also shortens the time duration of the reaction process. The as-fabricated HKUST-1 thin film device has been found to show a highly uniform bipolar resistive switching behavior with excellent endurance of >10<sup>7</sup> cycles under bending with a small radius of 4.5 mm [74], as shown in Figure 3c–d.

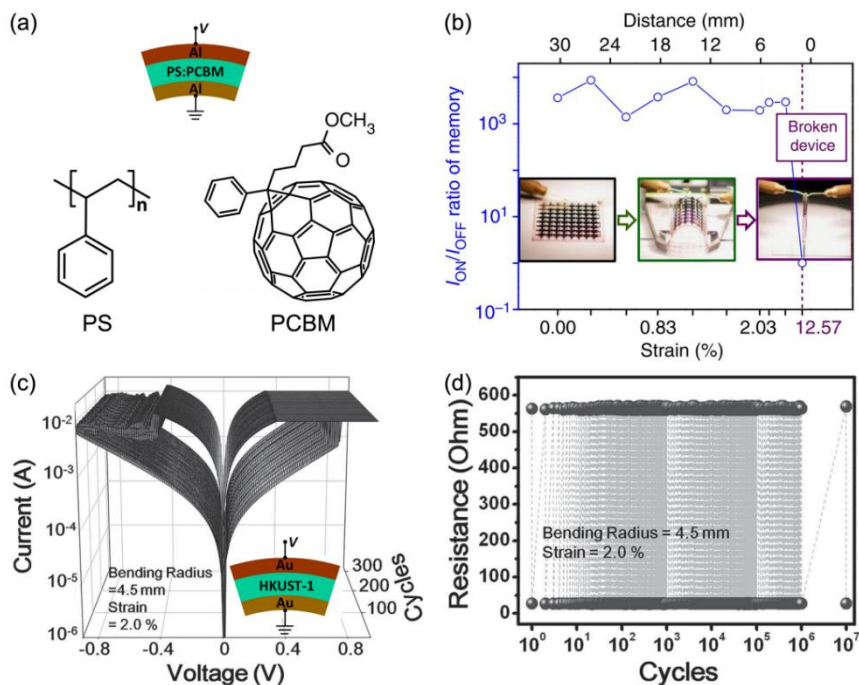


Figure 3. Switching performances of flexible (a–b) PS:PCBM and (c–d) HKUST-1 resistive switching devices. (a) Schematic device structure and chemical structures of PS and PCBM. (b) Memory window of the flexible PS:PCBM resistive switching device against bending distance and strain. The device worked normally until a bending strain of 6.28% (~1 mm bending radius), but failed at a bending strain of 12.57% (~0.5 mm bending radius). Reproduced with permission from Ref. 66. Copyright © 2013, Macmillan Publishers Limited, part of Springer Nature. (c)  $I$ – $V$  characteristic over 300 consecutive switching cycles and (d) endurance performance in pulse-mode operation of the flexible HKUST-1 resistive switching device at a 4.5 mm bending radius, corresponding to a bending strain of about 2.0%. Reproduced with permission from Ref. 74. Copyright © 2015, WILEY-VCH Verlag GmbH & Co. KGaA, Weinheim, Germany.

## 2.2. Electrode Materials

The electrode used in the resistive switching memories may not only be responsible for conducting current in the integrated circuits, but could also take part in the occurrence of resistive switching. Therefore, selection of electrode materials for flexible memory requires to consider both the

mechanical and electrical properties. According to the chemical composition, electrode materials can be classified into metals, metal alloys, carbon/silicon materials, nitrides and conductive oxides. To date, a large number of electrode materials have been employed to fabricate flexible resistive switching memories. Among them, metals such as Mg, [19] Al, [36] Ti, [54] Ni, [13] Cu, [58] Ru, [45] Ag, [16] W, [57] Pt [76] and Au [15] are certainly the most popular ones due to high conductivity and good flexibility. For example, Jang et al. [15] reported a flexible Ag<sub>2</sub>Se resistive switching device with Ag as the top electrode and Au as the bottom electrode, which can work properly at a 16 mm bending radius even after 10<sup>3</sup> bending cycles. To make the fabricated resistive switching memories not only flexible but also transparent, many transparent and conducting materials have been intentionally introduced as electrodes, such as graphene, [50] indium tin oxide (ITO), [8] indium-zinc-oxide (IZO), [12] Ga-doped ZnO (GZO), [77] ITO/Ag/ITO multilayer [78] and ZnS/Ag/ZnS multilayer [79]. Shang et al. [8] recently reported a flexible HfO<sub>x</sub> resistive switching device with ITO as both top and bottom electrodes, which exhibited good optical transmittance of over 75% in the visible region. Other flexible electrode materials may include carbon, [35] PEDOT:PSS [33] and p-Si [52]. The former two enable related flexible resistive switching memories to be fabricated by low-cost all-printing approaches, while p-Si can make related flexible resistive switching memories to show a self-rectifying resistive switching behavior with natural immunity to the annoying sneak-path issue.

### **2.3. Substrate Materials**

To fabricate flexible resistive switching memories, substrates that are to replace plate glass substrates must meet requirements including minimized surface roughness, thermal and thermomechanical stability, chemical inertness, and the most important of all, mechanical flexibility. Comparatively, polymers with high intrinsic flexibility, such as parylene, [57] PI, [53] PEN, [66] PES, [32] PET [16] and PDMS [50], are certainly

the most popular substrate materials. For example, with PEN as the substrate, Ji et al. [66] fabricated a flexible crossbar resistive switching memory array, which can work properly after being rolled with 3.4 mm radius and even being twisted with a maximum angle of 30°. Metal substrates including Al foil, [22] Cu foil [16] and stainless steel [40] are frequently used as well. Due to their high intrinsic conductivity, they can act as the substrate and bottom electrode simultaneously, e.g., in the flexible Ag/hBN/Cu foil resistive switching device [16]. Mica [49] and paper [35] are also employed as flexible substrates for resistive switching memories. For instance, the use of mica as the flexible substrate enables resistive switching memories to be fabricated under high temperature and thus exhibit good thermal stability, while paper substrates make resistive switching memories physical transient when being subject to heat/fire and wetness for security purposes.

### **3. DEVICE FABRICATION TECHNOLOGIES AND PERFORMANCE**

As typical thin-film electronic devices, the fabrication of flexible resistive switching memories depends mainly on various thin-film deposition methods, including thermal evaporation, [55, 80] magnetron sputtering, [8, 12] spin-coating, [63, 66] inkjet printing, [35, 76] and so on. These methods can be roughly grouped into vapor-based approaches including thermal evaporation and magnetron sputtering, and solution-type methods such as spin-coating and inkjet printing. Generally, vapor-type methods are more mature and compatible with the standard CMOS process, while solution-type methods stand out in terms of simple fabrication and low cost. In this section, flexible resistive switching memories fabricated by all-vapor methods, vapor-solution hybrid methods and even all-solution methods will be discussed separately and thoroughly, with a particular emphasis on device performances under bending conditions.

### 3.1. All-Vapor Methods

Since vapor-type thin-film deposition methods are more mature and compatible with the standard CMOS process, the research in fabricating flexible resistive switching memories by all-vapor methods is certainly of great significance and has aroused extensive attention throughout. To date, a large number of flexible resistive switching memories have been fabricated by all-vapor methods, most of which are inorganic (e.g., IZO/Al<sub>2</sub>O<sub>3</sub>/IZO/PET, [12] Ag/hBN/ITO/PET, [16] ITO/HfO<sub>x</sub>/ITO/PET [8] and Au/BTCO/SRO/mica [49]) while only a few organic examples such as Al/parylene/W/parylene [57] and Cu/pEGDMA/ITO/PET [58]. The involved deposition methods for switching layers include mainly atomic layer deposition (ALD), [36] chemical vapor deposition (CVD), [16] radio frequency (RF) magnetron sputtering, [8] pulsed laser deposition (PLD) [49] and plasma oxidation, [38] while that for electrodes are mostly thermal evaporation, [58] electron beam evaporation, [16] direct current (DC) magnetron sputtering [45] and also PLD [8].

Shang et al. [8] recently reported a flexible and even transparent ITO/HfO<sub>x</sub>/ITO/PET resistive switching device with superior electrical, thermal and mechanical performances, as shown in Figure 4a–h. To fabricate the device, a commercially available ITO/PET substrate was adopted, and the HfO<sub>x</sub> switching layer was deposited on it by RF magnetron sputtering, followed by covering the ITO top electrode by PLD. It is noted that the microstructure of the HfO<sub>x</sub> switching layer was intentionally designed to be mixed amorphous-nanocrystalline to guarantee better resistive switching performance, as revealed previously in Figure 2a–b.

Basically, the device shows good optical transmittance of over 75% in the visible region and superior bipolar resistive switching performances including uniform switching parameters (operation voltages:  $V_{\text{SET}}$  and  $V_{\text{RESET}}$ ; state resistances:  $R_{\text{ON}}$  and  $R_{\text{OFF}}$ ), stable data retention of 10 years, switching endurance up to  $10^8$  cycles and a large working temperature range of 170~370 K (Figure 4a–f). With a bending radius of  $\geq 5$  mm, corresponding to a bending strain of  $\leq 1.27\%$ , switching performance of the

device is found to be scarcely affected, even after 1200 bending cycles, as demonstrated in Figure 4g–h.

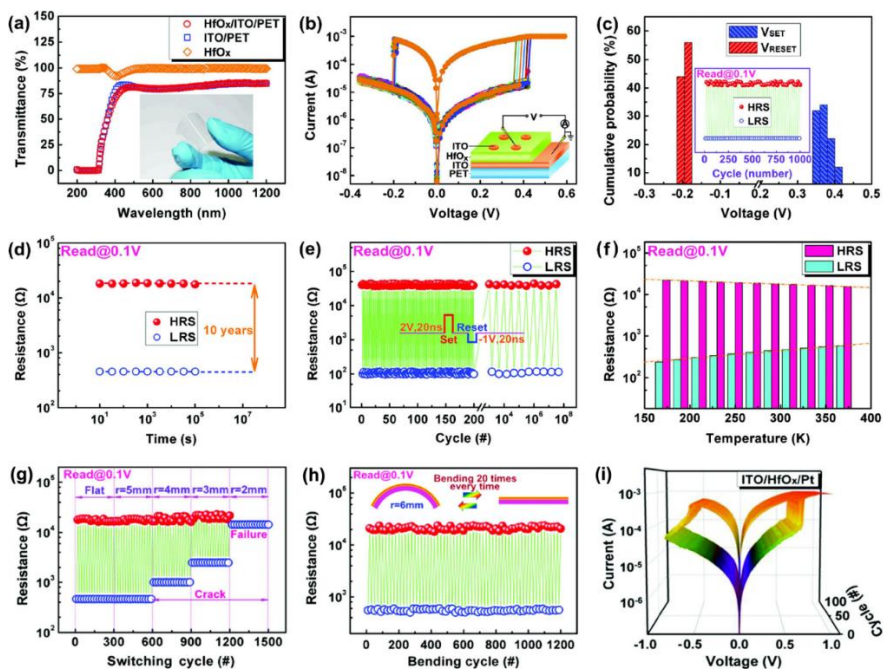


Figure 4. Switching performances of (a–h) the flexible and transparent ITO/HfO<sub>x</sub>/ITO/PET resistive switching device and (i) the flexible ITO/HfO<sub>x</sub>/Pt/PET resistive switching device. (a) Optical transmittance of the ITO/HfO<sub>x</sub>/ITO/PET device. Inset: Digital image of the device under bending. (b)  $I$ - $V$  characteristic of the ITO/HfO<sub>x</sub>/ITO/PET device in the flat state over 1000 consecutive switching cycles at room temperature. Inset: Schematic device structure with measurement configuration. (c) Cumulative probabilities of  $V_{\text{SET}}$  and  $V_{\text{RESET}}$ . Inset: The uniform distribution of  $R_{\text{ON}}$  and  $R_{\text{OFF}}$ . The data sets were retrieved from the  $I$ - $V$  curves in (b). (d) Room temperature retention characteristic of the ITO/HfO<sub>x</sub>/ITO/PET device in the flat state. (e) Endurance performance of the ITO/HfO<sub>x</sub>/ITO/PET device in the flat state with pulse-mode operation. (f) Evolution characteristics of  $R_{\text{ON}}$  and  $R_{\text{OFF}}$  of the ITO/HfO<sub>x</sub>/ITO/PET device in the flat state against working temperature. (g) Evolution characteristics of  $R_{\text{ON}}$  and  $R_{\text{OFF}}$  of the ITO/HfO<sub>x</sub>/ITO/PET device against the bending radius. (h) Continuous bending fatigue test of the ITO/HfO<sub>x</sub>/ITO/PET device with a radius of 6 mm for 1200 cycles. (i)  $I$ - $V$  characteristic of the ITO/HfO<sub>x</sub>/Pt/PET device at a bending radius of 2 mm. Reproduced with permission from Ref. 8. Copyright © 2017, The Royal Society of Chemistry.



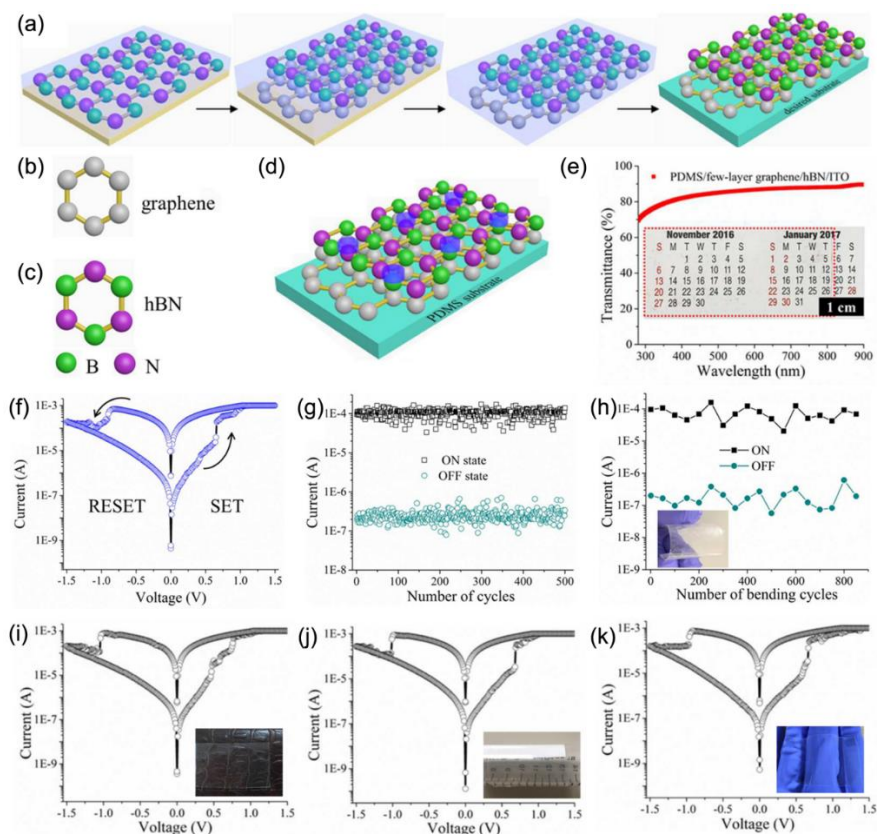


Figure 5. Switching performance of the flexible and transferable ITO/hBN/FLG/PDMS resistive switching device. (a) Schematic device fabrication process on any desired substrate. (b) and (c) are the chemical structures of graphene for the bottom electrode and hBN for the switching layer, respectively. (d) Schematic of the device on a soft PDMS substrate. (e) Optical transmittance of the device. The inset shows the actual memory device (highlighted by the closed region), indicating transparent characteristics. (f)  $I$ - $V$  characteristic of the device in the flat state after electroforming process. (g) 500 consecutive switching cycles of the device in the flat state. (h) Bending test of the device with 14 mm radius. Inset: Actual transparent flexible ITO/hBN/FLG/PDMS device on a PET substrate. Switching characteristics of the ITO/hBN/FLG/PDMS memory labels tagged on (i) a rough and soft wallet and (j) a centrifuge tube with  $\sim 8$  mm radius, and (k) attached onto fingers. Reproduced with permission from Ref. 50. Copyright © 2017, American Chemical Society.

If the bending radius is further decreased, the memory window of the device starts to deteriorate and finally disappears at 2 mm bending radius (Figure 4g). This was attributed to the formation of cracks in the ITO

bottom electrode, rather than in the  $\text{HfO}_x$  switching layer. After replacing the ITO bottom electrode with more durable Pt deposited by RF magnetron sputtering, highly stable bipolar resistive switching behavior can be observed even at a bending radius as small as 2 mm, as confirmed in Figure 4i. These results demonstrate that with careful design of the microstructure and structure of devices, it is possible to fabricate high-performance flexible resistive switching memories by all-vapor methods.

For more realistic applications, the fabrication of flexible resistive switching memories on arbitrary nonconventional substrates (for example, soft and non-planar ones) is highly desired. However, for common oxide switching layers and metal electrodes, the detachment phenomenon under repetitive bending or strain conditions is very significant due to their poor adhesion property. To solve this issue, Qian et al. [50] recently proposed and demonstrated a flexible ITO/hBN/FLG/PDMS resistive switching device that can be transferred to arbitrary substrates without performance degradation, as shown in Figure 5. The key point is to use hBN as the switching layer, few-layer graphene (FLG) as the bottom electrode and PDMS as the substrate, wherein hBN and FLG are intrinsic 2D materials with good adhesion properties and PDMS is a typical soft substrate. The detailed device fabrication process is schematically illustrated in Figure 5a–d. In short, the  $\sim 5$  nm CVD-deposited hBN switching layer was first transferred to a commercially available FLG/Cu foil substrate via a conventional wet transfer approach. Then the hBN/FLG bilayer was transferred to the desired PDMS substrate after Cu foil etching by an ammonia persulfate solution. Finally, the ITO top electrode with a diameter of  $\sim 250$   $\mu\text{m}$  was covered by RF magnetron sputtering with the help of a hard shadow mask. Figure 3e demonstrates that the device has good optical transmittance of  $\sim 85\%$  over the visible wavelength range. For switching performance, the device shows steady bipolar resistive switching behavior during 500 operation cycles in the flat state and little memory window degradation during 850 bending cycles with a 14 mm radius (Figure 5f–h). More importantly, after the device was stuck onto a rough and soft wallet (flat surface, Figure 5i), a centrifuge tube ( $\sim 8$  mm radius, Figure 5j) or even fingers (Figure 5k), it was still completely switchable

and operated normally. These results demonstrate that the flexible ITO/hBN/FLG/PDMS resistive switching device can conform to various objects with robust operation and reliable switching characteristics, promising an opportunity for epidermal electronics applications.

The application of flexible resistive switching memories in harsh environments such as photon radiation and high temperature is an emerging and important research topic. Apparently, conventional flexible resistive switching memories with organic substrates and low-temperature fabrication are insufficient for such application. As a preliminary attempt, Yang et al. [49] recently demonstrated a flexible Au/BaTi<sub>0.95</sub>Co<sub>0.05</sub>O<sub>3</sub> (BTCO)/SrRuO<sub>3</sub>(SRO)/mica resistive switching device. To fabricate the device, a 10 μm-thick mica substrate was first separated from fluorocrystal mica (AlF<sub>2</sub>O<sub>10</sub>Si<sub>33</sub>Mg) by mechanical exfoliation. Then the BTCO/SRO bilayer was grown on the mica substrate by PLD at 680°C and 1 Pa oxygen pressure. The BTCO/SRO/mica tri-layer structure is semitransparent in the visible region. Finally, the Au top electrode was also covered by PLD but at 25°C and 10<sup>-4</sup> Pa oxygen pressure. In the flat state, the device shows stable bipolar resistive switching behavior with endurance up to 10<sup>5</sup> cycles and data retention over 2 × 10<sup>4</sup> s. At a 2.2 mm bending radius or after 10,000 bending cycles with 3 mm radius, there is almost no degradation in device performance. More importantly, even at a 2.2 mm bending radius, the device can work properly under visible photon radiation of 150 mW/cm<sup>2</sup> and between 25~180°C or even after being annealed at 500°C. These results suggest that the Au/BTCO/SRO/mica resistive switching device is very promising for wide use in wearable devices, flexible display screens, and so on.

### **3.2. Vapor-Solution Hybrid Methods**

Normally, electrodes deposited by vapor-type methods have higher conductivity and adhesion properties, while switching layers deposited by solution-type methods have huge advantages such as simple fabrication and low cost.

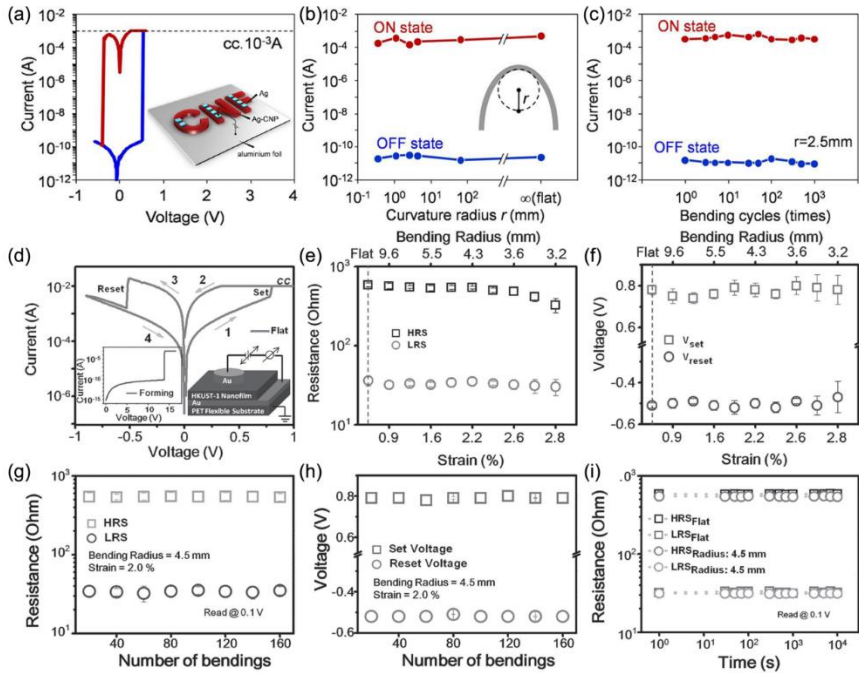


Figure 6. Switching performances of flexible (a–c) Ag/cellulose:Ag/Al foil and (d–i) Au/HKUST-1/Au/PET resistive switching devices. (a)  $I$ - $V$  characteristic of the Ag/cellulose:Ag/Al foil device in the flat state. Inset: Schematic device structure. Current evolution characteristics of ON and OFF states of the Ag/cellulose:Ag/Al foil device against (b) strain level and (c) bending cycle with a 2.5 mm radius. Reproduced with permission from Ref. 22. Copyright © 2014, Macmillan Publishers Limited, part of Springer Nature. (d)  $I$ - $V$  characteristics of the Au/HKUST-1/Au/PET device in the flat state. Insets: Forming process and schematic configuration of the device. Evolution characteristics of (e)  $R_{ON}$  and  $R_{OFF}$  and (f)  $V_{set}$  and  $V_{reset}$  of the Au/HKUST-1/Au/PET device against the bending radius. Evolution characteristics of (g)  $R_{ON}$  and  $R_{OFF}$  and (h)  $V_{set}$  and  $V_{reset}$  of the Au/HKUST-1/Au/PET device against the bending cycle. (i) Retention characteristic of the Au/HKUST-1/Au/PET device under bending. The data in (g–i) were all collected at 4.5 mm bending radius, corresponding to a strain level of about 2.0%. Reproduced with permission from Ref. 74. Copyright © 2015, WILEY-VCH Verlag GmbH & Co. KGaA, Weinheim, Germany.

To combine these two points together, a large number of flexible resistive switching memories have been fabricated by vapor-solution hybrid methods. The involved vapor-type methods are mainly DC and RF magnetron sputtering, [13, 22, 76] thermal evaporation [15, 66] and electron beam evaporation [63] for metal electrodes and CVD for graphene

electrode, [64] whereas the involved solution-type methods for switching layers are mostly spin coating, [63, 66] drop casting, [22] spray coating, [81] inkjet printing [76] and liquid phase epitaxy [74]. With these solution-type methods, organic materials (e.g., Alq<sub>3</sub>, [18] egg albumen, [82] GO, [55] PS:PCBM, [66] PMMA:P3HT, [64] cellulose:Ag, [22] PMMA:Fe<sub>3</sub>O<sub>4</sub> [80] and HKUST-1 [74]) have become the dominating material for switching layers. Many flexible resistive switching memories with superior device performance under bending have been demonstrated using vapor-solution hybrid methods. Nagashima et al. [22] reported a flexible Ag/cellulose:Ag/Al foil resistive switching device that can work properly at a record low bending radius of 350 μm, as shown in Figure 6a–b. The cellulose:Ag switching layer and the Ag top electrode were deposited by drop casting and sputtering, respectively. Such high bending tolerance of the device was attributed by the authors to the small width (4 nm) of cellulose nanofibers and network structure in the cellulose:Ag switching layer. Moreover, the device shows almost no degradation in the memory window after 10<sup>3</sup> bending cycles with 2.5 mm radius, as demonstrated in Figure 6c. On the other hand, Pan et al. [74] reported a flexible Au/HKUST-1/Au/PET resistive switching device that can work properly under a strain of as high as 2.8%, as shown in Figure 6d–f. The HKUST-1 switching layer and the Au top and bottom electrodes were deposited by liquid phase epitaxy and sputtering, respectively. Under a strain level of about 2.0%, the device shows no degradation in  $R_{ON}$ ,  $R_{OFF}$ ,  $V_{set}$  and  $V_{reset}$  after 160 bending cycles and stable data retention of >10<sup>4</sup> s, as confirmed in Figure 6g–i. Also, excellent switching endurance of >10<sup>7</sup> cycles has been demonstrated at such strain level, as shown previously in Figure 3d. Such high device performance under bending was attributed by the authors to the peculiar metal-organic framework structure of HKUST-1 that can possess the features of both inorganic and organic materials.

With vapor-solution hybrid methods, the fabrication process of flexible and transferable resistive switching memories can be greatly simplified. This is because the adopted organic switching layers can directly act as the protecting layer during transfer process, [64, 80, 82] while for devices fabricated by all-vapor methods, an additional organic protecting layer has

to be deposited before and removed after the transfer process [50]. Lin et al. [80] recently reported a flexible and transferable resistive switching device with a spin-coated PMMA:Fe<sub>3</sub>O<sub>4</sub> layer acting as the switching and protecting layers simultaneously, as shown in Figure 7a. The bottom and top electrodes of the device are both thermally evaporated Al. After being transferred onto a PET substrate, the device shows very stable bipolar resistive switching behavior with a high memory window of  $\sim 10^5$ , before and after being bended from 2-cm-long flat state to lengths of 1.6, 1.2, 0.8 and 0.4 cm even up to  $10^4$  cycles, as demonstrated in Figure 7b–d. More importantly, the device shows almost similar resistive switching behavior after being transferred onto a flexible printing paper, a glass dome hemisphere with a 3-D surface, a PDMS substrate and second transfer on to a latex glove, and even a pectin substrate and then onto skin (Figure 7e–h), indicating very high transfer performance. Similarly, Lai et al. [64] and Zhu et al. [82] succeeded in the fabrication of flexible and transferable Al/PMMA:P3HT/graphene and Ag/egg albumen/Al resistive switching devices with high performance, respectively. All these results demonstrate the easy fabrication of high-performance flexible and transferable resistive switching memories by vapor-solution hybrid methods.

The vapor-solution hybrid methods have also been demonstrated as the optimal approach for fabricating high-performance flexible crossbar resistive switching memory arrays with integrated selection devices. For realistic applications, the integration of selection devices such as transistors and diodes is indispensable to settle the sneak-path issue that can lead to serious misreading problems [4, 83]. Unfortunately, inorganic flexible crossbar resistive switching memory arrays with a one transistor-one resistor (1T1R) or a one diode-one resistor (1D1R) integration architecture by all-vapor methods are poor in bending performance, showing a bending radius of no less than 8.4 mm and strain no larger than 0.25% [36, 38].

To make a breakthrough, Ji et al. [66] proposed and fabricated an organic flexible crossbar resistive switching memory array with a 1D1R integration architecture by the vapor-solution hybrid method, where the diode and memory stacks are Au/P3HT/Al and Al/PS:PCBM/Al, respectively. The P3HT and PS:PCBM functional layers were both

deposited by spin coating, with all metal layers by thermal evaporation. They found that the memory cells in the integrated Au/P3HT/Al/PS:PCBM/Al 1D1R array on a flexible PEN substrate can work properly with a superposed  $I$ - $V$  characteristic of discrete Au/P3HT/Al diode and Al/PS:PCBM/Al memory cells, as shown in Figure 8a-c.

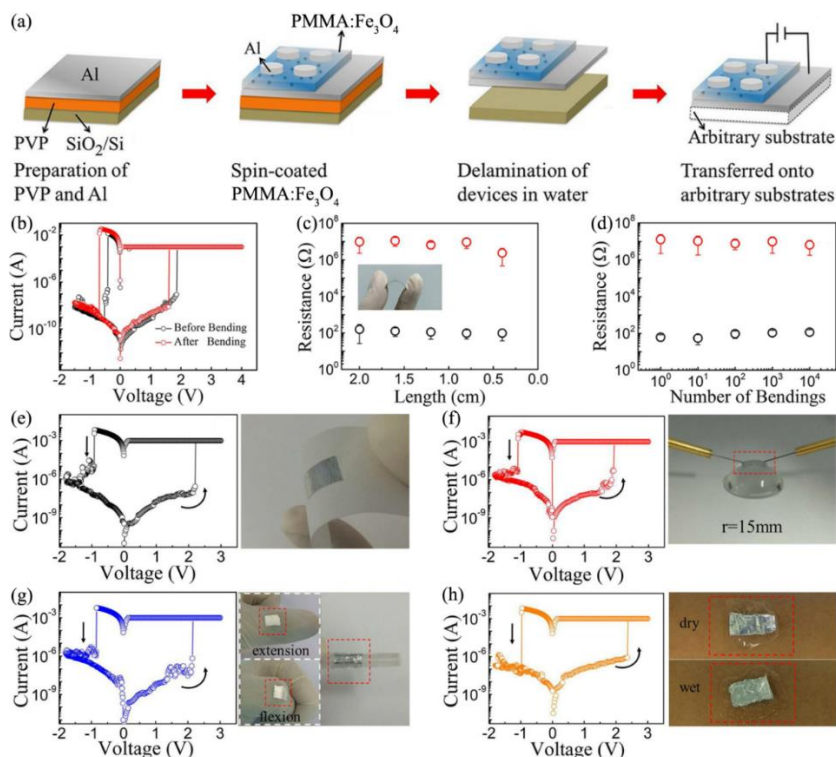


Figure 7. Switching performance of the flexible and transferable Al/PMMA:Fe<sub>3</sub>O<sub>4</sub>/Al resistive switching device. (a) Schematic device fabrication process by transfer approach. (b)  $I$ - $V$  characteristics of the device on a PET substrate before and after  $10^4$  bending cycles. Evolution characteristics of  $R_{ON}$  and  $R_{OFF}$  of the device on a PET substrate against (c) the bending length and (d) the bending cycle. Inset in (b): Optical image of device on a PET substrate under bending. Demonstrations of the device stuck onto various nonconventional substrates with the corresponding  $I$ - $V$  characteristics alongside, including (e) a flexible printing paper, (f) a glass dome hemisphere with a 3-D surface, (g) a PDMS substrate and second transfer on to a latex glove, and (h) a pectin substrate and then onto skin. Reproduced with permission from Ref. 80. Copyright © 2017, AIP Publishing LLC.

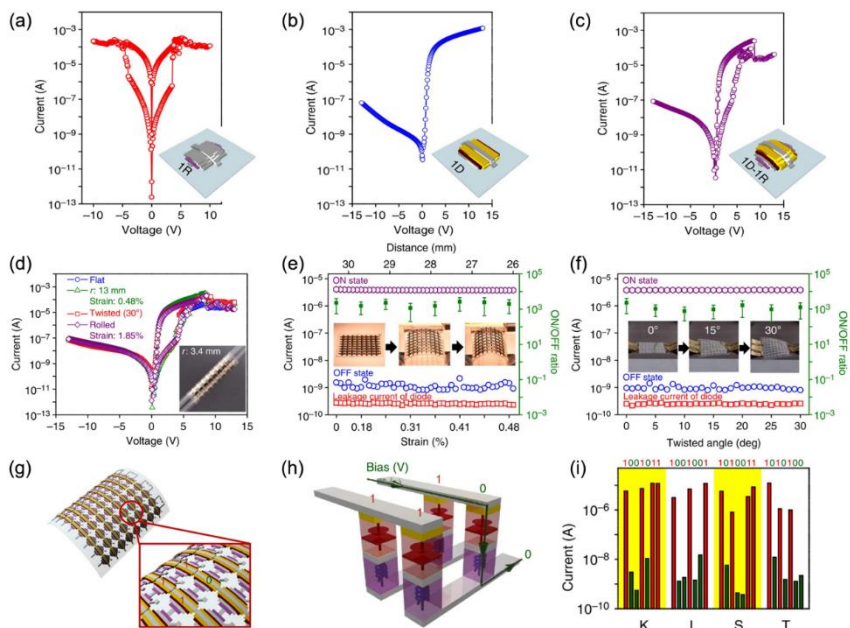


Figure 8. Switching performance of the flexible Au/P3HT/Al/PS:PCBM/Al/PEN 1D1R resistive switching device.  $I$ - $V$  characteristics of (a) 1R, (b) 1D and (c) integrated 1D1R devices. (d)  $I$ - $V$  characteristics of the 1D1R device before and after being bended, twisted and rolled. Inset: Optical image of the device being rolled. Evolution characteristics of ON state current, OFF state current, ON/OFF current ratio and reverse leakage current of the 1D1R device against (e) strain level and (f) twist angle. Inset in (e): Optical images of the device under various bending conditions. Inset in (f): Optical images of the device under various twist angles. (g) Programmed current states of four 1D1R cells in the  $8 \times 8$  crossbar array. (h) Current path through the four programmed 1D1R cells. (i) The output currents histogram exhibiting the letter 'KIST' by standard ASCII characters within the  $8 \times 8$  1D1R crossbar array. Reproduced with permission from Ref. 66. Copyright © 2013, Macmillan Publishers Limited, part of Springer Nature.

More importantly, the cells show no degradation in switching performance even under bending with a 3.4 mm radius (corresponding to a large strain of 1.85%) or under a  $30^\circ$  twisting, as demonstrated in Figure 8d–f. Also, as expected, the sneak-path issue has been successfully settled in the fabricated flexible 1D1R crossbar array (Figure 8g–i). More interestingly, Nau et al. [18] recently reported the integration of Al/Ca/rr-P3HT:PCBM/ITO photodiodes with Ag/Alq<sub>3</sub>/Ag/Al resistive switching memory cells by vapor-solution hybrid methods, leading to a Ag/Alq<sub>3</sub>/Ag/



Al/Ca/r-P3HT:PCBM/ITO 1D1R crossbar array able to detect and store image information simultaneously.

### 3.3. All-Solution Methods

With unparalleled advantages of simple fabrication and low cost, the fabrication of flexible resistive switching memories by all-solution methods is increasingly attractive in the past few years. The involved solution-type methods include inkjet printing, [30, 33, 35] screen printing, [30, 35] electrohydrodynamic (EDH) printing, [23, 69] reverse offset printing, [69] Langmuir-Blodgett method, [30] etc. With these methods, a lot of flexible resistive switching memories have been fabricated thus far, which can be roughly grouped into two types based on switching layer materials.

The first type refers to flexible resistive switching memories with inorganic switching layers such as  $\text{TiO}_2$ , [35]  $\text{ZrO}_2$ , [84]  $\text{MoO}_x/\text{MoS}_2$ , [30]  $\text{WO}_x/\text{WS}_2$  [30] and spin-on-glass [33]. Bessonov et al. [30] reported a flexible and multifunctional  $\text{Ag}/\text{MoO}_x/\text{MoS}_2/\text{Ag}/\text{PEN}$  resistive switching device, as shown in Figure 9a–f. The  $\text{MoO}_x/\text{MoS}_2$  switching layer was fabricated by the Langmuir-Blodgett method with post-oxidation in air, while the Ag bottom and top electrodes were deposited by screen printing and inkjet printing, respectively. In the flat state, the device shows stable bipolar resistive switching behavior with a high ON/OFF ratio of  $>10^4$  and a low operation voltage of  $<0.2$  V (Figure 9a), accompanied by remarkable memcapacitive characteristics (Figure 9b) and a frequency-dependent memory window (Figure 9c) which can be used for applications in advanced computer logic and non-volatile memory. Also, synaptic short-term and long-term potentiation (STP and LTP) behaviors have been mimicked using this device (Figure 9d–e). More importantly, the device shows no performance degradation during repeated bending up to 10,000 times with 10 mm radius (Figure 9f), which is highly promising for flexible memory application.

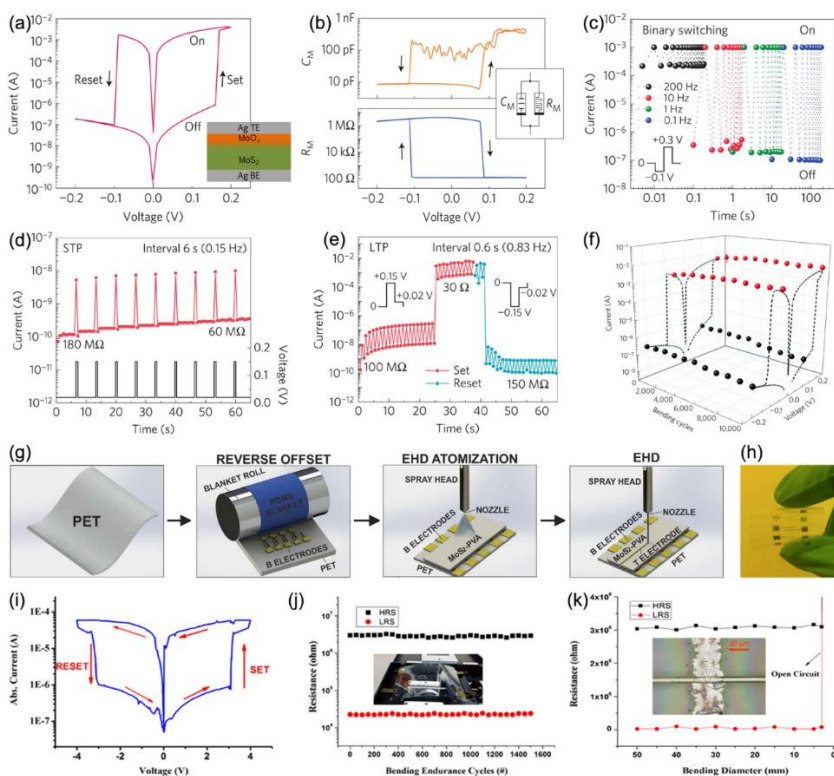


Figure 9. Switching performances of flexible (a–f) Ag/MoO<sub>x</sub>/MoS<sub>2</sub>/Ag/PEN and (g–k) Ag/PVA:MoS<sub>2</sub>/Ag/PET resistive switching devices. (a)  $I$ – $V$  characteristic, (b) memcapacitive characteristic and (c) frequency-dependent switching of the Ag/MoO<sub>x</sub>/MoS<sub>2</sub>/Ag/PEN device. Inset in (a): Schematic device structure. Demonstration of synaptic (d) STP and (e) LTP functions based on the Ag/MoO<sub>x</sub>/MoS<sub>2</sub>/Ag/PEN device. (f)  $I$ – $V$  characteristic evolution of the Ag/MoO<sub>x</sub>/MoS<sub>2</sub>/Ag/PEN device against the bending cycle with 10 mm radius with permission from Ref. 30. Copyright © 2014, Macmillan Publishers Limited, part of Springer Nature. (g) Schematic fabrication process of the Ag/PVA:MoS<sub>2</sub>/Ag/PET device by all-printing approach. (h) Optical image and (i)  $I$ – $V$  characteristic of the Ag/PVA:MoS<sub>2</sub>/Ag/PET device. Evolution characteristics of  $R_{ON}$  and  $R_{OFF}$  of the Ag/PVA:MoS<sub>2</sub>/Ag/PET device against (j) the bending cycle with a 5 mm radius and (k) the bending diameter. Inset in (j): Optical image of the device in a bending machine. Inset in (k): Optical image of the open circuit device by bending to 1 mm radius, exhibiting clearly the crack-induced broken electrodes. Reproduced with permission from Ref. 69. Copyright © 2016, Macmillan Publishers Limited, part of Springer Nature.

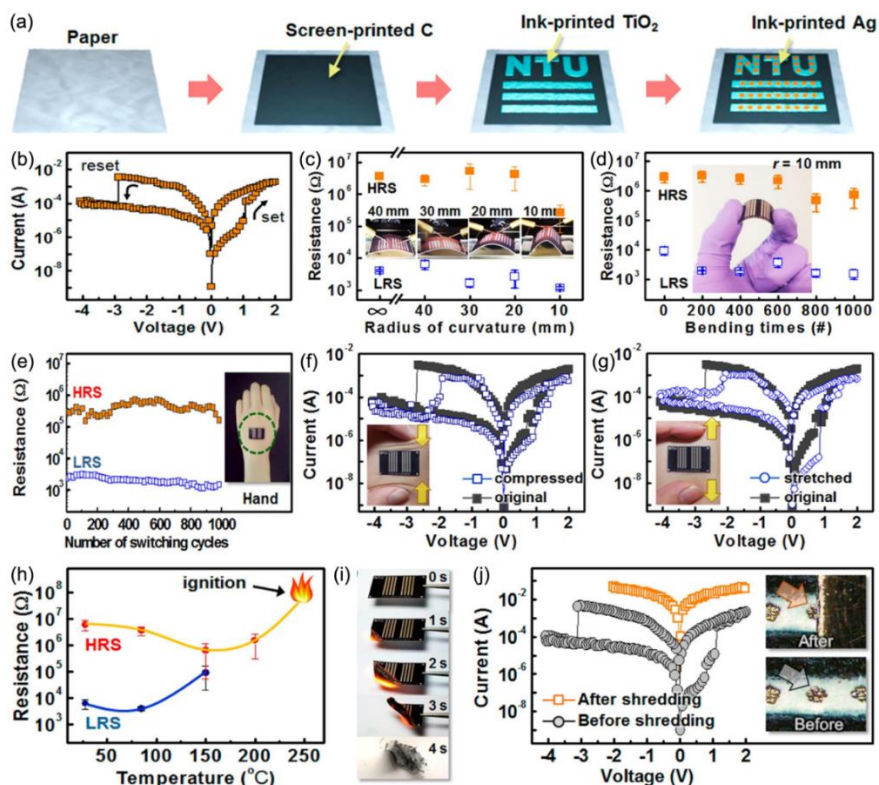


Figure 10. Switching performance of the flexible Ag/TiO<sub>2</sub>/C/paper resistive switching device. (a) Schematic device fabrication process by an all-printing approach. (b)  $I$ - $V$  characteristic of the device in the flat state. Evolution characteristics of  $R_{ON}$  and  $R_{OFF}$  of the device against (c) the bending radius and (d) the bending cycle with a 10 mm radius. Inset in (c): Optical images of the device under various bending conditions. (e) Endurance of the device on undeformed skin of the human body.  $I$ - $V$  characteristics of the device on (f) compressed and (g) stretched skin of the human body. (h) Evolution characteristics of  $R_{ON}$  and  $R_{OFF}$  of the device against environmental temperature. (i) Sequence of pictures showing the ignition process of the device at 250°C within 4 s, leading to permanent data removal. (j)  $I$ - $V$  characteristics of the device before and after being shredded and the corresponding optical microscopy images. Reproduced with permission from Ref. 35. Copyright © 2014, American Chemical Society.

The other type refers to flexible resistive switching memories with organic-inorganic composite switching layers such as PVA:MoS<sub>2</sub>, [69] PVOH:hBN [23] and PVOH-ZnSnO<sub>3</sub> [70]. Rehman et al. [69] reported a flexible Ag/PVA:MoS<sub>2</sub>/Ag/PET resistive switching device fabricated by the all-printing approach, as shown in Figure 9g-k. The Ag bottom

electrode, PVA:MoS<sub>2</sub> switching layer and Ag top electrode were deposited in sequence by reverse offset printing, EDH atomization printing and EDH patterning printing, respectively (Figure 9g–h). The device can exhibit stable bipolar resistive switching behavior even after 1,500 bending cycles with a 5 mm radius or when being bended with a >1 mm radius (Figure 9i–k). If further bended to a  $\leq 1$  mm radius, the device will fail with an open circuit state due to crack-induced breakage of top and bottom Ag electrodes, as shown by the inset in Figure 9k.

With all-solution methods (more precisely, all-printing approaches), the fabrication cost of flexible resistive switching memories can be further reduced by the use of paper as substrates [35]. Since paper substrates are rough and porous due to their fibrous nature, they are not compatible with the conventional physical and chemical vapor deposition methods [85]. Besides lower cost, paper substrates are also foldable, retrievable, disposable and even biodegradable [85]. Lien et al. [35] fabricated a flexible Ag/TiO<sub>2</sub>/C/paper resistive switching device by the combination of screen and inkjet printing techniques, as shown in Figure 10a. The device can exhibit stable bipolar resistive switching behavior when bended with a  $\geq 10$  mm radius or even after 1000 bending cycles with 10 mm radius (Figure 10b–d). Also, the device can work properly after stuck onto undeformed, compressed and stretched skin of the human body (Figure 10e–g). More importantly, the device can be burned off easily by being lit with a match or heated over 250°C (Figure 10h–i), leading the stored data to be eliminated totally and irreversibly. Alternatively, the stored data can be destroyed by simply shredding the device, as confirmed in Figure 10j.

#### **4. CHALLENGES AND PROSPECTS**

Due to the great efforts devoted by scientists all around the world in the past decade, significant progress has been made in the field flexible resistive switching memories thus far. Nevertheless, the commercialization of flexible resistive switching memories still faces some serious

challenges. First, a thorough understanding of the dependence of device bendability on switching mechanisms (for example, ion migration *vs.* charge trapping/de-trapping) and device structures (for instance, vertical *vs.* planar) is urgently needed. Such knowledge will be highly beneficial to the performance optimization of flexible resistive switching memories in the future. It is also necessary to introduce organic electrodes into flexible resistive switching memories, as the inorganic electrodes have been demonstrated as the main limit for device performance when working under severe bending conditions [8, 69]. Finally, studies of flexible resistive switching memories under twisting and stretching conditions deserve much attention, because real application environments of flexible electronic devices are usually more complex than being only bended. With all these challenges resolved, flexible resistive switching memories will certainly be a popular component in our day-to-day flexible electronic devices in the near future. In addition, further research of flexible resistive switching memories for novel logic-in-memory and synaptic emulation applications should be investigated, as this could lead to a great revolution in computing architecture [29, 31].

## REFERENCES

- [1] Han, S. T., Peng, H., Sun, Q., Venkatesh, S., Chung, K. S., Lau, S. C., Zhou, Y., Roy, V. A. L. *Adv. Mater.* 2017, 29, 1700375.
- [2] Liu, Y., Pharr, M., Salvatore, G. A. *ACS Nano* 2017, 11, 9614-9635.
- [3] Ghoneim, M., Hussain, M. *Electronics* 2015, 4, 424-479.
- [4] Pan, F., Gao, S., Chen, C., Song, C., Zeng, F. *Mater. Sci. Eng. R* 2014, 83, 1-59.
- [5] Yang, Y., Gao, P., Gaba, S., Chang, T., Pan, X., Lu, W. *Nat. Commun.* 2012, 3, 732.
- [6] Gao, S., Song, C., Chen, C., Zeng, F., Pan, F. *J. Phys. Chem. C* 2012, 116, 17955-17959.
- [7] Gao, S., Zeng, F., Li, F., Wang, M., Mao, H., Wang, G., Song, C., Pan, F. *Nanoscale* 2015, 7, 6031-6038.

- [8] Shang, J., Xue, W., Ji, Z., Liu, G., Niu, X., Yi, X., Pan, L., Zhan, Q., Xu, X. H., Li, R. W. *Nanoscale* 2017, 9, 7037-7046.
- [9] Hwang, S. K., Lee, J. M., Kim, S., Park, J. S., Park, H. I., Ahn, C. W., Lee, K. J., Lee, T., Kim, S. O. *Nano Lett.* 2012, 12, 2217-2221.
- [10] Tan, H., Liu, G., Zhu, X., Yang, H., Chen, B., Chen, X., Shang, J., Lu, W. D., Wu, Y., Li, R. W. *Adv. Mater.* 2015, 27, 2797-2803.
- [11] Chen, J. Y., Hsin, C. L., Huang, C. W., Chiu, C. H., Huang, Y. T., Lin, S. J., Wu, W. W., Chen, L. J. *Nano Lett.* 2013, 13, 3671-3677.
- [12] Yeom, S. W., Shin, S. C., Kim, T. Y., Ha, H. J., Lee, Y. H., Shim, J. W., Ju, B. K. *Nanotechnology* 2016, 27, 07LT01.
- [13] Kim, S., Son, J. H., Lee, S. H., You, B. K., Park, K. I., Lee, H. K., Byun, M., Lee, K. J. *Adv. Mater.* 2014, 26, 7480-7487.
- [14] Ji, Y., Yang, Y., Lee, S. K., Ruan, G., Kim, T. W., Fei, H., Lee, S. H., Kim, D. Y., Yoon, J., Tour, J. M. *ACS Nano* 2016, 10, 7598-7603.
- [15] Jang, J., Pan, F., Braam, K., Subramanian, V. *Adv. Mater.* 2012, 24, 3573-3576.
- [16] Qian, K., Tay, R. Y., Nguyen, V. C., Wang, J., Cai, G., Chen, T., Teo, E. H. T., Lee, P. S. *Adv. Funct. Mater.* 2016, 26, 2176-2184.
- [17] Zhao, F., Cheng, H., Hu, Y., Song, L., Zhang, Z., Jiang, L., Qu, L. *Sci. Rep.* 2014, 4, 5882.
- [18] Nau, S., Wolf, C., Sax, S., List-Kratochvil, E. J. W. *Adv. Mater.* 2015, 27, 1048-1052.
- [19] Hosseini, N. R., Lee, J. S. *Adv. Funct. Mater.* 2015, 25, 5586-5592.
- [20] Jang, B. C., Seong, H., Kim, S. K., Kim, J. Y., Koo, B. J., Choi, J., Yang, S. Y., Im, S. G., Choi, S. Y. *ACS Appl. Mater. Interfaces* 2016, 8, 12951-12958.
- [21] Son, D. I., Kim, T. W., Shim, J. H., Jung, J. H., Lee, D. U., Lee, J. M., Park, W. I., Choi, W. K. *Nano Lett.* 2010, 10, 2441-2447.
- [22] Nagashima, K., Koga, H., Celano, U., Zhuge, F., Kanai, M., Rahong, S., Meng, G., He, Y., De Boeck, J., Jurczak, M., Vandervorst, W., Kitaoka, T., Nogi, M., Yanagida, T. *Sci. Rep.* 2014, 4, 5532.
- [23] Siddiqui, G. U., Rehman, M. M., Yang, Y. J., Choi, K. H. *J. Mater. Chem. C* 2017, 5, 862-871.

- [24] Tsai, C. L., Xiong, F., Pop, E., Shim, M. *ACS Nano* 2013, 7, 5360-5366.
- [25] Torrezan, A. C., Strachan, J. P., Medeiros-Ribeiro, G., Williams, R. S. *Nanotechnology* 2011, 22, 485203.
- [26] Lee, M. J., Lee, C. B., Lee, D., Lee, S. R., Chang, M., Hur, J. H., Kim, Y. B., Kim, C. J., Seo, D. H., Seo, S., Chung, U. I., Yoo, I. K., Kim, K. *Nat. Mater.* 2011, 10, 625- 630.
- [27] Han, S. T., Zhou, Y., Roy, V. A. L. *Adv. Mater.* 2013, 25, 5425-5449.
- [28] Kang, D. H., Choi, W. Y., Woo, H., Jang, S., Park, H. Y., Shim, J., Choi, J. W., Kim, S., Jeon, S., Lee, S., Park, J. H. *ACS Appl. Mater. Interfaces* 2017, 9, 27073-27082.
- [29] Jang, B. C., Yang, S. Y., Seong, H., Kim, S. K., Choi, J., Im, S. G., Choi, S. Y. *Nano Res.* 2017, 10, 2459-2470.
- [30] Bessonov, A. A., Kirikova, M. N., Petukhov, D. I., Allen, M., Ryhänen, T., Bailey, M. J. A. *Nat. Mater.* 2014, 14, 199-204.
- [31] Park, Y., Lee, J. S. *ACS Nano* 2017, 11, 8962-8969.
- [32] Kim, S., Choi, Y. K. *Appl. Phys. Lett.* 2008, 92, 223508.
- [33] Huber, B., Popp, P. B., Kaiser, M., Ruediger, A., Schindler, C. *Appl. Phys. Lett.* 2017, 110, 143503.
- [34] Wang, G., Raji, A. R. O., Lee, J. H., Tour, J. M. *ACS Nano* 2014, 8, 1410-1418.
- [35] Lien, D. H., Kao, Z. K., Huang, T. H., Liao, Y. C., Lee, S. C., He, J. H. *ACS Nano* 2014, 8, 7613-7619.
- [36] Kim, S., Jeong, H. Y., Kim, S. K., Choi, S. Y., Lee, K. J. *Nano Lett.* 2011, 11, 5438-5442.
- [37] Wang, H., Zou, C., Zhou, L., Tian, C., Fu, D. *Microelectron. Eng.* 2012, 91, 144-146.
- [38] Yoo, H. G., Kim, S., Lee, K. J. *RSC Adv.* 2014, 4, 20017-20023.
- [39] Park, K., Lee, J. S. *Nanotechnology* 2016, 27, 125203.
- [40] Lee, S., Kim, H., Yun, D. J., Rhee, S. W., Yong, K. *Appl. Phys. Lett.* 2009, 95, 262113.
- [41] Park, S., Lee, J. H., Kim, H. D., Hong, S. M., An, H. M., Kim, T. G. *Phys. Status Solidi RRL* 2013, 7, 493-496.

- [42] Cheng, C. H., Yeh, F. S., Chin, A. *Adv. Mater.* 2011, *23*, 902-905.
- [43] Zheng, Z. W., Cheng, C. H., Chou, K. I., Liu, M., Chin, A. *Appl. Phys. Lett.* 2012, *101*, 243507.
- [44] Mondal, S., Chueh, C. H., Pan, T. M. *IEEE Electron Dev. Lett.* 2013, *34*, 1145-1147.
- [45] Mondal, S., Her, J. L., Koyama, K., Pan, T. M. *Nanoscale Res. Lett.* 2014, *9*, 3.
- [46] Tian, H., Chen, H. Y., Ren, T. L., Li, C., Xue, Q. T., Mohammad, M. A., Wu, C., Yang, Y., Wong, H. S. P. *Nano Lett.* 2014, *14*, 3214-3219.
- [47] Liang, L., Li, K., Xiao, C., Fan, S., Liu, J., Zhang, W., Xu, W., Tong, W., Liao, J., Zhou, Y., Ye, B., Xie, Y. *J. Am. Chem. Soc.* 2015, *137*, 3102-3108.
- [48] Ali, S., Bae, J., Lee, C. H. *Curr. Appl. Phys.* 2016, *16*, 757-762.
- [49] Yang, Y., Yuan, G., Yan, Z., Wang, Y., Lu, X., Liu, J. M. *Adv. Mater.* 2017, *29*, 1700425.
- [50] Qian, K., Tay, R. Y., Lin, M. F., Chen, J., Li, H., Lin, J., Wang, J., Cai, G., Nguyen, V. C., Teo, E. H. T., Chen, T., Lee, P. S. *ACS Nano* 2017, *11*, 1712-1718.
- [51] Hu, Y., Zhang, S., Miao, X., Su, L., Bai, F., Qiu, T., Liu, J., Yuan, G. *Adv. Mater. Interfaces* 2017, *4*, 1700131.
- [52] Moon, T., Kang, J., Han, Y., Kim, C., Jeon, Y., Kim, H., Kim, S. *ACS Appl. Mater. Interfaces* 2011, *3*, 3957-3961.
- [53] Qian, K., Nguyen, V. C., Chen, T., Lee, P. S. *Adv. Electron. Mater.* 2016, *2*, 1500370.
- [54] Nagareddy, V. K., Barnes, M. D., Zipoli, F., Lai, K. T., Alexeev, A. M., Craciun, M. F., Wright, C. D. *ACS Nano* 2017, *11*, 3010-3021.
- [55] Jeong, H. Y., Kim, J. Y., Kim, J. W., Hwang, J. O., Kim, J. E., Lee, J. Y., Yoon, T. H., Cho, B. J., Kim, S. O., Ruoff, R. S., Choi, S. Y. *Nano Lett.* 2010, *10*, 4381-4386.
- [56] Park, Y., Lee, J. S. *ACS Appl. Mater. Interfaces* 2017, *9*, 6207-6212.
- [57] Cai, Y., Tan, J., YeFan, L., Lin, M., Huang, R. *Nanotechnology* 2016, *27*, 275206.



- [58] Lee, B. H., Bae, H., Seong, H., Lee, D. I., Park, H., Choi, Y. J., Im, S. G., Kim, S. O., Choi, Y. K. *ACS Nano* 2015, 9, 7306-7313.
- [59] Wu, H. C., Yu, A. D., Lee, W. Y., Liu, C. L., Chen, W. C. *Chem. Commun.* 2012, 48, 9135-9137.
- [60] Yu, A. D., Kurosawa, T., Lai, Y. C., Higashihara, T., Ueda, M., Liu, C. L., Chen, W. C. *J. Mater. Chem.* 2012, 22, 20754-20763.
- [61] Raeis-Hosseini, N., Lee, J. S. *ACS Appl. Mater. Interfaces* 2016, 8, 7326-7332.
- [62] Seung, H. M., Kwon, K. C., Lee, G. S., Park, J. G. *Nanotechnology* 2014, 25, 435204.
- [63] Ji, Y., Cho, B., Song, S., Kim, T. W., Choe, M., Kahng, Y. H., Lee, T. *Adv. Mater.* 2010, 22, 3071-3075.
- [64] Lai, Y. C., Wang, Y. X., Huang, Y. C., Lin, T. Y., Hsieh, Y. P., Yang, Y. J., Chen, Y. F. *Adv. Funct. Mater.* 2014, 24, 1430-1438.
- [65] Ho Lee, M., Yeol Yun, D., Min Park, H., Whan Kim, T. *Appl. Phys. Lett.* 2011, 99, 183301.
- [66] Ji, Y., Zeigler, D. F., Lee, D. S., Choi, H., Jen, A. K. Y., Ko, H. C., Kim, T. W. *Nat. Commun.* 2013, 4, 2707.
- [67] Khurana, G., Misra, P., Kumar, N., Katiyar, R. S. *J. Phys. Chem. C* 2014, 118, 21357-21364.
- [68] Son, D. I., Shim, J. H., Park, D. H., Jung, J. H., Lee, J. M., Park, W. I., Kim, T. W., Choi, W. K. *Nanotechnology* 2011, 22, 295203.
- [69] Rehman, M. M., Siddiqui, G. U., Gul, J. Z., Kim, S. W., Lim, J. H., Choi, K. H. *Sci. Rep.* 2016, 6, 36195.
- [70] Siddiqui, G. U., Rehman, M. M., Choi, K. H. *Polymer* 2016, 100, 102-110.
- [71] Ali, S., Bae, J., Lee, C. H., Choi, K. H., Doh, Y. H. *Org. Electron.* 2015, 25, 225-231.
- [72] Gu, C., Lee, J. S. *ACS Nano* 2016, 10, 5413-5418.
- [73] Choi, J., Le, Q. V., Hong, K., Moon, C. W., Han, J. S., Kwon, K. C., Cha, P. R., Kwon, Y., Kim, S. Y., Jang, H. W. *ACS Appl. Mater. Interfaces* 2017, 9, 30764-30771.
- [74] Pan, L., Ji, Z., Yi, X., Zhu, X., Chen, X., Shang, J., Liu, G., Li, R. W. *Adv. Funct. Mater.* 2015, 25, 2677-2685.

- [75] Park, M. J., Lee, J. S. *RSC Adv.* 2017, 7, 21045-21049.
- [76] Mohapatra, S. R., Tsuruoka, T., Hasegawa, T., Terabe, K., Aono, M. *AIP Adv.* 2012, 2, 022144.
- [77] Kinoshita, K., Okutani, T., Tanaka, H., Hinoki, T., Agura, H., Yazawa, K., Ohmi, K., Kishida, S. *Solid-State Electron.* 2011, 58, 48-53.
- [78] Won Seo, J., Park, J. W., Lim, K. S., Kang, S. J., Hong, Y. H., Yang, J. H., Fang, L., Sung, G. Y., Kim, H. K. *Appl. Phys. Lett.* 2009, 95, 133508.
- [79] Kim, M., Choi, K. C. *IEEE Trans. Electron Dev.* 2017, 64, 3508-3510.
- [80] Lin, Y., Xu, H. Y., Wang, Z. Q., Cong, T., Liu, W. Z., Ma, H. L., Liu, Y. C. *Appl. Phys. Lett.* 2017, 110, 193503.
- [81] Son, D., Chae, S. I., Kim, M., Choi, M. K., Yang, J., Park, K., Kale, V. S., Koo, J. H., Choi, C., Lee, M., Kim, J. H., Hyeon, T., Kim, D. H. *Adv. Mater.* 2016, 28, 9326-9332.
- [82] Zhu, J. X., Zhou, W. L., Wang, Z. Q., Xu, H. Y., Lin, Y., Liu, W. Z., Ma, J. G., Liu, Y. C. *RSC Adv.* 2017, 7, 32114-32119.
- [83] Seok, J. Y., Song, S. J., Yoon, J. H., Yoon, K. J., Park, T. H., Kwon, D. E., Lim, H., Kim, G. H., Jeong, D. S., Hwang, C. S. *Adv. Funct. Mater.* 2014, 24, 5316-5339.
- [84] Awais, M. N., Kim, H. C., Doh, Y. H., Choi, K. H. *Thin Solid Films* 2013, 536, 308-312.
- [85] Tobjörk, D., Österbacka, R. *Adv. Mater.* 2011, 23, 1935-1961.

*Chapter 5*

**IMPROVING THE OCTANE NUMBER  
OF GASOLINES THROUGH  
THE TRANSFORMATION OF N-HEXANE  
INTO BRANCHED ISOMERS**

*Angela Martins\* and Nelson Nunes*

Área Departamental de Engenharia Química,  
Instituto Superior de Engenharia de Lisboa, Lisboa, Portugal  
CQB and CQE, Universidade de Lisboa, Lisboa, Portugal

**ABSTRACT**

A tendency to eliminate benzene and other aromatic hydrocarbons from gasoline, keeping a high-octane number, is a current topic in refining industry due to strict environmental legislation. Therefore, the transformation of short chain n-paraffins (n-pentane or n-hexane) into branched isomers, with minimal cracking, is one of the key processes in the production of high octane gasolines through catalytic hydroisomerization reactions. These reactions are generally carried out over bifunctional heterogeneous catalysts, containing small amounts of

---

\* Corresponding Author Email: [amartins@deq.isel.ipl.pt](mailto:amartins@deq.isel.ipl.pt).

metal particles, like platinum or palladium, dispersed on an acid support such as zeolites.

According to the bifunctional mechanism, linear alkanes, such as *n*-hexane, suffers dehydrogenation on a metallic site, resulting on *n*-hexene. This reactive intermediate undergoes one or more skeletal isomerization reactions on the acid sites, or even cracking, before being hydrogenating on another metallic site, resulting in a mixture of dimethylbutanes, methylpentanes, or cracking products. The balance between the number of active sites, acid and metallic, as well as the pore geometry and accessibility to molecular transport are determinant factors that influence the product distribution, being dimethylbutanes (2,2 and 2,3-dimethylbutane) the most desired products due to their higher RON (research octane number) and cracking products the ones to be avoided.

This chapter aims to provide a comprehensive examination of the different catalysts used in hydroisomerization reactions, focusing: the acid support, mainly zeolites, the precious metals that offer the hydrogenating sites and the methodologies used to produce effective bifunctional catalysts. This chapter will survey the catalysts used in industrial refining processes as well as new trends from the academic research.

## 1. INTRODUCTION

Nowadays, over 80 million barrels of petroleum are processed in refineries around the world to meet the demands for liquid transportation fuels such as gasoline, diesel and jet fuel. Despite the advances performed on automotive industry such as electric and hybrid cars, worldwide consumption of transportation fuels continues to grow and is expected to remain strong in the next decades.

The quality of fuels, specifically gasoline, is evaluated by measuring its octane rating or octane number which quantifies the resistance of a gasoline and other fuels to detonation (engine knocking) in spark-ignition internal combustion engines. Therefore, higher octane number means higher knocking resistance tendency. This property is measured in a test engine against a mixture of isooctane and *n*-heptane. If a gasoline sample has the same anti-knocking quality as that of a mixture containing 95% isooctane and 5% *n*-heptane, so the octane number for that sample is 95. Some hydrocarbons have higher anti-knocking capacity than isooctane,

such as, for example benzene. Therefore, octane number definition is extended to allow octane numbers higher than 100. Depending on the measurement techniques there are mainly two definitions of octane number, the Research Octane Number (RON) and the Motor Octane Number (MON). The most commonly used octane number is RON and is determined by running the fuel in a test engine under controlled conditions and variable compression ratios, the results are then compared with those obtained with known compositions of isooctane and *n*-heptane. On the other hand, the determination of MON uses a similar test engine but with a preheated fuel mixture, higher engine speed (900 rpm instead of 600 rpm used in RON) and a variable ignition timing to further stress the knocking effect. Table 1 exemplifies the RON and MON values for a series of hydrocarbons. As can be observed, for molecules with the same number of carbon atoms, there is an increase on both RON and MON with the degree of branching of the molecules [1].

Environmental regulations are requiring significant improvements in the quality of diesel and gasoline in many parts of the world. For instance, the oil and auto industry have been working in a cooperative effort called the Auto-Oil Air Quality Research Program to understand the relationship between fuel composition and vehicle emissions. This collaboration aims to implement cost-effective improvements, both in automotive industry and refineries, to minimize the adverse impacts of the combustion fossil fuels on the environment. [2]. On the other hand, Environmental Agencies from Europe and United States impose strong regulations to improve the quality of diesel and gasoline. For the European Union, since 2005, the regulation for gasoline with a minimum research octane number of 95 (RON = 95) the maximum limits comprise 50 ppm for sulfur, 35% aromatics, with 1% maximum in benzene, 2.7% oxygen and 18% olefins (values expressed in v/v%) [3]. To satisfy environmental regulations and, simultaneously, keeping a high-octane number to ensure the good quality of gasolines the refineries implemented some modifications in the last decades in order to transform low octane number molecules such as *n*-pentane (C<sub>5</sub>) and *n*-hexane (C<sub>6</sub>) into high octane multibranched isomers [4]. For *n*-hexane, two types of isomers can be formed, monobranched and

dibranched isomers (Figure 1). Monobranched isomers are 2-methylpentane and 3-methylpentane, with octane number of about 75. Dibranched isomers are 2,2-dimethylbutane and 2,3-dimethylbutane, with octane number higher than 90. Therefore, the operation conditions and the catalysts used in the isomerization process are focused to privilege the formation of dibranched isomers.

**Table 1. Octane number expressed as RON and MON for several hydrocarbons. Adapted from [1]**

Molecule	RON	MON
<i>n</i> -Butane	94	89.1
<i>n</i> -Pentane	61.7	61.9
Isopentane	92.3	90.3
2,2-Dimethylbutane	91.8	93.4
2,3-Dimethylbutane	100.5	94.3
2-Methylpentane	73.4	73.5
3-Methylpentane	74.5	74.3
<i>n</i> -Hexane	24.8	26
2,2-Dimethylpentane	92.8	93
2,3-Dimethylpentane	91.1	89
2,4-Dimethylpentane	83.1	82
3,3-Dimethylpentane	80.8	84
2-Methylhexane	42.4	45
3-Methylhexane	52	55.8
Benzene	105	102.8
<i>n</i> -Heptane	0	0
Isooctane	100	100

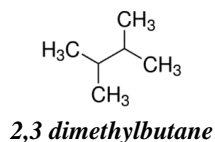
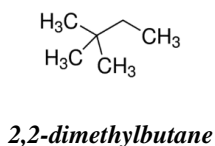
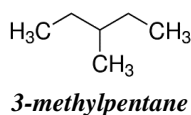
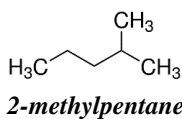


Figure 1. Monobranched and dibranched isomers obtained from isomerization of *n*-hexane.

## **2. THE ISOMERIZATION PROCESS**

### **2.1. The Feed**

In a typical refinery plant, crude oil entering the process is first fractionated according to the different boiling ranges – atmospheric pipestills (APS) and vacuum pipestills (VPS). Both APS and VPS are then submitted to several transformations, most of them occurring in the presence of catalysts. A simple schematic representation of a typical refinery is displayed in Figure 2.

The lighter liquid petroleum fraction in the gasoline boiling range is called naphtha, which can be processed in several ways such as isomerization, hydrotreating and/or reforming. The destilate fraction in the range needed to produce diesel and jet fuel is either hydrotreated to remove heteroatoms such as sulfur and nitrogen or hydrocracked to produce gasoline. The next boiling fraction is called vacuum gas oil (VGO) is commonly sent to the fluid catalytic cracking (FCC) unit. Hydrotreating of the VGO prior to FCC is common in order to avoid catalysts poisoning. The heaviest residual fraction contains the highest concentration of poisonous that cannot be treated in processes involving catalysts. So, these molecules are usually converted through non-catalytic thermal processes known as Coking which generates lighter liquid streams and a solid coke by-product [5]. In brief, the purpose of petroleum refinery is the complex redistribution of atoms aiming to accomplish fuel composition requirements, especially the octane number.

The isomerization processes are relatively flexible regarding the feeds that can be processed. The C<sub>5</sub> and C<sub>6</sub> feeds come either from the straight-run crude distillation – naphtha – or from the catalytic reforming. For the naphtha pool, the distillation cut point is chosen at around 70 – 80°C to avoid the presence of large amounts of benzene, cyclohexane and hydrocarbons with more than seven carbon atoms since the presence of these compounds in the isomerization feed unit causes the decrease in the final octane number. Commonly, the contents usually allowed are: 2% for benzene, 1-2% for cyclohexane and less than 2% for C<sub>7+</sub> hydrocarbons.

Considering the reformate, its composition is separated in two fractions: one of them containing heavy  $C_{7+}$  molecules and another one containing lighter molecules and benzene. This light reformate can be sent to the isomerization unit after hydrogenation, alone or mixed with naphta.

Table 2 displays a typical isomerization feed. Depending the origin of the feed the  $C_5/C_6$  ratio may vary [1].

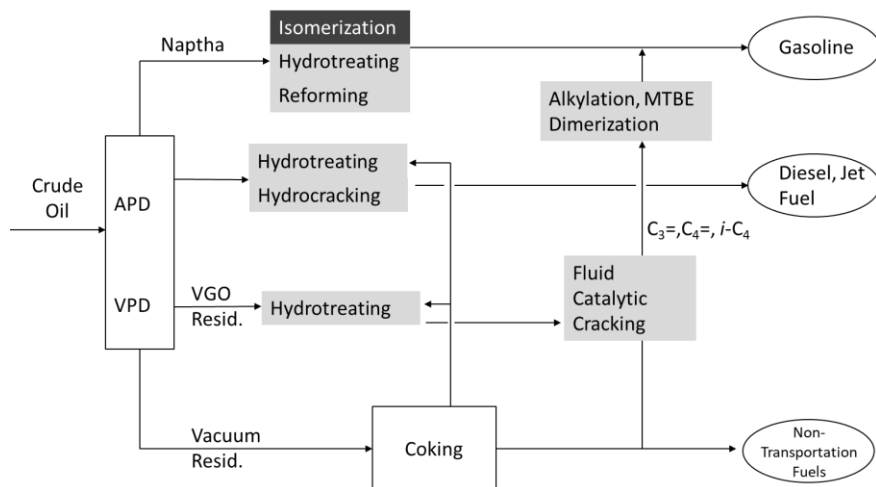


Figure 2. Simplified scheme for a typical refinery.

**Table 2. Typical composition of the isomerization feed**

Component	wt. %
Isopentane	20.0
n-Pentane	29.0
Cyclopentane	1.0
2,2-Dimethylbutane	0.3
2,3-Dimethylbutane	1.5
2-Methylpentane	11.0
3-Methylpentane	8.2
n-Hexane	19.5
Methylcyclopentane	5.0
Cyclohexane	1.5
Benzene	2.0
$C_{7+}$	1.0



## 2.2. The Catalysts

The isomerization reaction is very slightly exothermic ( $\Delta H = -4$  to  $-20$   $\text{kJ mol}^{-1}$ ) and is independent of pressure, since there is no change in the number of moles between reactants and products. The thermodynamic equilibrium curves presented on Figure 3 show that the most desired isomers, considering its octane number, are formed at low temperature [4,6]. Industrially, the softer operation temperature possible is necessary to get maximum high-octane number isomers. The catalysts used in this process have to be very active in order to maximize the yields of dibranched isomers by working at the lowest temperature [4].

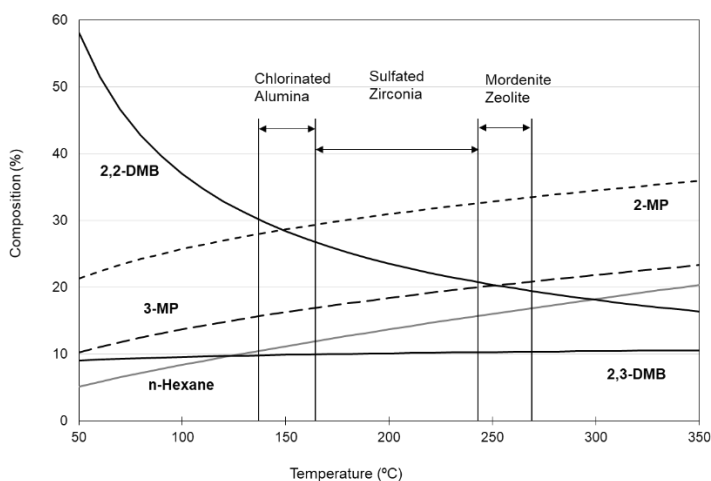


Figure 3. Equilibrium distribution of hexanes.

The industrial use of isomerization catalysts started in 1933 when researchers showed that *n*-hexane and *n*-heptane could be isomerized in the presence of Friedel-Crafts  $\text{AlCl}_3$  catalysts, which exhibit very high activity at low temperature, ranging from 80 to 100°C. However, these catalysts were difficult to handle since they were very sensitive to impurities in the feed and generated reactor corrosion. Nowadays, there are three types of industrial catalysts operating in refineries worldwide. They are all based in bifunctional catalysts consisting in a noble metal, generally Pt, dispersed

on an acidic support and operate in the presence of hydrogen, being this the reason why the process is also known as hydroisomerization. The acidic support currently used in most refineries are: chlorinated alumina and zeolites. Sulfated zirconia is also an industrial catalyst, although much less used.

The main properties of the three most used industrial catalysts are resumed in Table 3.

**Table 3. Main properties of chlorinated alumina, sulfated zirconia and mordenite based catalysts**

Catalyst	Pt/chlorinated alumina	Pt/sulfated zirconia	Pt/mordenite
Activity	High	Medium	Low
Sensitivity to contaminants	High	Medium to low	Low
RON gain	12-14	10-12	8-10

In the following sub-subsection, a small description of these three types of catalysts is made, focusing in more detail in zeolites, since this type of catalyst is the most used in refineries worldwide.

### 2.2.1. Chlorinated Alumina

Chlorinated alumina catalyst contains 6-10% and 0.2-0.5% Pt (wt. %). The reaction is usually performed at low temperature (120 – 200°C), which favors the selectivity to multibranched isomers. Earlier methods for catalysts preparation involved the reaction of Pt/Al<sub>2</sub>O<sub>3</sub> with CCl<sub>4</sub> or AlCl<sub>3</sub> at 500°C, or a succession of both, which creates a surface with very strong Lewis acid sites but implies that the solids need to be converted into Friedel-Crafts catalysts by treatment with HCl [7, 8]. Nowadays it is preferred to impregnate alumina with a solution containing organochloro-aluminic compounds such as the sesquichloride (Al<sub>2</sub>Cl<sub>3</sub>(C<sub>2</sub>H<sub>5</sub>)<sub>3</sub>) or the dichloride (Al<sub>2</sub>Cl<sub>2</sub>C<sub>2</sub>H<sub>5</sub>) and then activate such precursors either at high temperature in the presence of chlorine compounds or under milder conditions [9]. Although more active and selective than other types of catalysts, chlorinated alumina catalysts present the disadvantage of

requiring the continuous adding of chlorine during the process which causes corrosion of the reactor. On the other hand, this catalyst is highly sensitive to all kinds of feed contaminants, especially water and sulfur [4, 10].

### 2.2.2. Sulfated Zirconia

Sulfated zirconia is an attractive catalyst for the isomerization of short chain linear paraffin since it offers a good alternative for the corrosive halogen containing solid catalysts at the medium operation temperature (200-280°C) allowing a good selectivity to the desired dibranched isomers and can be regenerated, which is an important advantage when compared to chlorinated alumina catalysts. Zirconia modified with sulfates, typically around 2.0 wt.% in sulfur [11] showed improved catalytic activity and stability since the presence of sulfates increases the content of catalytically active tetragonal crystal phase, transforming the catalysts into a super acid [11, 12].

Sulfated zirconia has been reported to isomerize *n*-hexane even at room temperature in the absence of the metal function, but the catalysts deactivation is fast. To solve this problem, noble metal Pt or Pd are generally loaded in the catalyst acting as metal function, with an optimum metal loading of about 0.15 wt. % being reported [11]. The high costs associated to noble metals led to some attempts to develop new non-precious metal loaded sulfated zirconia, using metals such as Cr, Mn, Fe, Co and Ni, being Ni the one that attracted most attention [13]. As an alternative, mixtures of metals, allow decreasing the cost associated to the metal function, and, simultaneously synergistic effects between the two metals were also noticed, as reported by Ma et al. that studied the effect of Pd-Ni and observed that the presence of the two metals increased both conversion and selectivity in *n*-hexane isomerization [14]. Nevertheless, sulfated zirconia type catalysts generally suffer from extreme sensitivity to feedstock poisons, particularly water, which makes them less attractive in industrial applications.

### 2.2.3. Zeolites – Mordenite (MOR) Based Catalysts

Zeolitic catalysts are much more tolerant to feedstock contaminants, such as water and sulphur, and this higher tolerance often compensates their lower activity and selectivity, since the operation temperature (250–270°C) is higher than the one used with other catalysts and does not privilege the formation of dibranched isomers. Mordenite zeolite (MOR structure) loaded with small amounts of Pt (less than 1 wt. %) is the most used isomerization catalyst due to its high thermal stability and strong acidity.

MOR is a natural zeolite, although in industrial applications the synthetic version of the zeolite is mostly used. MOR structure (Figure 4) is comprised by a tubular porous network, without cavities, presenting large parallel channels with elliptic openings ( $6.7 \times 7 \text{ \AA}$ ) connected through small channels ( $2.9 \times 5.7 \text{ \AA}$ ) [15].

The diffusion of small molecules such as  $\text{N}_2$  or  $\text{O}_2$  is made through both channel systems. However, larger organic molecules, such as *n*-hexane, only diffuse through larger channel, so from the catalytic perspective this zeolite structure is considered unidirectional [16].

Commercial isomerization catalyst comprises alumina binded to platinum impregnated dealuminated MOR zeolite. The influence of silica to alumina (Si/Al) ratio of the zeolite strongly affects its catalytic behavior. For instance, for a Si/Al ratio of 5 the relative activity for pentane isomerization is 100 that increases for 135 for a Si/Al ratio of about 8.5 but decreases for 84 for a Si/Al ratio of 12.5. Thus, the catalysts formulation generally includes dealumination treatments in order to adjust the Si/Al ratio of the catalyst. The dealumination procedures can be performed by different methods such as steaming or acid treatments. Whatever the method used the effects are the decreasing of the number of acid sites and the generation of larger pores (mesopores) inside the zeolite crystallites [17].

Concerning the catalyst activity these two effects are acting in opposite direction, but both contribute to an optimal catalysts formulation. The loss of active sites is a negative effect but the creation of mesoporosity makes the remaining sites more accessible.

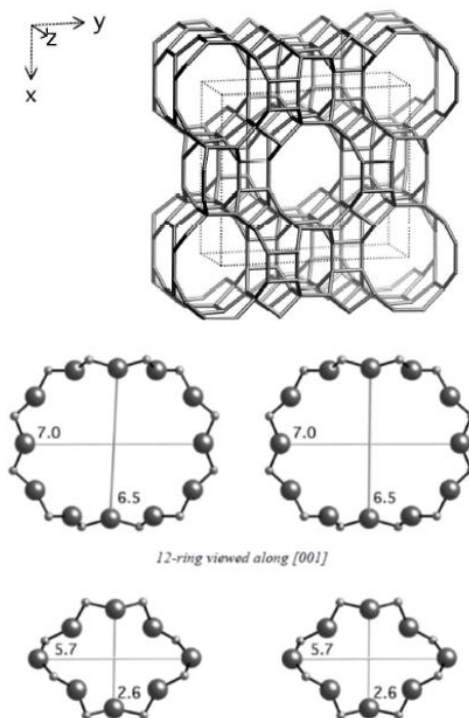


Figure 4. MOR zeolite structure [15].

On the other hand, the enlargement of the porosity decreases diffusion limitations, which causes shorter residence times and facilitates desorption of the reaction products, limiting the occurrence of secondary reactions [6, 18]. Alkaline treatments were also performed on MOR zeolite using NaOH solutions to generate mesoporosity inside the zeolite pore structure and, thus, facilitate molecular diffusion inside the unidirectional channels. It was found that using soft alkaline treatment with 0.1 M NaOH solution led to a slight enlarge of the zeolite porosity, preserving the acidity, that led to an increased selectivity into multibranched isomers [19]. These results showed that the use of zeolite structures with two levels of porosity, that is, hierarchical structures could be an interesting tool to improve the selectivity into multibranched isomers using zeolite-based catalysts.

### 2.2.4. Other Zeolite Structures

Although Pt/MOR is currently the most used industrial zeolite-based catalyst for isomerization of C<sub>5</sub>-C<sub>6</sub> linear paraffins due to its strong acidity and thermal stability, other zeolite structures have been proposed to replace MOR attempting to find a more active zeolite structure that can operate at lower temperatures and thus, increase the yield in multibranched products.

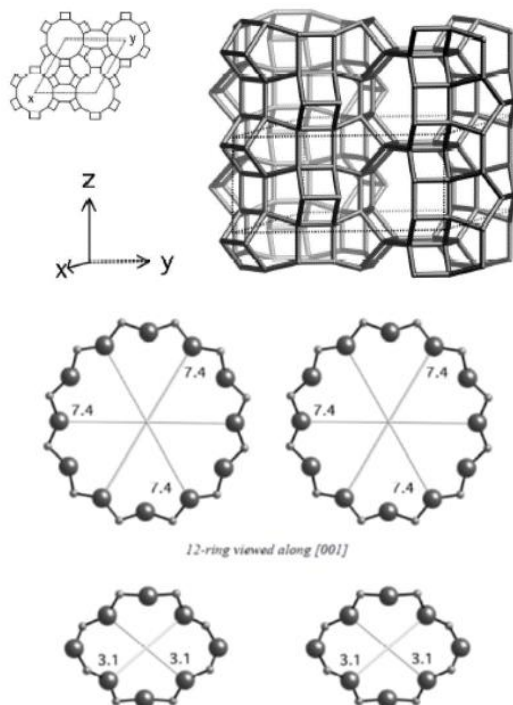


Figure 5. MAZ zeolite structure [15].

Among several proposals, laboratory studies performed in the beginning of the last decade of 20<sup>th</sup> century have shown that omega zeolite (MAZ structure) had improved catalytic properties, when compared with MOR, giving higher yields in multibranched isomers. This effect was attributed by Allain *et al.* to the higher pore dimensions of this zeolite structure, thus decreasing the stereochemical limitations to the formation of multibranched isomers [20]. In fact, MAZ zeolite (Figure 5) is a

unidirectional zeolite structure, identical to MOR, but the pore openings are round and wider ( $7.4 \times 7.4 \text{ \AA}$  and  $3.1 \times 3.1 \text{ \AA}$ ) [15]. However, it was also shown that the number and strength of the acid sites typical of this zeolite is very heterogeneous, with significant variations, depending on the zeolite synthesis conditions, which makes it difficult to use this zeolite structure in industrial scale.

ITQ-4 (IFR structure) is another unidirectional zeolite that was proposed as an alternative acid matrix to isomerization catalysts. Chica *et al.* [21] demonstrated that in spite of MOR zeolite being more active than ITQ-4, the yield into multibranched isomers of *n*-hexane is about 10% higher using the same operational conditions that was attributed to van der Waals interactions during the adsorption steps.

The use of unidirectional zeolites as acid supports have some limitations, since the introduction of the metal phase may cause some pore occlusion, limiting the access of reactants to the active sites located inside the pore structure. In this sense, several tridimensional structures have been proposed as acid matrices for isomerization reactions, namely Y (FAU structure) [22], Beta (BEA structure) [23, 24] ZSM-5 (MFI structure) [25] and MCM-22 (MWW structure) [26, 27]. Among the several studied structures the results obtained with Beta zeolite have been particularly relevant. Chica *et al.* [28] studied the behavior of this zeolite structure and compare it with traditional MOR zeolite. It was found that Beta zeolite can be a good alternative to traditional MOR zeolite especially when significant amount of *n*-heptane is present in the feed. In fact, MOR zeolite cracked all the *n*-C<sub>7</sub> present in the feed and in the presence of Beta zeolite 50% of *n*-C<sub>7</sub> were converted into branched products [28]. The effect of the generation of mesoporosity on tridimensional structures such as ZSM-5 and Beta zeolites is also being studied and according to Moddhera *et al.* [29], hierarchical zeolite Beta was found to be able to work at milder reaction conditions. These preliminary results show once again the good perspectives in the use of hierarchical zeolites structures as bifunctional catalysts for isomerization reactions that needs further exploration and optimization.

### 2.3. Reaction Mechanism

Isomerization is also called hydroisomerization since the reaction occurs in the presence of hydrogen and requires two types of active sites: acid sites, located inside an active support, commonly a zeolite, and a metallic function that can be either located within the zeolite micropores and/or on the outer surface of the crystals, or even supported on alumina, forming a composite Pt/Al<sub>2</sub>O<sub>3</sub>-HZeolite [30]. Figure 6 shows a general schematic representation of *n*-paraffin isomerization over bifunctional Pt/HZeolite catalysts.

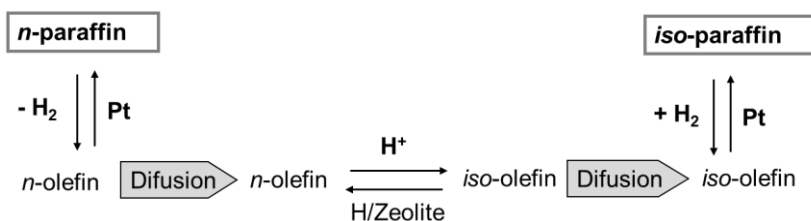


Figure 6. General scheme of *n*-paraffin isomerization over bifunctional Pt/HZeolite.

As can be visualized from the figure above. The aim of metal sites is to dehydrogenate saturated molecules (*n*-paraffin) and to hydrogenate unsaturated ones (*iso*-olefins) while the role of acid sites is to isomerize or crack the olefinic intermediates. Physical steps, comprising molecular diffusion through the gas film surrounding the catalysts particles or along the zeolite micropores are other essential parts of the reaction scheme. Catalyst activity, stability and selectivity depends on two main parameters: the diffusion path of the molecules outside and inside the pores and the characteristics of the active sites (acid and metallic) [31].

The diffusion path of the molecules is affected mainly by the kinetic diameter of the micropores and the distance between metal and acid sites. These characteristics define the molecular diffusion from the acid to metal sites (and vice-versa) as well as the average number of successive transformations suffered by the olefinic intermediates during their diffusion path.



The characteristics of the active sites can be quantified by the ratio between the metal and acid sites, that is, the hydrogenating/acid balance ( $C_{Pt}/C_A$ ). This effect was systematically studied by Guisnet and co-workers using *n*-heptane and *n*-decane as reactants and Pt/HY zeolites as catalysts, changing the Si/Al ratio from 5 to 40 and Pt contents from 0.07 to 1.5 wt. % [31–33]. For the particular case where *n*-C<sub>10</sub> was used as a model molecule the authors observed that [33]:

- For  $C_{Pt}/C_A < 0.03$ , (where  $C_{Pt}$  is the concentration of metal sites and  $C_A$  is the concentration of acid sites) the reaction is limited by the dehydro-hydrogenations steps. The catalysts stability is poor, and a fast deactivation occurs since all products (mono, di and tribranched isomers as well as cracking products) are formed simultaneously.
- For  $C_{Pt}/C_A > 0.17$  the number of acid sites found by olefinic intermediates during their diffusion between two metal sites is such that only one transformation occurs at the acid sites. Accordingly, *n*-C<sub>10</sub> transforms successively into mono, bi and tri-branched isomers plus cracking products. In these conditions the selectivity into isomers is maximal, no deactivation occurs, and the catalyst is considered ideal.
- For intermediate  $C_{Pt}/C_A$  values a moderate deactivation occurs as well as partially successive reaction scheme can be observed, where more than one transformation can occur during the diffusion of the intermediates from one metal site to the other.

The  $C_{Pt}/C_A$  ratio is naturally affected by the intrinsic acidity of the zeolite and by the amount of Pt introduced that is generally comprised between 0.3 and 1wt. %. The mode of Pt introduction is also a relevant issue since the metal dispersion has a direct influence on the number and location of the metal sites. Martins *et al.* [27] characterized Pt/MCM-22 catalysts whereas the same amount of Pt (1 wt %) was introduced by several methods such as ion exchange with  $Pt(NH_3)_4^{2+}$  and incipient wetness impregnation with  $PtCl_6H_2$ . It was shown, using Transmission

Electron Microscopy (TEM) that in the case of ion exchanged catalysts the Pt is dispersed as very small particles inside the micropores as well as at the external surface. On the other hand, the incipient wetness impregnation method originated large metal particles that are restricted to the outer surface of the zeolite crystals (Figure 7).

Another strategy to modify the hydrogenation function is the use of mixtures of metals, being the most common Pt-Ni mixtures. This strategy allows the reduction amount of the more expensive precious metal, Pt, and simultaneously increases the hydrogenating capacity of the catalyst due to the synergistic effect between the two metals, which as a positive impact on the catalytic activity and selectivity in *n*-hexane isomerization reaction [34, 35].

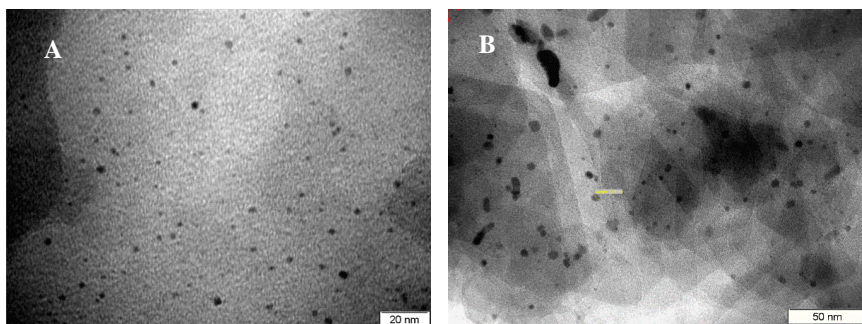


Figure 7. TEM images of Pt dispersed on MCM-22 zeolite by ion exchange (A) and incipient wetness impregnation (B).

The modification on the acid function is also an alternative to modify the  $C_{Pv}/C_A$  ratio. For example, it is known that presence of small amounts of rare earth elements such as lanthanum (La), ytterbium (Yb) and neodymium (Nd) has a proven influence in the acidity of zeolites [36, 37], being part of the formulation of FCC catalysts [38]. Following this trend, Martins *et al.* [24] studied the effect of the introduction of small amounts of rare earth elements on Pt loaded BEA zeolite and found that in the presence of less than 0.5 wt. % of La and Nd causes an increase in catalytic activity and selectivity into multibranched isomers. On the other hand, for higher loadings a higher selectivity into undesired cracking products was

noticed as a consequence of stereochemical limitations inside the zeolite pore structure. The effect of rare earth elements was also studied on Pt loaded MCM-22 zeolite. However, in the case of this peculiar zeolite structure, with two independent inner pore systems, one of them containing supercages, as well as a large external surface area, the effect of rare earth elements introduction decreases the selectivity into multibranched isomers. Instead, secondary reactions occurred leading to an increase selectivity into cracking products [26].

### **3. INDUSTRIAL PROCESSES**

Refineries worldwide use mainly chlorinated alumina or zeolite-based catalysts in their processes. The chlorinated alumina catalysts, although more active than zeolite-based catalysts, have the strong disadvantage of being highly sensitive to all kinds of feed contaminants, especially water and sulfur. Zeolite catalyst are much more tolerant to these feedstock poisons, which generally compensates their lower catalytic activity and selectivity [39].

Each type of catalyst has a corresponding specific process flow scheme, which is exemplified in Figures 8 and 9.

With Pt/Chlorinated alumina catalysts the process needs to use driers on the feed and the hydrogen due to the strong “bonds” of the catalyst to water. It also needs a continuous chlorine injection to preserve the needed amount of chlorine and maintain the catalyst active. The most used chlorinated compounds are carbon tetrachloride ( $\text{CCl}_4$ ) and perchloroethylene ( $\text{C}_2\text{Cl}_4$ ), which is less toxic. A scrubber is also required to eliminate the hydrochloric acid from the produced gases.

When a Pt/HZeolite is used the process must include a compressor to recycle hydrogen. Also, due to the lower performance of zeolite-based catalysts, when compared with chlorinated alumina ones, the unconverted n-paraffins and even the lower-octane-number single-branched isomers are recycled to obtain the maximum octane number. The separation of these compounds can be carried out using large distillation columns

(depentanizer, deisohexanizer) or by adsorption on molecular sieves [1]. The first commercial zeolite catalyst-based process was developed by Shell and was named Hysomer<sup>®</sup> [40]. The reactor operates at 27 to 30 atm hydrogen pressure and 250°C temperature. The gain in octane number is reported to be up to 10 points. Sulfur is claimed to be tolerant until 35 ppm and water level until 50 ppm does not weaken the catalytic performance. A further octane number improvement was achieved by integrating the zeolitic catalyst isomerization section with a molecular sieve *n/iso*-paraffin separation section, where the *n*-paraffins adsorbed on the sieves are removed by means of a hot hydrogen flow. This integrated solution, presented in Figure 10 in a simplified process scheme, was developed by UOP and was named Total Isomerization Process (TIP<sup>®</sup>) [1].

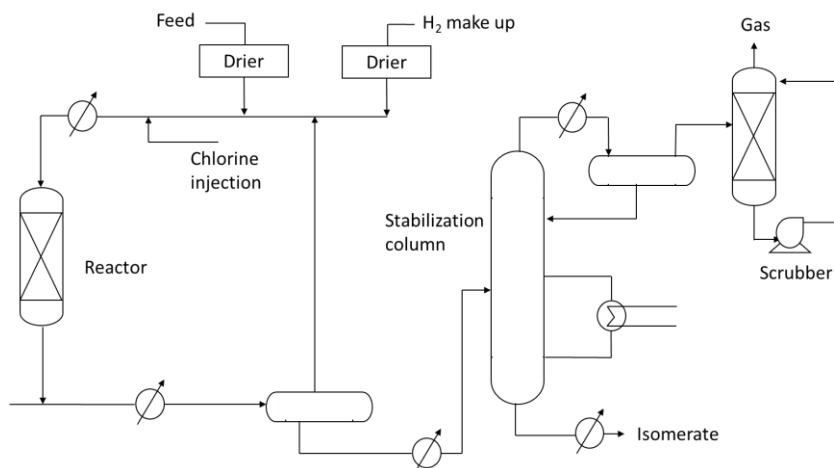


Figure 8. Simplified scheme for the isomerization process using Pt/chlorinated alumina as catalyst.

Alternative technologies using zeolites were developed by Süd-Chemie – HYSOPAR<sup>®</sup> – that can operate at sulfur levels exceeding 50 ppm. This process uses a Pt containing modified MOR zeolite as catalyst and had the first commercial application in 1993, in a refinery plant belonging to CEPSA at Algeciras (Spain). Since then more than 20 refineries around the world employ this robust catalyst [41, 42]. In what concerns the industrial

use of metal oxide – sulfated zirconia - catalyst at industrial scale, its applications have been limited due to the high intolerance to feedstock impurities.

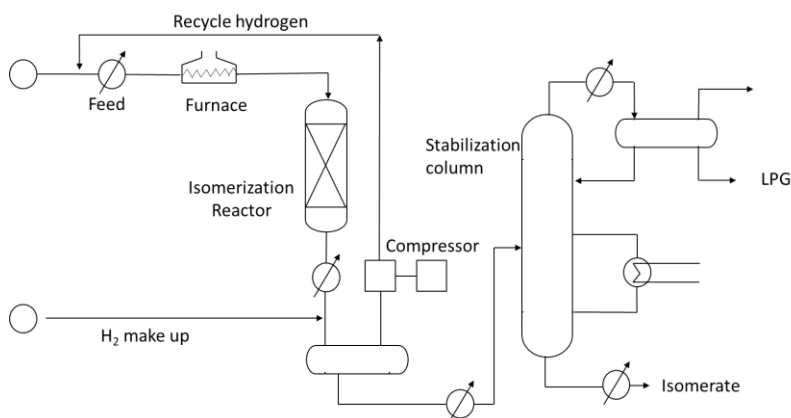


Figure 9. Simplified scheme for the isomerization process using Pt/Hzeolite as catalyst.

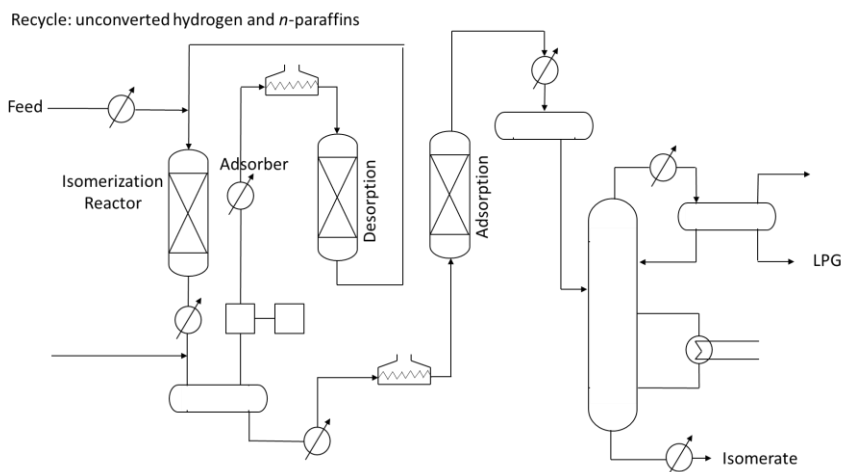


Figure 10. Simplified diagram of Total Isomerization Process (TIP®) by UOP.

However, the recently developed HYSOPAR-SA® catalyst by Süd-Chemie has proven an outstanding activity along with an improve tolerance to feedstock impurities. The octane number over zeolite base

catalysts is up to 3 RON points, depending on the feedstock composition, being the catalytic activity and selectivity closer to chlorinated catalyst than zeolitic catalysts [42].

## CONCLUSION

The operation of a modern refinery nowadays is becoming more demanding due to the world-wide public concerns about the earth environment and health considerations. These concerns led to the implementation of restrictive regulations all around the world. To satisfy environmental regulations and, simultaneously maintain high-octane number gasolines, the refineries had to find ways to transform low octane number molecules such as *n*-hexane into high octane multibranched isomers through isomerization process in the presence of bifunctional catalysts comprising an acid and metal function. Most refineries usually have to choose between robust, highly active and selective catalysts based on chloride alumina, with the drawback of high sensitivity to feed contaminants or zeolite-based catalysts characterized by their outstanding tolerance to feedstock poisons such as sulfur and water, but with lower activity and selectivity. Other options are being studied and optimized such as the recently developed industrial catalyst based on sulfated zirconia or the academic studies regarding the use of hierarchical zeolites with tuned textural and acidic properties that may have new opportunities as isomerization catalysts, operating at milder reaction conditions, thus leading to high yields in multibranched isomers.

## ACKNOWLEDGMENTS

The authors thank the support of FCT (pluriannual program of CQB through strategic project PEST UID/MULTI/00612/2013).

**REFERENCES**

- [1] Travers, C. (IFP) Isomerization of Light Paraffins, in: P. LePrince (Ed.), *Pet. Refining. 3 - Convers. Process.*, 1st Edition, Éditions Technip, Paris, 2001.
- [2] *The State of Texas Air Quality Research Program*, <http://aqrp.ceer.utexas.edu/>, (accessed July 5, 2018).
- [3] E. E. A. *Technical, EU fuel quality monitoring — 2014 Summary report*, 2015.
- [4] Vermeiren, W., Gilson, J. P. Impact of zeolites on the petroleum and petrochemical industry, *Top. Catal.* 52 (2009) 1131–1161.
- [5] Kaufmann, T. G., Kaldor, A., Stuntz, G. F., Kerby, M. C., Ansell, L. L. Catalysis science and technology for cleaner transportation fuels, *Catal. Today* 62 (2000) 77–90.
- [6] Guisnet, M., Gilson, J. P. C4-C6 Alkane Isomerization, in: M. Guisnet, J. P. Gilson (Eds.), *Zeolites Clean. Technol.*, 1st Edition, Imperial College Press, London, 2002, 153–166.
- [7] Goble, P., Lawrence, A. G. in: *Proc. Third Int. Congr. Catal.*, 1964.
- [8] Burk, J., Crest, E. H., Mooi, H. *Method for manufacturing an active catalyst composition*, US3047514, 1962.
- [9] Ducourty, B., Szabo, G., Dath, J. P., Gilson, J. P., Goupil, J. M., Cornet, D. Pt/Al<sub>2</sub>O<sub>3</sub>-Cl catalysts derived from ethylaluminum dichloride: Activity and stability in hydroisomerization of C<sub>6</sub> alkanes, *Appl. Catal. A Gen.* 269 (2004) 203–214.
- [10] Hidalgo, J., Zbuzek, M., Cerny, R., Jísa, P. Current uses in catalytic isomerization, alkylation and etherification processes to improve gasoline quality, *Cent. Eur. J. Chem.* 12 (2014) 1-13.
- [11] Duchet, J. C., Guillaume, D., Monnier, A., Dujardin, C., Gilson, J. P., Van Gestel, J., Szabo, G., Nascimento, P. Isomerization of n-hexane over sulfated zirconia: Influence of hydrogen and platinum, *J. Catal.* 198 (2001) 328–337.
- [12] Kumar, A., Badoni, R. P., Singhal, S., Agarwal, S., Tripathi, A. R. Synthesis and characterization of zirconia-based catalyst for the isomerization of n-hexane, *Chem. Eng. Commun.* 205 (2018) 92–101.

- [13] McIntosh, D. J., Kydd, R. A., Hill, J. M. Comparison of Cr, Mn, Fe, Co, and Ni as promoters for n-butane conversion over sulfated zirconia, *Chem. Eng. Commun.* 191 (2004) 137–149.
- [14] Ma, Z., Meng, X., Liu, N., Shi, L. Pd-Ni doped sulfated zirconia: Study of hydrogen spillover and isomerization of n-hexane, *Mol. Catal.* 449 (2018) 114–121.
- [15] Baerlocher, D. H., Meier, Ch., Olson, W. M. *Atlas of Zeolite Framework Types*, 5<sup>th</sup> Edition, Elsevier, 2001.
- [16] Csicsery, S. M. Shape selective catalysis, in: J. A. Rabo (Ed.), *Zeolite Chem. Catal.*, ACS Monograph 171, Washington, 1976.
- [17] Karge, J., Weitkamp, H. G. Untersuchungen an dealuminierten Mordenit- Katalysatoren [Investigations on dealuminated mordenite catalysts], *Chem. Eng. Tech.* 58 (1986) 946-959.
- [18] Lazaro, A., Frontela, J., Corma, J. *Process for the obtainment of a light paraffin isomerization catalyst*, EP 0409303A1, 1990.
- [19] Monteiro, R., Ania, C. O., Rocha, J., Carvalho, A. P., Martins, A. Catalytic behavior of alkali-treated Pt/HMOR in n-hexane hydroisomerization, *Appl. Catal. A Gen.* 476 (2014) 148–157.
- [20] Allain, M., Magnoux, J. P., Schulz, P., Guisnet, P. Hydro isomerization of n-hexane over platinum mazzite and platinum mordenite catalysts kinetics and mechanism, *Appl. Catal. A Gen.* 152 (1997) 221.
- [21] Chica, A., Corma, A., Miguel, P. J. Isomerization of C5 – C7 n-alkanes on unidirectional large pore zeolites : activity, selectivity and adsorption features, *Catal. Today* 65 (2001) 101–110.
- [22] Calero, S., Schenk, M., Dubbeldam, D., Maesen, T. L. M., Smit, B. The selectivity of n-hexane hydroconversion on MOR-, MAZ-, and FAU-type zeolites, *J. Catal.* 228 (2004) 121–129.
- [23] Pisarenko, E. V., Ponomarev, A. B., Pisarenko, V. N. Analysis and Modeling of the Hydroisomerization Process for n -Hexane, *Theor. Found. Chem. Eng.* 52 (2018) 24–34.
- [24] Martins, A., Silva, J. M., Ribeiro, M. F. “Applied Catalysis A : General Influence of rare earth elements on the acid and metal sites



- of Pt/HBEA catalyst for short chain n -alkane hydroisomerization,” *Applied Catal. A, Gen.* 466 (2013) 293–299.
- [25] Aboul-Gheit, A. K., Awadallah, A. E., Aboul-Gheit, N. A. K., Abdel-Hamid, S. M. Hydrohalogenation of platinum-palladium/H-ZSM-5 catalysts for n-hexane hydroconversion, *Pet. Sci. Technol.* 33 (2015) 39–50.
- [26] Martins, A., Silva, J. M., Ribeiro, F. R., Ribeiro, M. F. Study of Pt/MCM-22 based catalysts in the transformation of n-hexane: Effect of rare earth elements and mode of platinum introduction, *React. Kinet. Mech. Catal.* 104 (2011) 417–428.
- [27] Martins, A., Silva, J. M., Ribeiro, F. R., Guisnet, M., Ribeiro, M. F. n-Hexane hydroisomerisation over bifunctional Pt/MCM-22 catalysts. Influence of the mode of Pt introduction, *Stud. Surf. Sci. Catal.* 174 (2008) 1135–1138.
- [28] Chica, A., Corma, A. Hydroisomerization of pentane, hexane, and heptane for improving the octane number of gasoline, *J. Catal.* 187 (1999) 167–176.
- [29] Modhera, B. K., Chakraborty, M., Bajaj, H. C., Parikh, P. A. Influences of mesoporosity generation in ZSM-5 and zeolite beta on catalytic performance during n-hexane isomerization, *Catal. Letters.* 141 (2011) 1182–1190.
- [30] Batalha, N., Pinard, L., Pouilloux, Y., Guisnet, M. Bifunctional hydrogenating/acid catalysis: Quantification of the intimacy criterion, *Catal. Letters.* 143 (2013) 587–591.
- [31] Guisnet, M. “ideal” bifunctional catalysis over Pt-acid zeolites, *Catal. Today.* 218–219 (2013) 123–134.
- [32] Guisnet, M., Alvarez, F., Giannetto, G. Hydroisomerization and hydrocracking of n-heptane on Pth zeolites. Effect of the porosity and of the distribution of metallic and acid sites, *Catal Today.* 1 (1987) 415–433.
- [33] Alvarez, M. G. F., Ribeiro, F. R., Pérot, G., Thomazeau, C. Hydroisomerization and Hydrocracking of Alkanes: 7. Influence of the Balance between Acid and Hydrogenating Functions on the

- Transformation of n-Decane on PtHY Catalysts, *J. Catal.* 162 (1996) 179–189.
- [34] Paixão, V., Santos, C., Nunes, R., Silva, J. M., Pires, J., Carvalho, A. P., Martins, A. N-hexane hydroisomerization over composite catalysts based on BEA zeolite and mesoporous materials, *Catal. Letters.* 129 (2009) 331–335.
- [35] Eswaramoorthi, I., Lingappan, N. Ni-Pt/H-Y zeolite catalysts for hydroisomerization of n -hexane and n-heptane, *Catal. Letters.* 87 (2003) 133–142.
- [36] Martins, A., Silva, J. M., Henriques, C., Ribeiro, F. R., Ribeiro, M. F. Influence of rare earth elements La, Nd and Yb on the acidity of H-MCM-22 and H-Beta zeolites, *Catal. Today.* 107–108 (2005) 663–670.
- [37] Lemos, E. F., Lopes, J. M., Ramôa Ribeiro, F. Influence of cerium on the catalytic properties of ZSM-20 zeolite in the cracking of n-heptane: Comparison with rare earth Y zeolites, *Appl. Catal.* 49 (1989) 175–181.
- [38] Scherzer, R. E. R. J. Ion-Exchanged Ultrastable Y Zeolites. 3. Gas Oil Cracking over Rare Earth-Exchanged Ultrastable Y Zeolites, *Ind. Eng. Chem. Res.* 17 (1978) 219–223.
- [39] Martínez, C., Corma, A. Inorganic molecular sieves: Preparation, modification and industrial application in catalytic processes, *Coord. Chem. Rev.* 255 (2011) 1558–1580.
- [40] van Zijll, W. C., Kouwenhoven, H. W. Shells hydro-isomerization process, *Chem. Eng. Prog.* 67 (1971) 65.
- [41] Lazaro, J. F., Corma, A. *Process for the obtainment of a light paraffin isomerization catalyst*, US 5057471, 1991.
- [42] Weyda, H., Köhler, E. Modern refining concepts - An update on naphtha-isomerization to modern gasoline manufacture, *Catal. Today.* 81 (2003) 51–55.

*Chapter 6*

**THE APPLICATION OF STRONTIUM  
DODECEYL SULFATE,  $Sr(DS)_2$   
IN THE SYNTHESIS OF 4,4'-  
DIAMINOTRIARYLMETHANES-LEUCO  
MALACHITE MATERIALS**

*Najmeh Dashtaki and Farahnaz K. Behbahani\**

Department of Chemistry, Karaj Branch,  
Islamic Azad University, Karaj, Iran

**ABSTRACT**

A fast, efficient and versatile route for the synthesis of 4,4'-diaminotriarylmethanes using  $Sr(DS)_2$  as a Lewis acid-surfactant-combined catalyst (LASCs) in the presence of *N,N*-dimethyl aniline and aryl aldehydes is reported. LASCs not only act as a Lewis acid to activate substrate molecules, but also serve as a surfactant to form stable colloidal dispersion systems with organic substrates. Also, the others advantages of LASCs are easy separation and recovery, high activity, selectivity, as a

---

\* Corresponding Author Email: Farahnazkargar@yahoo.com, Tel: 02634182305.

Lewis acid to activate the substrate molecules and as a surfactant to help to solubilize the organic compounds in water.

**Keywords:** Sr(DS)<sub>2</sub>; *N,N*-dimethyl aniline; aldehyde; catalyst, surfactant

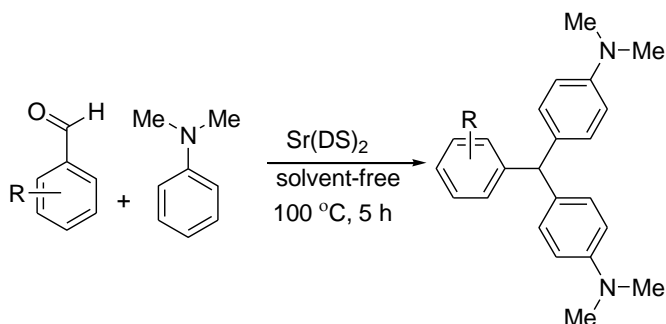
## 1. INTRODUCTION

Dyes may be classified according to chemical structure or by their usage or application methods. According to the chemical structure classification, triarylmethane dyes are among the most important dyes. Triarylmethane dyes are monomethine synthetic dyes with three terminal aryl groups, of which at least one, but preferably two or three, are substituted by a donor group para to the methane carbon atom. Due to the importance of *N,N*-dimethyl aniline (DTM) compounds, several reviews have disclosed on di- and triphenylmethane derivatives [1-5]. These compounds have a broad range of applications in color-forming, manufacturing of novel types of various colorless copying papers, pressure-sensitive heat-sensitive materials, high-speed photo duplicating copying papers, light-sensitive papers, ultrasonic recording papers, electrothermic heat-sensitive recording papers, inks, crayons, typewritten ribbons, and photoimaging systems[6]. Accordingly, different methods for the preparation of the aforementioned compounds have been described such as those from arene nucleophiles and triethyl orthoformate, or benzhydrol in the presence of acid catalysts, [7-10] from condensation of amines and anilines using acids [11] or zeolites [12] and also by reaction of aniline derivatives with metal catalysts such as Pd(OAc)<sub>2</sub> [13] or clay-mediated oxidative coupling of disubstituted anilines using microwave radiation, in which DTM derivatives were obtained in low to moderate yields [14]. One of the most useful methods for the synthesis of DTM is the reaction of arylaldehydes with *N,N*-dimethylaniline in the presence of an acid such as sulfuric acid, HCl, *p*-TSA, zeolites or montmorillonite K-10 [15-20]. Although different methods for the preparation of the aforementioned compounds have been described, most of them however,

suffer from drawbacks such as the use of corrosive acids or toxic or hazardous chemicals, excess of solvents and harsh reaction conditions, which will result in generation of waste streams, complicated workup procedures, byproducts and isomeric mixtures and consequently, low yields. Therefore, there is still a demand to search for a better catalyst with regards to toxicity, selectivity, availability and operational simplicity for the synthesis of triarylmethane compounds.

LASCs (Lewis acid-surfactant-combined catalyst) firstly developed by Kobayashi [21-22] as one of the most widely investigated catalytic system, has attracted increasing attentions during the past decades. Not only LASCs act as a Lewis acid to activate substrate molecules, but also serve as a surfactant to form stable colloidal dispersion systems with organic substrates. Most reports on LASCs enhanced on their uses in organic reactions such as aldol, Diels–Alder, allylation of aldehydes, propargylamines reactions, asymmetric hydroxylation, hydroxy-methylation, ring–opening reactions and so on [23]. Also, due to easy separation and recovery, high activity, selectivity, as a Lewis acid to activate the substrate molecules and as a surfactant to help to solubilize the organic compounds in water, there is still demand for developing LASCs and its usage in organic transformations.

In this communication, we wish to report a green synthesis method for the preparation of DTMs using arylamines and aldehyde derivatives in the presence of strontium dodecyl sulfate as a LASCs (Scheme 1).



Scheme 1. Preparation of DTMs using strontium dodecyl sulfate

## 2. RESULTS AND DISCUSSION

Our initial attempts to test the feasibility of the reaction employed 4-chlorobenzaldehyde and *N,N*-dimethyl aniline under various reaction conditions. Firstly, optimization of different solvents was studied in the benchmark reaction. The results were revealed, that the catalyst more efficiently worked under solvent-free conditions at 100 °C (Table 1). The authors believe strontium dodecyl sulfate as a LASCs homogenizes reaction mixture in the absence of solvent.

**Table 1. Optimizing of kind of solvent and temperature in the synthesis of dimethyl-4-[[4-(dimethylamino)phenyl](4-Chlorophenyl)methyl] aniline**

Entry	Solvent	<i>t</i> / °C	Yield / % <sup>a</sup>
1	free	r.t.	-
2	free	110 °C	93
3	CH <sub>2</sub> Cl <sub>2</sub>	reflux	68
4	H <sub>2</sub> O	“	-

<sup>a</sup>Yields of the isolated products from the reaction of 4-chlorobenzaldehyde (1.5 mmol, 0.2 g), *N,N*-dimethylaniline (4.5 mmol, 0.54 g) Sr(DS)<sub>2</sub> (5 mol%).

**Table 2. Optimizing of the catalyst amount in the synthesis of dimethyl-4-[[4-(dimethylamino)phenyl](4-Chlorophenyl)methyl] aniline**

Entry	Sr(DS) <sub>2</sub> (mol%)	T / h	Yield / % <sup>a</sup>
1	free	24	24
2	2	7	70
3	5	5	93
4	10	5	93
5	15	5	93
6	20	5	93

<sup>a</sup>Yields of the isolated products from the reaction of 4-chlorobenzaldehyde (1.5 mmol, 0.2 g), *N,N*-dimethylaniline (4.5 mmol, 0.54 g) Sr(DS)<sub>2</sub> (5 mol%).

Also the effect of catalytic amount of Sr(DS)<sub>2</sub> on the model reaction was investigated. It was found that amount of the catalyst played a major role in establishment of the desired product yield. The best optimized

reaction condition was found at 5 mol% of  $\text{Sr}(\text{DS})_2$  under solvent-free conditions at 100 °C (Table 2).

Therefore, a wide variety of substituents were subjected on the arene, in *ortho*-, *meta*- and *para*-positions. The aryl aldehydes with electron-withdrawing groups such as halo-substituents at the *para*- and nitro-substituents at the *ortho*-, *meta*-, and *para*-positions gave excellent yields. However with electron-donating groups such as methyl and *N,N*-dimethyl amino substituents, lower yields of the desired products were obtained due to decrease the electrophilicity of carbonyl group in the corresponding electrophilic aromatic substitution reactions (Table 3).

**Table 3. Synthesis of 4,4'-diaminotriarylmethane using aromatic aldehydes, *N,N*-dimethyl anillin and  $\text{Sr}(\text{DS})_2$ .**

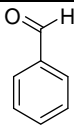
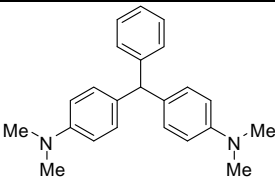
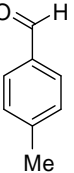
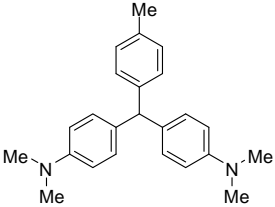
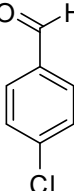
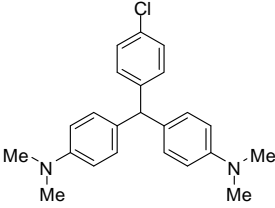
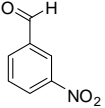
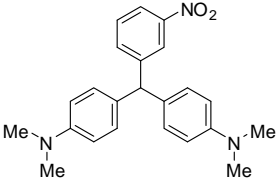
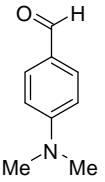
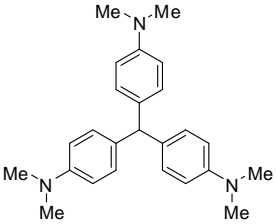
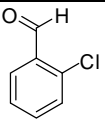
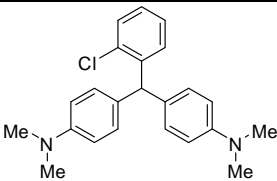
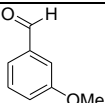
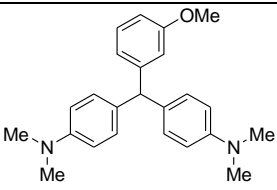
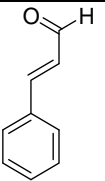
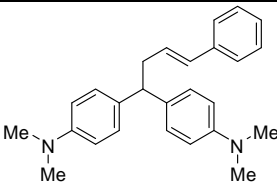
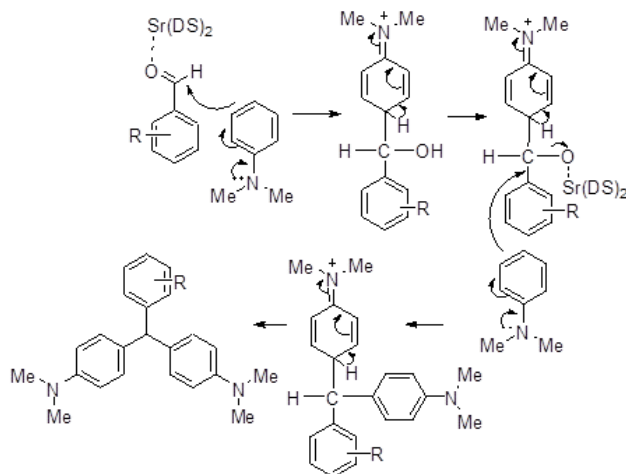
Entry	Aldehyde	Product	Time (h)	Yield %	Mp. °C
					Found Reported [ref.]
1			5	80	89–91 91–92 [24]
2			4	76	95–97 97–98 [24]
3			4	93	88–90 88–89 [24]

Table 3. (Continued)

Entry	Aldehyde	Product	Time (h)	Yield %	Mp. °C Found Reported [ref.]
4			6	94	145–147 146–148 [24]
5			5	70	166–167 167–68 [24]
6			6	94	107-108 108-109 [25]
7			5	80	oil
8			5	85	oil



Proposed mechanism for the synthesis of 4,4'-diaminotriarylmethane has been depicted in scheme 2.



Scheme 2. Suggested mechanism for the synthesis of DTMs using strontium dodecyl sulfate

### 3. EXPERIMENTAL

Melting points were measured by using the capillary tube method with an electro thermal 9200 apparatus. IR spectra were recorded on Perkin Elmer FT-IR spectrometer did scanning between 4000–400  $\text{cm}^{-1}$ .  $^1\text{H}$  NMR spectra were obtained on Bruker DRX-300MHz NMR instrument in  $\text{CDCl}_3$ . Analytical TLC of all reactions was performed on Merck precoated plates (silica gel 60F-254 on aluminium). All compounds are known and spectra and physical data were compared with those of authentic samples [24, 25].

#### 3.1. Preparation of $\text{Sr}(\text{DS})_2$ from $\text{Sr}(\text{NO}_3)_2$ and Sodium Dodecyl Sulfate [21]

To a stirring solution of sodium dodecyl sulfate (40 mmol, 11.51 g) in distilled water (300 mL) was added a solution of  $\text{Sr}(\text{DS})_2$  (10 mmol, 2.11

g) in water (100 mL) at room temperature. A white precipitate appeared immediately and the mixture was stirred for another 30 min. The white solid was separated by filtration and washed with water ( $2 \times 150$  mL). The isolated solid product was dried under reduced pressure and Sr(DS)<sub>2</sub> as a white powder was obtained in 87% yield (10 g). Mp. 168 °C (dec).

### **3.2. Synthesis of 4,4'-Diaminotriarylmethane Using Sr(DS)<sub>2</sub>. General Procedure**

A vial equipped with a stir bar was charged with aryl aldehyde (0.5 mmol, 1eq), *N,N*-dimethyl aniline (1.5mmol, 3eq) and Sr(DS)<sub>2</sub> (20 mol %) and the vial was capped. The resulting mixture was heated in an oil bath at about 100 °C for 5-6 h, and the course of the reaction was monitored by TLC on silica gel with ethyl acetate: n-hexane (1:4) as eluent. Finally, the reaction mixture was cooled, dichloromethane (15 ml) was added and the catalyst was removed by filtration. After evaporation of the solvent, the crude product was resulted and crystallized from ethanol.

### **3.3. Recycling of the Catalyst**

After the completion of the reaction, dichloromethane (15 ml) was added to the reaction mixture, and then, the catalyst was separated by filtration. The precipitate was washed with dichloromethane and then air dried for the catalyst reusability. The catalyst was recycled for the synthesis of dimethyl-4-[[4-(dimethylamino)phenyl](4-Chlorophenyl)methyl] aniline three times (95, 89, 85)% (entry 3, Table 3).

## **CONCLUSION**

In summary, the authors have developed a simple, efficient and green methodology for the synthesis of a diaminotriarylmethane leuco base

materials using a catalytic amount of strontium dodecyl sulfate under solvent-free conditions. The simple experimental procedure, solvent-free reaction conditions, and good yields, easy separation and recovery of the catalyst are the advantages of the present method.

## REFERENCES

- [1] Lubs, H.A. *Chemistry of Synthetic Dyes and Pigments*. Reinhold Publishing Corporation; New York; 1955.
- [2] Kimura, K., Mizutani, R., Yokoyama, M., Arakawa, R., Sakurai, Y. (2000) Metal-ion complexation and photochromism of triphenylmethane dye derivatives incorporating monoaza-15-crown-5 moieties. *J. Am. Chem. Soc.* 122:5448-54.
- [3] Duxbury, D.F. (1993) The photochemistry and photophysics of triphenylmethane dyes in solid and liquid media. *Chem. Rev.* 93:381-433.
- [4] Karukstis, K.K., Gullledge, A.V. (1998) Analysis of the solvatochromic behavior of the disubstituted triphenylmethane dye brilliant green. *Anal. Chem.* 70:4212-7.
- [5] Kolpashchikov, D.M. Binary malachite green aptamer for fluorescent detection of nucleic acids. *J. Am. Chem. Soc.* 2005; 127:12442-3.
- [6] Muthyala, R. In *Chemistry and Applications of Leuco Dyes*, Eds.: Katrizky AR, Sabongi, G.J., Plenum New York, 1997.
- [7] Casiraghi, G., Casnati, G., Cornia, M. (1973) Regiospecific reactions of phenol salts: reaction-pathways of alkylphenoxy-magnesiumhalides with triethylorthoformate. *Tetrahedron Lett.* 14:679-82.
- [8] Pindur, U., Flo, C. (1989) First reactions of dialkoxycarbenium tetrafluoroborates with pyrroles, 5H- dibenz [b, f] azepines, and electron- rich arenes. *J. Heterocyc. Chem.* 26:1563-8.
- [9] Burmester, A., Stegmann, H.B. (1989) Alkylierung von 2-t-Butylphenol mit Diarylcarbinolen. *Synthesis.* 1981; 1981:125-6.

- [10] Jafarpour, F., Bardajee, G.R., Pirelahi, H., Oroojpour, V., Dehnamaki, H., Rahmdel, S. (2009) An Efficient Solvent-free Synthetic Technique of 4, 4'- Diaminotriarylmethane Leuco Materials. *Chin. J. Chem.* 27(7):1415-9.
- [11] Weil, H., Sapper, E., Krämer, E., Klöter, K., Selberg, H. (1928) Über Diamino- triphenylmethan und Ähnliches. *Eur. J. Inorg. Chem.* 61:1294-307.
- [12] Alvaro, M., García, H., Sanjuán, A., Esplá, M. (1998) Hydroxyalkylation of benzene derivatives by benzaldehyde in the presence of acid zeolites. *Appl. Catal. A: Genl.* 175:105-12.
- [13] Sato, H. (1998) The Formation of Crystal Violet by the Reaction of N, N-Dimethylaniline with Aluminum Chloride. *Bull. Chem. Soc. Japan.* 1965; 38:1719-21.
- [14] López-Cortés, J.G., Penieres-Carrillo, G., Ortega-Alfaro, M.C., Gutiérrez-Pérez, R., Toscano, R.A., Alvarez-Toledano, C. (2000) Oxidative coupling-type mechanism of N, N-dialkylanilines in solvent-free conditions forming crystal violet derivatives. A clay-mediated and microwave-promoted approach. *Can. J. Chem.* 78:1299-304.
- [15] Alvaro, M., García, H., Sanjuán, A., Esplá, M. (1998) Hydroxyalkylation of benzene derivatives by benzaldehyde in the presence of acid zeolites. *Appl. Catal. A: Genl.* 175:105-12.
- [16] Pratt, E.F., Green, L.Q. (1953) Reaction rates by distillation. IV. The Effect of Changes in Structure on the Rate of the Baeyer Condensation. *J. Am. Chem. Soc.* 75:275-8.
- [17] Fukui, K., Inamoto, Y., Kitano, H., Nagata, C. (1959) Reaction of 4-Dimethylaminoazobenzene and Related Compounds with 4, 4'-Bis-(dimethylamino)-benzhydrol. *J. Am. Chem. Soc.* 81:5954-7.
- [18] Zhang, Z.H., Yang, F., Li, T.S., Fu, C.G. (1997) Montmorillonite clay catalysis VII: Synthesis of triarylmethanes via Baeyer condensation of aromatic aldehydes with N, N-dimethylaniline catalysed by montmorillonite K-10. *Synthetic communications.* 27:3823-8.

- [19] Guzman-Lucero, D., Guzman, J., Likhatchev, D., Martinez-Palou, R. (2005) Microwave-assisted synthesis of 4, 4'-diaminotriphenylmethanes. *Tetrahedron. lett.* 46:1119-22.
- [20] Zolfigol, M.A., Salehi, P., Shiri, M., Tanbakouchian, Z. (2007) A new catalytic method for the preparation of bis-indolyl and tris-indolyl methanes in aqueous media. *Catal. Commun.* 8:173-8.
- [21] Kobayashi, S., Manabe, K. (2002) Development of novel Lewis acid catalysts for selective organic reactions in aqueous media. *Acc. Chem. Res.* 35:209-17.
- [22] Kobayashi, S., Wakabayashi, T., Nagayama, S., Oyamada, H. (1997) Lewis acid catalysis in micellar systems. Sc(OTf)<sub>3</sub>-catalyzed aqueous aldol reactions of silyl enol ethers with aldehydes in the presence of a surfactant. *Tetrahedron. lett.* 38:4559-62.
- [23] Jafarpour, M., Rezaeifard, A., Aliabadi, M. (2010) An environmentally benign catalytic method for efficient and selective nucleophilic ring opening of oxiranes by zirconium tetrakis (dodecyl sulfate). *Helv. Chim. Act.* 93:405-13.
- [24] Behbahani, F.K., Khademloo, E. (2014) Solvent-free synthesis of 4, 4'-diaminotriarylmethanes-leuco malachite materials in the presence of FePO<sub>4</sub>. *Russ. J. Appl. Chem.* 87:1507-10.
- [25] Bardajee, G., Jafarpour, F. (2009) Bi(NO<sub>3</sub>)<sub>3</sub>· 5H<sub>2</sub>O mediated synthesis of 4, 4'-diaminotriarylmethane leuco malachite compounds under solvent-free conditions. *Open Chem.* 7:138-42.



# INDEX

## A

absorption spectra, 100  
acid, viii, xi, 188, 194, 195, 196, 199, 200, 201, 202, 203, 206, 208, 209, 211, 212, 213, 220, 221  
acidic, 194, 206  
acidity, 196, 197, 198, 201, 202, 210  
acoustics, 77, 81, 82, 97  
activated carbon, 118, 153  
activation energy, 8, 13  
active site, xi, 188, 196, 199, 200, 201  
adhesion, 118, 126, 170, 171  
adhesion properties, 170, 171  
adsorption, 4, 8, 9, 19, 26, 118, 152, 155, 199, 204, 208  
aldehydes, viii, xi, 211, 212, 213, 215, 216, 218, 220, 221  
angstroms, 129, 133, 141  
aniline, viii, xi, 211, 212, 214, 218  
anisotropy, 62, 63, 79  
argon, 18, 41, 42, 44, 45, 46, 116, 125, 145, 148, 150, 152, 153  
aromatic hydrocarbons, x, 187  
atmosphere, 37, 163  
atmospheric pressure, 21

atomic positions, 122  
atoms, viii, x, 2, 3, 4, 5, 6, 7, 8, 14, 21, 25, 33, 35, 36, 42, 46, 48, 49, 60, 62, 73, 92, 97, 116, 117, 118, 119, 120, 121, 122, 125, 126, 127, 128, 129, 131, 132, 133, 134, 135, 136, 139, 141, 142, 144, 145, 146, 147, 148, 149, 152, 155, 191

## B

bending, 38, 160, 161, 162, 163, 164, 165, 166, 167, 168, 170, 171, 172, 173, 174, 175, 176, 177, 178, 179, 180, 181  
benzene, x, 118, 152, 153, 187, 189, 191, 220  
binary oxides, 161  
binding energy, 118  
biosphere, 117  
birefringence, 87  
Boltzmann constant, 8, 62  
bombardment, vii, x, 3, 7, 8, 18, 20, 21, 33, 36, 39, 40, 49, 116, 117, 118, 119, 120, 121, 128, 129, 130, 131, 132, 133, 134, 136, 137, 138, 139, 140, 141, 142, 143, 144, 145, 146, 147, 148, 149, 150, 152, 153, 155, 156

bonding, 93, 96, 97, 122  
 bonds, 98, 123, 130, 131, 136, 146, 148,  
 203  
 branched isomers, xi, 187, 201, 203  
 Brillouin, L., v, vii, ix, 11, 59, 60, 61, 67,  
 68, 69, 70, 71, 74, 75, 79, 86, 100, 102,  
 111, 113  
 brittleness, 158, 161  
 Bruker DRX, 217  
 building blocks, 43

## C

cadmium, 151, 152  
 carbon, vii, viii, 1, 2, 3, 4, 5, 7, 8, 10, 11, 12,  
 13, 15, 17, 18, 19, 20, 21, 22, 23, 24, 25,  
 26, 28, 29, 30, 33, 36, 37, 38, 39, 40, 41,  
 43, 46, 47, 48, 49, 118, 121, 125, 128,  
 145, 146, 152, 154, 156, 162, 165, 189,  
 191, 203, 212  
 carbon atoms, 7, 8, 11, 13, 17, 21, 24, 25,  
 28, 29, 33, 48, 128, 146, 189, 191  
 carbon dioxide, 145  
 carbon film, 12, 22, 49  
 carbon nanostructures, v, vii, viii, 1, 2, 3, 4,  
 5, 7, 18, 37, 38, 39, 41, 43, 47, 49  
 carbon nanotubes, vii, viii, 1, 3, 14, 38, 40,  
 43, 154  
 carbon tetrachloride, 203  
 catalysis, 208, 209, 220, 221  
 catalyst, viii, xi, 2, 3, 4, 6, 8, 12, 16, 19, 24,  
 25, 26, 27, 28, 29, 30, 31, 33, 34, 35, 36,  
 37, 38, 40, 47, 48, 49, 194, 195, 196,  
 198, 200, 201, 202, 203, 204, 205, 206,  
 207, 208, 210, 211, 212, 213, 214, 218,  
 219  
 catalytic activity, 195, 202, 203, 206  
 catalytic properties, 198, 210  
 catalytic system, 213  
 cellulose, 163, 172, 173  
 chalcogenides, 159

charge trapping, 159, 181  
 charge trapping/de-trapping, 159, 181  
 chemical, 2, 39, 44, 74, 81, 85, 87, 92, 93,  
 94, 97, 122, 150, 154, 164, 165, 167,  
 169, 180, 212  
 chemical etching, 39  
 chemical inertness, 165  
 chemical properties, 2, 74  
 chemical structures, 164, 169  
 chemical vapor deposition, 150, 167, 180  
 chemical vapour deposition, 2  
 cluster beam, 117, 118, 119, 120, 130, 133,  
 135, 140, 141, 142, 143, 144, 146, 147,  
 148, 150  
 cluster bomb, 118, 130, 134, 140, 144, 145,  
 146, 147, 149, 150, 152, 153, 156  
 cluster impacts, 120, 121, 128, 130  
 clusters, vii, ix, 94, 115, 116, 117, 118, 119,  
 120, 121, 124, 129, 130, 131, 132, 133,  
 134, 135, 136, 137, 138, 139, 140, 141,  
 142, 144, 145, 146, 148, 149, 152, 153,  
 155, 156  
 combustion, 188, 189  
 composition, 43, 46, 76, 78, 80, 82, 84, 85,  
 86, 87, 93, 94, 95, 96, 99, 101, 165, 189,  
 191, 192, 206, 207  
 compounds, 117, 154, 191, 194, 203, 212,  
 217, 221  
 compression, 189  
 computer, 120, 153, 154, 155, 177  
 conductive filament, 161  
 conductivity, 165, 166, 171  
 configuration, 159, 168, 172  
 contamination, ix, 115, 163  
 cooling, 62, 74, 75, 76, 77, 81, 83  
 copper, vii, ix, 115, 116, 120, 121, 124, 125,  
 128, 129, 130, 132, 145, 146, 147, 148,  
 149, 150, 151, 152, 153  
 cost, 88, 163, 165, 166, 171, 177, 180, 189,  
 195  
 covalent bond, 123, 145  
 covalent bonding, 123



crystalline, vii, ix, 38, 59, 71, 73, 75, 88, 89, 146, 148  
 crystallization, 83, 85, 94, 97, 101  
 crystals, vii, ix, 59, 62, 66, 71, 72, 73, 87, 88, 101, 146, 161, 200, 202  
 cycles, 128, 130, 137, 158, 159, 161, 163, 164, 165, 167, 168, 169, 170, 171, 173, 174, 175, 180

## D

data retention time, 160  
 decomposition, 7, 11, 15, 17, 18, 20, 21, 22, 26, 27, 48, 77, 101  
 deconvolution, 72, 79, 100  
 defects, 40, 71, 87, 126  
 deformation, 38, 135  
 degradation, 117, 170, 171, 173, 176, 177  
 density fluctuations, 60, 62, 63, 64, 68, 73, 74, 82, 83, 84  
 density functional theory, 120, 146  
 density profile, 127, 134, 135, 149  
 depolarization, 63, 77, 79, 81  
 deposition, viii, 2, 3, 5, 6, 7, 8, 12, 21, 24, 25, 31, 32, 39, 40, 44, 48, 126, 152, 167  
 depth, 8, 14, 15, 16, 17, 48, 91  
 derivatives, 212, 213, 219, 220  
 desorption, 4, 9, 26, 27, 33, 119, 154, 197  
 destruction, 18, 129  
 detachment, 135, 136, 138, 144, 147, 149, 170  
 detection, 67, 118, 219  
 dielectric constant, 83  
 diffusion, 4, 5, 8, 11, 12, 23, 24, 25, 26, 27, 29, 30, 31, 33, 37, 44, 49, 68, 127, 129, 130, 142, 196, 197, 200, 201  
 dispersion, viii, xi, 201, 211, 213  
 dissociation, 7, 8, 11, 18, 20, 21, 22, 26, 27, 31, 33, 42, 48  
 divacancy, 118, 126  
 dopants, 75, 76, 83, 92, 93, 94, 95, 96

## E

edges of graphene, 120, 149, 150  
 electric field, 3, 38, 39, 40, 49, 87, 88  
 electrode/insulator/electrode, 158  
 electrodes, 89, 116, 165, 167, 170, 171, 173, 174, 177, 178, 180, 181  
 electron, 4, 8, 26, 42, 44, 45, 46, 47, 86, 98, 145, 150, 151, 167, 172, 215, 219  
 electron microscopy, 86  
 electronic systems, 158, 161  
 electrooptical fiber, 60, 102  
 electro-optical properties, 92  
 endurance, 158, 159, 161, 163, 164, 167, 171, 173  
 energy, ix, 2, 4, 8, 9, 12, 13, 15, 16, 17, 18, 21, 26, 32, 33, 40, 48, 49, 88, 98, 115, 116, 118, 119, 122, 124, 128, 129, 130, 131, 132, 133, 134, 135, 136, 137, 138, 139, 140, 141, 142, 144, 145, 146, 147, 148, 149, 150, 152, 153, 155, 159  
 energy consumption, 159  
 energy transfer, 98, 118  
 environment, viii, ix, 2, 5, 6, 21, 24, 33, 34, 37, 38, 41, 48, 115, 118, 189, 206  
 environmental regulations, 189, 206  
 environments, 117, 171, 181  
 etching, viii, 2, 5, 6, 7, 13, 14, 16, 17, 18, 19, 24, 25, 35, 36, 37, 40, 48, 49, 170  
 evolution, 66, 101, 136, 149, 161, 172, 178  
 extraction, 118, 119, 151

## F

fabrication, x, 158, 161, 163, 166, 169, 170, 171, 173, 175, 177, 178, 179, 180  
 feedstock, 7, 43, 195, 196, 203, 205, 206  
 film, ix, 12, 13, 14, 15, 16, 17, 18, 20, 22, 23, 37, 40, 44, 116, 118, 120, 121, 126, 127, 128, 129, 130, 131, 132, 133, 134, 135, 136, 137, 138, 139, 141, 142, 143,

145, 146, 147, 148, 149, 151, 152, 153,  
155, 156, 163, 166, 167, 200  
film formation, 16, 120  
film thickness, 23, 134  
films, 39, 43, 120, 145, 146, 155  
flexibility, 116, 161, 163, 165  
flexible, v, vii, x, 157, 158, 159, 160, 162,  
163, 164, 165, 166, 167, 168, 169, 170,  
171, 172, 173, 174, 175, 176, 177, 178,  
179, 180, 191  
fluctuations, 60, 62, 63, 64, 76, 77, 79, 82,  
83, 84, 85, 95, 129, 131  
formation, ix, 2, 5, 12, 16, 17, 18, 20, 22,  
37, 38, 40, 43, 44, 47, 48, 85, 94, 122,  
161, 162, 169, 190, 196, 198

## G

glass, vii, ix, 59, 60, 61, 62, 64, 67, 68, 69,  
70, 73, 74, 75, 76, 77, 78, 79, 80, 81, 82,  
83, 84, 85, 86, 87, 89, 91, 92, 93, 94, 95,  
96, 97, 98, 99, 100, 101, 102, 103, 104,  
105, 106, 107, 108, 110, 111, 112, 113,  
114, 165, 174, 175, 177  
glass transition, 73, 80, 101  
glass transition temperature, 73, 80  
glass-ceramics, 60, 101  
glasses, vii, ix, 59, 60, 62, 63, 64, 66, 68,  
69, 70, 73, 75, 80, 81, 82, 83, 84, 85, 86,  
87, 88, 89, 90, 91, 92, 93, 95, 96, 97, 98,  
101, 102, 111, 112, 113  
graphene, v, vii, ix, 25, 27, 28, 29, 37, 38,  
115, 116, 117, 118, 119, 120, 121, 123,  
126, 127, 128, 129, 130, 131, 132, 133,  
134, 135, 136, 137, 138, 139, 140, 141,  
142, 143, 144, 145, 146, 147, 148, 149,  
150, 151, 152, 153, 154, 155, 156, 163,  
165, 169, 170, 172, 174  
graphene sheet, ix, 25, 27, 28, 29, 116, 117,  
120, 121, 123, 126, 128, 129, 130, 131,  
132, 140, 141, 145, 146, 150

graphite, 117, 118, 153, 163  
growth, vii, viii, 1, 2, 3, 4, 5, 6, 7, 12, 13,  
14, 15, 16, 17, 18, 19, 20, 21, 22, 23, 24,  
27, 29, 30, 31, 32, 33, 34, 35, 36, 37, 38,  
39, 40, 41, 42, 43, 44, 45, 46, 47, 48, 49,  
77, 80, 81, 85, 91, 93, 94, 97, 99, 131  
growth mechanism, viii, 2  
growth models, 2  
growth rate, viii, 2, 5, 12, 13, 14, 15, 16, 17,  
18, 19, 20, 29, 30, 31, 32, 33, 35, 37, 43,  
47  
growth temperature, 20  
growth time, 22

## H

heat capacity, 128  
heat loss, 33  
heat release, 32, 33  
heat transfer, 38  
heavy metals, vii, ix, 115, 118, 119, 147  
heptane, 188, 193, 199, 201, 209, 210  
hexane, x, xi, 187, 188, 189, 190, 193, 195,  
196, 199, 202, 206, 207, 208, 209, 210,  
218  
high performance computing, 112  
high resistance state, 158  
hybrid, 38, 40, 43, 44, 163, 166, 172, 173,  
174, 188  
hydrocarbons, 45, 154, 188, 190, 191  
hydrogen, 3, 7, 9, 10, 13, 17, 24, 26, 28, 31,  
33, 35, 36, 37, 40, 41, 42, 43, 46, 47,  
117, 126, 150, 194, 200, 203, 207, 208  
hydrogen atoms, 17, 31, 35, 40, 42, 46, 117,  
126  
hydrogenation, 133, 192, 202

## I

impurities, 67, 75, 83, 98, 193, 205

incidence, vii, ix, 115, 118, 132, 138, 139, 140, 141, 142, 143, 144, 147, 148, 149

incident angle, ix, 115, 118, 120, 128, 129, 130, 131, 132, 133, 138, 139, 141, 145, 148, 150

industry, x, 187, 188, 189, 207

inhomogeneity, 9, 43, 86

integrated circuits, 164

integration, 159, 160, 163, 174

interface, 12, 28, 33, 34, 35, 151

interference, 64, 65, 66, 67

ion bombardment, 3, 7, 8, 18, 20, 21, 33, 36, 39, 40, 155

ion implantation, 16, 18

ion migration, 159, 181

ions, vii, viii, ix, 2, 5, 6, 7, 8, 9, 10, 13, 14, 15, 16, 17, 18, 20, 21, 25, 35, 36, 37, 40, 41, 43, 44, 45, 46, 47, 48, 59, 60, 64, 73, 83, 92, 93, 94, 96, 97, 98, 117, 145

irradiation, 40, 117, 119, 146, 147, 149, 150, 151, 155

isomerization, xi, 188, 190, 191, 192, 193, 195, 196, 198, 199, 200, 202, 204, 205, 206, 207, 208, 209, 210

isomers, xi, 187, 189, 190, 193, 194, 195, 196, 197, 198, 199, 201, 202, 203, 206

## K

kinetic model, 44

kinetic parameters, 96

kinetics, 44, 97, 208

## L

laboratory studies, 198

Landau-Placzek ratio, 60, 62, 63, 64, 68, 69, 70, 72, 75, 77, 79, 81, 82, 84, 86, 96, 99, 100, 101

lasers, 66, 93, 94, 102

Lennard-Jones potential, 125, 126

light, 60, 61, 62, 64, 65, 66, 67, 70, 72, 79, 87, 88, 90, 101, 162, 192, 208, 210, 212

light beam, 62

light scattering, 60, 61, 64, 67, 79, 101

logic-in-memory, 160, 181

low resistance state, 158

low temperatures, 18, 48, 123

luminescence, 67, 83, 92, 93, 96, 97, 98, 112

## M

magnetic field, 38

magnitude, 36, 117, 135, 138, 144

Mandelstam, L., 60, 68, 69, 70, 75, 86, 100, 102, 111, 113

manufacturing, 73, 83, 88, 91, 101, 207, 212

materials, vii, viii, ix, x, 59, 60, 61, 67, 84, 88, 89, 99, 101, 102, 115, 117, 152, 157, 158, 159, 160, 161, 162, 163, 164, 166, 170, 173, 177, 212, 219, 221

materials science, 101

mechanical performances, 167

media, 61, 87, 89, 93, 98, 118, 151, 160, 161, 163, 219, 221

melt, 62, 64, 73, 74, 77, 80, 81, 83, 85, 93, 94

melting, 75, 78, 81, 128, 139, 145

melting temperature, 128

memory, 158, 159, 160, 161, 163, 164, 166, 169, 170, 173, 174, 177, 181

memory performance, 161, 163

mercury, vii, ix, 115, 116, 118, 119, 124, 125, 128, 139, 140, 141, 142, 147, 148, 149, 153, 154, 155, 156

mesoporous materials, 210

metal function, 195, 206

metals, viii, ix, xi, 115, 117, 119, 124, 125, 126, 146, 148, 151, 154, 156, 165, 188, 195, 202

microcrystalline, 44

microstructure, 161, 162, 167  
 microstructures, 87  
 modelling, v, vii, viii, 1, 4, 5, 6, 21, 24, 37,  
 39, 41, 44, 47, 48, 153, 154  
 models, vii, viii, 2, 4, 5, 39, 41, 43, 47, 48,  
 120  
 molecular dynamics, vii, ix, 39, 40, 115,  
 116, 117, 121, 146, 150, 152, 154, 156  
 molecules, viii, xi, 7, 14, 17, 18, 19, 28, 33,  
 35, 36, 39, 40, 42, 43, 47, 159, 189, 191,  
 192, 196, 200, 206, 211, 213  
 Moliere potential, 125  
 Morse potential, 125, 148, 154  
 multi-component systems, 122

## N

*N,N*-dimethyl aniline, viii, xi, 211, 212, 214,  
 218  
 nanocomposites, 2, 123  
 nanocrystals, 98, 102, 113  
 nanofibers, vii, viii, 1, 2, 3, 37, 173  
 nanomaterials, 48  
 nanometer, 85, 86  
 nanometer scale, 86  
 nanoparticles, viii, 2, 3, 5, 7, 16, 19, 31, 35,  
 36, 37, 38, 44, 45, 47, 48, 49, 152, 153,  
 154  
 nanostructured materials, 150  
 nanostructures, vii, viii, 1, 2, 3, 4, 5, 7, 18,  
 35, 36, 38, 39, 41, 43, 47, 49, 117  
 nanotechnology, 145  
 nanotube, 3, 6, 8, 14, 15, 16, 17, 18, 19, 20,  
 36, 156  
 neutral, viii, 2, 4, 8, 9, 12, 14, 17, 21, 29, 31,  
 33, 35, 36, 38, 39, 41, 42, 44, 45, 46, 48,  
 153  
 nitrides, 159, 161, 165  
 nitrobenzene, 89  
 nitrogen, 154, 191  
 noble metals, 146, 195

nonequilibrium, 44, 61  
 nonvolatile memory, 158  
 nucleation, 3, 4, 21, 37, 38, 40, 44, 49  
 nucleic acid, 219  
 nucleophiles, 212

## O

octane, x, xi, 187, 188, 189, 191, 193, 203,  
 205, 206, 209  
 octane number, x, xi, 187, 188, 189, 190,  
 191, 193, 203, 205, 206, 209  
 optical fiber, vii, ix, 59, 74, 84, 88, 90  
 optical microscopy, 179  
 optical parameters, vii, ix, 59, 101  
 optical properties, 153  
 optimization, 76, 91, 98, 163, 181, 199, 214  
 organic compounds, xi, 212, 213  
 oxidation, 75, 117, 167, 177  
 oxygen, 97, 171, 189

## P

palladium, xi, 188, 209  
 particle bombardment, 155  
 phase decomposition, 94, 101  
 phase transitions, 73  
 phosphate, 90, 97, 112, 113  
 phosphate glasses, 90, 97, 112, 113  
 physical properties, 99, 116, 151  
 plasma enhanced chemical vapour  
 deposition, 2, 3  
 plasma-assisted growth, vii, viii, 1, 5, 24, 47  
 platinum, xi, 188, 196, 207, 208, 209  
 polymeric composites, 163  
 polymers, 159, 163, 165  
 preparation, iv, 43, 194, 212, 213, 221  
 production technology, 88, 89  
 purification, vii, x, 116, 132, 147

## Q

quantum dot, vii, ix, 59, 60, 98, 100, 102, 113

## R

radiation, 33, 61, 87, 92, 96, 98, 99, 102, 171  
 radicals, 21, 37, 39, 43, 46, 48  
 radius, 8, 28, 30, 45, 99, 125, 159, 160, 161, 162, 163, 164, 165, 166, 167, 168, 169, 170, 171, 172, 173, 174, 177, 178, 179, 180  
 Raman, 60, 65, 84, 85, 90, 91, 97, 100, 102, 106, 111, 113, 153  
 Raman spectra, 85, 90, 153  
 Raman spectroscopy, 84  
 rare earth elements, 202, 208, 209, 210  
 rare-earth ions, 60  
 raw materials, 75  
 Rayleigh, v, vii, ix, 59, 60, 61, 62, 63, 64, 68, 69, 70, 71, 73, 74, 75, 76, 77, 79, 81, 82, 83, 84, 85, 86, 87, 90, 91, 94, 98, 99, 100, 101, 102, 111, 112, 113  
 reactions, viii, xi, 7, 11, 20, 21, 24, 26, 31, 33, 39, 44, 46, 150, 187, 188, 197, 199, 203, 213, 217, 219, 221  
 recovery, xi, 211, 213, 219  
 refractive index, 80, 87, 88  
 reset process, 159  
 resistive random access memory, 158  
 resistive switching, vii, x, 157, 158, 159, 160, 161, 162, 163, 164, 165, 166, 167, 168, 169, 170, 171, 172, 173, 174, 175, 176, 177, 178, 179, 180  
 resistive switching memories, vii, x, 157, 158, 159, 160, 162, 164, 165, 166, 167, 170, 171, 172, 173, 177, 179, 180  
 room temperature, 63, 68, 70, 73, 74, 118, 168, 195, 218

roughness, x, 116, 126, 127, 131, 138, 139, 144, 146, 148, 149, 150, 163, 165  
 Royal Society, 162, 168  
 Russia, 59, 74, 75, 76, 98, 115  
 Russian literature, 60

## S

scattering, v, vii, ix, 59, 60, 61, 62, 63, 64, 65, 66, 67, 68, 69, 70, 73, 74, 75, 76, 77, 79, 81, 82, 83, 84, 85, 86, 87, 90, 91, 94, 97, 98, 99, 100, 101, 102, 103, 106, 111, 113, 114, 153  
 scattering intensity, 64, 82, 85, 94, 99  
 Schwerdtfeger, 124, 140, 154  
 segregation, 60, 92, 94, 95, 96, 97  
 selectivity, xi, 194, 195, 196, 197, 200, 201, 202, 203, 206, 208, 211, 213  
 self-diffusion coefficient, 127, 129, 130, 142  
 self-organization, 38  
 set process, 159  
 silica, 74, 75, 76, 77, 84, 91, 97, 98, 196, 217, 218  
 silicon, 34, 41, 146, 151, 155, 165  
 sodium dodecyl sulfate, 217  
 species, vii, viii, 2, 3, 4, 5, 6, 7, 8, 9, 10, 12, 18, 19, 21, 24, 25, 26, 31, 35, 38, 41, 42, 43, 44, 45, 47, 48, 85  
 spectroscopy, vii, ix, 59, 60, 65, 68, 70, 72, 73, 77, 84, 86, 87, 96, 99, 102, 111, 113  
 spin, 152, 166, 173, 174, 175, 177  
 Sr(DS)<sub>2</sub>, vi, viii, xi, 211, 212, 214, 215, 217, 218  
 storage media, x, 157, 160, 161, 162, 163  
 stress, 69, 102, 126, 127, 129, 130, 131, 137, 138, 143, 144, 149, 189  
 strontium, 213, 214, 217, 219  
 structure, ix, 33, 49, 60, 64, 73, 77, 81, 84, 87, 91, 92, 93, 96, 101, 116, 117, 120, 122, 126, 147, 153, 155, 159, 161, 164,

168, 170, 171, 172, 173, 178, 196, 197, 198, 199, 203, 212

substrate, viii, x, xi, 2, 3, 4, 5, 6, 7, 17, 20, 21, 22, 23, 24, 32, 33, 34, 35, 36, 37, 38, 43, 47, 48, 49, 120, 125, 128, 129, 132, 141, 146, 147, 150, 155, 157, 160, 166, 167, 169, 170, 171, 174, 175, 211, 213

substrates, viii, xi, 3, 41, 153, 163, 165, 170, 171, 175, 180, 211, 213

sulfate, 213, 214, 217, 219, 221

sulfur, 189, 191, 195, 203, 204, 206

surface roughness, 127, 165

surfactant, viii, xi, 118, 151, 211, 212, 213, 221

switching endurance, 159, 167, 173

synaptic emulation, 160, 181

synergistic effect, 195, 202

synthesis, viii, xi, 4, 20, 43, 48, 77, 79, 81, 92, 150, 199, 211, 212, 213, 214, 217, 218, 221

## T

target, vii, ix, 115, 117, 119, 121, 129, 134, 138, 142, 144, 146, 147, 148, 155

temperature, viii, 2, 5, 8, 14, 18, 20, 21, 22, 23, 24, 26, 30, 32, 33, 34, 35, 36, 37, 38, 40, 48, 62, 64, 66, 71, 73, 74, 75, 76, 77, 78, 79, 81, 82, 83, 92, 97, 99, 101, 102, 111, 113, 128, 139, 154, 158, 166, 167, 168, 171, 179, 193, 194, 195, 196, 204, 214

temperature dependence, 34, 83, 101

Tersoff potential, 122

thermal evaporation, 166, 167, 172, 175

thermal expansion, 101

thermal stability, 152, 166, 196, 198

thermochemical reaction, 159

thermodynamic equilibrium, 146, 193

transformation, x, 147, 187, 201, 209

transformations, 191, 200, 213

transmission electron microscopy, 162, 202

treatment, 76, 100, 101, 194, 197

## V

vapor, 166, 167, 170, 171, 173, 174

velocity, 8, 61, 62, 63, 69, 70, 74, 76, 77, 78, 80, 119, 126, 142

viscosity, 73, 74, 75

volatility, 158

Voronoi polyhedron, 126

## W

Washington, 74, 208

waste, 213

wastewater, 119

water, xi, 18, 77, 81, 82, 83, 112, 113, 118, 151, 152, 153, 195, 196, 203, 204, 206, 212, 213, 218

water purification, 153

wave vector, 65

wavelengths, 88

wetting, 147

withdrawal, 136

workers, 38, 201

worldwide, 188, 193, 194, 203

## X

xenon, 116, 125, 142, 155, 156

## Z

zeolites, viii, xi, 154, 188, 194, 196, 199, 201, 202, 204, 206, 207, 208, 209, 210, 212, 220

zinc, 151, 165

zirconia, 194, 195, 205, 206, 207, 208

zirconium, 221